University of Arkansas, Fayetteville
ScholarWorks@UARK

Graduate Theses and Dissertations

12-2021

Study of Thick Indium Gallium Nitride Graded Structures for Future Solar Cell Applications

Manal Abdullah Aldawsari
University of Arkansas, Fayetteville

Follow this and additional works at: https://scholarworks.uark.edu/etd

Part of the Electromagnetics and Photonics Commons, Nanoscience and Nanotechnology Commons, and the Nanotechnology Fabrication Commons

Citation
Aldawsari, M. A. (2021). Study of Thick Indium Gallium Nitride Graded Structures for Future Solar Cell Applications. *Graduate Theses and Dissertations* Retrieved from https://scholarworks.uark.edu/etd/4315

This Dissertation is brought to you for free and open access by ScholarWorks@UARK. It has been accepted for inclusion in Graduate Theses and Dissertations by an authorized administrator of ScholarWorks@UARK. For more information, please contact uarepos@uark.edu.

Study of Thick Indium Gallium Nitride Graded Structures for Future Solar Cell Applications

A dissertation submitted in partial fulfillment
of the requirements for the degree of
Doctor of Philosophy in Microelectronics-Photonics

by

Manal Abdullah Aldawsari
Princess Nora bint Abdulrahman University
Bachelor of Science in Physics, 2007
University of Arkansas
Master of Science in Microelectronics-Photonics, 2015

December 2021
University of Arkansas

This dissertation is approved for recommendation to the Graduate Council.

Morgan Ware, Ph.D.
Dissertation Director

Shui-Qing Yu, Ph.D.
Committee Member

Cynthia Sides, Ph.D.
Committee Member

Douglas Hutchings, Ph.D.
Committee Member

Matthew Leftwich, Ph.D.
Ex-Officio Member

The following signatories attest that all software used in this dissertation was legally licensed for use by Manal Abdullah Aldawsari for research purposes and publication.

________________________________ ________________________________

Ms. Manal Aldawsari, Student Dr. Morgan Ware, Dissertation Director

This dissertation was submitted to http://www.turnitin.com for plagiarism review by the TurnItIn company's software. The signatories have examined the report on this dissertation that was returned by TurnItIn and attest that, in their opinion, the items highlighted by the software are incidental to common usage and are not plagiarized material.

________________________________ ________________________________

Dr. Matthew Leftwich, Program Director Dr. Morgan Ware, Dissertation Director

Abstract

Indium gallium nitride ($In_xGa_{1-x}N$) materials have held great potential for the optoelectronic industry due to their electrical and optical properties. The tunable band gap that can span the solar spectrum was one of the most significant features that attracted researchers' attention. The band gap can be varied continuously from 0.77 eV for InN to 3.42 eV for GaN, covering the solar spectrum from near infrared to near ultraviolet. Additionally, it has a high absorption coefficient on the order of $\sim 10^5$ cm^{-1}, a direct band gap, high radiation resistance, thermal stability, and so on. Nevertheless, the epitaxial growth of high quality In-rich $In_xGa_{1-x}N$ material has faced numerous challenges to date due to lattice mismatch between InN and GaN (up to 11%) and the difference in growth temperatures. This can be the main reason for spinodal decomposition that results in phase separation, relaxation of the strain at the interface, or compositional pulling. Therefore, a high density of defects will be generated in the $In_xGa_{1-x}N$ layer, depending on the growth conditions, which can degrade the optical properties of the material. Thus, understanding and improving the growth conditions which also affect the amount of In incorporated in the material is significant.

Here, graded composition $In_xGa_{1-x}N$ layers have been grown on GaN/sapphire templates. The gradient was accomplished by a continuous increase of the In mole fraction in the atomic flux used to grow the crystal. The growth was done at different temperatures (555 °C to 475 °C) in plasma-assisted molecular beam epitaxy (MBE) to establish good parameters to grow a thick film grading the entire range from x = 0 to 1. Furthermore, this study focused on the optical and structural characterization of the material. It was found that the composition was not linearly graded as expected and was accompanied by strain relaxation along the growth direction. As expected, lower growth temperatures allowed for higher In content. A simple growth model was

used to understand the growth conditions and the parameters that affect the In content in the material. Moreover, nextnano^3 software was used to simulate the band structure and determine the optical transition probabilities as well as the ground state wavefunctions, which can help in future device development.

Acknowledgements

It is not an easy task to acknowledge and appropriately thank all the people who have helped me over the past ten years in completing my doctoral studies. I first thank Allah for meeting all of my needs. It was such a long journey filled with many blessings as well as difficulties. I remember how I started this journey overwhelmed with much fear and hesitation, however, it turned out this journey and this decision to study abroad was a turning point in my life. It has opened many opportunities to learn in both a personal and professional sense. Little did I know that another country could be another home for me, and people with a different language can be my family!

The most important thing I learned and earned from my experiments all these years is that you never fail. It was all a learning process, and if we did not get the desired outcomes, we just needed to explore other approaches and other directions. I can apply that in many aspects of my life, which will help me to go forward.

Being able to get to this point during the pandemic is a blessing! I do not know if it is possible to say that I am glad I weathered the storm and achieved my goal. It was a tough time where the whole world was affected or is even still in the effect of Covid-19. Thus, I am grateful and pleased that I managed to find my way. My forever favorite quote is “if there is a will, there is a way”!

I am very grateful to many people who have helped me earn my PhD degree. I would like to express my gratitude and appreciation to my PhD advisor Dr. Morgan Ware, without whose support I would not be here today. It has really been an incredible pleasure and honor to finish my dissertation under his direction. He gave me the opportunity to work with him and learn from not only his great and deep knowledge, but also how he approaches scientific problems and

solves them. His feedback helped me to bring my work to a higher level. He showed me that each obstacle is just a surmountable challenge that needs hard work and dedication. His support, his smile, his encouragement, and his comments sharpen my thinking and helped me get to where I am today. His door is always open for us, and during the pandemic he showed us how to press on. I am grateful I was able to conduct my research under his guidance. Thank you, Dr. Morgan Ware, for everything.

I would like to recognize the guidance I always received from Dr. Rick Wise. He made earning my degree possible through his advice and support in all the stages of this work. His comments, suggestions and insight encouraged me to conquer all the difficulties I came across. Especially during this past year that was difficult on everyone, he made it bearable being there and answering our questions and supporting us. I am glad I got the chance to do my dissertation with him as the director of the Microelectronics Photonics program. As he approaches his retirement, I wish him all the best in the next chapter of his life.

I would like to thank Dr. Matthew Leftwich the new director of Materials Science & Engineering (MSEN) Graduate Program for continuing my dissertation revision. I sincerely appreciate your assistance and support.

I am also grateful to Renee Jones-Hearon. Without her tremendous support and help I would not have gotten to this day. She is always there assisting all the students and supporting everyone. She helped us to do all the paperwork we needed and to turn in all the requirements, which would have been challenging without her assistance.

I am thankful to my committee members who accepted being a part of this project and for their comments and suggestions for my proposal. I learned persistence and hard work from Dr. Fisher Yu and his lab. I learned from Dr. Cynthia Sides' class critical thinking and thinking out

of the box, which she encouraged me to do. I learned from Dr. Douglas Hutchings that “you cannot guarantee success, but you can guarantee how much work you put in it.”

I would like to acknowledge the wonderful colleagues and friends that I was lucky enough to get to work with. I am also thankful for Dr. Mourad Benamara for helping me and answering my questions about the SEM and TEM measurements. I am also grateful for Errol Porter who assisted and trained me at the High-Density Electronics Center (HiDEC) at the University of Arkansas. I want also to acknowledge the help and training I received from Tom Cannon at (HiDEC).

Throughout my education, I cannot forget the support and the unconditional love that my parents and family provided to me. I am grateful to my husband who supported me all the way to this day and was proud of every successful step that I made through the years. Having my kids here during my PhD degree was a blessing which brought me comfort and pushed me forward.

I thank from the bottom of my heart people around me who eased the ways and opened a lot of opportunities for me. They helped me to get where I am today and are still helping me to be the best I can. I hope to be the same for them.

I have been fortunate enough to work with such an amazing team that has helped me to get through so many difficulties and challenges. I would like to say a special thank-you to Pijush Ghosh, Mirsaeid Sarollahi, Alaa Kawagy, Malak Refaei, Alaa Alnami, Mohammad Zamani Alavijeh, Rohith Allaparthi, Christopher Matthews, and Kelly McKenzie for their help in the lab that I could not have done without their support. Also, I would like to give a special thanks to Hryhorii Stanchu for helping me and sharing his knowledge. I am grateful for Fernando Maia de Oliveira for his help and answering my questions in the lab. I am grateful to my friend Fahimeh Banihasheminan for always being there. I cannot thank her enough!

I am also grateful to my friends here in the USA: Lana Clark, Rachel Scholtes (Calandro), Stephanie Clark, Abigail Woodward, Katie Hartness Barrales, Asmaa Sadoon, and Najla Alnami. Their love and continuous support helped me during the past 10 years being here away from my family and friends. I cannot thank them enough.

I am very grateful to my friends in Saudi Arabia without whose love and support I would not be here today: Mona Alshardan, Fatimah Alhanaya, Tahani Albashiri, and Moneerah Alahmari.

Also, I am grateful to my friends who I met here in the USA: Ebtehal Alosimy, Hala Alshammari, Najla Aldosari, and Nada Alhassan. Our friendship here makes living abroad bearable. I am grateful I got to know them. I cannot thank them enough for their support and encouragement all the way to this day!

My sisters Maha, Haya and Hind are always by my side which has helped me and given me the strength to continue despite all the obstacles. I am grateful to all my brothers and sisters.

Without my parents' love and support, and that of my parents-in-law from the beginning all the way to this day, I would not have been able to achieve my goals. You taught me and showed me the value of education and encouraged me to pursue my dreams.

Remembering where this began and what made it possible to make my dream come true, I am grateful to King Saud bin Abdulaziz University for Health Sciences (KSAU-HS) and the King Abdullah Scholarship program for giving me this valuable opportunity to continue my education and supporting me financially from learning English to getting my PhD degree. I cannot thank them enough, and I will be forever grateful.

I am pleased to arrive at this day. It is such an honor. I cannot wait to start this new chapter in my life and explore more opportunities and experience new things.

Dedication

This dissertation and this hard work are dedicated to my parents Abdullah Aldawsari and Ghazail Alhanaya, my husband Abdullah Alshardan, and my kids (Fahd, Jood, and Sultan), as well as my family, brothers and sisters, and my friends. Your adequate support and never-ending love shape me into the individual I am today, enabling me to achieve my goals and make my dreams come true.

Table of Contents

Chapter 1: Introduction and Physical Properties of III-Nitride Materials....................................1

1.1Band Gap of Group III-Nitrides 1

1.2 Crystal Structure of Group III-Nitrides..1

1.3 Properties of Nitride Alloys 5

1.3.1 Polarization Effects 5

1.3.2 Lattice Mismatch and Strain 8

1.4 Growth of $In_xGa_{1-x}N$ 10

1.5 Photovoltaic Devices...12

1.5.1 P-N Junction 13

1.5.2 Ideal I-V Characteristic 14

1.5.3 Recombination and Generation...16

1.5.4 Solar Spectrum...17

1.5.5 Energy Band Structure 19

1.5.6 Output Parameters of Solar Cells..20

1.6 Organization 21

Chapter 2: Literature Review...23

2.1 State-of-the-Art InGaN Solar Cells 23

Chapter 3: Experimental Methods 30

3.1 Molecular Beam Epitaxy (MBE)...32

3.2 Transmission..33

3.3 Photoluminescence (PL) 35

3.4 X-ray Diffraction (XRD)..38

3.5 Scanning Electron Microscopy (SEM) 40

3.6 Transmission Electron Microscopy (TEM)...41

3.7 Atomic Force Microscopy (AFM)...41

3.8 Raman Scattering..44

3.8.1 Phonon Modes in Nitrides 44

3.9 Secondary Ion Mass Spectrometry (SIMS)...47

Chapter 4: Graded InGaN Thick Films Grown by MBE as a Function of Temperature.............49

4.1. Structure and Band Diagram Simulation 49

4.2. Experimental Results and Discussions 57

4.2.1. Atomic Force Microscopy (AFM) 57

4.2.2 Optical Microscope 59

4.2.3 Scanning Electron Microscopy (SEM)...62

4.2.4 Transmission...62

4.2.5 Photoluminescence (PL)..68

4.2.6 X-ray Diffraction (XRD)..77

4.2.7 Secondary Ion Mass Spectrometry (SIMS): 83

4.2.8 Comparison of the Experimental Band Gap Energies and nextnano^3 Band Gap Energies 86

Chapter 5: Full Composition $In_xGa_{1-x}N$ Thick Film Grown by Molecular Beam Epitaxy.........103

5.1 Structure and Band Diagram Simulation 103

5.2 Experimental Results and Discussions 110

5.2.1 Atomic Force Microscopy (AFM) 110

5.2.2 Optical Microscope Images 111
5.2.3 Transmission 113
5.2.4 Room Temperature Photoluminescence 114
5.2.5 X-ray Diffraction (XRD) 116
5.2.6 Secondary Ion Mass Spectrometry (SIMS) 118
5.2.7 Transmission Electron Microscope (TEM): 123

Chapter 6: A Growth Model for Graded InGaN 129

Chapter 7: Strain -RSM-Raman-Scattering Study of Graded $In_xGa_{1-x}N$ Thick Film 138
7.1 Lattice Parameters and Composition (RSM) 138
7.2 Raman Scattering for Graded InGaN 141
7.2.1 Strain Corrected Frequency: 150

Chapter 8: Preliminary Results for Future Work 152
8.1 Experimental Details 156
8.2 Results and Discussions 161
8.3 Summary 167
8.4 Conclusion 168
8.5 Future Work 168

References 169
Appendix I: The Fabrication Process of Graded InGaN Solar Cell 182
Appendix A: Descriptive of Research for Popular Publication 187
Appendix B: Executive Summary of Newly Created Intellectual Property 189

Appendix C: Potential Patent and Commercialization Aspects of Listed Intellectual Property Items 190

C.1 Applicability of Research Methods to Other Problems 190

C.2 Impact of Research Results on U.S. and Global Society 190

C.3 Impact of Research Results on the Environment 190

Appendix D: Broader Impact of Research 191

D.1 Applicability of Research Methods to Other Problems 191

D.2 Impact of Research Results on U.S. and Global Society 192

D.3 Impact of Research Results on the Environment 192

Appendix E: Microsoft Project for MS MicroEP Degree Plan 193

Appendix F: Identification of All Software Used in Research and Dissertation Generation 199

Appendix G: All Publications Published, Submitted and Planned 201

List of Figures

Figure 1. Strain free band gap energy of InGaN vs. In content..2

Figure 2. Schematic diagram of the wurtzite unit cell and zinc blende of III-nitrides. 3

Figure 3. The bond between Ga and N atoms. 4

Figure 4. Schematic diagram of polarization doping in InGaN..7

Figure 5. Schematics of polar (c-plane), semipolar, and nonpolar (m-plane)...............................8

Figure 6. Compressive and tensile strained films on a substrate 9

Figure 7. Binodal (solid curve) and spinodal (dashed curve) for InGaN....................................11

Figure 8. Migration of electrons and holes in a PN-junction 13

Figure 9. A schematic diagram of solar panel 14

Figure 10. The current-voltage curve (I-V) 15

Figure 11. Standard solar spectra..18

Figure 12. A schematic of energy band diagram for a direct band gap material.........................19

Figure 13. A schematic diagram of the MBE chamber. 33

Figure 14. MBE nitrides chamber at the University of Arkansas...34

Figure 15. The sensitivity range in Shimadzu UV3600 Spectrophotometer...............................35

Figure 16. Photoluminescence (PL) measurement system. 36

Figure 17. A schematic diagram of the photoluminescence (PL) setup. 37

Figure 18. The principle of X-ray difraction (Bragg’s law). 38

Figure 19. The diffraction x-ray occurs in reciprocal space...39

Figure 20. A schematic diagram of SEM microscope. 40

Figure 21. A schematic diagram of TEM microscope. 42

Figure 22. A schematic diagram of AFM basic setup...43

Figure 23. A schematic diagram of Raman scattering measurements setup. 45

Figure 24. Raman scattering microscope. 46

Figure 25. The optical phonon modes in wurtzite group III-nitride crystals...............................47

Figure 26. A schematic diagram of SIMS technique. 48

Figure 27. Absorption coefficient spectra of GaN substrate and InGaN layers at different In Content 50

Figure 28. A schematic diagram of graded InGaN layers structure..52

Figure 29. In profile that was simulated in nextnano^3. 52

Figure 30. The band diagram for strained InGaN. 53

Figure 31.The band diagram for fully relaxed InGaN. 54

Figure 32. Band diagram and electron and hole wavefunction for the homogeneous strain state. 56

Figure 33. Band diagram and electron and hole wavefunction for no strain state. 56

Figure 34. Electron and hole charge densities. 58

Figure 35. AFM images for graded $In_{1-x}Ga_xN$ active layers at different growth temperatures.....59

Figure 36. Optical microscope images for In droplets in: (a) graded InGaN (555 °C), (b) graded InGaN (515 °C), and (c) graded InGaN (475 °C) before etching. 60

Figure 37. Optical microscope images for In droplets in: (a) graded InGaN (555 °C), (b) graded InGaN (515 °C) and (c) graded InGaN (475 °C) after etching. 61

Figure 38. SEM images that show In droplets on the surface of graded InGaN. 64

Figure 39. EDX mapping for In droplets on graded InGaN surface...65

Figure 40. EDX line scans. 66

Figure 41. Room temperature transmission spectra 67

Figure 42. Tauc plot for graded In1-xGaxN active layers at different growth temperatures........67

Figure 43. Graded InGaN PL measurements at room temperature and 15 K for different growth temperatures. 69

Figure 44. The absorption coefficient for InGaN at different In content. 72

Figure 45. Graded InGaN (555 °C) PL measurements at 16 K at different excitation powers. 74

Figure 46. Graded InGaN (515 °C) PL measurements at 16 K at different excitation power. 75

Figure 47. Graded InGaN (475 °C) PL measurements at 16 K at different excitation power. 76

Figure 48. Integrated PL intensity of InGaN films as a function of laser excitation power. 77

Figure 49. Symmetric (0002) X-ray diffraction of thick graded InGaN films at different temperatures. 78

Figure 50. (a) ω/2θ scan and (b) RSM showing the (105) reflection for the graded InGaN (555 °C). 80

Figure 51. (a) ω/2θ scan and (b) RSM showing the (105) reflection for the graded InGaN (515 °C). 81

Figure 52. (a) ω/2θ scan and (b)RSM showing the (105) reflection for the graded InGaN (475 °C). 82

Figure 53. SIMS profile for graded InGaN (555 °C). 83

Figure 54. SIMS profile for graded InGaN (515 °C). 84

Figure 55. SIMS profile for graded InGaN (475 °C). 84

Figure 56. In profile for graded InGaN (555°C). 87

Figure 57. The band diagram for strained InGaN (555 °C). 88

Figure 58. The band diagram for fully relaxed InGaN (555 °C). 89

Figure 59. InGaN (555 °C) band diagram and electron and hole wavefunction for homogenous strain state. 91

Figure 60. InGaN (555 °C) band diagram and electron and hole wavefunction for no strain state. 91

Figure 61. Electron and hole density in InGaN (555 °C). 92

Figure 62. In profile for graded InGaN (515 °C). 93

Figure 63. The band diagram for strained InGaN (515 °C). 94

Figure 64. The band diagram for fully relaxed InGaN (515 °C). 94

Figure 65. InGaN (515°C) band diagram and electron and hole wavefunction for homogenous strain state....................................96

Figure 66. InGaN (515°C) band diagram and electron and hole wavefunction for no strain state 96

Figure 67. Electron and hole density in InGaN (515 °C). 97

Figure 68. In profile for graded InGaN (475 °C). 98

Figure 69. The band diagram for strained InGaN (475 °C). 98

Figure 70. The band diagram for fully relaxed InGaN (475 °C). 99

Figure 71. InGaN (475 °C) band diagram and electron and hole wavefunction for homogenous strain state....................................101

Figure 72. InGaN (475 °C) band diagram and electron and hole wavefunction for the no strain state. 101

Figure 73. Electron and hole density in InGaN (475 °C). 102

Figure 74. The In profile for the ideal case. 103

Figure 75. The band diagram for strained InGaN (475 + 400 °C). 104

Figure 76. The band diagram for fully relaxed InGaN (475 + 400 °C). 104

Figure 77. InGaN band gap against In composition for strained and relaxed material. 105

Figure 78. Graded InGaN band diagram and electron and hole wavefunction for homogenous strain state....................................107

Figure 79. Graded InGaN band diagram and electron and hole wavefunction for no strain state. 107

Figure 80. The electron and hole density for full graded InGaN. 108

Figure 81. A schematic diagram for graded InGaN sample (475 + 400 °C). 109

Figure 82. AFM images of 5 × 5 μm in (a) and 1 × 1 μm in (b). 111

Figure 83. Optical microscope images for graded InGaN (475 °C + 400 °C): (a) before HCl etching and (b) after HCl etching. 112

Figure 84. Transmission spectra for graded InGaN (475 °C + 400 °C)....................................113

Figure 85. Tauc plot for graded InGaN (475 °C + 400 °C)..114

Figure 86. Room temperature PL measurement for graded InGaN...115

Figure 87. XRD ω/2θ of the plane (0002) and RSM for full graded InGaN.............................117

Figure 88. Graded full composition InGaN SIMS profile...118

Figure 89. In SIMS profile for full graded composition InGaN..119

Figure 90. InGaN (475°C + 400 °C) band diagram for homogeneous strain...........................120

Figure 91. InGaN (475°C + 400 °C) band diagram for no strain. 121

Figure 92. InGaN (475 °C + 400 °C) band diagram and electron and hole wavefunction for homogenous strain state. 122

Figure 93. InGaN (475 °C + 400 °C) band diagram and electron and hole wavefunction for no strain state...123

Figure 94. Electron and hole density for full graded InGaN...124

Figure 95. TEM images for graded full composition InGaN. 125

Figure 96. TEM and FFT images for full graded composition InGaN. 126

Figure 97. EDS image that shows the composition profile in the graded InGaN layer.............127

Figure 98. Simulation of In SIMS profile for graded InGaN (555 °C)....................................131

Figure 99. Simulation of In SIMS profile for graded InGaN (515 °C)....................................131

Figure 100. Simulation of In SIMS profile for graded InGaN (475 °C)..................................132

Figure 101. Simulation of In SIMS profile for graded InGaN (475 + 400 °C).........................132

Figure 102. The critical thickness for graded InGaN vs. In composition from different theories. 135

Figure 103. Simulation of strain component for graded InGaN..136

Figure 104. GaN template Raman spectra...142

Figure 105. Raman scattering for graded InGaN excited with a 532 nm laser line...................143

Figure 106. Room temperature Raman spectra of graded InGaN excited with a 632.8 nm laser. 144

Figure 107. Raman spectra of graded InGaN excited with a 532 nm laser. 145

Figure 108. InN/GaN Raman spectra. 146

Figure 109. Full graded InGaN Raman spectra. 146

Figure 110. Measured frequency of the A_1(LO) phonon and the MREI model (dashed line). 147

Figure 111. The strain corrected A1(LO) frequency. 151

Figure 112. A schematic diagram for the light intensity passing through a graded material. 154

Figure 113. In profile from SIMS measurements. 155

Figure 114. The optical generation rate in graded InGaN. 155

Figure 115. In profile from SIMS measurements. 156

Figure 116. The optical generation rate in graded InGaN. 157

Figure 117. The mesa mask. 158

Figure 118. The contact mask. 159

Figure 119. The graded InGaN device in a chip carrier. 160

Figure 120. Current-voltage measurements of graded InGaN device under dark and illumination. 161

Figure 121. The photocurrent of graded InGaN. 162

Figure 122. The IV curve first derivative. 163

Figure 123. EQE spectrum for graded InGaN device. 165

Figure 124. EQE for certain wavelength at different bias voltages. 166

List of Tables

Table 1: The lattice parameters and spontaneous polarizations for GaN, InN and AlN................5

Table 2. The efficiency of InGaN based solar cells for different structures and compositions. ...27

Table 3. Raman-active mode frequencies of nitride materials (wurtzite structure)......................47

Table 4. The estimated thickness for an absorber layer. 50

Table 5. The energy band gap for both strained and fully relaxed InGaN at different depths......55

Table 6. The calculated penetration depth of the UV laser (325 nm) in InGaN...........................72

Table 7. The band gap energy of graded InGaN from different measurements...........................86

Table 8. The energy band gap and the corresponding In composition for InGaN (555 °C). 90

Table 9. The energy band gap and the corrsponding In composition for InGaN (515 °C)...........95

Table 10. The energy band gap and the corrsponding In composition for InGaN (475 °C).......100

Table 11. The energy band gap for graded full composition InGaN. 106

Table 12. Experimental band gap energy for graded full composition InGaN. 119

Table 13 The energy band gap for full graded composition InGaN (475 + 400 °C).................122

Table 14. The critical thickness calculated values..137

Table 15. The converted lattice constants. 139

Table 16. Strain and relaxation degree calculations. 140

Table 17. The penetration depth for a 532 nm laser. 148

Table 18. The penetration depth for a 632.8 nm laser. 149

Table 19. The measured Raman frequencies and the calculated strain components. 149

Table 20. The strain corrected frequency. 151

Table 21. The parameters of GaN and InN that were used in the simulation. 152

Table 22. The calculated ideality factor using IV curve measurements. 164

Chapter 1: Introduction and Physical Properties of III-Nitride Materials

In 2014, the Nobel Prize in physics was awarded to engineers Isamu Akasaki, Hiroshi Amano, Shuji Nakamura for their GaN-based blue light-emitting diode (LED) invention in 1990[1]. That invention has opened many opportunities for III-nitride materials to be used not only in LED technology but also to other fields such as photovoltaics and power electronics. Though many difficulties are yet to be solved, the unique properties of III-nitride materials make them a great candidate for many applications.

1.1 Band Gap of Group III-Nitrides

Ternary group III-nitrides (like $In_xGa_{1-x}N$ and $Al_xGa_{1-x}N$) have a wide and direct band gap that can be varied depending on the alloy composition, from 0.64 eV for InN to 3.43 eV for GaN and extending to 6.14 eV for AlN[2],[3].

Vegard's law is normally used to determine the band gap of the alloy as follows:

$$E_g(\text{InGaN}) = \Big((1-x) \times E_g\,(\text{GaN})\Big) + (x \times E_g\,(\text{InN})) - (b \times x \times (1-x)) \qquad \text{(Equation 1)}$$

where the E_g (GaN) at 300 K is 3.39 eV, E_g (InN) is 0.7 eV and b is a bowing parameter which estimates the deviation between InN and GaN. Many values have been reported for the bowing parameter, b, such as 1.43, 1.36 and 1.65 eV, as a result of strain, phase separation, fluctuation of composition, and so on, making it difficult to determine an accurate value. Figure 1 demonstrates the band gap values versus In composition where b = 1.43.

1.2 Crystal Structure f Group III-Nitrides

There are three types of crystal structure structures that group III nitrides share wurtzite,

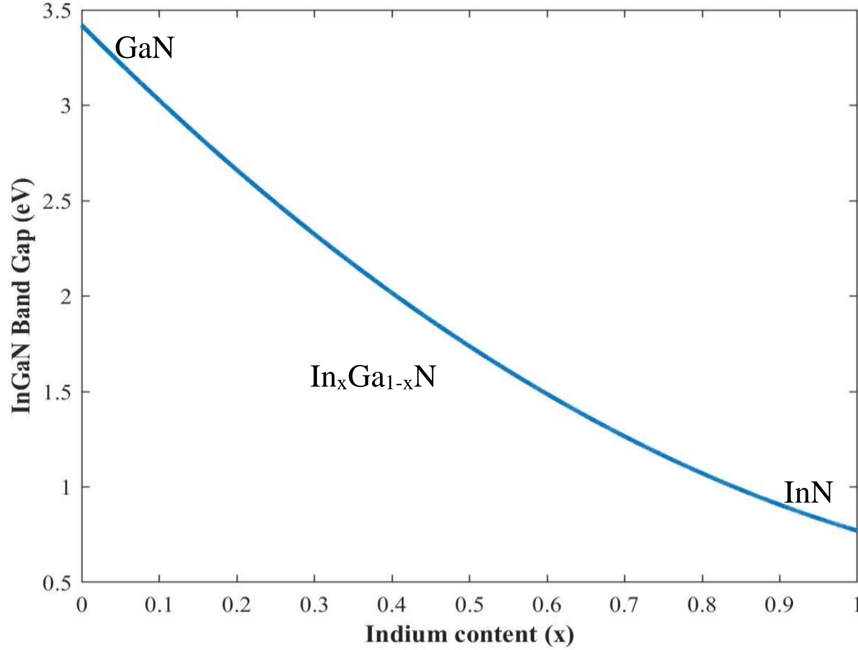

Figure 1. Strain free band gap energy of InGaN vs. In content

zinc blende and rock-salt. For bulk nitride material (AlN, GaN, and InN), the wurtzite structure is the thermodynamically most stable phase. Nitrogen atoms have larger electronegativity compared to the other elements of group V, which leads to higher ionicity in III-nitrides than other semiconductors. This causes the crystal structure of group III-nitrides to favor the wurtzite structure[4].

The unit cell of the zincblende phase is formed by two penetrating face-centered cubic (fcc) lattices which have a bond length of 1.623 Å. In each corner of the cubic lattice there is one atom of group III attached tetrahedrally to four N atoms. On the other hand, the unit cell of the wurtzite phase is a hexagonal structure which has the lattice parameters a and c where the ratio is as follows:

$$c/a = \sqrt{8/3} = 1.633 \qquad \text{(Equation 2)}$$

Moreover, the wurtzite structure includes two penetrating hexagonal close-packed (hcp) lattices that have the same axis but displaced by an amount u, where is u = 3/8 = 0.375 as a displacement along the c axis. The atoms in each unit cell are arranged in tetrahedral symmetry that is composed of an atom of group III attached to four nitrogen atoms[5]. The schematic diagram of the wurtzite unit cell and zinc blende unit cell of III-nitrides is shown in Figure 2.

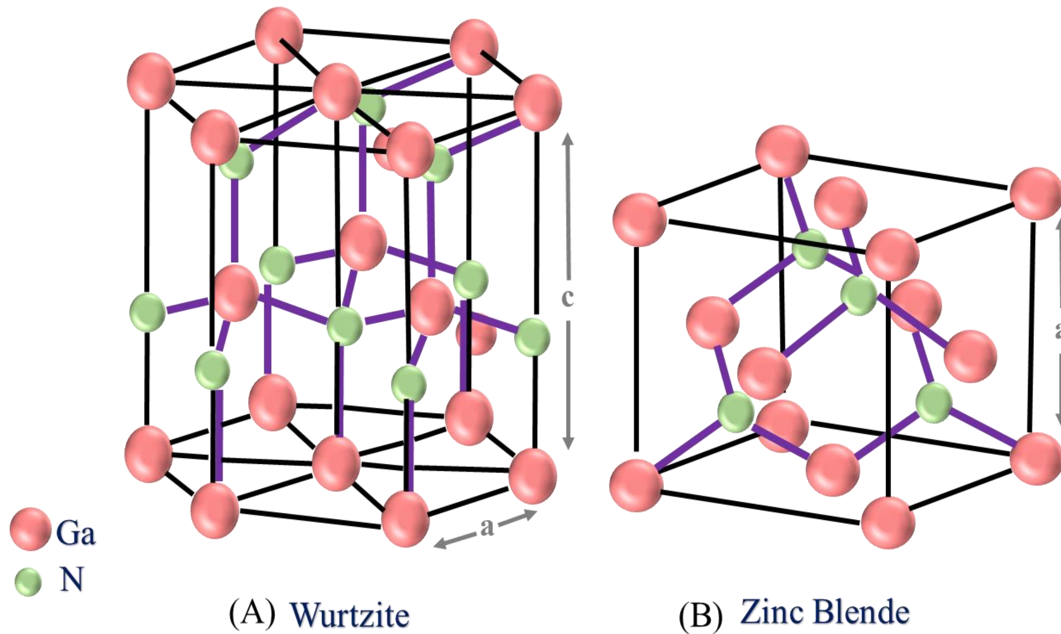

Figure 2. Schematic diagram of the wurtzite unit cell and zinc blende of III-nitrides.

The unit cell of GaN is a hexagon that has the bonds along the c-axis with different length than the bonds that are not on the c-axis. This results in spontaneous polarization. Another property in nitride materials is the electronegativity difference between group III metal cations and the nitrogen anion. It is another important characteristic that induces strain in the unit cell and results in another type of polarization. To explain, the electronegativity difference can be defined as the ability of an atom to attract electrons in a bond that it forms with another atom.

The nitrogen anion has a larger electronegativity (3.04) compared to the group III metal cations Ga (1.81), In (1.78), and Al (1.61), which affects the wurtzite structure.

Therefore, in GaN unit cell, Ga atom will be bonded to 4 N atoms and the electrons will be shifted towards N and less toward Ga as shown in Figure 3. This cause polarization along the bond (Ga-N) like a dipole. The total in-plane polarization will cancel each other but the total vertical polarization in the z direction (the growth direction) will not cancel each other. Therefore, the unit cell is polar acts and like a dipole. This will cause strain in the unit cell and induce piezoelectric polarization. In another words, an internal electric field arises along the c-axis direction which is called piezoelectric polarization; this will be discussed in the following section. The total polarization in the crystal will be the spontaneous polarization plus the piezoelectric polarization. This polarization effect leads to either a negative or positive effect depending on how it is engineered in the device[6].

The lattice constants and band gap energies as well as the spontaneous polarization are different in group III nitrides because of the difference in bonding energy with nitrogen and the

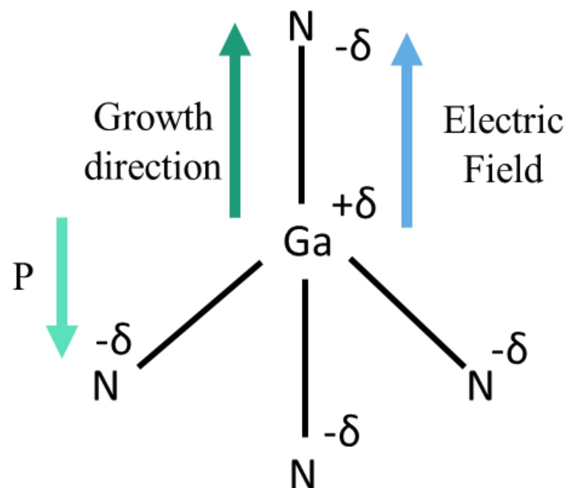

Figure 3. The bond between Ga and N atoms.

ionic radii[7]. Table 1 shows the lattice parameters and spontaneous polarizations for GaN, InN, and AlN[8],[9],[10].

Table 1: The lattice parameters and spontaneous polarizations for GaN, InN and AlN.

Parameter	GaN	InN	AlN
Lattice constant c (Å)	5.186	5.685	4.9808
Lattice constant a (Å)	3.189	3.517	3.112
c/a ratio (ideal = 1.633)	1.62606	1.616	1.60054
u (ideal = 0.375)	0.3789	0.377	0.3869
Spontaneous polarization (C/m^2)	-0.029	-0.032	-0.81

1.3 Properties of Nitride Alloys

1.3.1 Polarization Effects

One of the important properties inherent in the III-V nitride semiconductors (GaN, AlN, InN) is large polarization effects. Unlike the zinc-blende crystal structure, the wurtzite crystal structure is non-centrosymmetric, meaning it lacks inversion symmetry which causes spontaneous polarization. In addition, the bond between Ga and N exhibits large ionicity that induces a piezoelectric polarization effect. Thus, both zinc-blende and wurtzite crystal structures exhibit piezoelectric polarization, whereas the symmetry in the zinc-blende structure prohibits spontaneous polarization. Another characteristic of nitride materials is that the heterostructures of III-nitride materials possess a large difference in lattice constants of the binary compounds GaN, AlN, and InN. This large lattice mismatch during epitaxial growth induces strain in the top epitaxial layer to adjust its lattice constant to the underlying semiconductor. This, in turn, results in piezoelectric polarization which can dramatically affect device performance. Therefore, the net polarization in the wurtzite structure of nitride materials is comprised of two components: spontaneous polarization which is inherent in the material, and piezoelectric polarization which

is induced by strain in the material. A considerable amount of literature has been published on polarization-engineered III-nitride materials which results in polarization doping, carrier confinement and band engineering[11],[6],[12].

The most common epitaxial growth direction of III-V nitrides is the c-axis of the wurtzite hexagonal structure. Spontaneous polarization exists along the c-axis which is the growth direction. Polarization can be detrimental to carrier collections in photovoltaic devices as it generates an internal electric field and potential wells that can increase the recombination rate. However, polarization can be engineered to improve device performance as well as realize polarization doping.

Polarization doping can be achieved through graded composition, which is an advantage of using a graded structure. It helps to get p-type doping without the introduction of any dopants, which is a challenge in GaN due to the high activation energy of Mg (E_A ~ 200 meV) [13]. Simon et al. introduced using this for ultraviolet light emitting diodes (UV LEDs) using AlGaN. It was demonstrated that using graded composition instead of sharp heterojunctions will produce regions of three-dimensional electron slabs (3DES) or 3D hole gas according to Equation 3:

$$\rho(z) = -\nabla.\bar{P}(z) = \left(\frac{\partial P}{\partial x}\right) \times \left(\frac{\partial x}{\partial z}\right) \qquad \text{(Equation 3)}$$

where $\rho(z)$ is the volume density of polarization charge in the z direction and ∇ is the divergence operator[13],[14].

In theory, grading from GaN to $In_xGa_{1-x}N$ will result in p-type material, while grading from $In_xGa_{1-x}N$ to GaN will result in n-type doping. The polarization (P) increases when x (In content) increases so the unbalanced bound charge in any two adjacent unit cells when the

material is graded down from GaN to $In_xGa_{1-x}N$ will be negative. Thus, equivalent holes will be introduced from native defects, such as background intrinsic carriers and Ga vacancies according to the Poisson equation[15]. These holes will neutralize the negative bound charge and result in p-type doping as they lower the Fermi level[16]. Likewise, a positive bound charge will be attained when grading up from $In_xGa_{1-x}N$ to GaN. Therefore, equivalent electrons such as donor-like surface states will be attracted to realize n-type material as demonstrated in Figure 4[13].

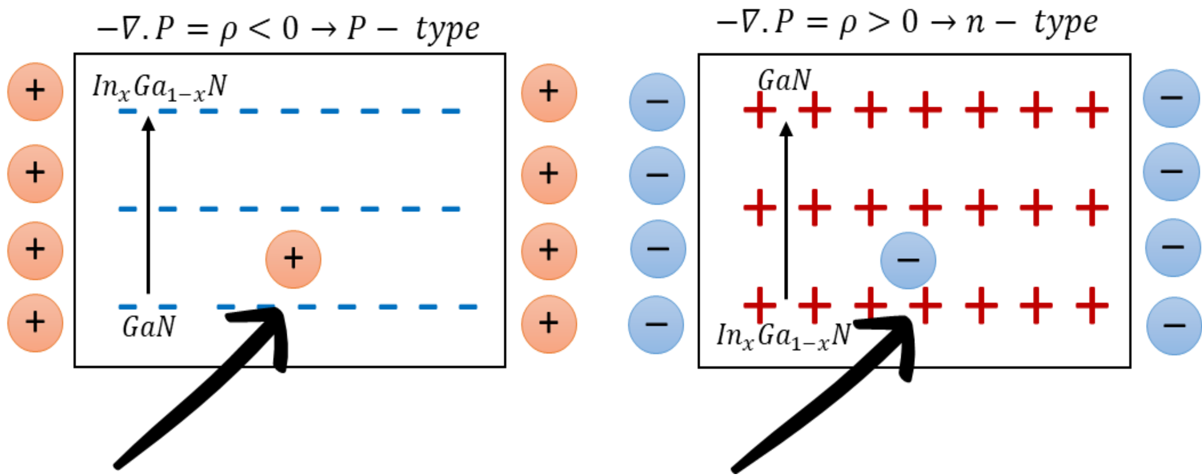

Figure 4. Schematic diagram of polarization doping in InGaN.

The crystal planes of the wurtzite structure of GaN can be classified based on their polarity into three categories: polar, for instance c-planes or (0001), semipolar such as $(30\bar{3}1)$, $(20\bar{2}1)$, $(10\bar{1}1)$, and nonpolar planes including m-planes or $(10\bar{1}0)$. A strong polarization-induced electric field is present when a device is grown along the c-axis, which affects the device performance due to the quantum-confined Stark effect (QCSE) and results in band bending. This phenomenon results in reduced electron-hole wavefunctions overlap, which in turn will decrease the efficiency. However, the semi-polar and non-polar devices show higher electron-hole

wavefunctions overlap because of the decreased QCSE due to the eliminated polarization effect.

This increases the rate of radiative recombination which leads to high efficiency devices[17]. Schematics of polar (c-plane), semipolar, and nonpolar (m-plane) were used from reference[17], as shown in Figure 5.

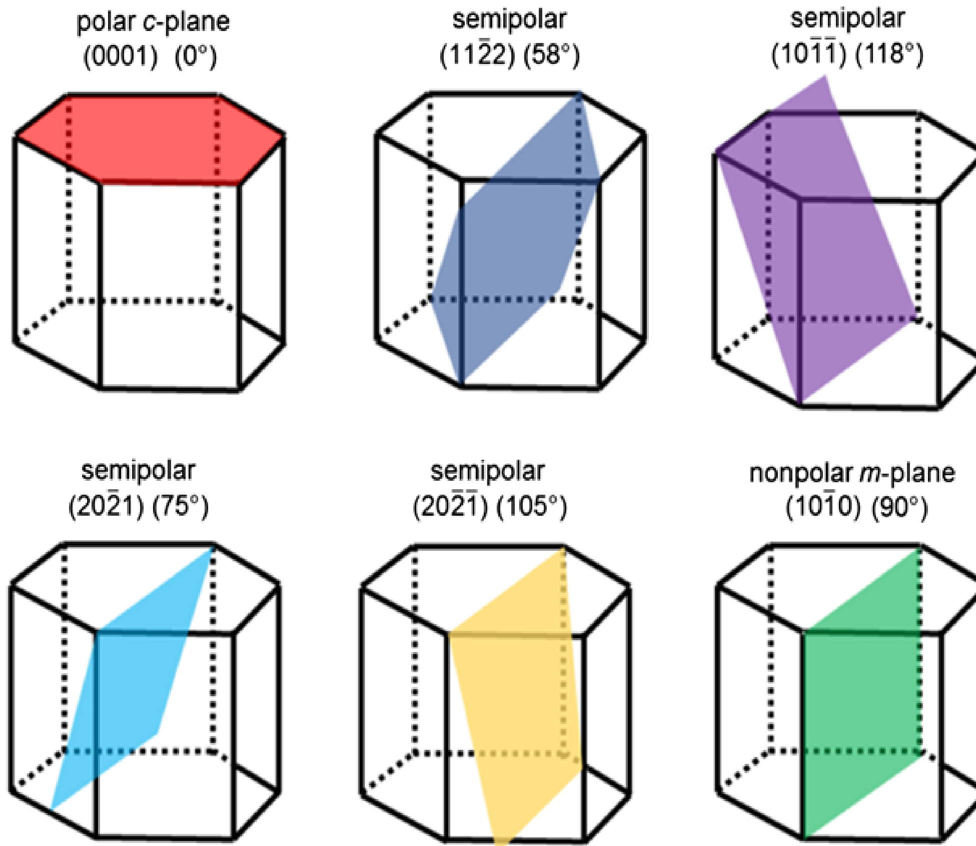

Figure 5. Schematics of polar (c-plane), semipolar, and nonpolar (m-plane)[17].

1.3.2 Lattice mismatch and Strain

The large mismatch in the lattice constants of sapphire substrate and group III-nitride material results in a strained layer if the thickness of the grown layer is below a critical thickness. However, if the growth is above the critical layer thickness, relaxation will occur due to defects present. Higher In mole fraction reduces this critical thickness[18]. The lattice mismatch strain

can be either compressive or tensile. In the case of $In_xGa_{1-x}N$ growth, InN has a larger lattice constant than GaN, which leads to compressive strain. However, it is the opposite when it comes to $Al_xGa_{1-x}N$ growth, as the AlN lattice constants are smaller than the GaN lattice constants, which causes tensile strain. Figure 6 presents the two types of lattice strain, and it shows this according to the equation[19]:

$$f = \frac{\Delta a}{a_s} = \frac{a_l - a_s}{a_s} \qquad \text{(Equation 4)}$$

where f is the lattice strain, a_l is the lattice constant for the layer, and a_s is the lattice constant of the substrate. Compressive strain occurs when the lattice constant of the layer is larger than the

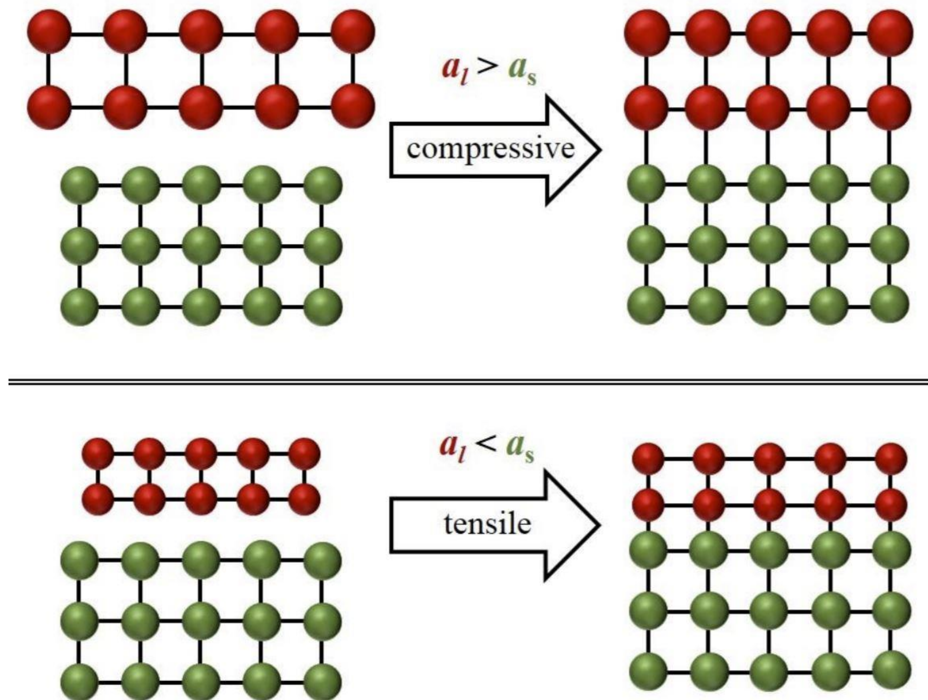

Figure 6. Compressive and tensile strained films (the red atoms) on a substrate (the green atoms) [19].

lattice constant of the substrate, and this is the case in InGaN. On the other hand, tensile strain occurs when the lattice of the layer is smaller than the lattice constant of the substrate, such as in AlGaN.

1.4 Growth of $In_xGa_{1-x}N$

Many growth methods of wurtzite $In_xGa_{1-x}N$ films on a sapphire substrate have been reported such as metal organic vapor phase epitaxy (MOVPE), molecular beam epitaxy (MBE), metal organic chemical vapor deposition (MOCVD), hydride vapor phase epitaxy (HVPE), and so on. In this research, molecular beam epitaxy (MBE) generally forms a two-dimensional layer-by-layer growth of thin films under a high vacuum at about 10^{-10} torr. This process requires a lower growth temperature compared to other techniques, especially with the presence of nitrogen plasma as a nitrogen source. With a plasma nitrogen source, nitride materials can be grown at low growth temperatures, which lowers the thermal stress [20].

The growth of $In_xGa_{1-x}N$ material is challenging due to two reasons: the large difference in the interatomic spacing between InN and GaN which causes a solid phase miscibility gap, and the low growth temperature of InN that is needed to overcome the thermal decomposition since it has high vapor pressure compared to GaN. The growth temperature of InN is generally below 550 °C, while GaN can be grown at temperatures above 800 °C. However, this low temperature will result in low-quality $In_xGa_{1-x}N$ material. Also, the low growth temperatures lead to indium segregation and the formation of metal droplets on the surface that hinders In incorporation in the material. These In clusters increase with decreasing the growth temperature[21],[22].

Other difficulties include distributing a uniform temperature across the substrate, which is due to radiation losses and the reflection of the coating of the back of the substrate material.

Overall, the growth can be optimized by controlling the growth parameters and monitoring the growth using reflection high energy electron diffraction (RHEED)[20]. Some parameters that can overcome some of these problems are the flux ratio of III/V that should be higher than one, a relatively low growth rate, and low growth pressure[23].

Phase separation is a major issue for $In_xGa_{1-x}N$ growth due to the miscibility gap. Ho and Stringfellow calculated the phase diagram for spinodal decomposition curve for strain free InGaN, but the strain must be considered for the growth of InGaN on GaN substrate. It was theoretically demonstrated that the interatomic difference between InN and GaN results in a big miscibility gap, as shown in Figure 7. At a temperature of 800 °C, the solubility of In in GaN is found to be 6%, which indicates that this gap is a substantial issue during the epitaxial growth[24].

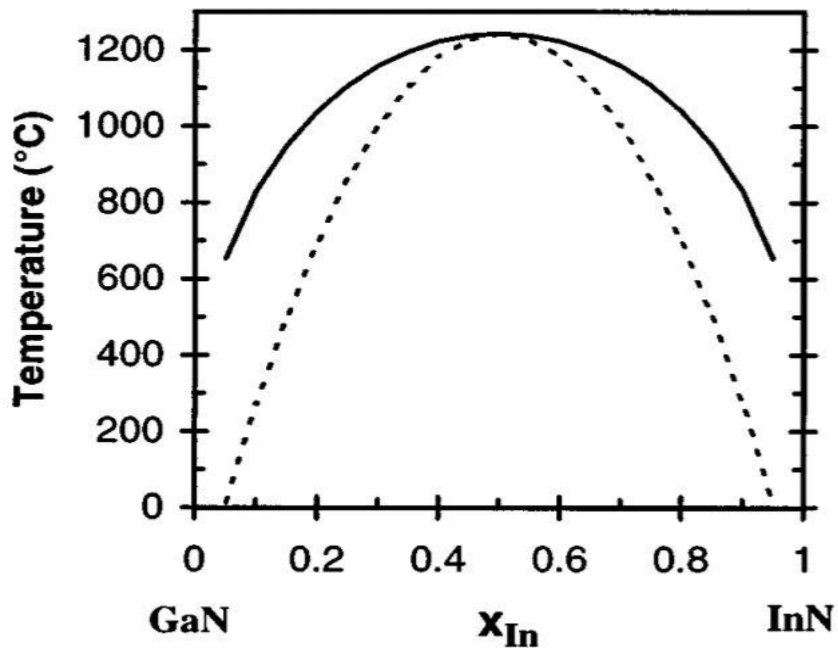

Figure 7 . Binodal (solid curve) and spinodal (dashed curve) for InGaN [24].

Additionally, the two lines of the spinodal and binodal were described by Karpov. It was observed that the miscibility gap shows a slightly asymmetric shape that is closer to the In-rich region due to the strain that increases with higher In content[25].

1.5 Photovoltaic Devices

The tunable band gap of III-nitride materials and their photovoltaic effects make them suitable for optoelectronic applications such as light emitting diodes (LED) and solar cells. The focus of this work is on solar cells, which will be discussed in this section.

A solar cell is a semiconductor device consisting of a p-type junction and an n-type junction that convert sunlight into electricity due to a photovoltaic effect. The most common material for solar cells is silicon (Si) because of its non-toxicity, abundance, and low manufacturing cost[26].

Silicon solar cells can absorb a wide range of solar spectrum, from NIR to UV, but it loses efficiency at energies higher than the bandgap which is lost to heat. Additionally, for high energy light such as UV and above, the absorption is too strong, and the light does not penetrate to the active region as it gets absorbed at the contacts. Thus, other materials and structures have been explored throughout the years, and a lot of improvements have been achieved.

One option is using $In_xGa_{1-x}N$ material to overcome these issues, as it has a wide and direct bandgap. Also, it absorbs a wide spectrum efficiently compared to Si solar cells. This work presents a lot of analysis and studies of the $In_xGa_{1-x}N$ material, but the physics of solar cells will be presented first.

1.5.1 P-N junction

Like a diode, a solar cell is a p-n junction that is formed by p-type material and n-type material. As demonstrated in Figure 8[27], under equilibrium conditions electrons flow from the high concentration of n-type to the p-type region. Similarly, holes tend to flow from the high concentration p-type region to the n-type region. This flow generates ionized charges on both sides of the junction which creates an internal electrical field opposite to the flow direction of electrons and holes. A depletion region (or space-charge region) will be formed in between the p-type and n-type materials that is depleted of mobile charges. The Fermi level is constant in this case and the width of depletion region depends on the doping density. A solar panel is composed of solar cells. They can be connected in series or parallel or a combination of both methods to obtain the needed electrical power. A schematic diagram of a solar panel is shown in Figure 9 [28].

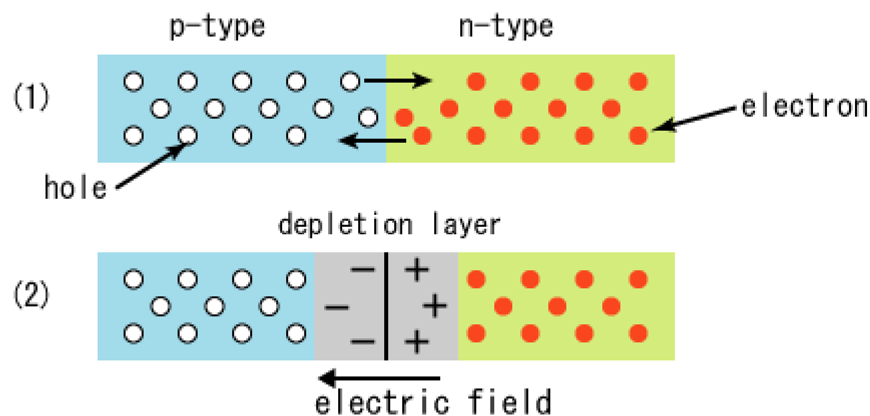

Figure 8. Migration of electrons and holes in a PN-junction [27].

When the solar panel is illuminated by sunlight, the energy of the incident photons is converted into electricity. Under open-circuit conditions, the net current inside the pn-junction is

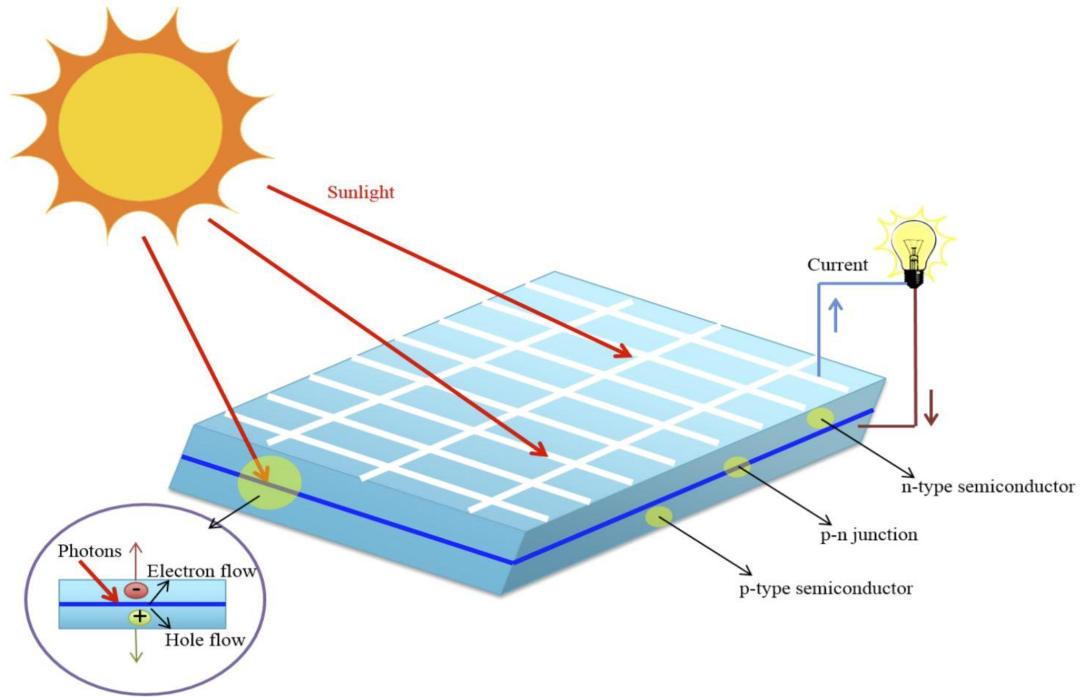

Figure 9. A schematic diagram of solar panel [28].

zero. Thus, the photo- and thermally generated carrier flux is equal to the recombination rate. On the other hand, when a load is applied between electrodes of a pn-junction under illumination, the photogenerated current will flow in an external circuit creating a flow of electricity[26].

1.5.2 Ideal I-V Characteristic

The p-n junction ideal I-V curve is explained by Shockley's equation:

$$I = I_{photon} - I_0(e^{\frac{qv}{KBT-1}}) \quad \text{(Equation 5)}$$

where I is the net current, I_0 is the dark saturation current which is the leakage current density in the absence of illumination, I_{photon} is light generated current, v is the applied voltage, q is the absolute value of electron charge, K is Boltzmann's constant, and T is the absolute temperature in degrees kelvin (K). The photogenerated current is described by the following equation:

$$I_{photon} = qAG(L_e + W + L_h) \quad \text{(Equation 6)}$$

where L_e is the electron minority carrier diffusion length, L_h is the hole minority carrier diffusion length, W is the depletion region depth, A is the cross-section area of the illuminated device, G is the electron-hole generation rate, and q is the electron charge. Current-voltage (I-V) measurements normally describe the potential current or power available from a solar cell as a function of the applied voltage.

The I-V curve as shown in Figure 10[29] describes the relationship between the current and voltage and identifies the device operation within an electrical circuit.This curve describes how in order to acquire the solar cell maximum power, the solar cell has to operate at the maximum power (P_{MP})[29].

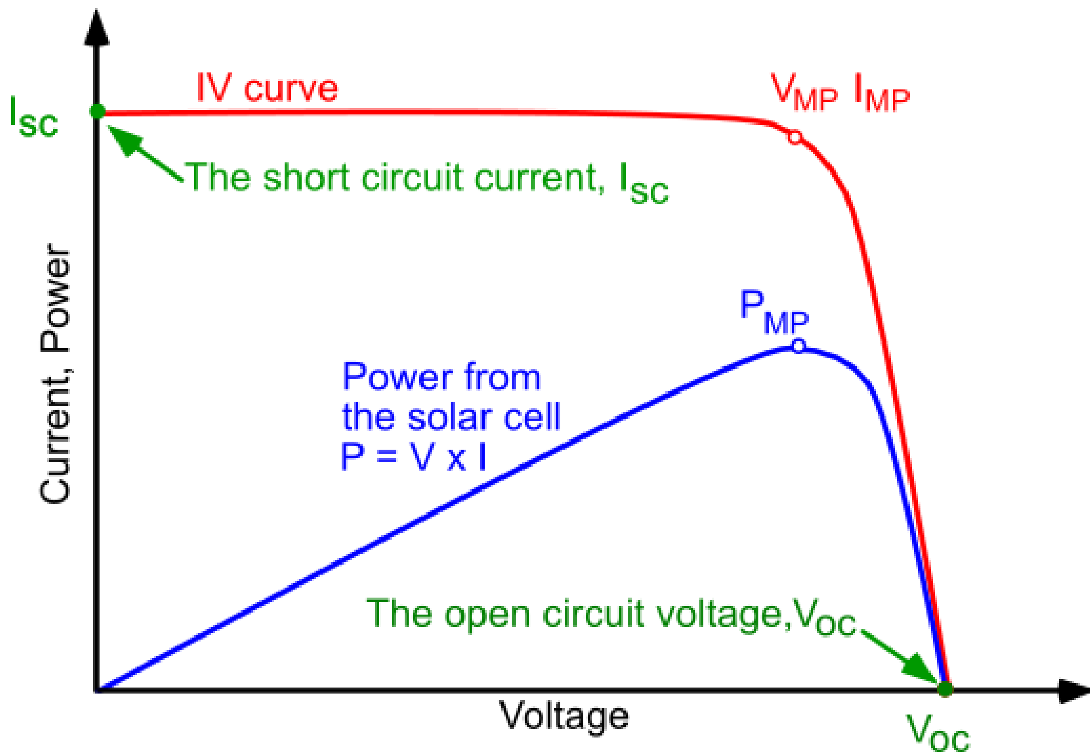

Figure 10. The current-voltage curve (I-V) [29].

1.5.3 Recombination and Generation

One of the most substantial elements that determines the photovoltaic device efficiency is recombination. Recombination is a process that happens when electrons lose their energies and move back to their valence band and recombine with holes.

There are three types of recombination: radiative, recombination through defect levels, and Auger. The two most dominant recombination processes are Auger recombination and recombination through defect levels[30].

Radiative Recombination

Radiative recombination, also known as band-to-band recombination, is a well known mechanism in direct bandgap semiconductors like light emitting diodes (LED), concentrators, and space solar cells. However, indirect bandgap semiconductors have very low rates of radiative recombination.

During radiative recombination, a photon is emitted after a recombination occurs between an electron from the conduction band directly with a hole in the valence band. The energy emitted from this process is similar to the energy of the band gap. Thus, the radiative recombination process is the opposite of the photon absorption process[30],[31].

Recombination through defect levels

Shockley-Read-Hall (SRH) recombination happens through a trap level or defect energy level in the band gap. In this type of recombination, a defect in the crystal lattice is introduced either unintentionally or intentionally to trap an electron or hole in the forbidden region by the energy state. The recombination occurs when the hole or electron rises up to the same energy level before the electron is re-emitted to the conduction band. The movement of a carrier in the

forbidden gap depends mainly on the distance of the introduced energy level from the band edges. As a result, there is less of a chance for recombination to happen. Therefore, the recombination between electrons and holes increases in the near mid-gap area[30].

Auger Rrecombination

Auger recombination is a non-radiative recombination that contributes to the efficiency loss of a device[32]. Three carriers are involved in this type of recombination. During the recombination of the electrons and holes, the released energy is given to a third carrier, an electron, in the conduction band instead of emitting it in the form of heat or a photon. Then, this electron moves back to the conduction band edge thermally.

This type of recombination is very important in materials with high carrier concentration, such as heavily-doped or high-level injected materials. Auger recombination affects the lifetime and efficiency of silicon-based solar cells because when the material is heavily doped, the Auger recombination lifetime is shorter[30],[33].

1.5.4 Solar Spectrum

The surface temperature of the sun is about 5762 K with a radiation spectrum approximated by the black body radiator. Radiation that is emitted from the sun is isotropic. Additionally, the great distance between the earth and the sun, about 150 million kilometers, has led to the fact that only those photons emitted directly at the earth will exist in the solar spectrum.

The radiation intensity or solar constant is about 1.353 kW/m^2. An air mass zero (AM0) radiation spectrum refers to the spectral distribution, and it used to determine how the spectral content and intensity of the solar radiation are affected by absorption of the atmosphere. The air

mass number is defined as:

$$\text{Air mass} = \frac{1}{\cos\theta} \quad \text{(Equation 7)}$$

where θ is the angle of incidence (θ = 0). The air mass number is always greater than or equal to 1 at the Earth's surface. The AM1.5 (θ = 48.2°) spectrum is the most commonly used standard to compare the performance of solar cells by normalizing it to a total power density of 1 kW/m^2. There are diffusive components in the solar spectrum at the Earth's surface that can account for up to 20% of the incident light on a solar cell. Therefore, the air mass can be calculated by either having or not having the diffusive components in the measured spectrum.

An AM1.5g (global) spectrum includes the diffuse component, while an AM1.5d (direct) does not include it. Black body (T = 5762 K) AM0 and AM1.5g radiation spectrums are shown in Figure 11[34],[35].

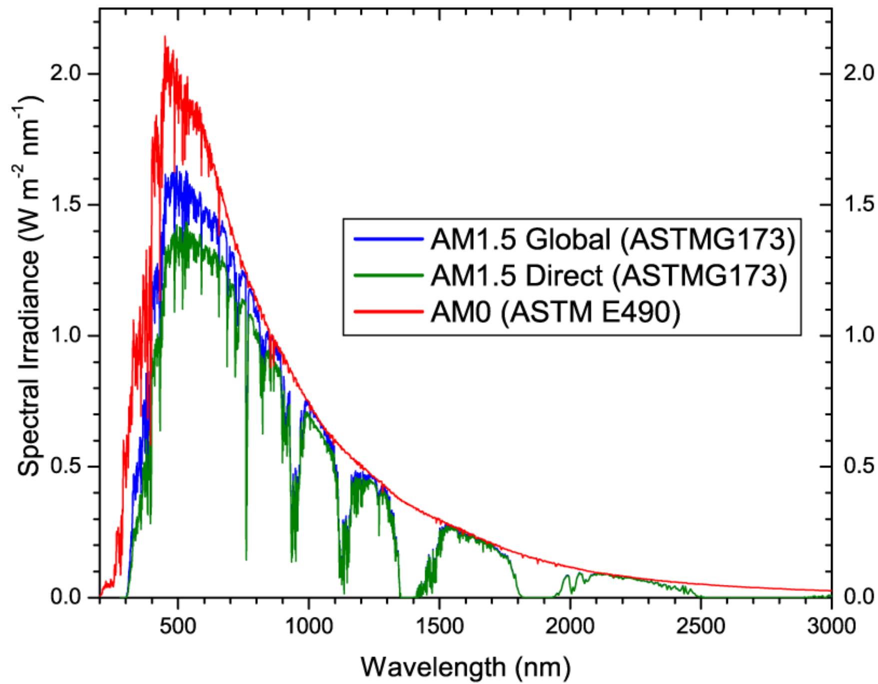

Figure 11. Standard solar spectra [35].

1.5.5 Energy Band Structure

Energy band structure is the relationship between the energy and momentum of electrons in the semiconductor. In free space, an electron is proportional to its mass, while in a crystal it is proportional to its effective mass. Solving the time-independent Schrodinger equation provides the electron wavefunction (ψ) that describes the dynamic behavior of the electron.

$$\nabla^2\psi + \frac{2m}{h^2}[E - U(\vec{r})] = 0 \qquad \text{(Equation 8)}$$

where E is the energy of the electron, m is electron mass, h is the reduced Planck constant, and $U(\vec{r})$ is the periodic potential energy inside the semiconductor[34].The shape of the top of the valence band and the bottom of the conduction band are parabolic shapes as shown in Figure 12. Thus, the electron effective mass and hole effective masses are constant in the bottom of conduction band and the top of valence band, respectively. When the bottom of the conduction

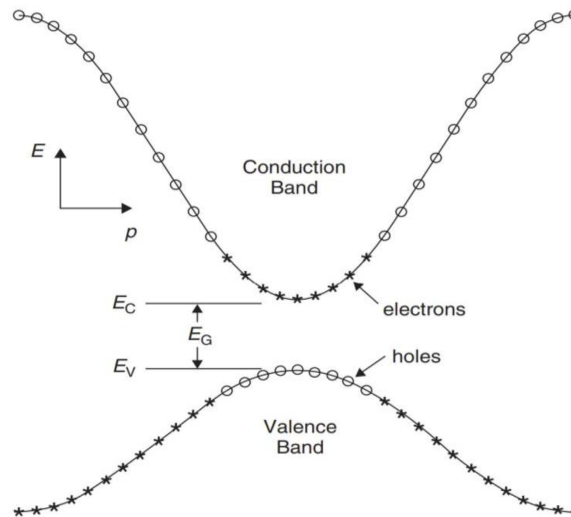

Figure 12. A schematic of energy band diagram for a direct band gap material [34].

band aligns with the top of the valence band, the semiconductor is considered a direct band gap semiconductor, and if they are not aligned, then it is an indirect band gap semiconductor[34].

1.5.6 Output Parameters of Solar Cells

Short Circuit Current of Solar Cell

Short circuit current is the maximum current that a solar cell can produce when the voltage is zero. The measurement is done by short circuiting the cell's terminals under optimized conditions to generate a maximum output. In the solar cell, the rate of production of current relies mainly on the light intensity and the incident angle at which the light hits the cell. In addition to that, it depends on the surface area that is exposed to the light. Therefore, the short circuit current can be defined as:

$$J_{sc} = \frac{I_{sc}}{A} \qquad \text{(Equation 9)}$$

where I_{sc} is the short circuit current, J_{sc} represents the maximum current density, and A is the area of the solar cell[34],[36].

Open-Circuit Voltage

By measuring the voltage across the solar cell terminals, the open-circuit voltage can be measured without a load connected to it. The open circuit voltage depends on the manufacturing techniques and temperature rather than on the intensity of light and area of the exposed surface. The most known range of an open circuit voltage (V_{oc}) solar cell is nearly equal to 0.5 to 0.6 V[37].

Fill Factor of Solar Cell

The definition of fill factor, FF, is the ratio between the maximum power (i.e., the power at which the product of the current and voltage reaches a maximum) to the product of short circuit current and open circuit voltage of the solar cell[36]:

$$FF = \frac{P_m}{I_{sc} \times V_{oc}} \qquad \text{(Equation 10)}$$

Where I_{sc} is the short-circuit current, V_{oc} is the open circuit voltage, and P_m is the maximum power.

Efficiency of Solar Cells

The solar efficiency is the ratio of maximum electrical power output (P_m)to the radiation power input to the cell (P_{in}). The efficiency of a solar cell is expressed in percentage using[37]:

$$\text{Efficiency}(\eta) = \frac{P_m}{P_{in}} \qquad \text{(Equation 11)}$$

1.6 Organization

This work starts with a literature review in Chapter 2, followed by the experimental methods in Chapter 3. Then, Chapter 4 demonstrates the results and discussion of graded composition $In_xGa_{1-x}N$ layers (3%-50% In) at different growth temperatures, as well as modeling and simulation of the band energy diagram and the probability of optical transitions and wave functions using nextnano^3. After that, Chapter 5 shows the results and discussion of the full

composition graded $In_xGa_{1-x}N$ layer. Chapter 6 demonstrates a growth model to understand the growth parameters. Then, Chapter 7 shows Raman and Reciprocal Space Map strain calculations. The fabrication of the full graded $In_xGa_{1-x}N$ layer is presented in Chapter 8.

Chapter 2: Literature Review

2.1 State-of-the-Art InGaN Solar Cells

The ternary $In_xGa_{1-x}N$ material is an excellent semiconductor for photovoltaic applications due to the wide, direct, and tunable band gap from 0.64 for InN to 3.4 eV for GaN that covers most of the available energy in the solar spectrum. Other advantages include high thermal conductivity, a high absorption coefficient (~10^5 cm^{-1}) that decreases the thickness required of a solar cell's absorber layer, and high carrier mobility. Additionally, the InGaN alloy is of great interest because of a high temperature resistance that allows it to be used for solar cells that operate under harsh environments. However, much of the research up to now has shown that it is a challenge to get high crystal quality InGaN active layers with a high In content, which are significant for high efficiency photovoltaic devices. Nevertheless, exceeding a certain thickness, called a critical thickness, h_c, results in defect generation such as V-pits, misfit dislocations, and cracks. In heteroepitaxial growth, h_c is a transition point between a relaxed and fully strained layer[38]. It has been shown that the critical thickness for strain relaxation of the InGaN layer is inversely proportional to In content, which limits the thickness of the absorber layer for solar cells[39].

Much of the previous research on $In_xGa_{1-x}N$ based solar cells has been carried out on bulk $In_xGa_{1-x}N$ absorption layers, either p-n junction or p-i-n structure. However, the primary challenge of the growth of such material is high defect generation because of relaxation and phase separation. This is due to the large difference between the covalent radii of Ga and In atoms, which are 1.26 Å and 1.44 Å respectively; this property induces internal strain [40]. The absence of a native GaN substrate is another problem that leads to threading dislocations in Ga and $In_xGa_{1-x}N$ epitaxial layers. That is because of the relatively high lattice mismatch (14%)

between the mostly used substrate, sapphire (Al_2O_3) with GaN template, which causes strain energy buildup that eventually induces defects[41].

These issues decrease the In content incorporated in the material; thus, most of the research on $In_xGa_{1-x}N$ has been at an In molar fraction less than 25%. Less In content reduces the coverage of the solar spectrum and the conversion efficiency of solar cells. Additionally, the low quantum efficiency of the device is another consequence of strain since it causes a large internal piezoelectric field in the active region which reduces the probability of recombination[42].

Therefore, other growth methods have been explored such as heterostructures like $In_xGa_{1-x}N$ / GaN, multiple quantum wells (MQWs), or superlattices (SL). In the $In_xGa_{1-x}N$ MQWs structure, the layers are less than the critical thickness (h_c) for strain relaxation, which permits more In content compared to a bulk $In_xGa_{1-x}N$ structure. Generally, the critical thickness for the $In_xGa_{1-x}N$ layer that is grown on GaN substrate is less than 100 nm when $x > 0.1$. This critical thickness reduces even more with the increasing In fraction, which results in an $In_xGa_{1-x}N$ layer with misfit dislocations that degrade the device performance[43],[44].

The strain effect on the incorporation of In in $In_xGa_{1-x}N$ materials was studied by S. Pereira et al.[40] It was found that the composition varies over depth, meaning that In atoms increase in $In_xGa_{1-x}N$ lattice along the growth direction. Therefore, as the material is grown thicker exceeding the critical thickness, it starts to relax and allows more In content to be incorporated. This means that strain hinders In content from uniform incorporation in the material, which is known as the compositional pulling effect[40],[45]. Consequently, strain relaxation has been a subject of great interest to date, since relieving the strain will solve the issue of limited solar spectrum absorption by increasing the In molar fraction. Strain engineering can be applied through various approaches such as relaxing the $In_xGa_{1-x}N$ buffer layers. Evan et

al. examined the effect of three types of relaxed pseudo-substrates with different lattice parameters on In incorporation. The emission of PL was redshifted not only for the buffer layer but also for the $In_xGa_{1-x}N$ /$In_yGa_{1-y}N$ MQW. Moreover, In content was increased as a result of the decreased impact of compositional pulling via strain relaxation. Also, the efficiency of long wavelengths was enhanced since the well width increased by the reduction of the internal electric field that is caused by the decreased lattice mismatch between the QW and buffer layer[46].

Insertion of an $In_xGa_{1-x}N$ underlayer (UL) with relatively low In content ($x < 0.01$) is a method to control and reduce the internal strain. Kusanagi et al. stated that the quality of the $In_xGa_{1-x}N$ QW was improved when reducing the strain. Additionally, the non-radiative recombination centers decreased, and the defects did not migrate to the $In_xGa_{1-x}N$ QW and were buried in the underlayer[47].

Enhancement in the growth of $In_xGa_{1-x}N$ layers - either higher-quality or higher In incorporation - has been demonstrated via adding a graded superlattice or compositionally graded $In_xGa_{1-x}N$ layer. Graded $In_xGa_{1-x}N$ buffer layers can relax the strain that can build up during the growth after critical thickness and decrease the compositional pulling effect [18],[39]. Besides the graded buffer layer's advantage as a strain relaxation layer, another advantage is its increasing the quantum efficiency of the device by enhancing the electron-hole wavefunction overlap in the absorber layer which improves the LED performance. In addition, the graded layer in fact allows for a clean and smooth surface without the accumulation of In droplets, which is beneficial for any of the following growths[48],[49].

However, the strain relaxation process in the hexagonal $In_xGa_{1-x}N$ wurtzite structure usually is accommodated with a high density of defects such as V-pit formation, stacking faults, dislocation inclination, and other mechanisms. Thus, it is important to investigate the relaxation

process to optimize the growth, since these types of defects could impact the performance of the device[50],[51].

Throughout the years, several studies have been done with different structures in order to overcome InGaN challenges and produce high efficiency solar cells. These structures, as demonstrated in Table 2, can be classified as homojunction or heterojunction. The heterojunction structure is similar to the InGaN-based LED, and while most of the recent good results obtained are with such structures, it still needs improvement. However, in homojunction InGaN solar cells even with higher In content, the solar cell efficiency is not high enough. One advantage of nitride-based solar cells is that they are still an ongoing topic. Another advantage is that all of the structures presented in Table 2 still have not reached high efficiency, which means that there still big room for improvement.

The primary objective of this study was to investigate the growth of a graded $In_xGa_{1-x}N$ layer, not simply as a buffer layer but as the active layer of the device. Incorporation of In mole fraction in the graded $In_xGa_{1-x}N$ layer versus substrate temperature was the first step to find the optimal conditions to incorporate the target composition. Then, a full composition graded $In_xGa_{1-x}N$ layer was grown based on previous results.

The study of graded $In_xGa_{1-x}N$ as an active layer is limited, especially full composition graded $In_xGa_{1-x}N$. Then, the material was fabricated into a solar cell device to study its electrical properties.

There is only one recent publication that demonstrates the growth of full composition graded InGaN on a GaN substrate. The composition was almost linearly graded along the growth direction with a gradual strain relaxation.

Table 2. The efficiency of InGaN based solar cells for different structures and compositions.

Structure (Growth method)	In content (Thickness)	Voc (V)	Jsc (mA/cm^2)	FF (%)	η (%)	Year Author	Reference
p-n InGaN Homojunction MBE	39% 300 nm	0.161	2.2	0.25	0.07	2011 Boney et al.	[52]
p-n InGaN Homojunction MOVPE	14.8%-16.8% 80 nm	1.47	0.26	57.56	0.05	2010 Jampana et al.	[53]
$In_{0.20}Ga_{0.80}N$/GaN MQW MOCVD	20% 30 periods (2.3 /4 nm) 200 nm	2.26	2.10	70.4	2.4	2013 Young et al.	[54]
$In_{0.12}Ga_{0.88}N$ Heterojunction MOVPE	12% 200 nm	0.48	1.12	30.2	0.16	2013 Zhang et al.	[55]
$In_{0.10}Ga_{0.90}N$ Heterojunction MOCVD	10% 150 nm	2.1	0.42	77.8	0.68	2010 Zheng et al.	[56]
$In_{0.10}Ga_{0.90}N$/GaN MQW MOVPE	10% 60 periods (1.3 /8.7 nm) 636 nm	2.3	0.68	56	0.88	2016 Mukhtarova et al.	[57]
Ga/InGaN/GaN Graded MQW MOCVD	16%-10% 14 periods (2/5 nm) 112 nm	1.88	0.92	64	1.11	2015 Tasi et al.	[58]
Ga/InGaN/GaN Graded InGaN layer MOVPE	0-11% 200 nm	1.33	0.59	0.65	0.51	2011 Lee et al.	[59]
n-Ga/i-InGaN/p-GaN MBE	10% 200 nm	0.96	0.71	48.4	0.33	2015 Fabien et al.	[60]

Another interesting finding was the observation of multiple quantum wells at the initial phase of the growth that were formed unintentionally.

It was explained that this phenomenon is due to the difference in growth modes as shown in RHEED patterns. The relatively high growth temperature at the first stage of the growth affects the diffusion length of In and Ga adatoms that have to increase in order to continue the 2D growth mode. Thus, these quantum wells resulted in a smooth surface with a sharp interface in between the high and low In mole fraction regions and the relaxation of in-plane strain.

Additionally, the absorption spectrum is discussed, and it showed a gradual change instead of a sharp absorption edge that is usually observed in InGaN material with single composition[61].

Numerical analysis of graded InGaN based solar cells has been investigated in the literature. Brown et al.[62] used a finite element approach to simulate a graded InGaN based solar cell. The graded layer was within the depletion region to eliminate the discontinuity in the valence band. The efficiency was predicted to be 28.9% for their tandem solar cell structure that include p-type GaN/n-$In_xGa_{1-x}N$/n-In0.5Ga0.5N/p-Si/n-Si. The thickness of the graded InGaN layer and the doping have a great impact on the solar cell efficiency. It was found that in order to get higher efficiency, the graded InGaN layer should be thin, since having a thicker layer than the depletion region produces a quasi-electric field in an opposite direction of the minority carriers' directions. Likewise, high doping results in a decrease in the depletion region which affects the solar cell efficiency. As a result, a very thin graded InGaN layer is required to attain high efficiency. Otherwise, the graded InGaN layer creates a barrier that inhibits the photogenerated hole collections. The collection of the holes could be improved via p-type graded InGaN, but the doping difficulties might hinder this kind of structure[62].

Lee et al.[13] numerically investigated the polarization doping of III-nitride n-i-p solar cells that is induced by the composition gradient. The p-type layer was linearly graded by increasing In composition (0%-30%) going from GaN to $In_{30}Ga_{70}N$, and the n-type layer was established by decreasing the In composition (30% to 0%) going from $In_{30}Ga_{70}N$ to GaN. The polarization doping removes valence and conduction bands discontinuity at the heterointerface. Additionally, the profile of the polarization charges can be well controlled in the graded InGaN layer when the charges are uniformly built in the unit cell. However, having random impurity charges can result in segregation or diffusion of the carriers. As expected, the graded layer showed small differences in the strain profile between the layers as opposed to heterostructure GaN/InGaN with constant composition.

It was reported that the short circuit current is independent of temperature, as the polarization charges do not require thermal energy to be activated, resulting in high efficiency solar cells[13].

Chapter 3: Experimental Methods

In this work, graded $In_xGa_{1-x}N$ active layers were investigated to determine the optimal growth conditions for In incorporation in the material. Thus, Veeco Gen II (Veeco, Plainview, New York, USA) plasma assisted molecular beam epitaxy (PAMBE) was used to grow thick compositionally graded $In_xGa_{1-x}N$ active layers with the same growth conditions but at different substrate temperatures.

The growth was done on c-plane unintentionally doped GaN on sapphire templates. As the template was transparent, the heat would not be distributed uniformly during growth, so a back titanium (Ti) coating was required. Thus, the template was coated with 1 μm thick Ti film to assist the radiative heating. The film was then removed after the growth using buffered oxide etch (BOE) to be able to perform transmission measurements.

A 180 nm thick buffer layer of GaN was first deposited at 775 °C (an hour of growth gave that thickness) to have a clean surface for the following growth. With the same grading profile and growth parameters, three samples were grown at different substrate temperatures: 555, 515, and 475 °C. Thus, the III/N and In/Ga ramped flux ratios were kept the same to examine the effect of growth temperature on the strain relaxation and In content incorporation.

The samples were grown with graded In composition over a 500 nm thick layer starting with 3% In to a maximum In of nominally 50%, followed by a thin layer (100 nm) with a reverse grade from 50% to ~30% In to create a pn-junction device without introduction of dopants such as Mg for p-type or Si for n-type. This could be realized by polarization doping with a top contact layer.

Then, another structure was grown with fully graded composition $In_xGa_{1-x}N$ with In composition from 3% to 50% over 500 nm at 475 °C, and another 500 nm with In content from

50% to 100% at 400 °C. This meant the active layer was 1 μm thick. This thick graded layer was followed by a thin layer (100 nm) with a reverse grade from 100% to ~70% In to obtain a p-n junction by polarization doping similar to the previous structure.

Structural and optical characterizations were performed using high-resolution X-Ray Diffraction (XRD) in a Phillips X'pert MRD (Malvern Panalytical, Malvern, UK) diffractometer, and atomic force microscopy (AFM) was performed in a Bruker 3000 Dimension III (Bruker, Billerica, MA, USA) atomic force microscope. Then, photoluminescence (PL) was performed in a closed cycle, helium cryostat at ~16K using a helium-cadmium (HeCd) laser for optical excitation at 325 nm, and optical absorption was performed in a Shimadzu 3600 (Shimadzu, Kyoto, Japan) spectrophotometer.

Also, microPL was used in order to study the optical properties of the full composition since the sensitivity of the CCD camera in the PL system did not detect far infrared. A Raman study was also performed to analyze the surface and determine the strain and composition of the samples.

Secondary Ion Mass Spectrometry (SIMS) was performed on all the samples to analyze the composition profile. The samples were sent to EAG Laboratories (EAG, San Diego, CA, USA) for this study.

The fully graded composition sample was prepared for Transmission Electron Microscopy (TEM) measurements to learn more about the growth.

Next, the fabrication process was done on the sample to obtain a simple solar cell device to study the External Quantum Efficiency (EQE) and the I-V characteristic of the p-n junction. The following sections contain more details about the equipment.

3.1 Molecular Beam Epitaxy (MBE)

Molecular beam epitaxy (MBE) is an ultra-high vacuum (UHV) system that is used for thin-film deposition. It has been widely used not only in research but also industrial production for epitaxial growth of metals, insulators, and semiconductors. The idea of MBE is based on evaporation, where thermal beams of atoms or molecules flow under UHV pressure (10^{-8} to 10^{-10} Torr) and react with a clean substrate[63].

The advantages of using MBE over other growth methods such as metalorganic chemical vapor deposition (MOCVD) are: (a) the relatively low growth temperature, which is important for very large-scale integration (VLSI) industry; (b) that MBE growth technique is based on evaporation, thus no chemical reaction is considered; (c)i situ growth monitoring; and, (d) the low growth rate, typically about 1 monolayer/second that helps to precisely control the composition and doping profiles.

In MBE, the substrate temperature, flux rate (III/V ratio), plasma power, and source temperature are significant variables that can be adjusted in order to acquire the target composition and stoichiometry and improve the quality of the growth. Additionally, Reflection High-Energy Electron Diffraction (RHEED) is one of the most crucial in-situ analytical methods.

A RHEED gun emits electrons towards the sample surface, then the incident beam is diffracted at a very low angle. This generates a diffraction pattern on a phosphor screen, which gives information about the quality of growth. Therefore, it is used to analyze the surface and the quality of the growth: for example, the surface morphology, surface reconstruction, atomic spacing, and growth rate.

The MBE system used has five effusion cells to introduce group III-metal sources (Ga, In, Al) as shown in Figure 13, and dopant materials as solid material are Mg (p-dopant), and Si

(n-dopant), placed in a crucible. Then, the crucible is heated to the required evaporation temperature for the material until it reaches a sublimation point and evaporates.

The MBE is also equipped with a nitrogen radio frequency (RF) plasma source for III-nitrides growth where pure N_2 is converted into active molecular species[64]. In this study, a Veeco Gen II plasma-assisted MBE (PAMBE) system was used, as shown in Figure 14.

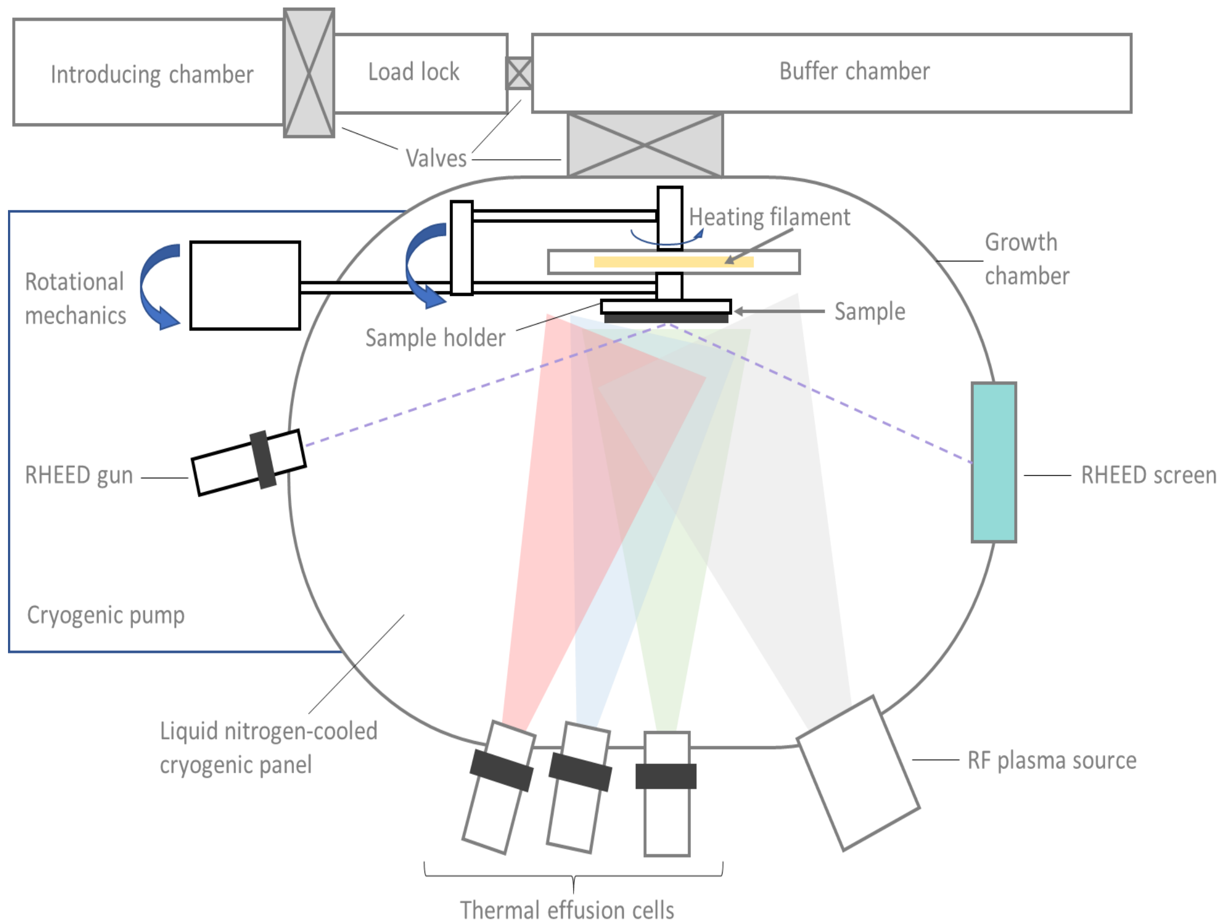

Figure 13. A schematic diagram of the MBE chamber.

3.2 Transmission

Transmission is the ratio of transmitted light intensity to the incident light intensity.

Transmission measurements are used to determine the band gap of the materials through the optical absorption coefficient[65].

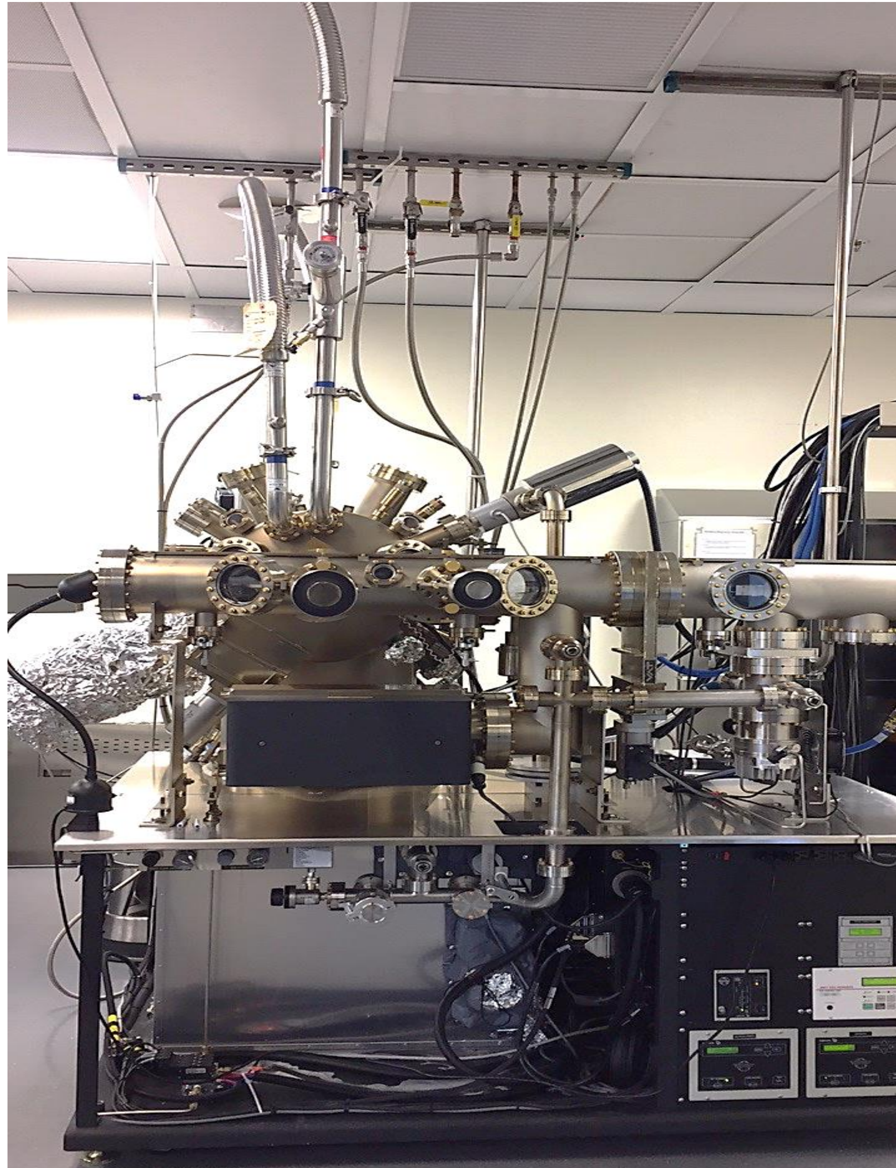

Figure 14. MBE nitrides chamber at the University of Arkansas.

If the incoming light energy is greater than or equal to the band gap of the material, the light is absorbed. Absorbance is defined as the negative logarithm of transmittance. The quality

of the material can be examined through the change in the transmitted light against wavelength when the light passes the material. Also, the thickness can be evaluated from the interference fringes in the transmission spectra. The sensitivity of the system depends on the detectors, as illustrated in Figure 15, adapted from Ref. [66].

In this research, a Shimadzu UV3600 Spectrophotometer was used to analyze the samples. The Shimadzu UV3600 spectrophotometer consists of three detectors to cover the spectrum from ultraviolet light (UV) through visible light to infrared (IR). It has a photomultiplier tube detector (PMT) to span the ultraviolet and visible regions of the electromagnetic spectrum. In addition, InGaAs and cooled PbS detectors are also used to cover the near infrared region[66].

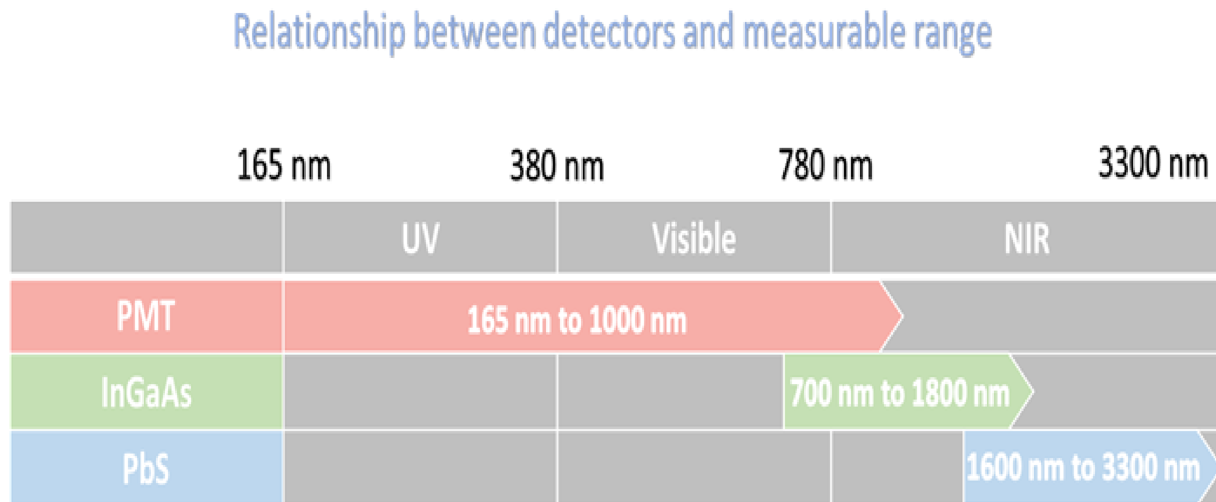

Figure 15. The sensitivity range in Shimadzu UV3600 Spectrophotometer.

3.3 Photoluminescence (PL)

Photoluminescence (PL) spectroscopy is a noninvasive analysis for the electronic structure of the material. When the material is illuminated with light, the photons are absorbed in

the material, and they excite the electrons in the material from an occupied state to an empty state. Then, the excess energy can deplete through the emission of light. This process is called photoluminescence, which is then plotted as the intensity of the emitted light against wavelength or energy.

In this work, as shown in Figure 16 and Figure 17, a helium-cadmium (He-Cd) laser (325 nm) was used as an excitation source in the UV range at both room temperature and low temperature (16 K).

Figure 16. Photoluminescence (PL) measurement system.

A parabolic reflector collected the light reflected from the sample and then focused it onto the spectrometer through a slit. To change the dispersion in the spectrometer, there are two different gratings from a low dispersion (75 grooves/mm) to a high dispersion (1200 grooves/mm). The slit size can be varied to change the resolution of the spectrum. The measurements taken in the μ-PL system were performed at room temperature with a He–Ne laser (632.8 nm) as an excitation source in a backscattering configuration.

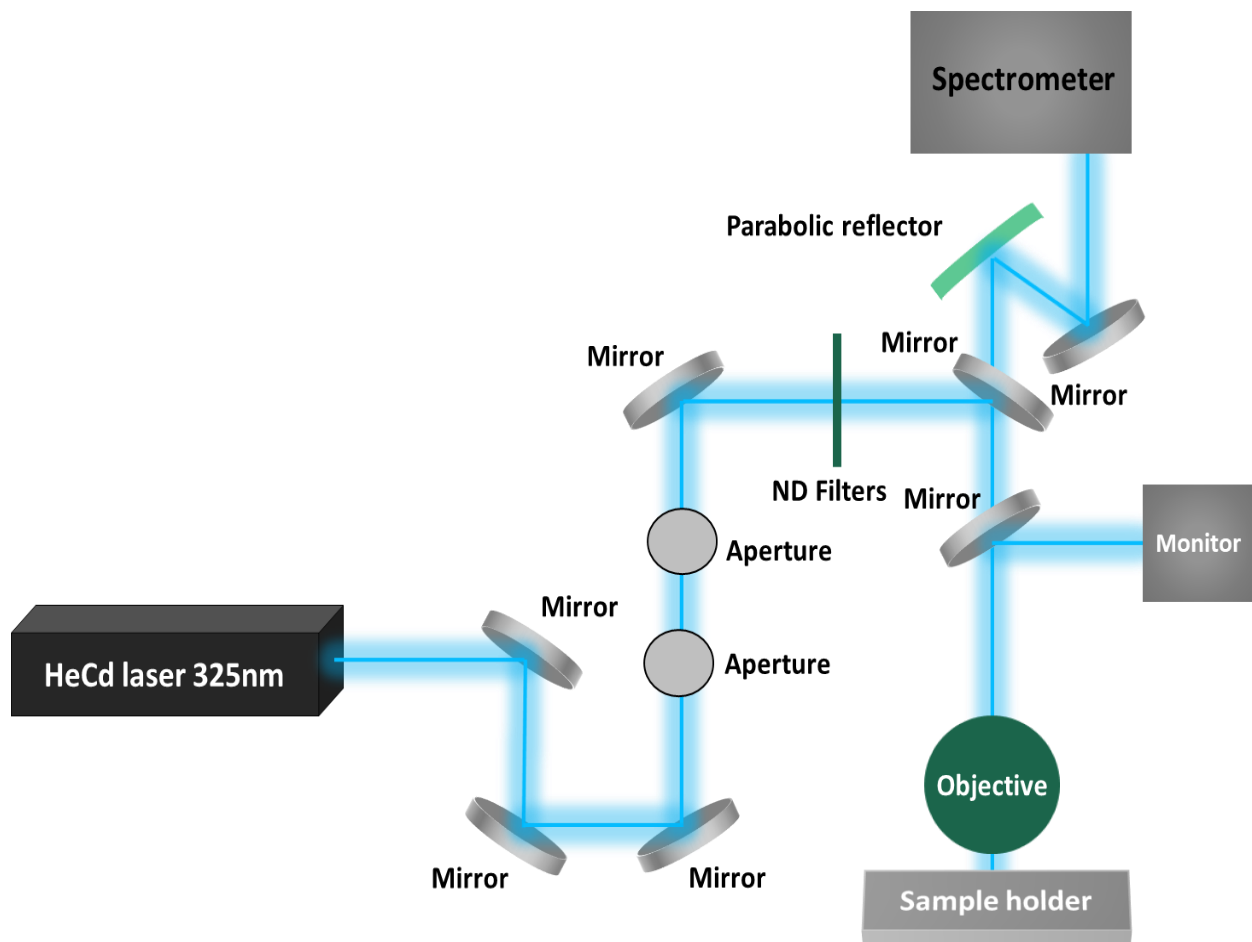

Figure 17. A schematic diagram of the photoluminescence (PL) setup.

Furthermore, the Micro-Photoluminescence system that has a Stanford Research System Lock-In Amplifier (Stanford Research Systems, Sunnyvale, CA, USA) was used to detect and

amplify very small AC signals. The system consists of a single channel detector cooled with liquid nitrogen (N_2) that can detect in the spectral sensitivity range from 300 nm up to 2000 nm. However, the PL system that was used first has a liquid nitrogen cooled Charged-Coupled Device (CCD) that can detect from about 300 nm to 1050 nm as well as an InGaAs (IGA) detector [67].

3.4 X-Ray Diffraction (XRD)

X-ray diffraction (XRD) is a nondestructive technique that is used to characterize crystalline materials without the need for sample preparation. It helps to determine the crystal quality, composition, strain, defects, grain size, orientation, and other structure-related information. The XRD system consists of an x-ray source, a detector that senses the x-ray beam, and a sample holder. As illustrated in Figure 18, at a certain angle, the x-ray beam is focused on the sample which results in a diffraction pattern. Then, this diffraction pattern is compared to a database that is provided by the International Centre of Diffraction Data (ICDD). As shown in Figure 18, constructive interference only occurs when Bragg's law is satisfied.

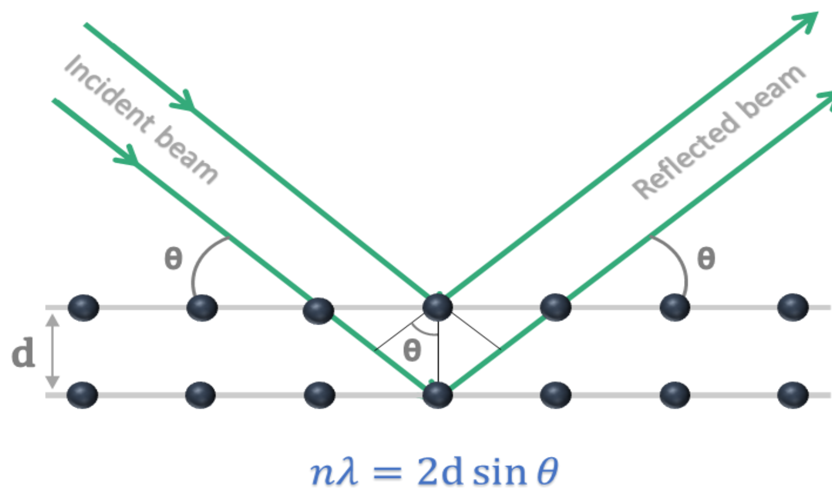

Figure 18.The principle of X-ray difraction (Bragg's law).

There are different types of scans, such as rocking curve, omega-two theta scan ($\omega/2\theta$), and reciprocal space map (RSM)[68],[69].

In this research, a Philips X'pert MRD system was used to perform High-Resolution X-Ray Diffraction (HRXRD). The system is equipped with a copper (Cu) anode, and the wavelength of the Kα1 radiation coming from the anode is 1.54056 Å. The x-ray radiation was generated with 1.6 kW with a four bounce (220) channel-cut germanium (Ge) crystal that is detected through a three-bounce (022) channel-cut Ge crystal.

To study the strain relaxation in the samples, ($\omega/2\theta$) scans as well as RSM were used to determine the lattice constants and gives information about the composition. RSM can be described through a geometry known as the Ewald sphere as illustrated in Figure 19. The line that has a radius of 1/λ represents the x-ray direction, and the sphere is centered on this line. The reciprocal lattice rotation is comparable to the crystal rotation around the Ewald sphere. Once the reciprocal lattice set of points (hkl) lies along the circumference of the Ewald sphere (blue line in the figure), a strong diffraction will occur with reflection planes (hkl)[70].

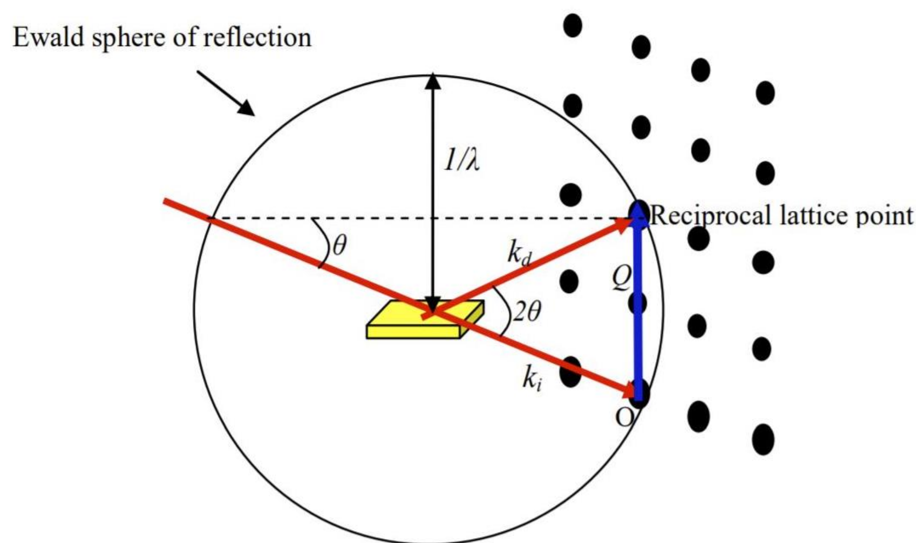

Figure 19. The diffraction x-ray occurs in reciprocal space [70].

3.5 Scanning Electron Microscopy (SEM)

A Scanning Electron Microscope (SEM) is used to study the surface of the sample. It consists of an electron beam that interacts with the atoms on the surface and reflects off the surface to produce the image[71]. Figure 20 shows a schematic of the SEM system which is

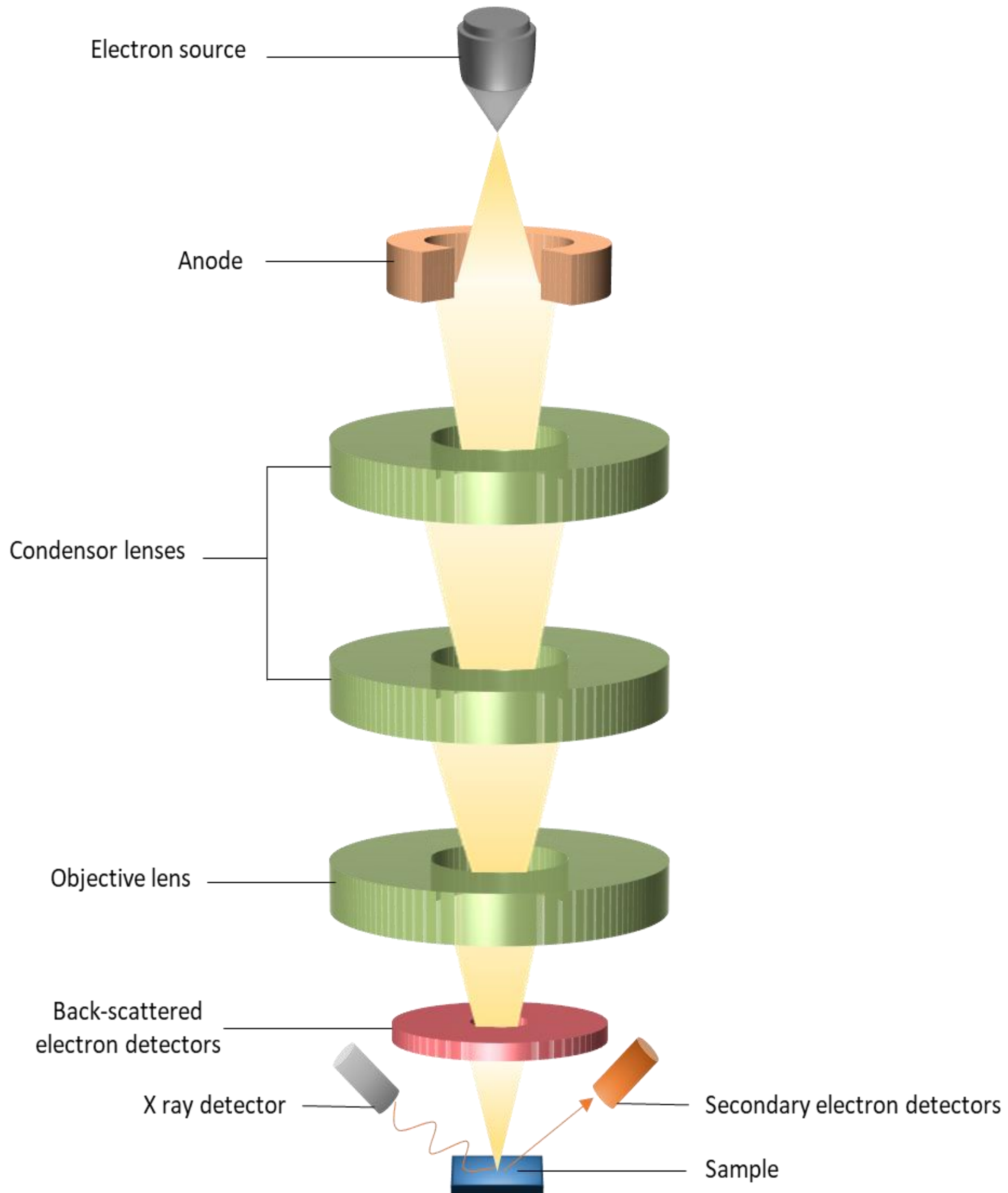

Figure 20. A schematic diagram of SEM microscope.

adapted from Ref. [72]. It is used to analyze the surface and provide information about elemental composition through Energy Dispersive X-ray spectroscopy (EDX) mapping. It is also used to measure very small features on the surface and study the morphology[73].

3.6 Transmission Electron Microscopy (TEM)

The transmission electron microscope (TEM) has the same principle as SEM in using electrons as an excitation source. The TEM system is equipped with a high-voltage electron beam to generate high-resolution images. The TEM system includes an electron gun to emit electrons toward the sample. The electrons pass through the microscope vacuum tube and are focused through an electromagnetic lens. When the electrons hit the thin sample, they either hit the fluorescent screen or scatter[72],[74]. Figure 21 is a schematic diagram of the TEM system, which is adapted from Ref.[72].

The sample needs extensive preparation before it can be installed in the TEM microscope. It starts with cutting the sample, then gluing two pieces face-to-face together so that the film to study is in the middle. Then, the sample is mounted on a TEM grid using superglue. Next, a polishing process is carried out that includes using diamond lapping films at different sizes. The last step is when the sample is about 30 μm thick, and then it will be ready for ion milling in order to create a hole in the middle of the sample.

3.7 Atomic Force Microscopy (AFM)

The atomic force microscope (AFM) is a high-resolution scanning probe microscope that analyzes the morphology of the surface at an atomic scale. This type of microscope combines principles of both the scanning tunneling microscope (STM) and the stylus profilometer. Both

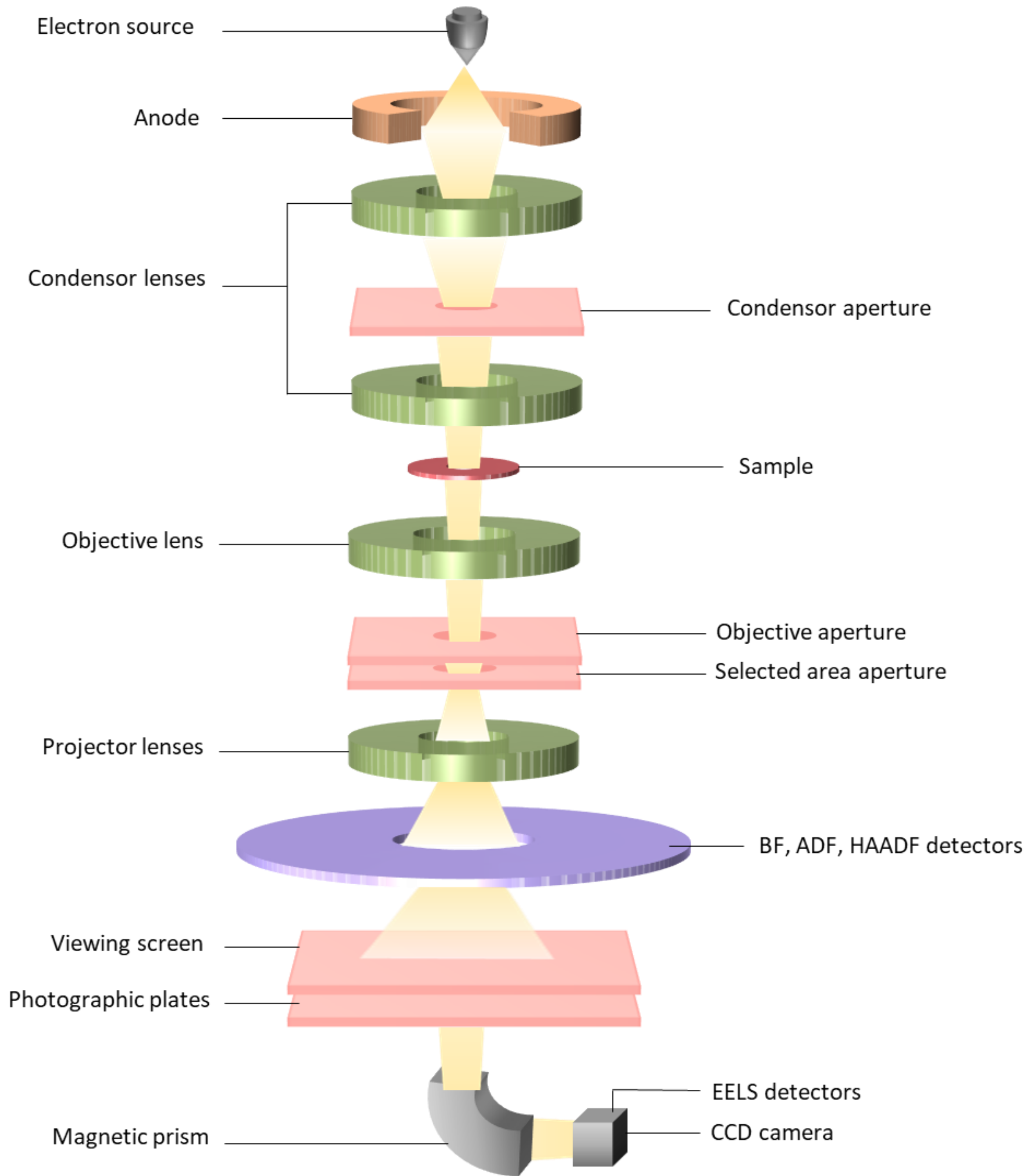

Figure 21. A schematic diagram of TEM microscope.

conductors and insulators can be measured using AFM with no coating or any requirements. This overcomes the limitations of using a STM, which requires conductivity of the materials it scans, since it operates based on tunneling current between the tip and the surface of sample[75]. The

AFM consists of a small sharp tip that is attached to a cantilever, a position-sensitive photodetector, and a laser beam.

The AFM operates by observing the interaction force of the tip and the sample surface. Then the image is produced by recording the deflection of the laser beam off the back of the cantilever using a position-sensitive photodetector[76].

There are two modes: contact mode and tapping mode, and the latter was used in the measurements. Figure 22 shows a schematic diagram that includes the key components of AFM measurements. The AFM measurements depend on the interaction between the tip and the sample. The force between them is calculated using Equation 12 which represents Hooke's law through the stiffness of the cantilever and the measurements of the cantilever deflection.

$$F = -kz \qquad \text{(Equation 12)}$$

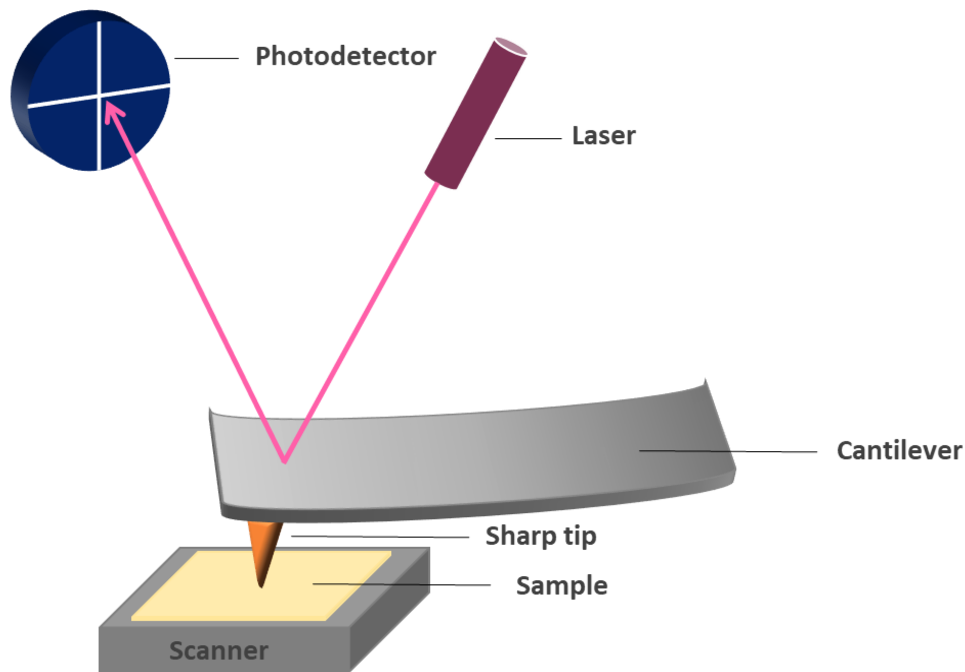

Figure 22. A schematic diagram of AFM basic setup.

Where F is the force between the AFM tip and the sample, k is the lever stiffness, and z is the distance that cantilever bends[77].

3.8 Raman Scattering

Raman scattering is an inelastic scattering of photons when incident light interacts with a crystal's modes of vibration. It helps to determine the strain, morphology, and composition of III-nitrides alloys[78]. However, the crystalline quality of the material degrades with increasing In mole fraction, which makes it difficult to interpret the results of Raman spectroscopy. In this study, micro-Raman scattering at room temperature was performed in a backscattering configuration along c-axis. Both the incident beam and scattered beam propagated along the z direction and perpendicular to the sample surface.

The system, as shown in Figure 23 and Figure 24, was equipped with an He-Ne laser (Melles Griot, Carlsbad, CA, USA) that had an excitation power of 5 mW and an excitation wavelength of 632.8 nm. Another laser was also utilized, the green laser (532 nm), to study the effect of excitation energy. The laser spot that was about 1 μm diameter was focused using in a Olympus BX41 microscope, with a 100x objective lens and a digital camera. A Horiba Jobin-Yvon LabRam HR800 (Horiba, Kyoto, Japan) spectrometer with a 0.75 m focal length was used to collect the signal. Also, the system had a thermoelectrically cooled Si charge-coupled device (CCD) camera. The software used to conduct the measurements was LabSpec (Horiba).

3.8.1 Phonon Modes in Nitrides

The wurtzite structure for GaN has eight phonon modes at the Γ point, consisting of $2A_1+2B_1+2E_1+2E_2$. There is one set of acoustic modes for both A_1 and E_1 modes and six optical

modes (A_1+E_1+2B_1+2E_2). As shown in Figure 25, six types of Raman active modes are displayed 2A_1+2E_1+E_2-Low (L)+E_2-Hight (H). The phono modes A_1 and B_1 vibrate in the plane in a parallel direction to the c-axis. However, E_1 and E_2 phonon modes vibrate in the plane perpendicular to the c-axis.

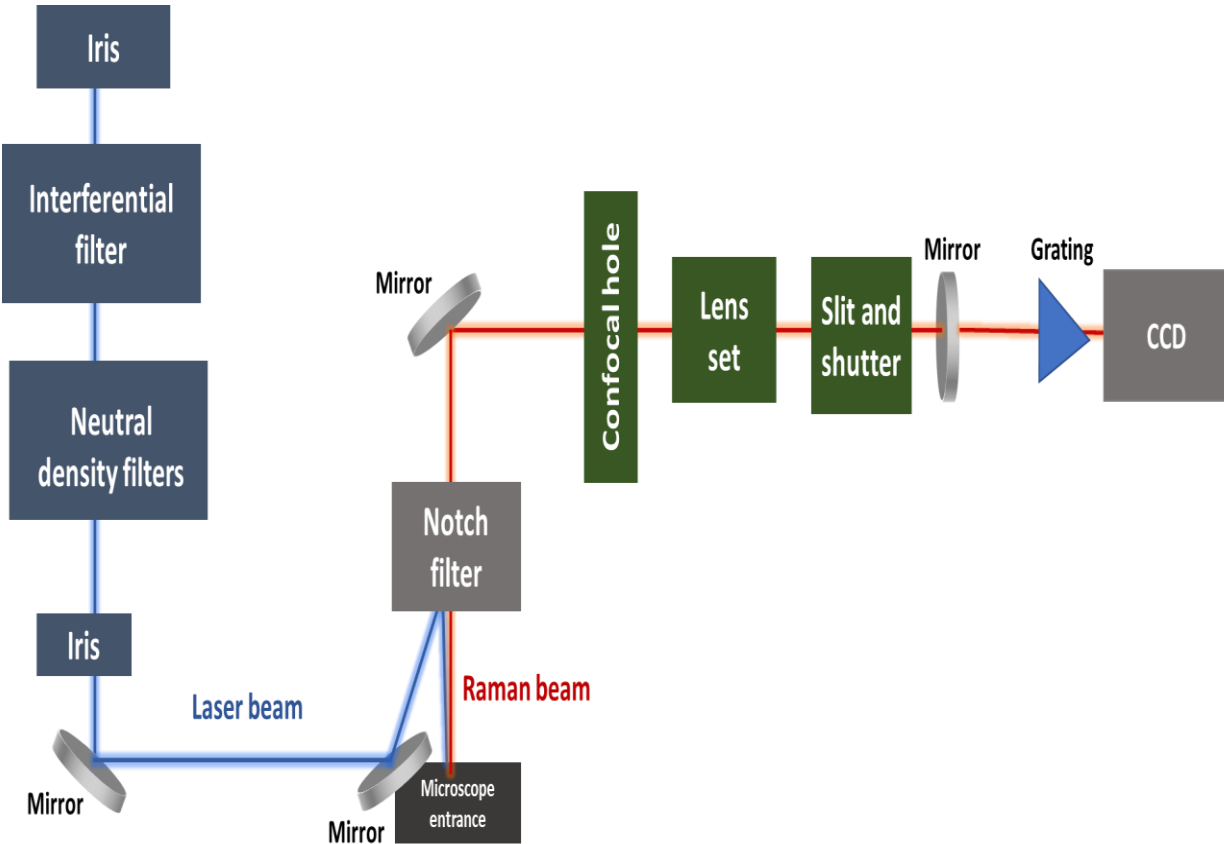

Figure 23. A schematic diagram of Raman scattering measurements setup.

The cations and anions of the E_2 phonon mode oscillate in opposite directions, which cancels the electric dipole, so the E_2 phonon modes are non-polar. On the other hand, A_1 and E_1 modes are polar modes since their cation and anion displacement modes is in the same direction [79],[80].

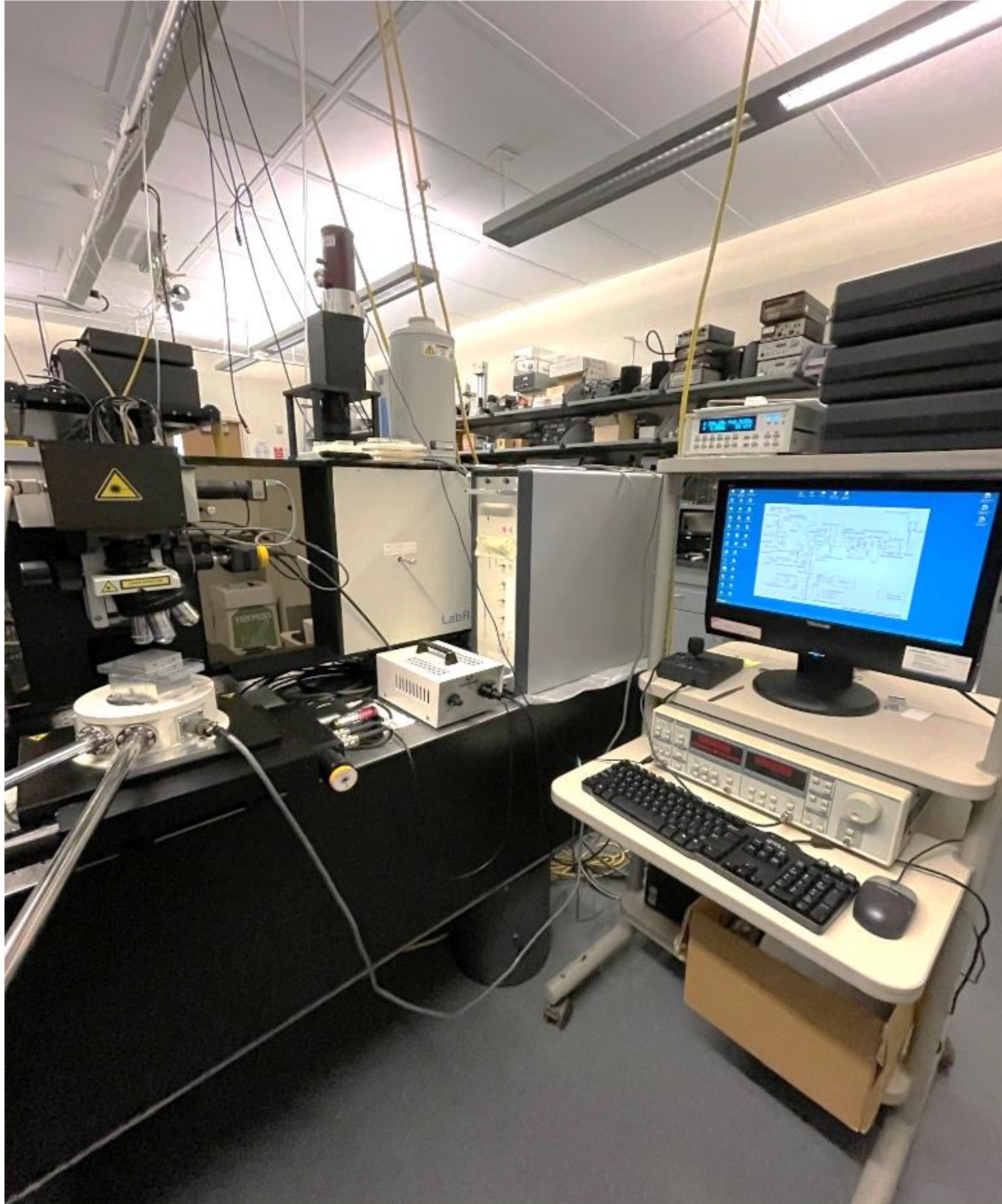

Figure 24. Raman Scattering Microscope.

In A1 and E1 phonon modes, the net dipole moment results in splitting them into longitudinal optical (LO) and transversal optical (TO) modes. Raman study in this work was done in a backscattering configuration that allows only the E_2 and the A_1(LO) modes[78]. Table 3 shows the phonon frequencies of GaN, AlN, and InN that are taken from literature[81],[82],[80].

Table 3. Raman-active mode frequencies of nitride materials (wurtzite structure).

Phonon mode	GaN (cm^{-1})	AlN (cm^{-1})	InN (cm^{-1})
E_2(low)	144	248.6	87
A_1(TO)	531.8	611	447
E_1(TO)	558.8	670.8	476
E_2(high)	567.6	657.4	488
A_1(LO)	734	890	586
E_1(LO)	741	912	593

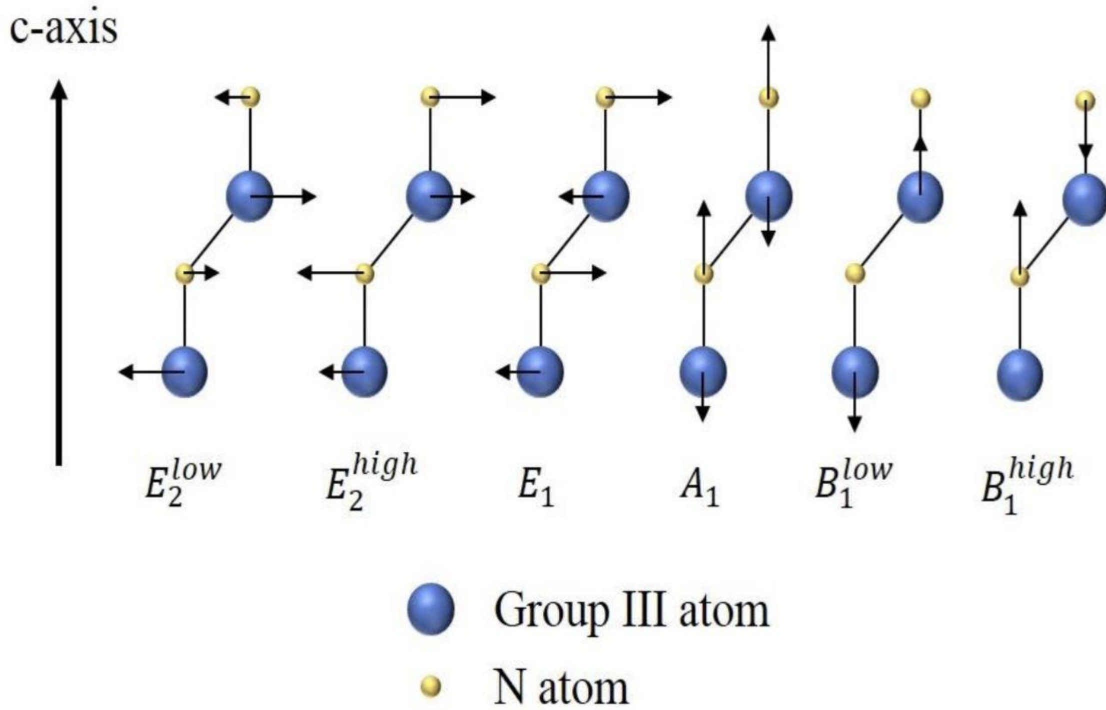

Figure 25. The optical phonon modes in wurtzite group III-nitride crystals [80].

3.9 Secondary Ion Mass Spectrometry (SIMS)

Secondary-ion mass spectrometry (SIMS) is a destructive method that is used to analyze the composition of the material. Additionally, the thickness of the growth can be determined using the composition profile that is extracted from SIMS.

As represented in Figure 26, the incident primary ion beam interacts under an ultrahigh vacuum with the surface which sputters and ionizes the elements on the material. Some of the sputtered material will be will be accelerated towards a double focusing mass spectrometer in order to characterize the exact quantity of various elements as a function of the depth of sputtering[83].

In this work, the samples were sent to EAG Laboratories to analyze the In composition in the graded composition InGaN materials.

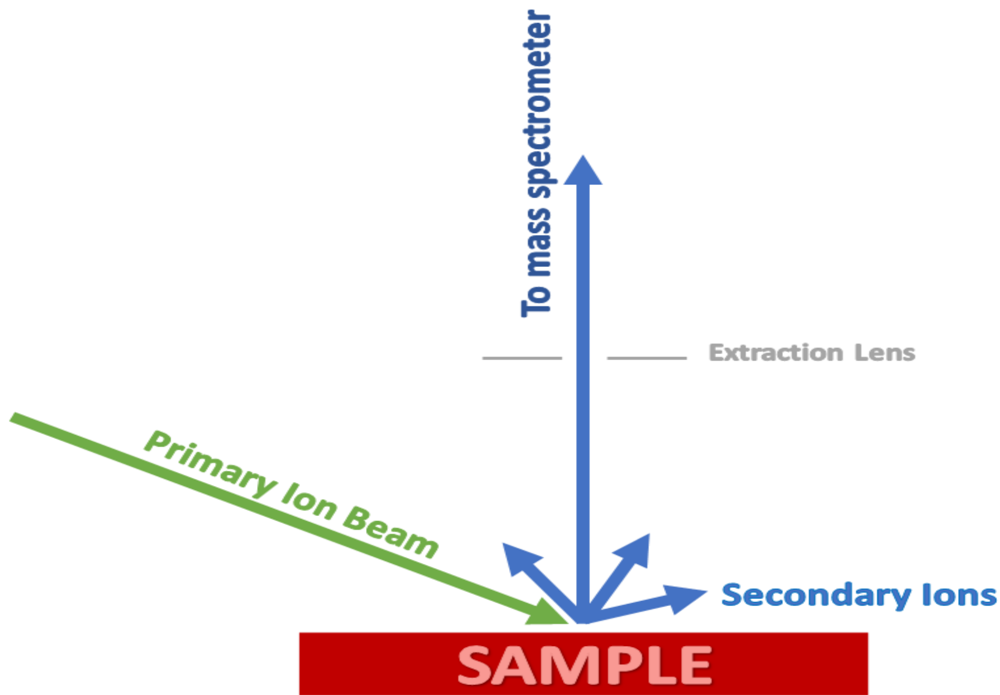

Figure 26. A schematic diagram of SIMS technique.

Chapter 4: Graded InGaN Thick Films Grown by MBE as a Function of Temperature

4.1. Structure and band diagram simulation

To estimate a sufficient thickness to grow the graded material in order to absorb most of the incident solar spectrum, an 90% absorption was used as a goal. The minimum thickness required to absorb 90% of the solar spectrum was then calculated for different In compositions using the following equations:

$$I = I_0 \, e^{-\alpha x} \quad \text{(Equation 13)}$$

$$x = \frac{1}{\alpha} \ln(10) \quad \text{(Equation 14)}$$

where α is the absorption coefficient, x is the thickness of the absorber layer, I_0 is initial light intensity, and I is the final light intensity, such that $I/I_0 = 0.1$. Subsequently, an average of the resulting thicknesses over the various compositions would be used as the minimum growth thickness for the compositionally graded film, with the assumption that each composition predominantly absorbs the light at its bandgap energy, leaving the lower energy light to be absorbed by the next layer.

The absorption spectra presented in Figure 27 was taken from Kazazis et al. [12]. The data was obtained via spectroscopic ellipsometry for $In_xGa_{1-x}N$ samples that were grown by MBE on commercial free-standing GaN substrates.

Thus, the absorption coefficient was taken at the absorption edge for each composition in the plot to give a rough estimation of the required thickness. Table 4 shows the thickness for an absorber layer with different composition required to absorb 90% of the light at the bandgap

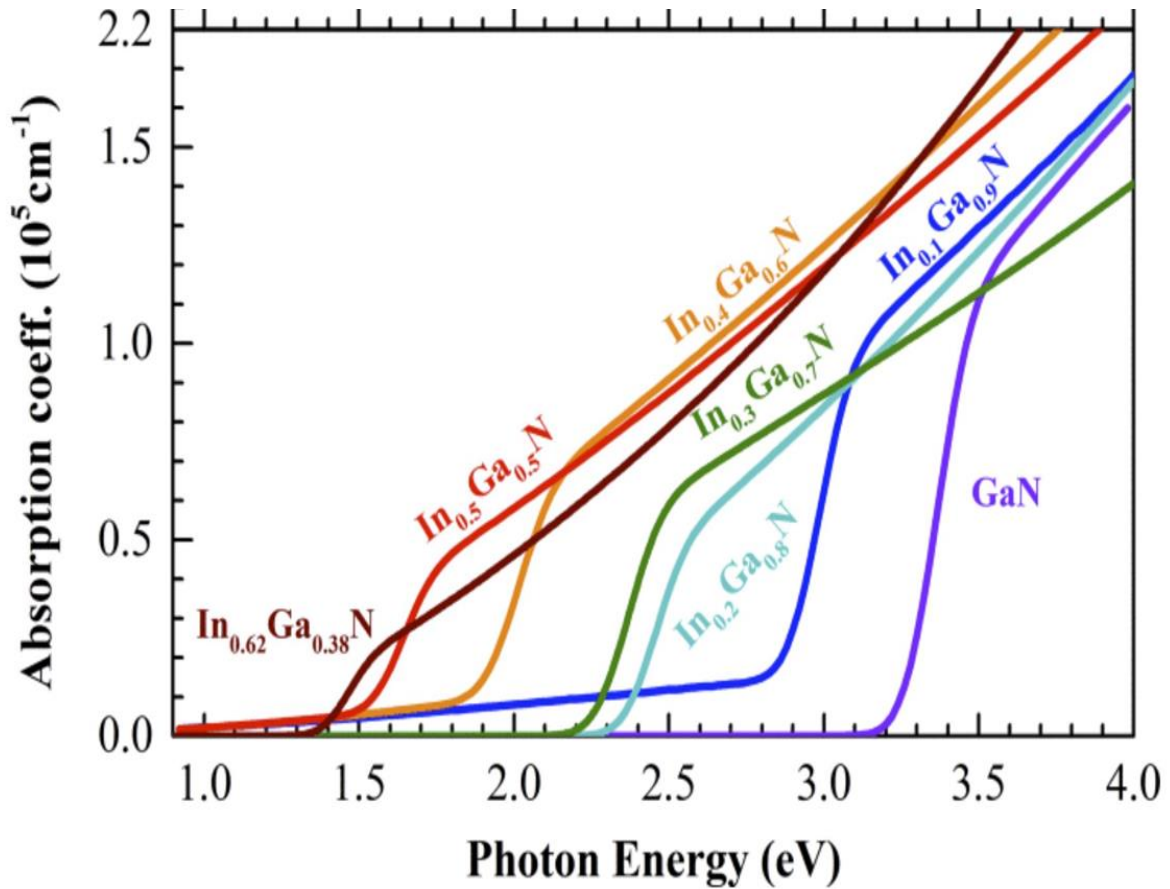

Figure 27. Absorption coefficient spectra of GaN substrate and InGaN layers at different In content[12].

Table 4. The estimated thickness for an absorber layer.

In composition	α (cm^{-1})$\times 10^5\ cm^{-1}$	Thickness (x) (nm)
0	1.15	200.22
10%	0.9	256
20%	0.5	461
30%	0.55	418.65
40%	0.6	384
50%	0.4	576
60%	0.25	921
Average thickness = 459.55 nm		

energy of that layer. The calculated thickness varied from 200.22 nm for GaN to around 921 nm for InGaN at 60% In content. The average was determined to be 459.55 nm. Thus, the graded composition with (0.03-0.50) In content InGaN active layer was done over 500 nm. It should be emphasized that this calculation is not comprehensive, but only used as an estimate to start the study of this material as an absorber for solar cells. However, other factors would need to be taken into consideration such as the lifetime of the carriers when choosing the thickness of the active layer.

The structure is demonstrated in Figure 28. It was grown at different temperatures to find the optimal conditions to grow graded composition InGaN with higher In content.

The electronic structure and optical properties were simulated using the nextnano^3 software package. The nextnano^3 software starts with strain calculation to obtain the band edges (conduction and valence bands) by applying band offsets and deformation potential theory. Then, this is followed by the Poisson, current, and the Schrödinger equations that are solved self-consistently including doping, pyroelectric charges, and excitonic effects. These calculations help to determine the built-in electrostatic potential, as well as calculating the energy levels and the wave functions [84],[85].

The nextnano^3 software package was employed to numerically simulate the band structure of ideal linearly graded InGaN active layers and calculate the optical transition probabilities. Only the ground states are highlighted here which are the lowest energy states.

The intended growth consisted of a composition graded from 3% to 50% In over a 500 nm layer, and then reverse graded over 100 nm with In content varying from 50% to 30% In, as shown in Figure 29. The background n-type doping, or unintentional doping resulting from impurities in the growth chamber and other intrinsic defects, for example, was set to the order of

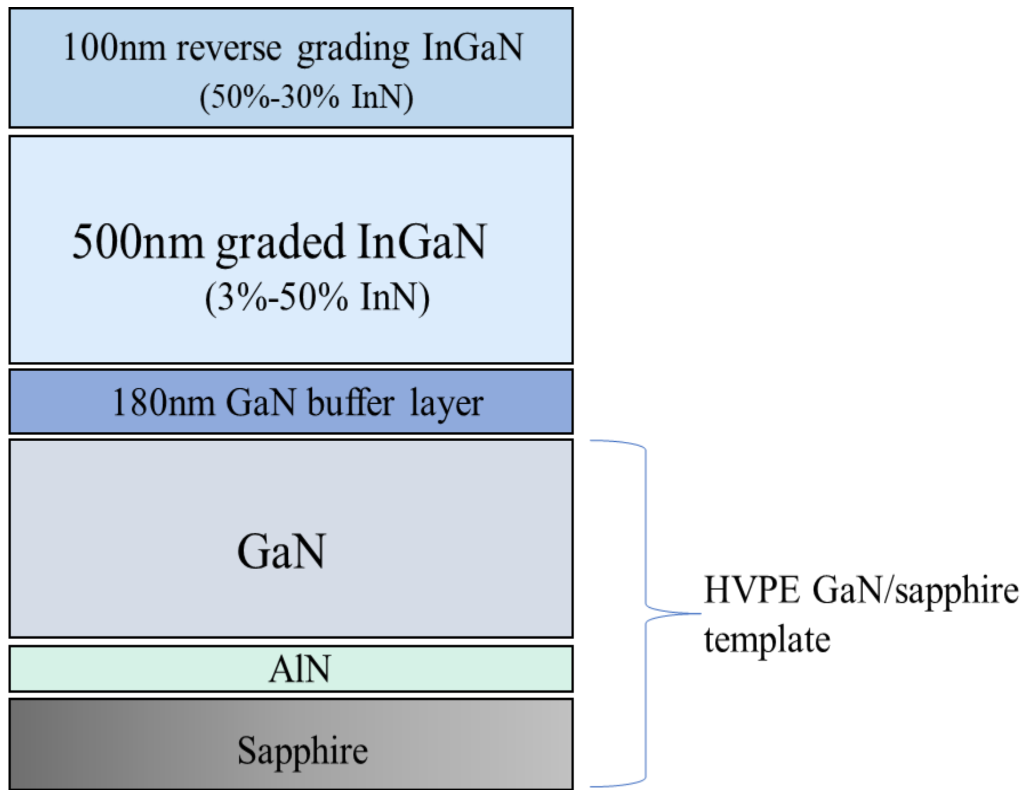

Figure 28. A schematic diagram of graded InGaN layers structure.

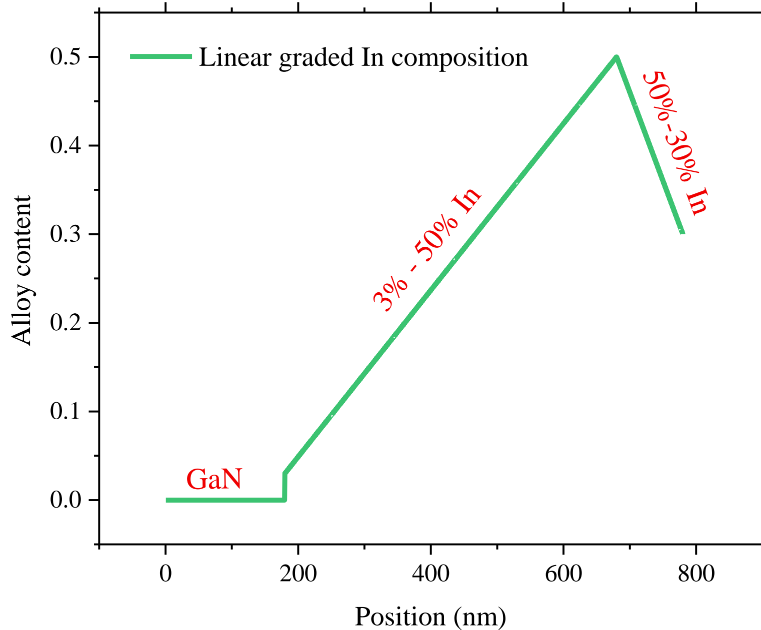

Figure 29. In profile that was simulated in nextnano^3.

10^{16}-10^{17} cm^{-3}, as it was proven through this research group's results that experiment results match the simulated results under this background doping. First, the ideal case was simulated for graded InGaN material with linear grade up over 500 nm (3%-50% In) and reverse grade down over 100 nm (50%-30% In).

Figure 30 shows the band diagram for homogenously strained material, i.e., strained to the GaN substrate in-plane lattice constant, and Figure 31 shows the band diagram for the same material with no strain, i.e., completely relaxed. The strain condition affected the band diagram greatly as well as the transition energies and probabilities.

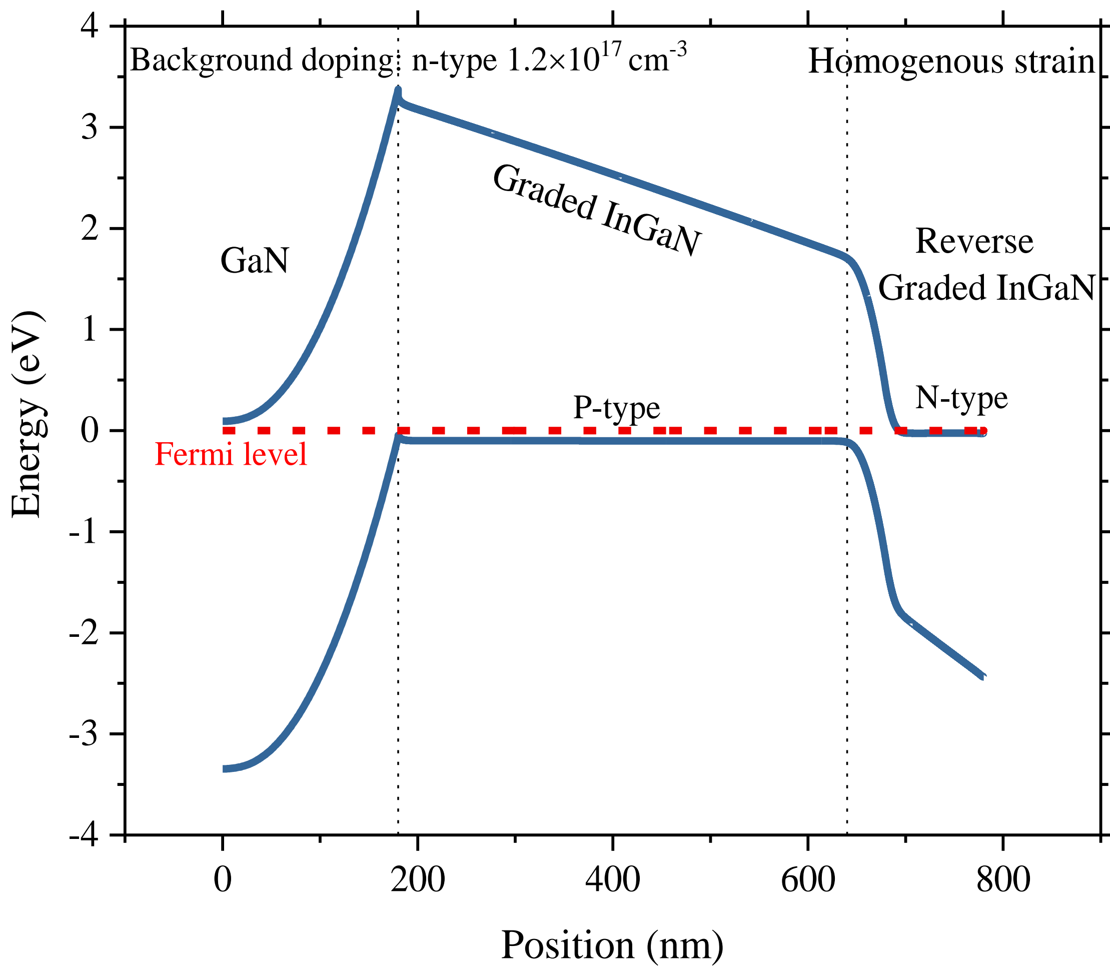

Figure 30. The band diagram for strained InGaN.

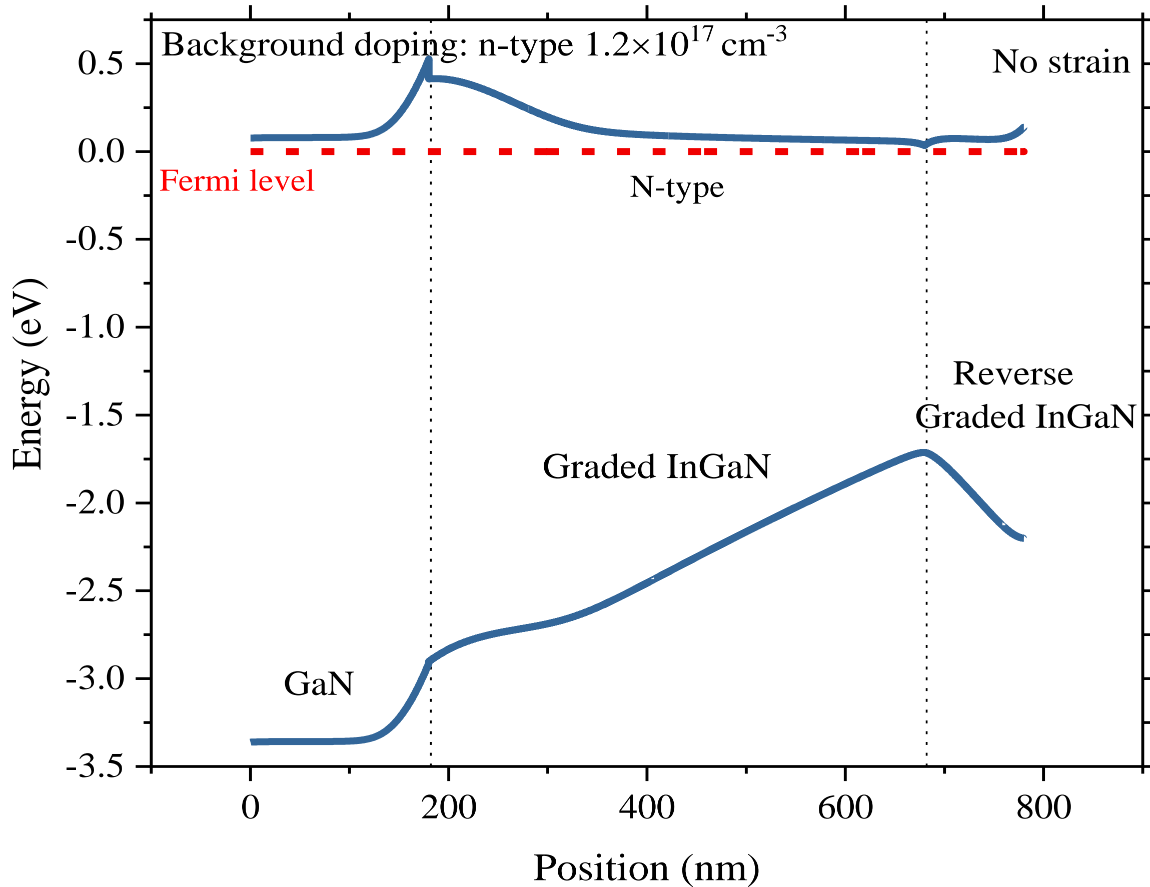

Figure 31.The band diagram for fully relaxed InGaN.

The polarization doping as demonstrated in Figure 30 resulted in p-type material in the graded up active layer (0.03-0.50) In composition, and n-type in the thin reverse graded layer (0.50-0.30) In composition. That is the expected case from the literature as mentioned in Chapter 1. However, the relaxed simulation in Figure 31 loses the p-type region, and generally takes on the doping of the background type and concentration. This highlights both the importance of the strain state, as well as some current uncertainty in the observed results, both in the present work and in other published works. The probability of transitions was examined for both the whole structures as well as at different depths in the structure, at the quantum region, i.e., the region over which the wavefunctions were calculated was isolated to specific regions of interest as

shown below. This helped to compare the simulated results to the effective observable band gaps that were found in the photoluminescence experiments due to the limited penetration depth of the UV laser that was only few nanometers close to the surface. This was as a result of UV light penetration depth in InGaN material being very small as will be discussed later.

Table 5 shows the band gap energies which were calculated using nextnano^3 that correspond to the highest transition probabilities at different depths. Then, the corresponding In composition could be determined using the In profile that was used in the simulation. In the homogeneous strain state, the transition occurs at the interface between the GaN substrate and graded InGaN.

Table 5. The energy band gap for both strained and fully relaxed InGaN at different depths.

Quantum region	Energy (eV) (Homogenous strain)	Energy (eV) (No strain)
All structure	3.37	1.76
Surface (30 nm)	2.25	2.20
Surface (70 nm)	1.97	1.97
Surface (120 nm)	1.89	1.76
Surface (200 nm)	1.95	1.76

However, in the fully relaxed state (no strain), the highest transition probability is closer to the surface. The wavefunction probabilities are demonstrated in Figure 32 and Figure 33. It can be seen that the transition energy for e581-hh1 for the homogenous strain state is around 3.37 eV (~180 nm) which corresponds to 3% In content. For the other strain state, which is the fully relaxed case, the transition energy for e2-hh1is around 1.76 eV (~678 nm) which represents 50% In content in the simulated linear graded composition profile.

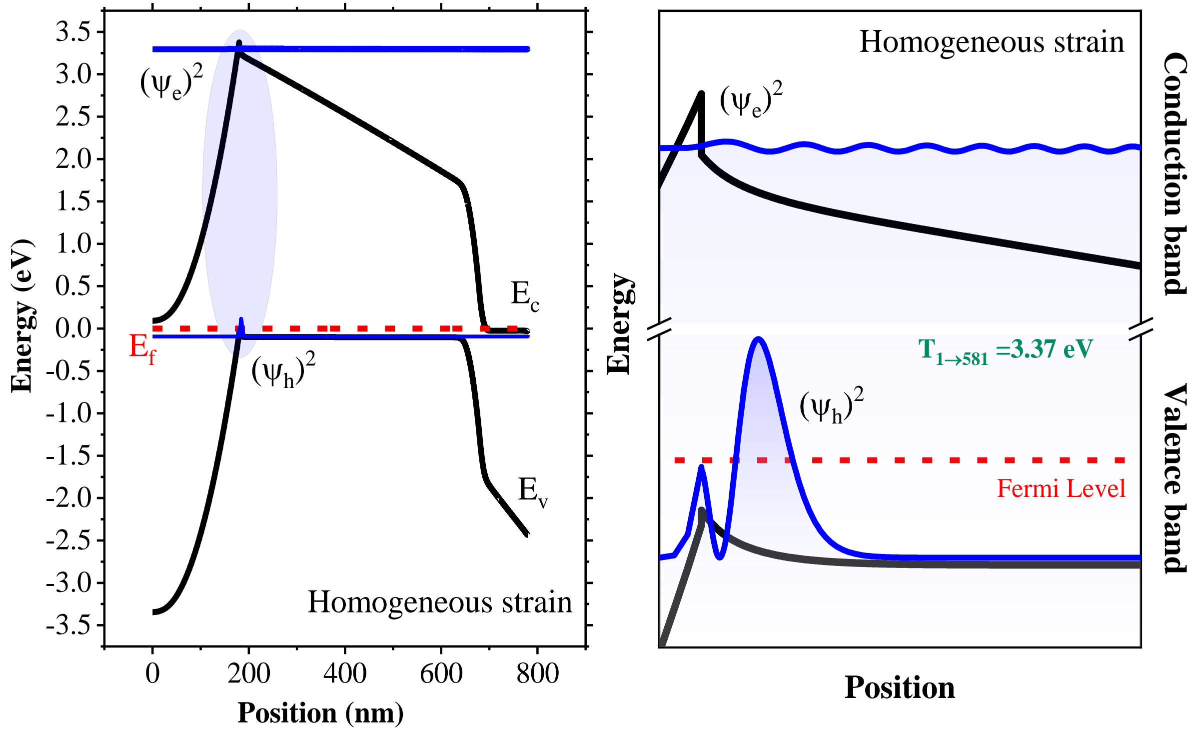

Figure 32. Band diagram and electron and hole wavefunction for the homogeneous strain state.

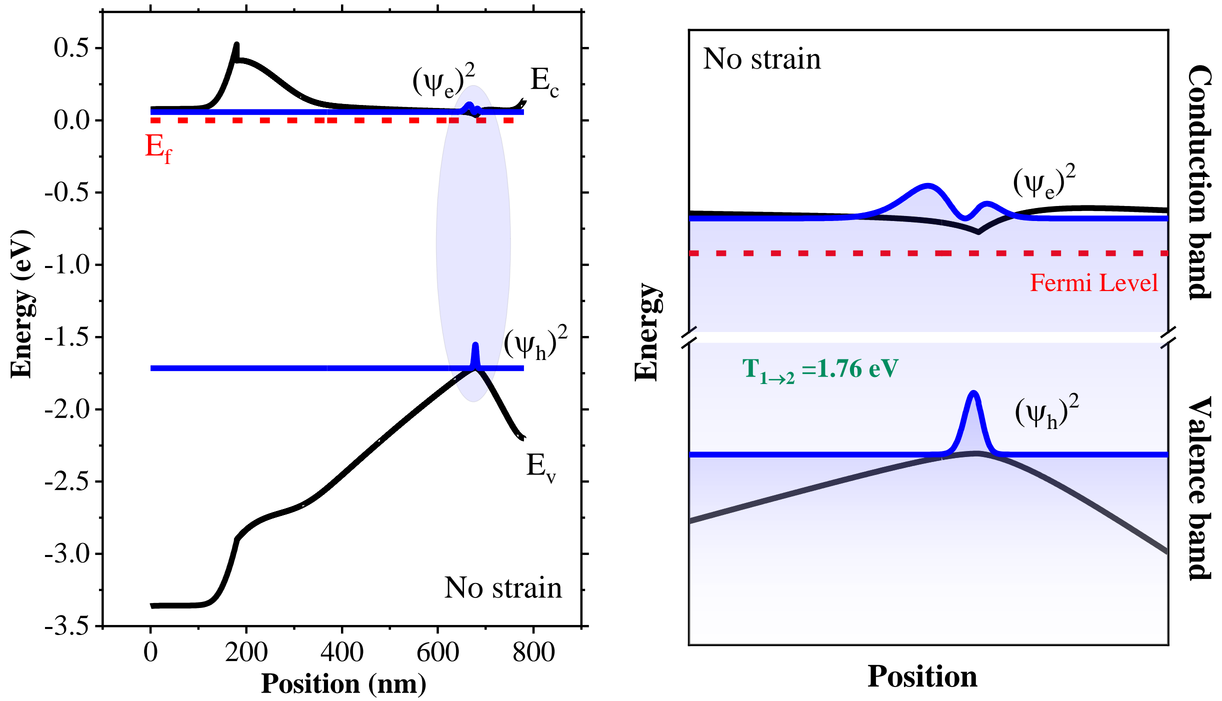

Figure 33. Band diagram and electron and hole wavefunction for no strain state.

The transition probabilities increased from 4.74% for the homogeneous strain condition to 84.2% for the fully relaxed condition. In this case of Figure 33, the fully relaxed strain state is the one that could be compared with the experimental results since it is near the surface, and it would be expected in the experiments to obtain a band gap energy that is closer to 1.76 eV (50% In).

The charge carrier densities are shown in Figure 34 for both homogeneous strain and relaxed (no strain). It is clear how the strain greatly impacts the polarization doping through the piezoelectric effect[86],[87]. In the homogenous strain case, the active layer is p-type while the top layer is n-type as expected. However, the relaxed case results in n-type active layer with lower electron charge density at the GaN/InGaN interface.

4.2. Experimental Results and Discussions

4.2.1. Atomic Force Microscopy (AFM)

The surface morphology of thick compositionally graded InGaN films were examined by AFM in tapping mode. The image scan size was 5 μm × 5 μm as shown in Figure 35. These surfaces were generally characterized by the underlying smooth, grainy texture. However, superimposed on that texture were small islands which appeared significantly less dense for higher growth temperatures. It is supposed that these were the result of excess In on the growth surface at lower growth temperatures; however, they need further study.

The overall surface roughness could be determined to increase with increasing the growth temperature, as the surface root-mean-square (rms) roughness decreased from 8.26 nm at a growth temperature of 475 °C to 5.20 nm at 555 °C. It was still considered a flat surface.

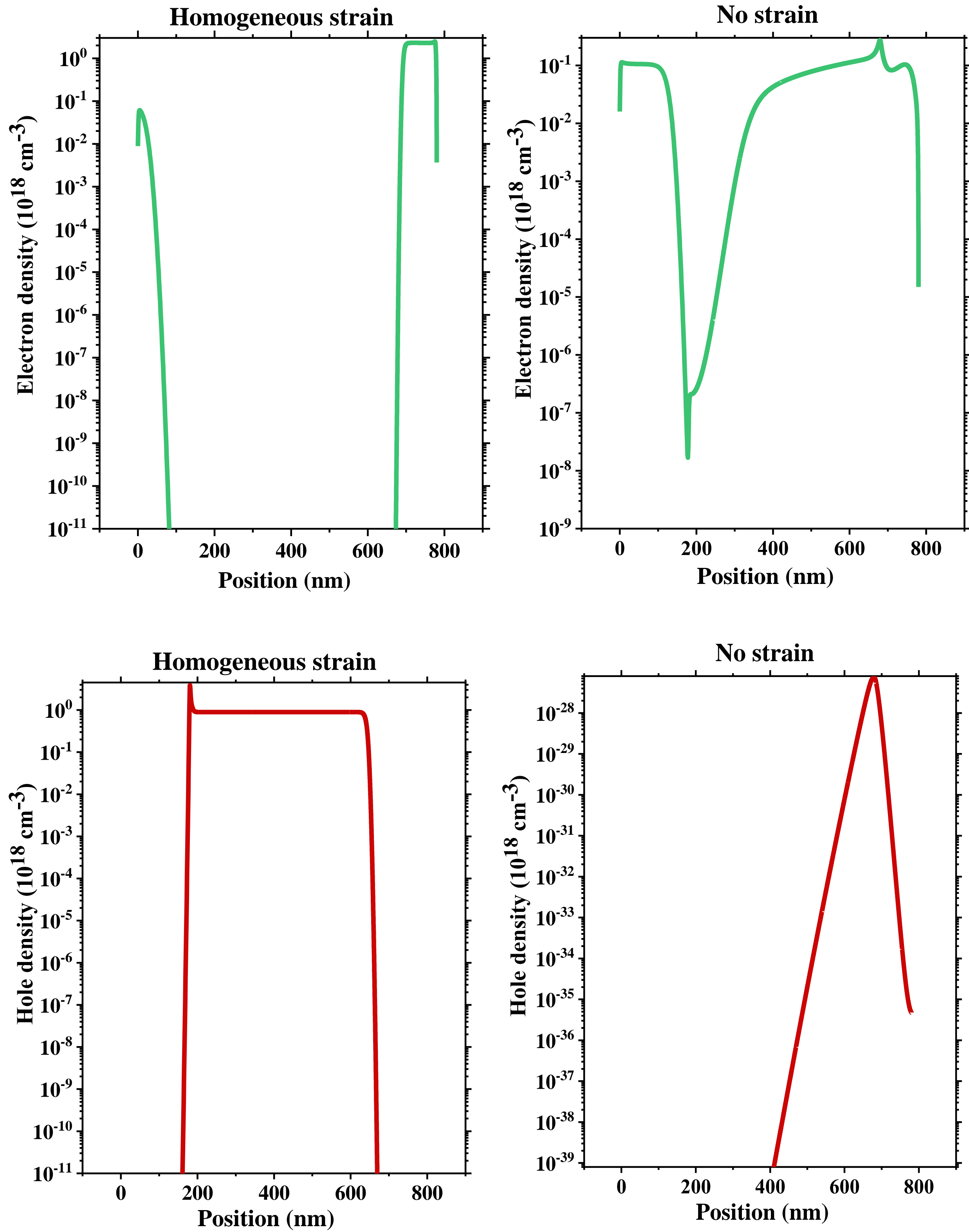

Figure 34. Electron and hole charge densities.

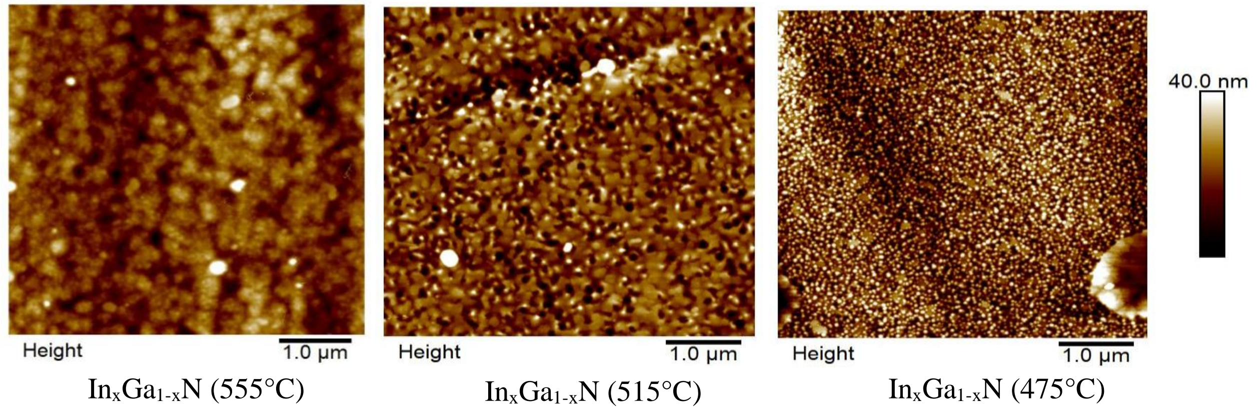

Figure 35. AFM images for graded $In_{1-x}Ga_xN$ active layers at different growth temperatures.

4.2.2 Optical Microscope

The accumulation of the metals on the surface is a common occurrence when the growth of InGaN is done in the MBE.

The main issue is the low maximum epitaxial growth temperature which is around 500-600 °C[88]. Additionally, the growth temperature of InGaN in MBE is generally so low that the In adatoms do not re-evaporate, particularly for InGaN with 25% In composition or higher. Also, the growth has to be kept under In-rich conditions to obtain a smooth surface so the excess In on the surface cannot evaporate fast, creating In droplets[89],[90].

Optical images were taken using a ZEISS (Carl Zeiss AG, Jena, Germany) optical microscope before and after etching In droplets using HCl. The microscope uses polarized reflected light microscopy and differential interference contrast microscopy (DIC) which presents detailed differences and features on the sample surface. This requires light shearing (Nomarski) prisms in addition to plane-polarized light. The DIC was used to examine the surface of the sample after In droplet etching. These methods are contrast enhancing methods to enhance the surface features[91],[92].

As demonstrated in Figure 36, at 20x and 100x magnification the droplet density increased with the decreasing temperature, following what was mentioned above that the growth temperature was lower than the re-evaporation temperature, which led to metal accumulation on the surface.

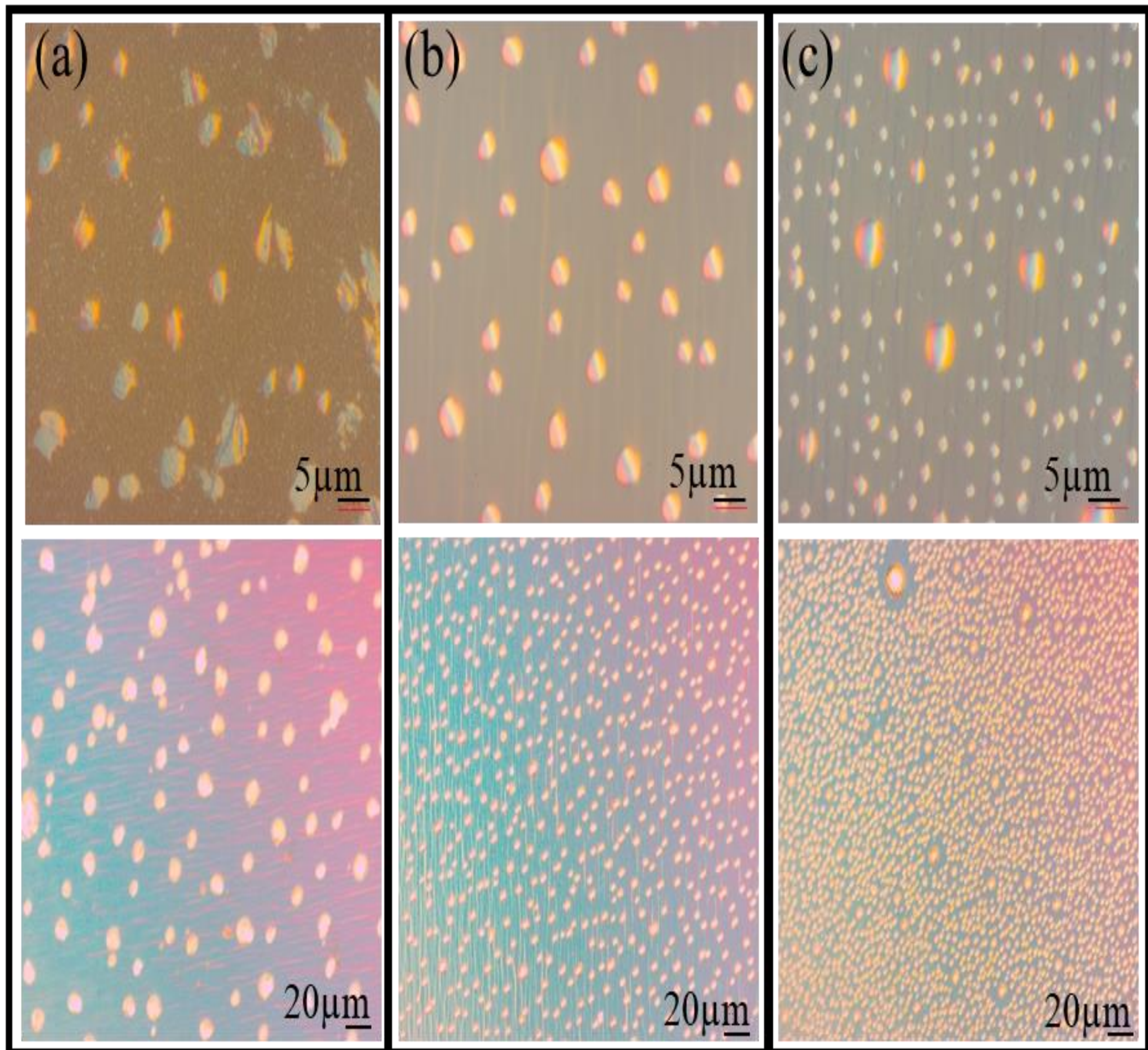

Figure 36. Optical microscope images for In droplets in: (a) graded InGaN (555 °C), (b) graded InGaN (515 °C), and (c) graded InGaN (475 °C) before etching.

The droplet sizes ranged from between around 1μm to 10 μm. It is obvious that at the 475 °C growth temperature, the small droplets merged to form larger droplets. Figure 37 shows the surface after HCl etching. It is observed at 515 °C)and 475 °C in Figure 37b and c, respectively, that the droplets tended to leave a ring-like structure behind following the HCl etching. Zheng et al.[93] proposed a model to explain the formation of In droplets and the ring-like structure considering the model proposed by Wu et al.[94] that explained Ga droplet formation. The energy difference on the surface promotes the expansion that occurred of the In droplets through the absorption of the In adatoms. This increased the surface tension until the droplet broke out and liquid In was released, which formed a larger ring.

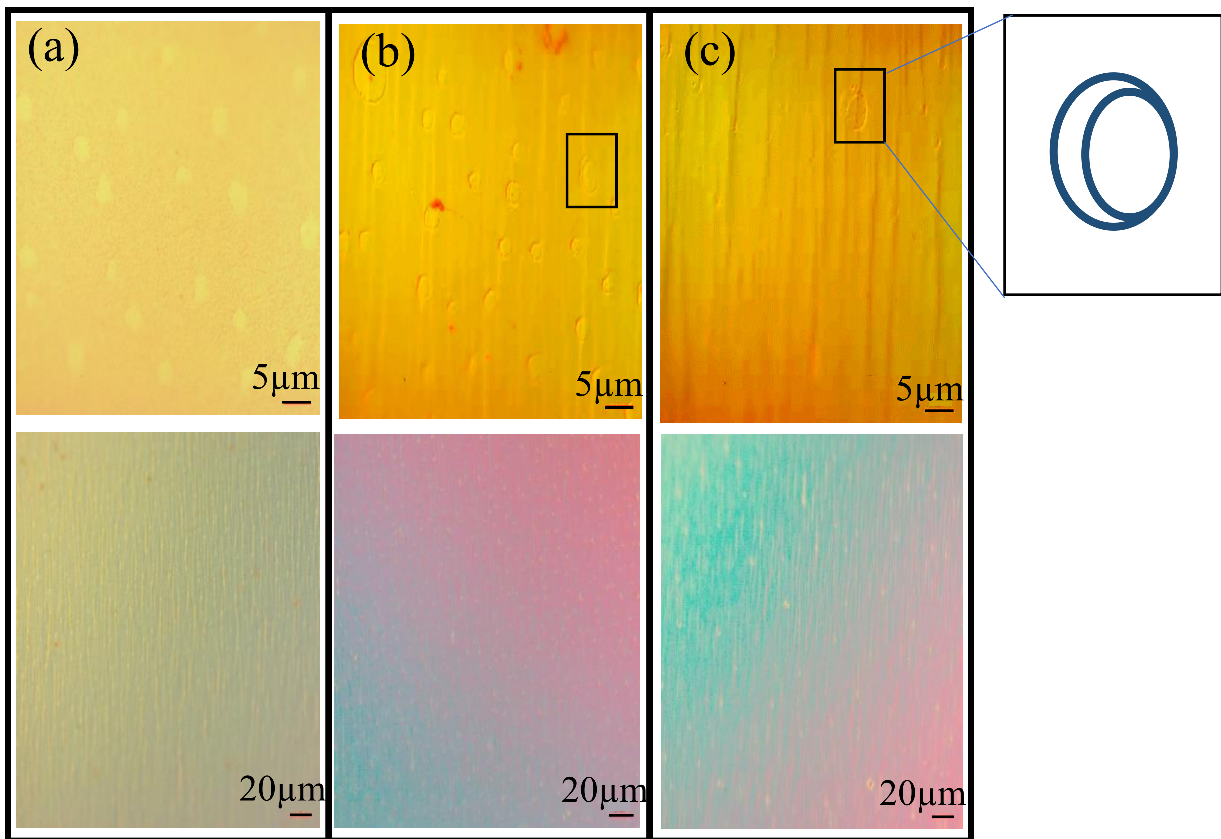

Figure 37. Optical microscope images for In droplets in: (a) graded InGaN (555 °C), (b) graded InGaN (515 °C) and (c) graded InGaN (475 °C) after etching.

4.2.3 Scanning Electron Microscopy (SEM)

Figure 38 shows the scanning electron microscopy (SEM) images before and after In droplet etching by HCl. It can be observed that the droplet accumulation on the surface increased with decreasing temperature as was demonstrated in the optical microscope images. The surface of the graded InGaN layers again showed higher density of metal droplets as the growth temperature decreased. However, the formation of the droplets at the higher growth temperature (555 °C) was incomplete formation or unstable which could have been as a result of the higher temperature. Senichev et al. noted that at 600 ° C growth temperatures or higher, indium desorption is observed[95].On the other hand, the merging of the small droplets into larger droplets was present at lower temperatures as shown in (b) and (c). Thus, the number of droplets decreased when this process occurred.

Energy dispersive x-ray spectroscopy (EDX) mapping confirmed that the metal droplets were actually composed mostly of In, as shown in Figure 39. The color of the droplet in the images was different in each sample, but all those colors represent In. Thus, the difference in colors did not represent or mean anything.

Additionally, line profile analysis in Figure 40 that goes over the droplets reveals that the In curve increased when the line was on the droplet. This means that those droplets had higher In content than the surface. Confirming that the droplets were pure In was significant to show that Ga atoms were incorporated in the material to form InGaN.

4.2.4 Transmission

The room temperature optical transmission measurements shown in Figure 41

demonstrate the variation of the average bandgap for each sample in comparison with the GaN substrate. For GaN, there was a sharp cutoff at ~365 nm which corresponds to the direct band gap at 3.4 eV. The $In_xGa_{1-x}N$ curves show a general shift toward longer wavelengths with decreasing the growth temperature, which implied higher In content in the material.

Additionally, the cutoff was not sharp which was likely the result of the graded bandgap. Examining Figure 41, on a linear scale there was an absorption cutoff at ~448 nm (2.8 eV) observed for the highest growth temperature sample (555 °C, red curve) which corresponds to ~ 18% In. For the lower growth temperatures (515 °C and 475 °C), the absorption edge was observed at ~585 nm (2.1 eV) and ~ 693 nm (1.7 eV), respectively. These corresponded to higher In compositions of 39% and 53%, respectively.

For a single composition film, one might estimate the bandgap energy through the use of a Tauc plot using Equation 15[96]:

$$(\alpha h\nu)^n = k(h\nu - E_g) \quad \text{(Equation 15)}$$

Here, k is a constant, α is the absorption coefficient, hν is the photon energy, and E_g is the bandgap energy. The exponent, n, determines the type of optical transition, by which value creates the best linear fit to the data at the band edge energy. It has been shown that if n = 2, then the transition is across a direct bandgap, and if n = ½, then the transition is across an indirect bandgap[97]. In Figure 42 Tauc plot analysis was used to determine the average optical bandgap of the material.

Here, $(\alpha h\nu)^2$ was plotted against the photon energy. The power, n = 2, was the best fit, reinforcing the understanding that here was a direct band gap transition. Then, a straight line was

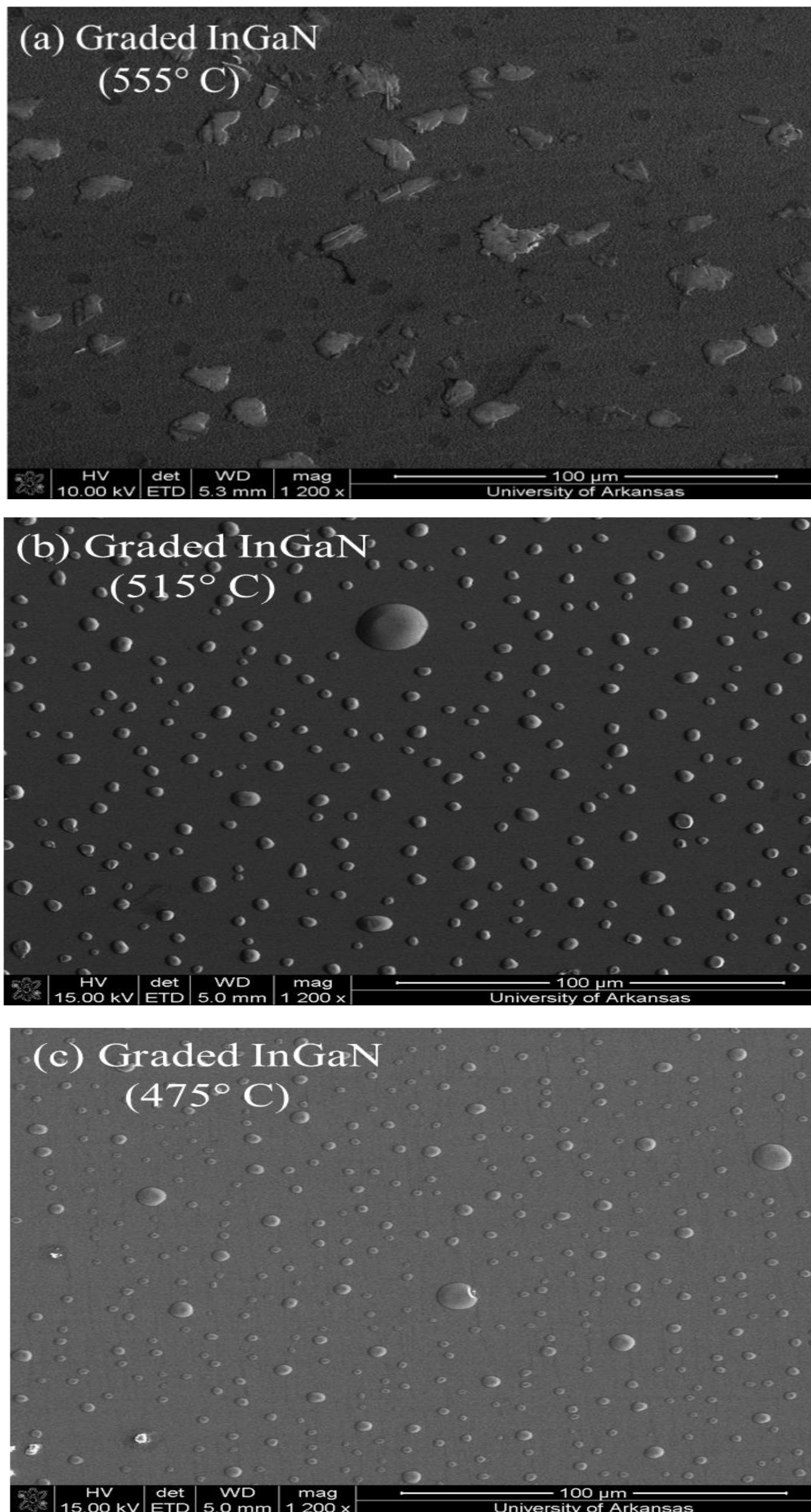

Figure 38. SEM images that show In droplets on the surface of graded InGaN.

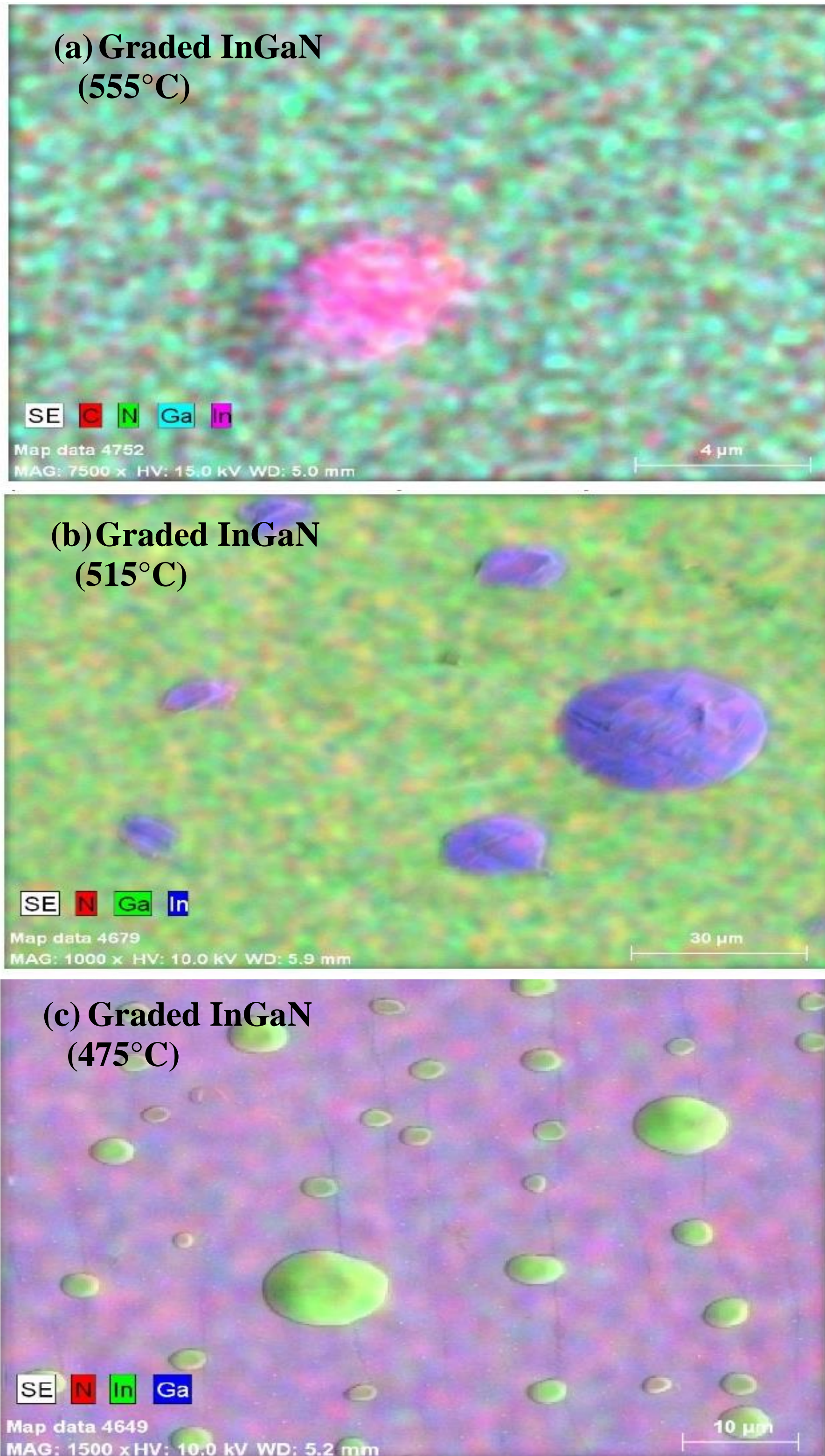

Figure 39. EDX mapping for In droplets on graded InGaN surface.

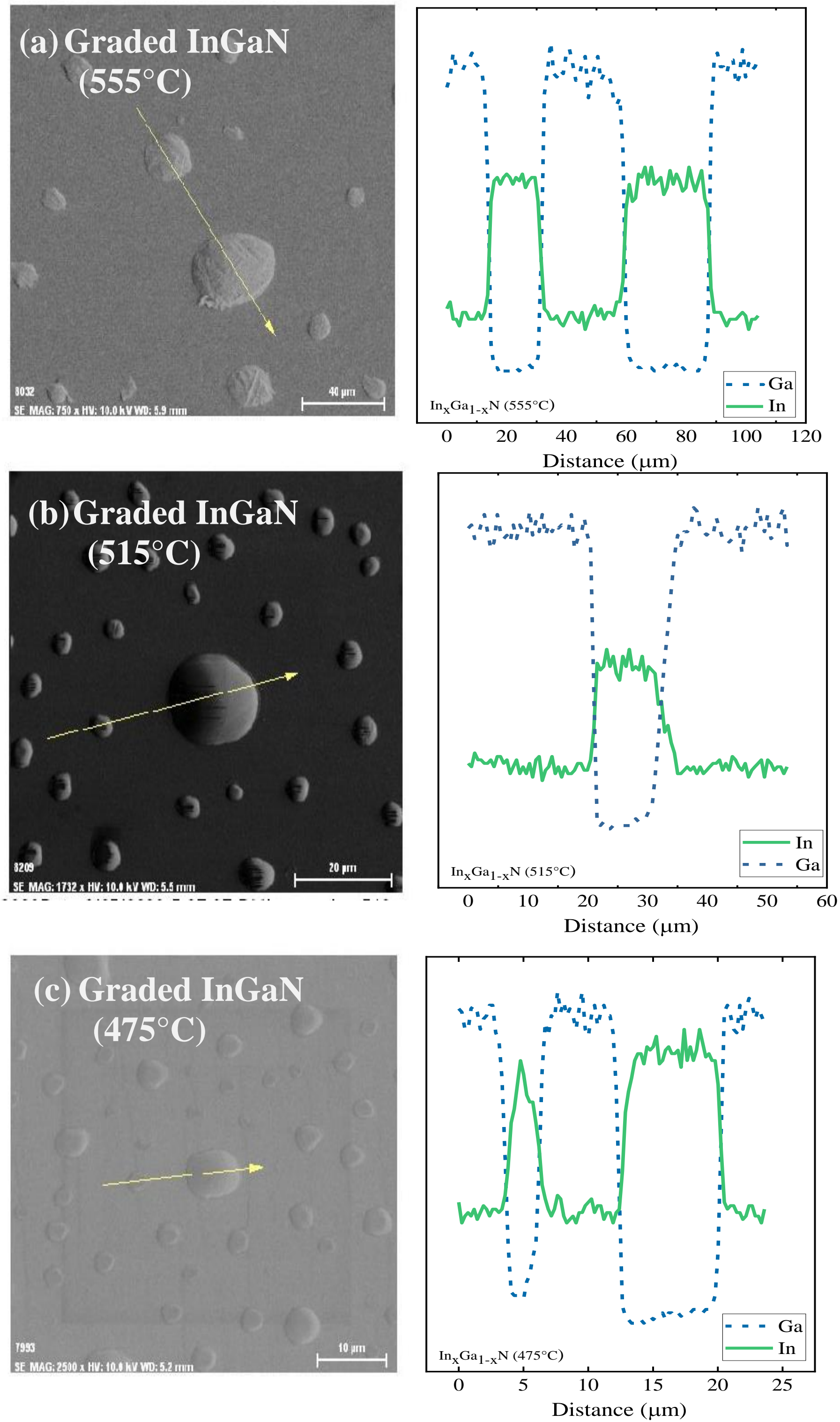

Figure 40. EDX line scans.

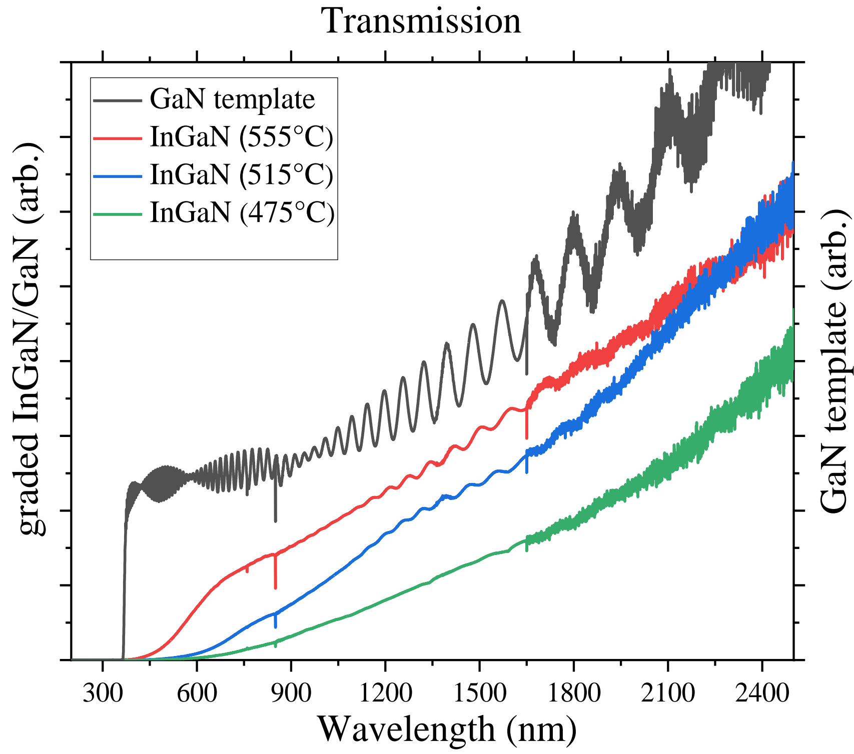

Figure 41. Room temperature transmission spectra

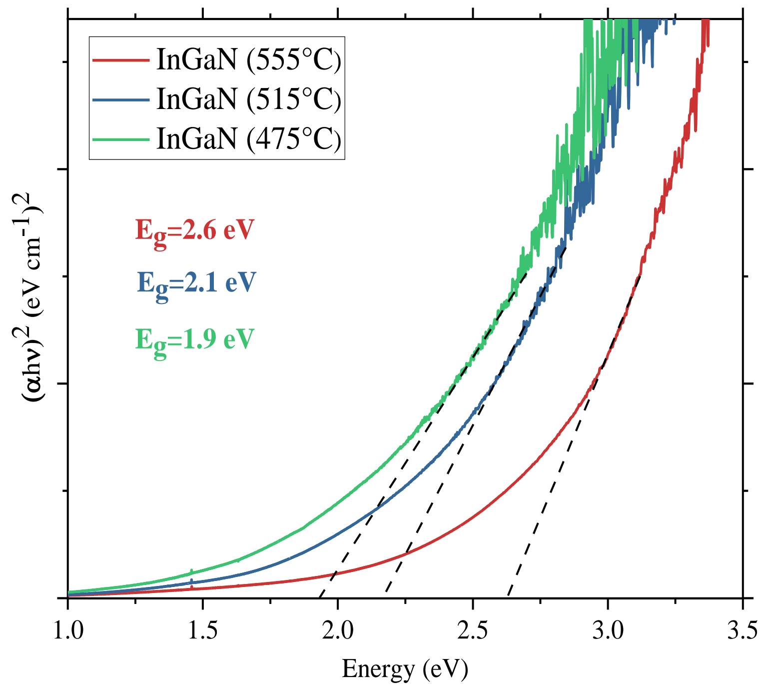

Figure 42. Tauc plot for graded In1-xGaxN active layers at different growth temperatures.

extended from the linear region in the resulting plot to the x axis which determined the bandgap energy.

The average band gaps determined for the three samples were 1.9, 2.1, and 2.6eV for the 475, 515, and 555 °C samples, respectively. This corresponded to In compositions of 24%, 40%, and 46%, again, respectively. All of the above compositions were determined from a Vegard's law calculation including bowing, shown in Equation 16[98]:

$$E_g(\mathrm{InGaN}) = \Big((1 - x) \times E_g(\mathrm{GaN})\Big) + (x \times E_g(\mathrm{InN}) - (b \times x \times (1 - x)) \quad \text{(Equation 16)}$$

Since both of these techniques—absorption edge and Tauc plot—are based on the assumption of a continuous film of a single composition, it was not clear which was more representative of the samples. They were examined by XRD and PL (below) for further corroboration.

4.2.5 Photoluminescence (PL)

The photoluminescence was excited with a UV, HeCd laser at 325 nm with a power of ~10 mW. The general redshift seen in the transmission with decreasing growth temperature was similarly observed in the PL.

Figure 43 shows the room temperature PL as well as the low temperature which showed a characteristic shift with temperature. It can be seen that the PL peaks at 16 K were blue shifted by about 0.15 eV compared to those taken at 300 K. This was approximately what would be expected from the shifting of the bandgap with temperature alone, which would indicate that the emission was coming from bulk-like regions of the material, i.e., not from phase separated localized regions of high indium composition.

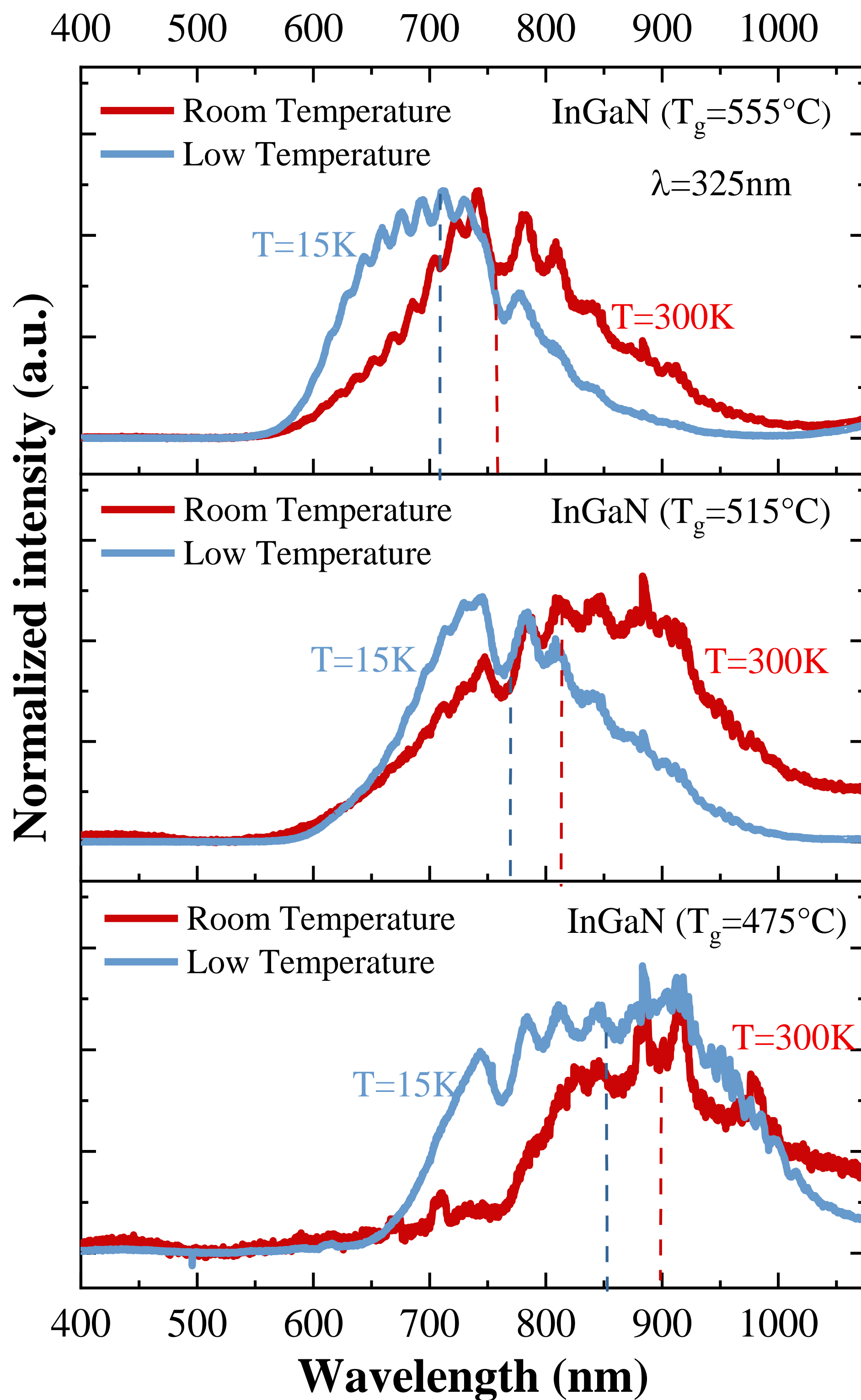

Figure 43. Graded InGaN PL measurements at room temperature and 15 K for different growth temperatures.

The low temperature PL at 15 K demonstrated an extremely wide spectra with all curves having full widths at half maximum (FWHM) of ~150 nm or ~0.5 eV. It was found that the representative PL peaks were significantly shifted to lower energy in comparison with the bandgaps derived from the transmission measurements. The PL peaks were at 1.44, 1.59, and 1.75 eV for the 475, 515, and 555 °C samples, respectively. If these were thick films of bulk relaxed material, the emission energies would represent In compositions of 51, 58, and 64%, respectively.

Additionally, the large dip and most of the oscillations present in these spectra were the result of interference in the collection optics and filters and were not features of the luminescence from the samples. Furthermore, the narrow lines seen in the room temperature data from the 475 °C sample, along with similar lines observed in the other samples, were artifacts due to long detector integration times and light leakage into the spectrometer. The recombination of photoexcited excitons was expected generally to occur at the interface between the grade up and grade down layers.d grade down layers.

This was a combination of the result of very low penetration depths for the 325 nm laser (~50-80 nm), and the relatively long diffusion length of excitons (up to ~100 nm) in III-nitride semiconductors[99]. Under these conditions, it was expected that the excitons would find the lowest energy band gap and, thus, the highest In composition for recombination. However, with the current simple models, what is not taken into account was the potential energy shift of the luminescence due to the built-in field of the p-n junction resulting from the polarization doping. That should lower the recombination energy resulting in an over-estimation of the In content[96], [39].

The penetration depth of the laser (h) was estimated using the absorption coefficient as a

function of the wavelength (α(λ)). The absorption coefficient depends not only on the photon energy but also on the composition of the film. The following relation was proposed by Brown et al. and was used to calculate and plot Figure 44:

$$\alpha(\lambda) = \alpha_0 \sqrt{a(x)(E - E_g) + b(x)(E - E_g)^2} \qquad \text{(Equation 17)}$$

Where a(x) and b(x) are fitting parameters and E is the energy of the photon (E = hc/ λ)[62]. However, the fitting parameters were given for small In content, thus Belghouthi et al. adjusted these parameters using the following relations[100]:

$$a_{fit} = 12.87x^4 - 37.79x^3 + 40.43x^2 - 18.35x + 3.52 \qquad \text{(Equation 18)}$$

$$b_{fit} = -2.92x^2 + 4.05x - 0.66 \qquad \text{(Equation 19)}$$

In Table 6, the absorption coefficient was calculated at different In compositions to determine the penetration depth of the UV laser (325 nm) in InGaN.

$$\text{Penetration depth (h)} = \frac{1}{\alpha}\,\text{(cm)} \qquad \text{(Equation 20)}$$

where h is the penetration depth of the laser in the material and α is the absorption coefficient.

Finally, there was a significant decrease in overall PL intensity with increasing indium content, i.e., decreasing growth temperature. This was demonstrated by the increased noise of the PL for the 475 °C sample.

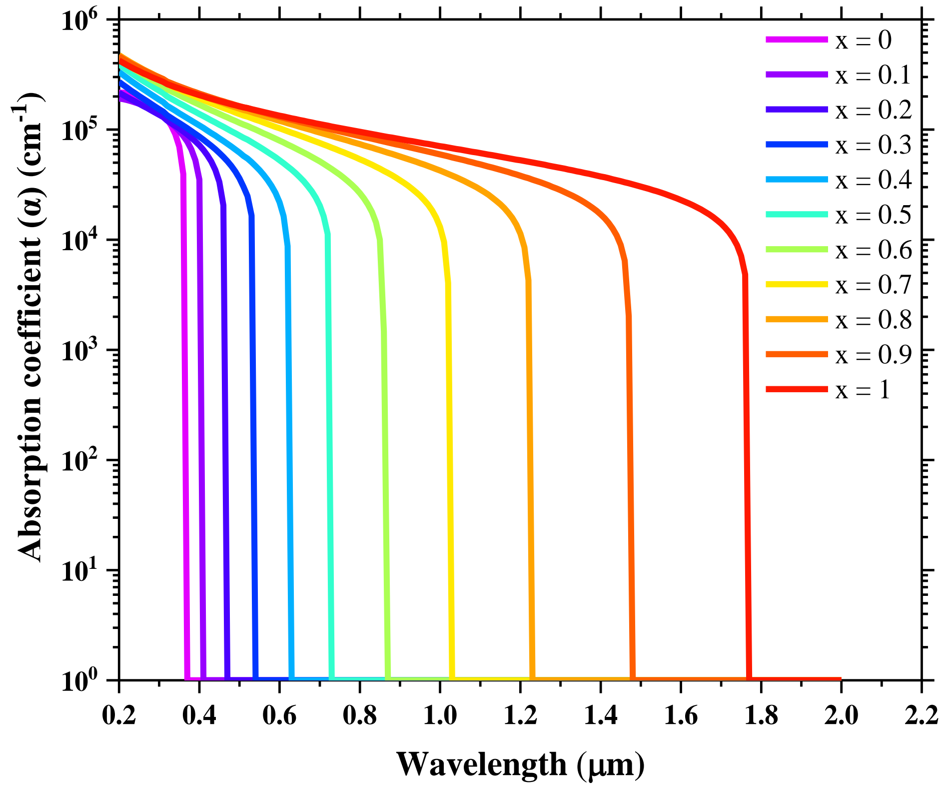

Figure 44. The absorption coefficient for InGaN at different In content.

Table 6. The calculated penetration depth of the UV laser (325 nm) in InGaN.

x	a_{fit}	b_{fit}	E_g (eV)	$E-E_g$ (eV)	α (cm^{-1})	Depth (cm)	Depth (nm)
0	3.52	-0.66	3.4	0.42	116115.23	8.61×10^{-6}	86.12
0.10	2.05	-0.28	3.00	0.81	121770.34	8.21×10^{-6}	82.12
0.20	1.19	0.03	2.63	1.18	120431.47	8.30×10^{-6}	83.03
0.30	0.74	0.29	2.29	1.53	134369.97	7.44×10^{-6}	74.42
0.40	0.56	0.49	1.98	1.84	164162.59	6.09×10^{-6}	61.00
0.50	0.53	0.64	1.69	2.12	199836.90	5.00×10^{-6}	50.00
0.60	0.57	0.72	1.44	2.38	232868.83	4.29×10^{-6}	42.90
0.70	0.61	0.74	1.21	2.61	257919.14	3.88×10^{-6}	38.80
0.80	0.64	0.71	1.01	2.80	271704.23	3.68×10^{-6}	36.80
0.90	0.65	0.62	0.84	2.97	272224.72	3.67×10^{-6}	36.80
1.00	0.68	0.47	0.70	3.12	258458.96	3.87×10^{-6}	38.80

Some of this noise appeared to be spectral information, however those were determined to be artifacts due to scattered room lights, which were only visible during very long low intensity integrations in the spectrometer. This was accentuated by the fact that the sample emission was gradually shifting into a range where the silicon CCD detector was becoming inefficient. To determine the true relative emission intensities of the types of samples, a long wavelength-sensitive detector was needed.

To further understand the origin of these emission bands, power dependent PL measurements were performed as demonstrated in Figure 45, Figure 46, and Figure 47. Figure 45 shows the power dependent PL of the 555 °C sample over nearly three decades of excitation power. Apparent, as with the other samples, was that there was no shift in energy with power. This indicated that this was bulk-like recombination, exhibiting no evidence of confinement either through state filling or quantum confined Stark shift. This indicated that the material from which the luminescence was derived was single phase with little phase separation.

Assuming the PL intensity (I) is proportional to the excitation power (P), the emission can be modeled through a power law expressed in Equation 21:

$$I \propto P^{\alpha} \qquad \text{(Equation 21)}$$

where the power law factor, α, represents various recombination processes. For bulk-like recombination, if α is equal to 1, it indicates that the radiative transition is generally exciton-like. If $\alpha = 2$, it indicates that the radiative transition is due to free carrier recombination where a free electron in the conduction band can recombine with any free hole in the valence band.

In addition to these values, if $\alpha > 1$, it indicates that a Shockley-Read-Hall (SRH)

defect mediated non-radiative recombination is competing with free carrier, radiative recombination. And finally, a value of $\alpha < 1$ suggests that the radiative recombination mechanism includes defects or impurities such as free-to-bound and donor-acceptor pair transitions which are spatially indirect transitions between electrons bound to donors and holes bound to acceptors[101].

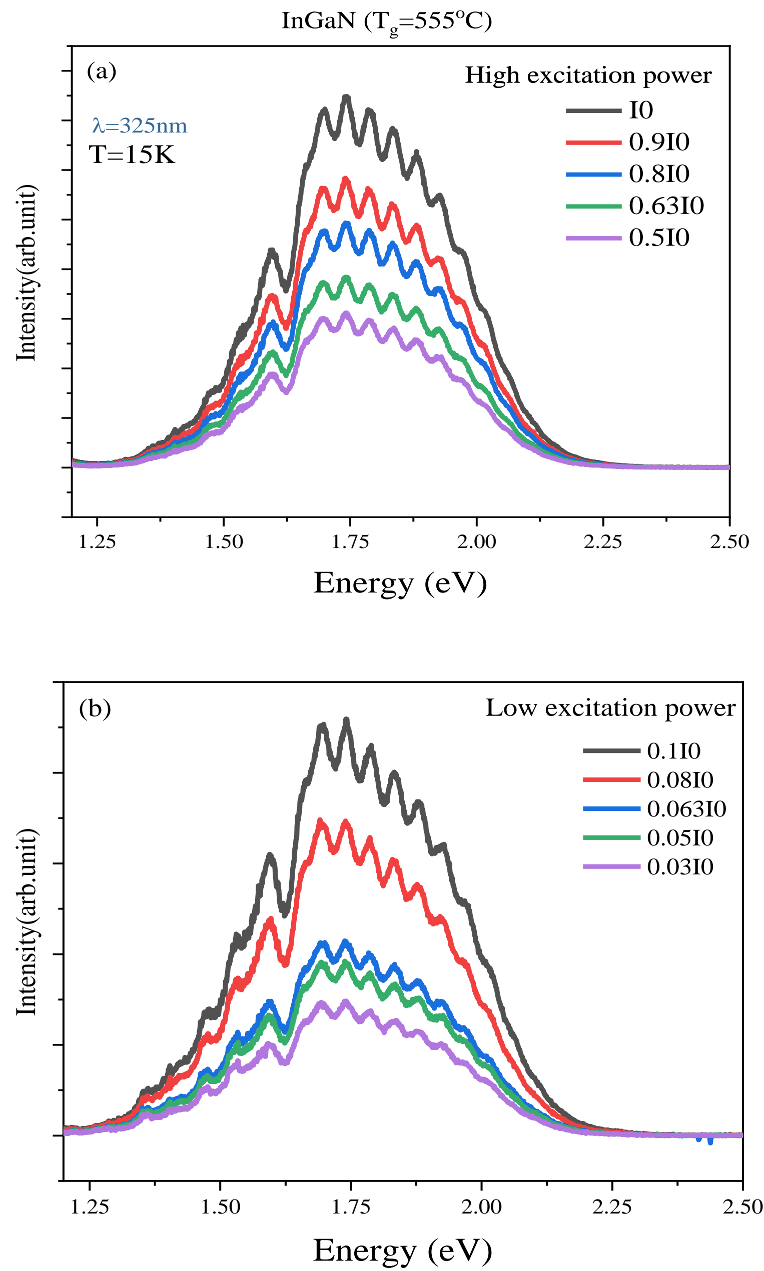

Figure 45.Graded InGaN (555 °C) PL measurements at 16 K at different excitation

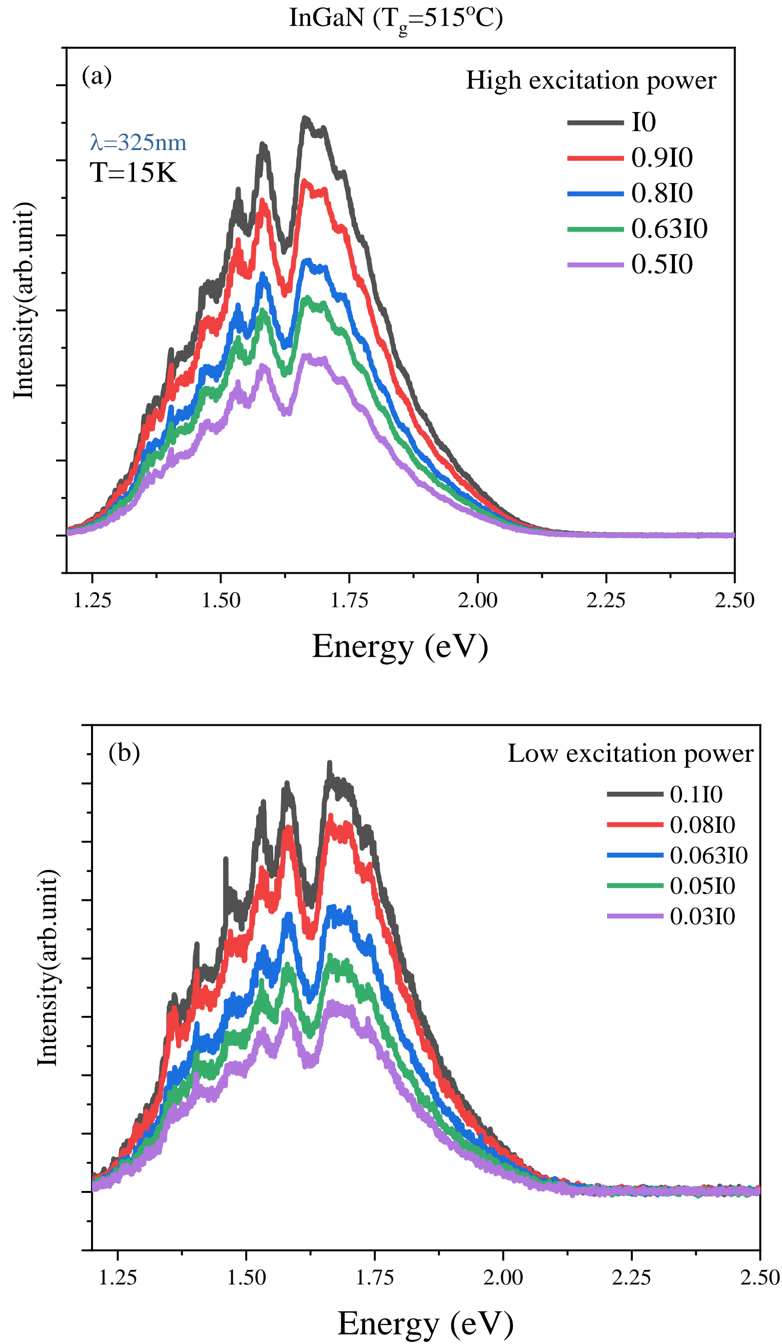

Figure 46. Graded InGaN (515 °C) PL measurements at 16 K at different excitation power.

The PL spectra were each fit using a single Gaussian to obtain the spectral parameters. In Figure 48, it was found that α for the low growth temperature samples was close to but slightly

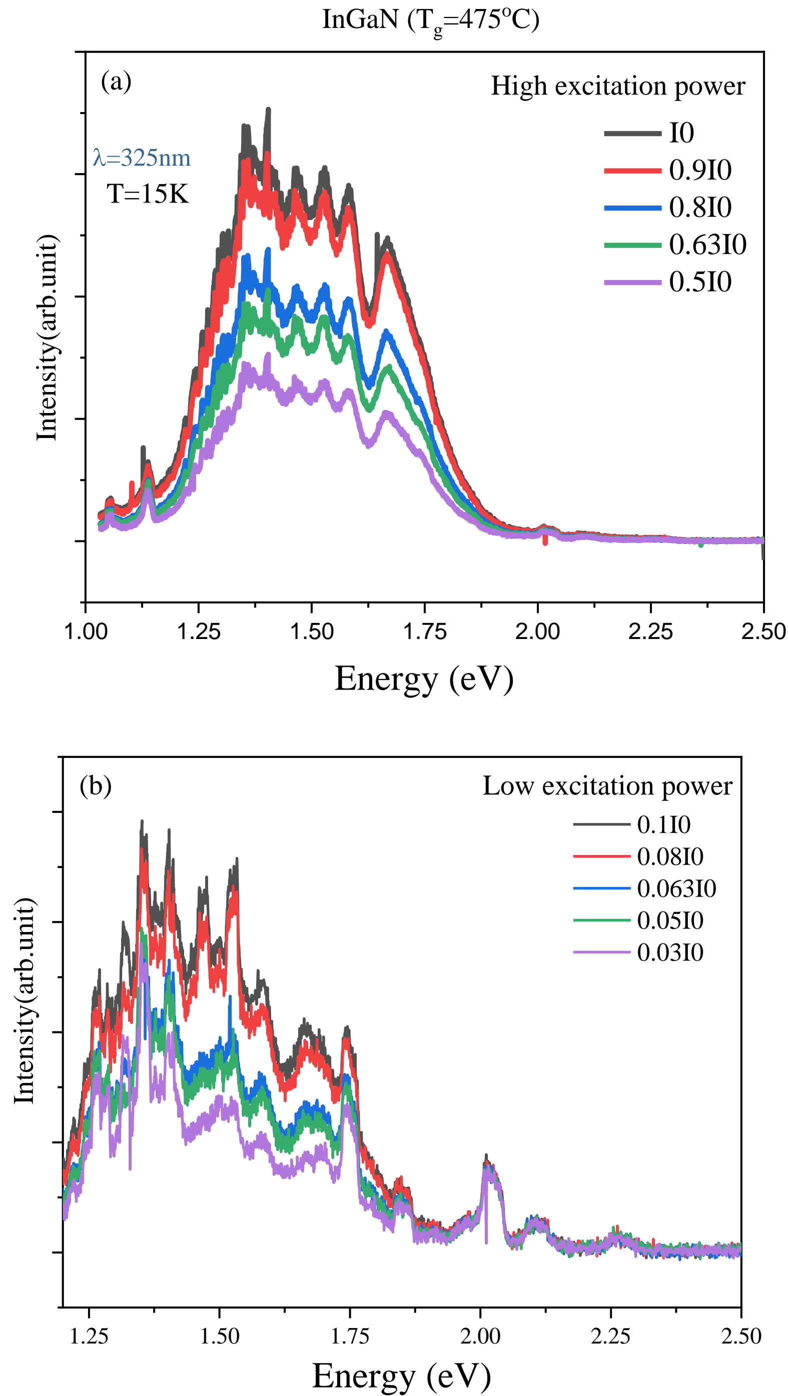

Figure 47. Graded InGaN (475 °C) PL measurements at 16 K at different excitation power.

greater than unity. Therefore, it was concluded that for low temperatures, the emission was generally due to bulk excitons with some competition from nonradiative channels, likely due to

defects or impurities. However, for the other two materials at 555 °C and 515 °C growth temperatures, they showed α greater than unity indicating a Shockley-Read-Hall (SRH) defect mediated non-radiative recombination.

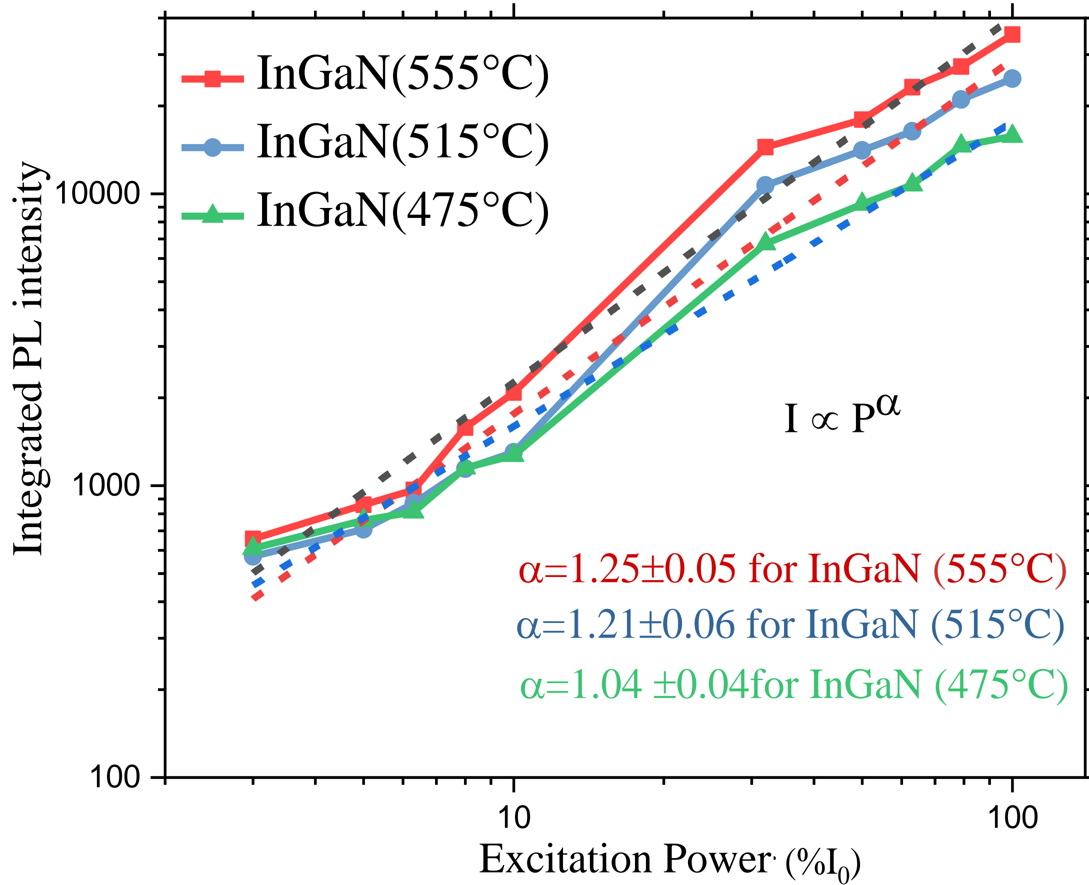

Figure 48. Integrated PL intensity of InGaN films as a function of laser excitation power.

4.2.6 X-Ray Diffraction (XRD)

Symmetric (0002) x-ray diffraction ω/2θ scans of the thick graded $In_xGa_{1-x}N$ samples in Figure 49 showed GaN and AlN peaks from the substrate. Additionally, each showed a long tail to low angle, which is a signature of graded films[102],[103]. The high temperature growth

(555 °C) showed a relatively uniform broad tail. The low angle extent of this tail decreased with the growth temperature, indicating that lower growth temperature allowed for higher In content, which is similar to the transmission results. However, the peaks evolving at the high and low end of the tail may have been the result of phase separation and/or relaxation in the film.

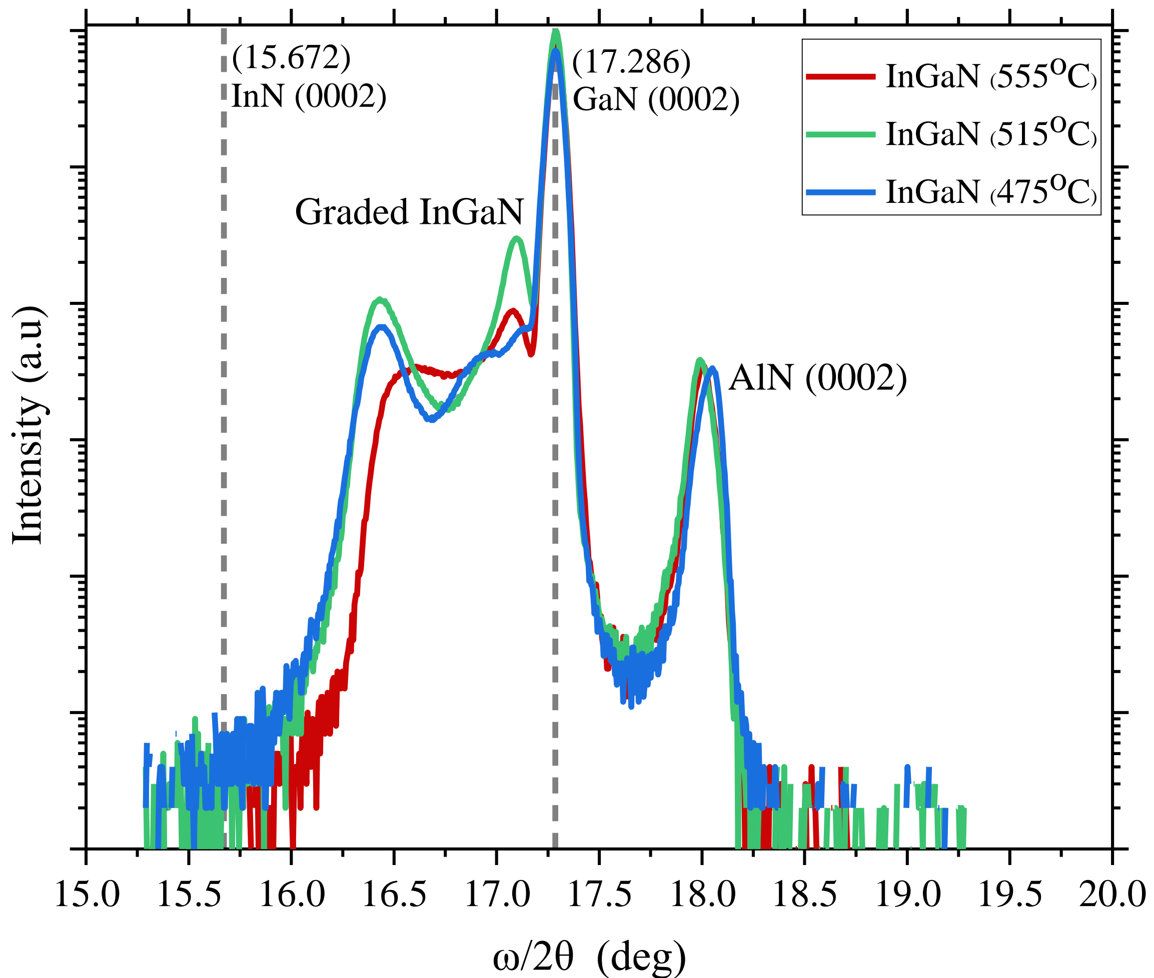

Figure 49. Symmetric (0002) X-ray diffraction of thick graded InGaN films at different temperatures.

Simple simulations of the structure assuming linear grades with no relaxation or phase

separation (not shown here) indicated that the maximum In composition according to the omega-2 theta scans was around 30%. However, more details could be found from the reciprocal space maps (RSMs) of the 475, 515, and 555 °C samples around the (105) reflection, shown in Figure 50, Figure 51, and Figure 52, respectively.

Immediately evident for all samples was the tail extending down from the main GaN (105) reflection due to the thick template layer of the substrate. However, for the lower temperature sample, Figure 52, the tail closely followed the relaxation line, which is shown as a dashed line, tilted from the fully strained line in each frame. This indicated that the layers were nearly fully relaxed and, in fact, some relaxation early in the growth appeared to have led to tensile strain in some of the material with higher In content as the reflections appeared to the right of the relaxation line.

Additionally, the maximum In content for each sample was determined without ambiguity to be 50, 40, and 32% for the 475, 515, and 555 °C samples, respectively. Those were found from the central position of the bottom right intensity maximum in each frame. It is not clear how the material continuously evolved throughout the graded layers. However, those RSMs did not indicate noticeable phase separation.

It might be expected that phase separation could appear as a separated, distinct reflection which is strained to the layer it is separated from, since this separation would be the result of loss of In in one region and gain in another, i.e., no general relaxation. However, to the contrary, it was found that the high In composition spot separated in both composition and lattice from the graded material, i.e., indicating that this material was the result of relaxation, not phase separation.

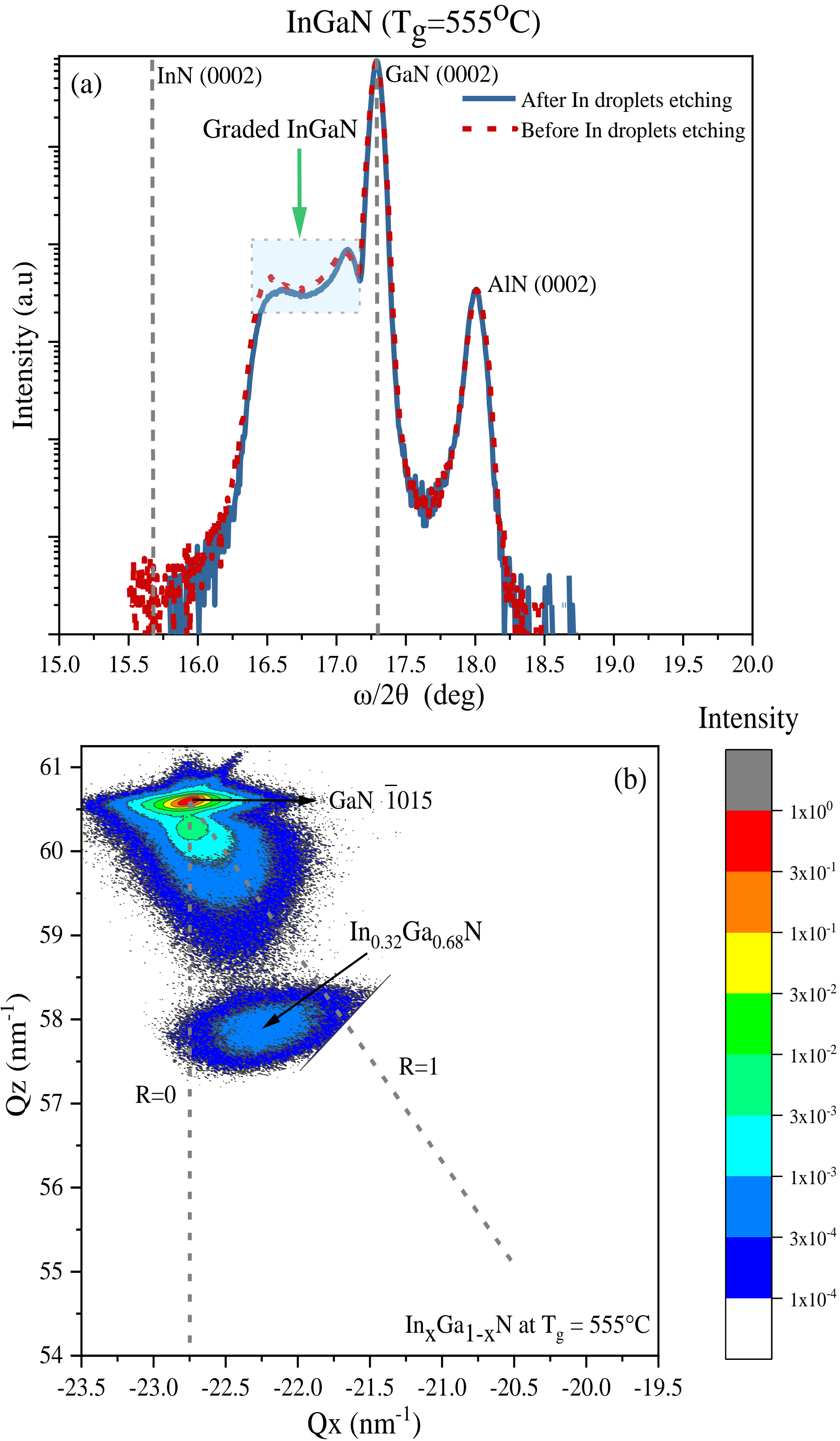

Figure 50. (a) ω/2θ scan and (b) RSM showing the (105) reflection for the graded InGaN (555 °C).

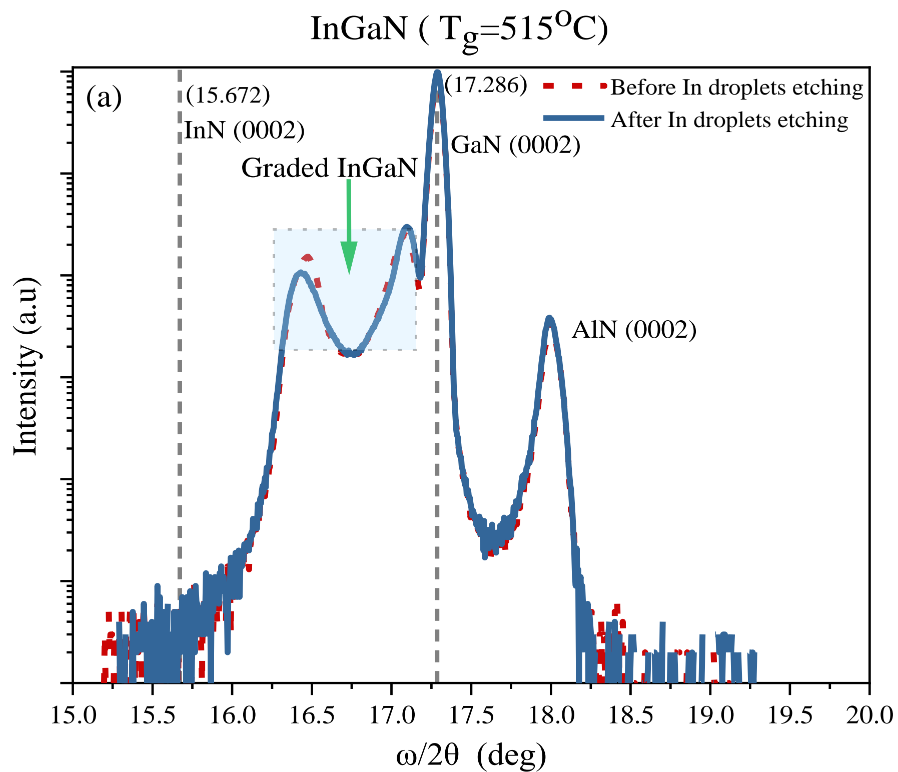

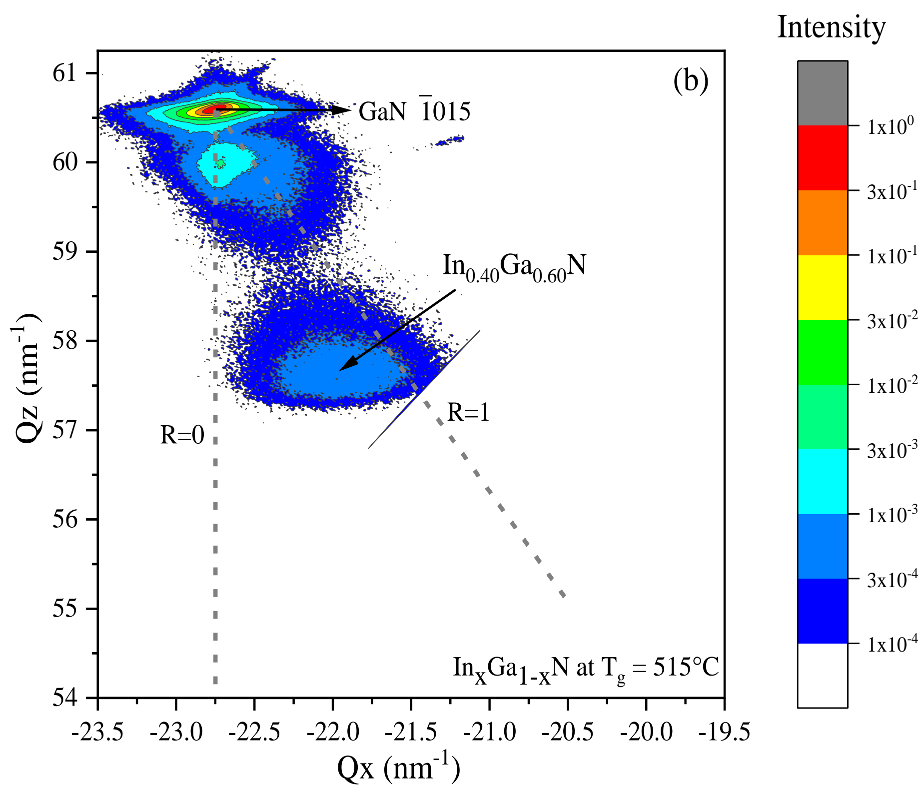

Figure 51. (a) ω/2θ scan and (b) RSM showing the (105) reflection for the graded InGaN (515 °C).

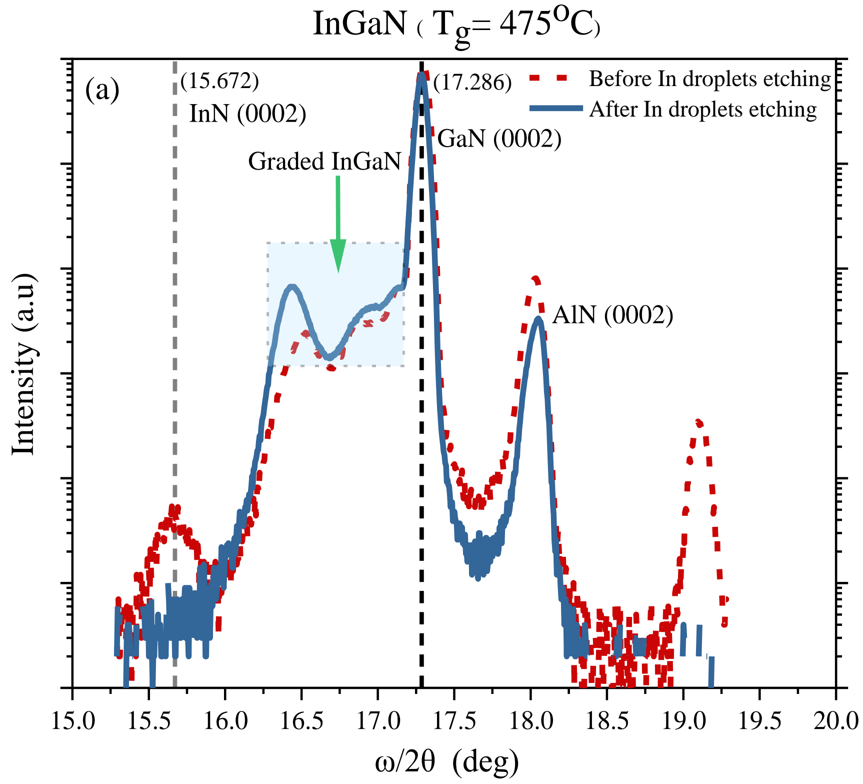

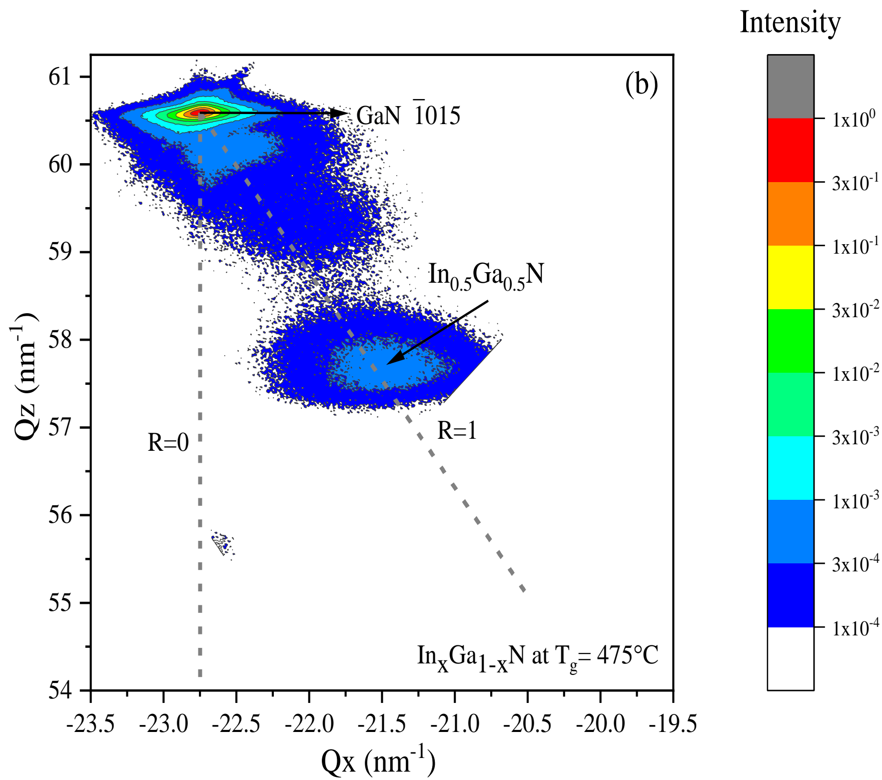

Figure 52. (a) ω/2θ scan and (b)RSM showing the (105) reflection for the graded InGaN (475 °C).

4.2.7 Secondary Ion Mass Spectrometry (SIMS):

Secondary ion mass spectrometry (SIMS) was used to determine the thickness and composition profile of the graded InGaN layer. The analysis was performed using a QUAD-SIMS instrument using a Cs+ ion beam with 3 keV energy. The angle of incidence was 60° to sample normal and the sputtered area was about 300 μm^2 to 500 μm^2. The analysis was done by EAG Laboratories.

The SIMS depth profiles in Figure 53, Figure 54, and Figure 55 revealed an increasing maximum In incorporation with decreasing growth temperature, which is generally accepted in the literature for constant composition InGaN films[104].

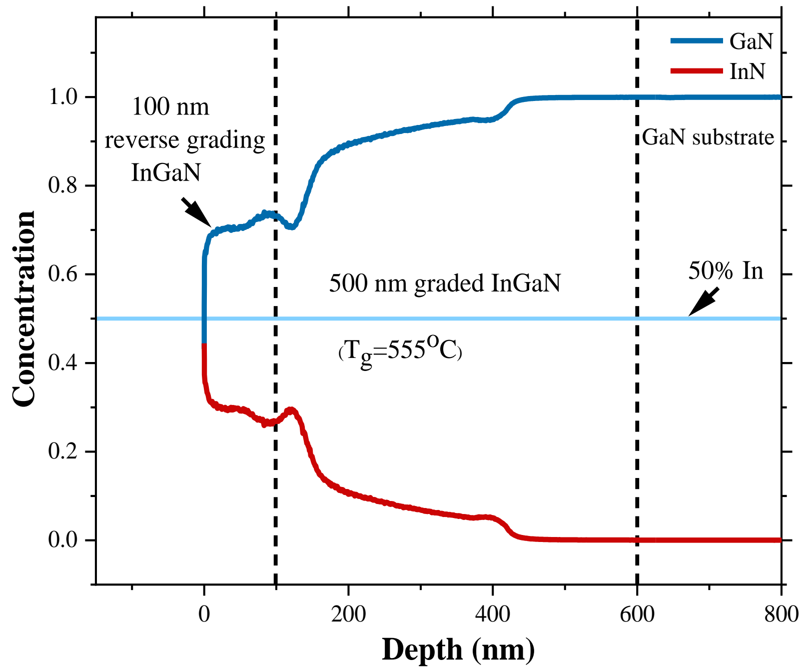

Figure 53. SIMS profile for graded InGaN (555 °C).

The high temperature growth (555 °C) showed a maximum In content of ~30%, which occurred at approximately the designed maximum point of 500 nm. This indicates that while the

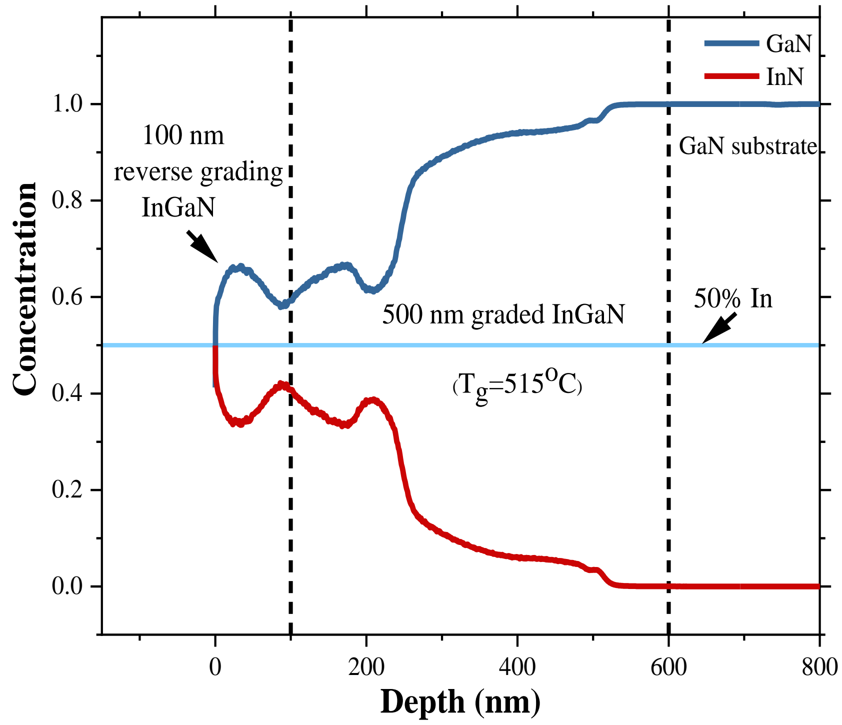

Figure 54. SIMS profile for graded InGaN (515 °C).

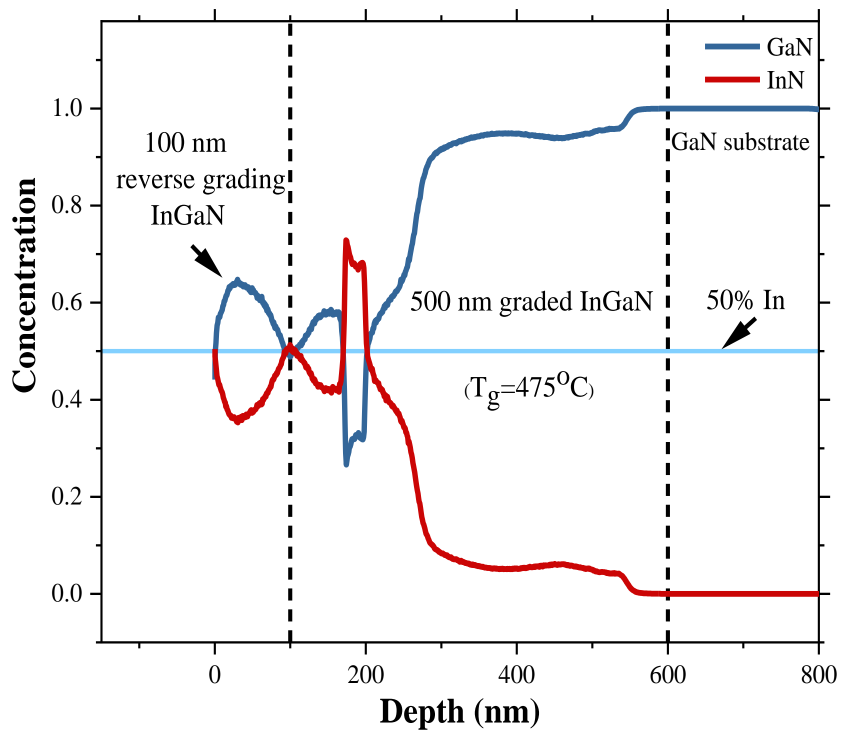

Figure 55. SIMS profile for graded InGaN (475 °C).

maximum content did not follow the designed ratio of Gal to In, the growth was still generally responsive to the changing flux.

Additionally, there were two main features of this composition profile that deserve attention. First, there was a significant thickness at the base of the growth, ~170 nm, where there was no In incorporation. Then, second, there was a significant thickness following the initial In incorporation where there In content remained relatively constant at ~7%, from ~170 to ~420 nm. The pure GaN growth at the beginning was likely due to excess Ga on the surface preferentially incorporating over In, only allowing InGaN to form when the surface concentration of Ga fell below the N stoichiometric point. And, the relatively constant composition between 170 and 420 nm was likely do to a compositional pulling effect.

In the case of the 515 °C sample as demonstrated in Figure 54, maximum In composition reached just over 40%, also at ~500 nm. However, there was a lesser maximum of ~38% reached at ~400 nm. Additionally, there were the same features as seen in the 555°C sample of no In incorporation (only for the first ~70 nm) and a significant growth with the same composition (~7% from ~70 nm to ~350 nm).

It is likely that the lesser maximum here was the result of strain buildup and relaxation. This relaxation could have resulted in a sudden increase in In content as the effects of compositional pulling were relaxed, followed by a deficiency of In resulting in the downturn in the composition.

Finally, the 475 °C sample in Figure 55 demonstrated a very high In maximum content of ~70%, however, this was not at the 500 nm mark. At 500 nm, the composition, in fact, was the as designed 50%. Similar to both the 555 and the 515 °C samples, the 475 °C sample also demonstrated a pure GaN region at the start of the growth for ~40 nm, and a relatively constant

5-7% region from ~40 to ~320 nm.

In addition, like the 515 °C sample, at ~320 nm the sample apparently experienced a relaxation event and suddenly increased in composition. It is believed that this was followed by two more relaxation events at ~400 nm and ~420 nm, where the relaxation creates a surface with high In composition of ~70%. This was followed by growth with a lower composition resulting from a sudden loss of available In. However, it is likely that this subsequent growth was strained to the larger lattice constant of the higher In content material. This explains the tensile strain observed in Figure 52.

4.2.8 Comparison of the Experimental Band Gap Energies and nextnano^3 Band Gap Energies

Table 7 summarizes all the effective observable band gap energies that were found using transmission, XRD-RSM, and PL. Then, the optical transitions that were simulated using nextnano^3 were used to compare with those values. For the ideal case, the band gap energy that was calculated using nextnano^3 was 3.37 eV for the homogeneous strain condition and 1.76 eV for no strain condition.

Table 7. The band gap energy of graded InGaN from different measurements

Measurement method	InGaN(555 °C) E_g	InGaN(515 °C) E_g	InGaN(475 °C) E_g
Transmission (Average band gap)	2.6 eV (24%)	2.1 eV (40%)	1.9 eV (46%)
XRD-Reciprocal Space Map (Surface average band gap)	2.2 eV (33%)	1.9 eV (40%)	1.6 eV (50%)
Photoluminescence (Observable band gap)	1.75 eV (51%)	1.59 eV (58%)	1.44 eV (64%)

Comparing PL results for all the samples to those values, it is clear that they were in between and closer to the fully relaxed band gap (1.76 eV) which was reasonable since the transition occurs close to the surface. However, the observable PL band gap for graded InGaN at 475 °C and 515 °C showed less band gap energy which meant higher In content than InGaN (555 °C). This could have been a result of the In accumulation on the surface, as was demonstrated in SEM and optical microscopes that higher In accumulation happened at lower temperatures.

nextnano^3 was also used to simulate an In profile that was determined by SIMS measurements since using these realistic material parameters helps to get a better understanding of the growth. Figure 56 represents the In profile for graded InGaN that was grown at 555 °C which was extracted from the SIMS plot.

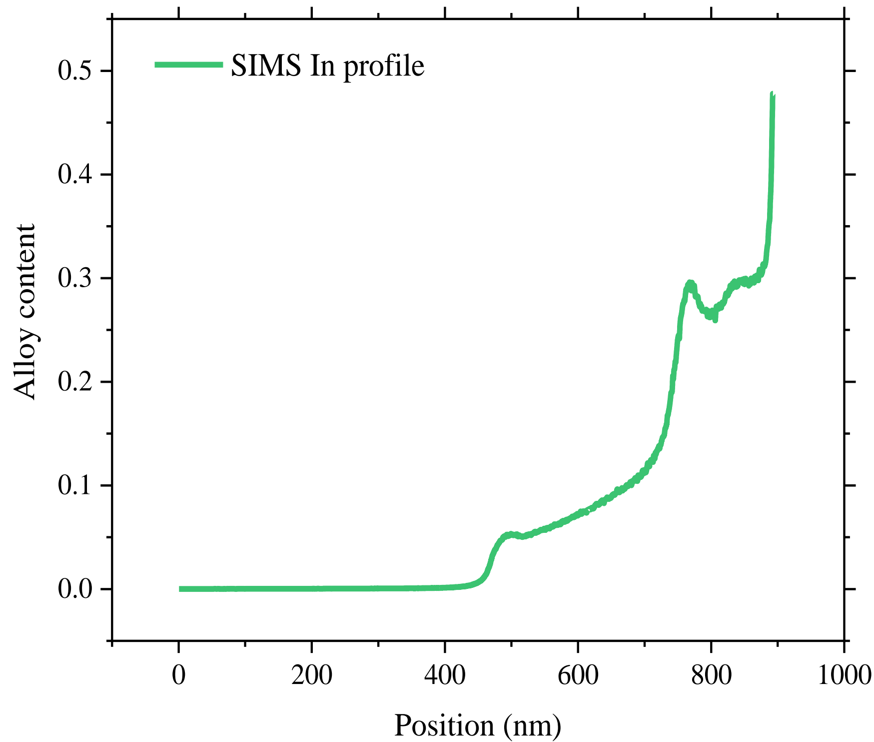

Figure 56. In profile for graded InGaN (555°C).

As the ideal case was simulated with a linear graded composition to determine the band structure and electron and hole wavefunction, the same was performed here. Figure 58 and Figure 58 show the band diagram for both strain states: strain and no strain (fully relaxed) material.

The homogenous strain case exhibited p-type doping for the initial grade, forming a depletion region at the interface with the GaN substrate. Thus, for the sample, a p-n junction was not expected to form within the optically active region, because there was no significant reverse grade to form the n-type region.

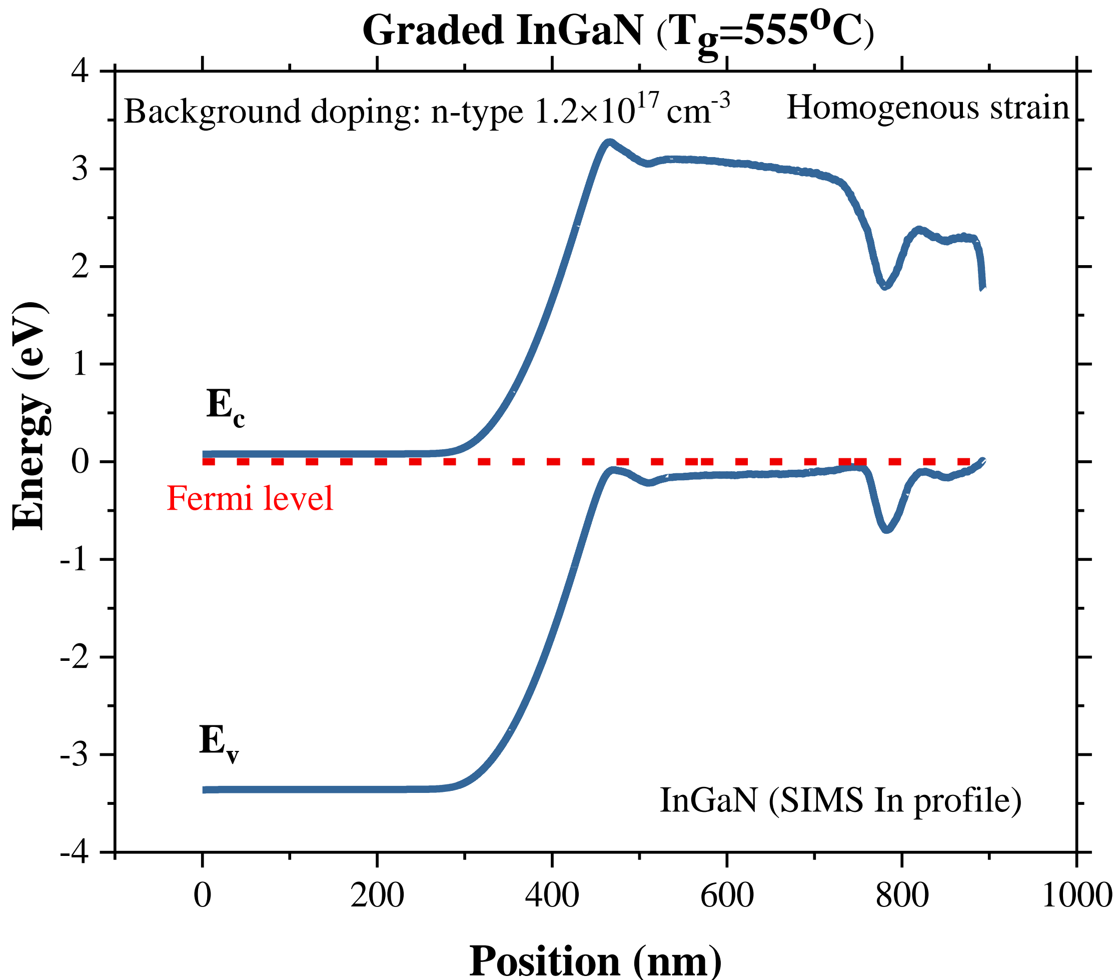

Figure 57. The band diagram for strained InGaN (555 °C).

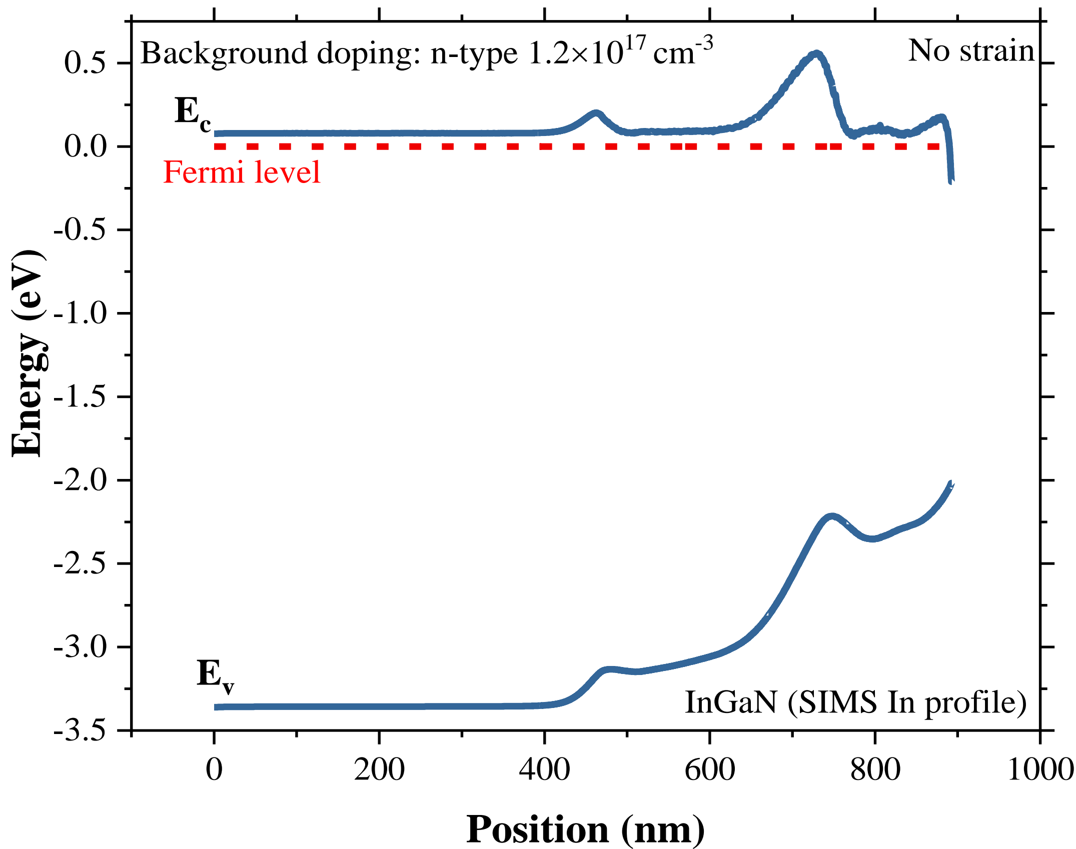

Figure 58. The band diagram for fully relaxed InGaN (555 °C).

In the relaxed material, the same In profile generated all n-type material as a result of removing the piezoelectric polarization component, similar to the ideal structure in Figure 31.

In the simulation shown in Table 8, the band gap energies were constants for both strain states even at different depths and background doping. Looking at the electron and hole wavefunctions that are illustrated in Figure 59 and Figure 60, the highest transition probability was at the surface for both strained and fully relaxed InGaN.

The transition energy in homogenous strain for e399-hh1 was 2.074 eV, at ~890 nm which represented (~37%) In content using the SIMS In profile in Figure 56. On the other hand,

Table 8. The energy band gap and the corresponding In composition for InGaN(555°C).

Quantum region	Energy (eV) (Homogenous strain)	Energy (eV) (No strain)
All structure	2.074	2.071
Surface (30 nm)	2.074	2.071
Surface (200 nm)	2.074	2.071

the fully relaxed condition showed a 2.071 eV transition energy for e1-hh1 at ~890 nm which was (~37%) In content.

Note, the notation e399, for example, represents the electron state 399 within a pseudo-continuum of electron energy levels calculated quantum mechanically with a ground state simply labeled as e1. In the above strained case, it was electron state 399 which maximized the transition probability with the heavy hole state, hh1, which was well localized at ~890 nm in the valence band of the structure. For the relaxed case, however, it was found that the maximum in transmission probability was found when the well localized heavy hole state, hh1, recombined with the similarly well localized electron state e1.

The transition probabilities were both high but decreased from 99.75% for the homogeneous strain to 96.96% for no strain. When comparing the band gap energies to the experimental results, they were closer to the RSM surface average band gap (2.2 eV), which corresponded to 33% In.

The profiles of the charge carrier densities resulting from using the measured In profiles from SIMS in the Nextnano^3 simulations are shown in Figure 61. This complicated structure should be compared to the ideal case with a linear In profile shown in Figure 34. Similar to the ideal case, here the strain had a great impact on the polarization doping in the material.

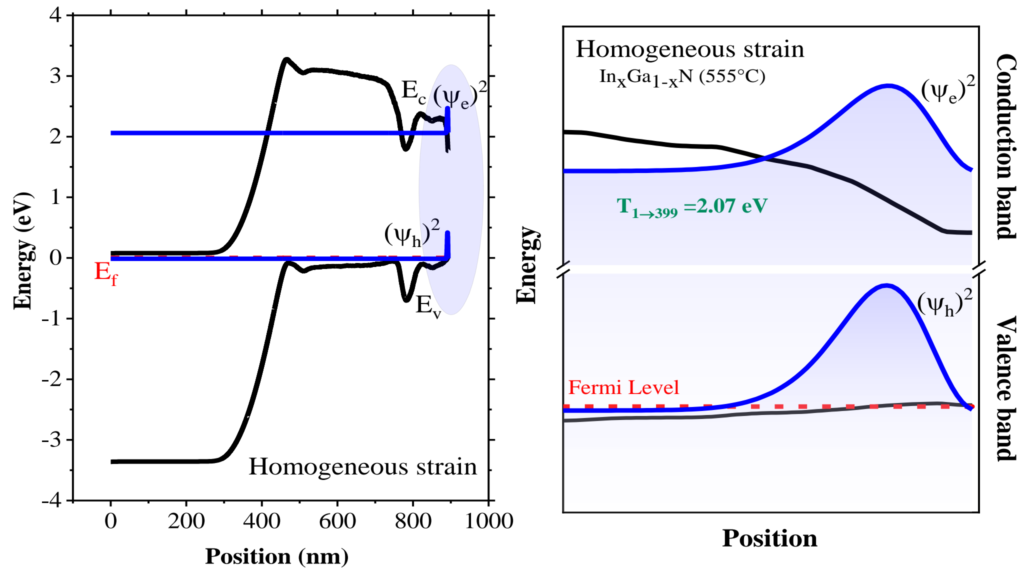

Figure 59. InGaN (555 °C) band diagram and electron and hole wavefunction for homogenous strain state.

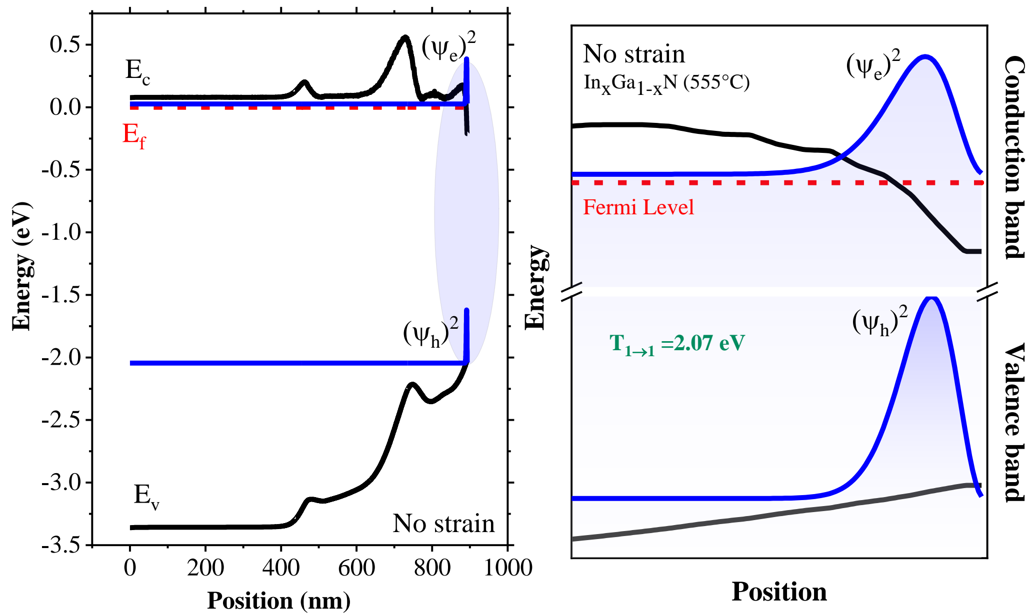

Figure 60. InGaN (555 °C) band diagram and electron and hole wavefunction for no strain state.

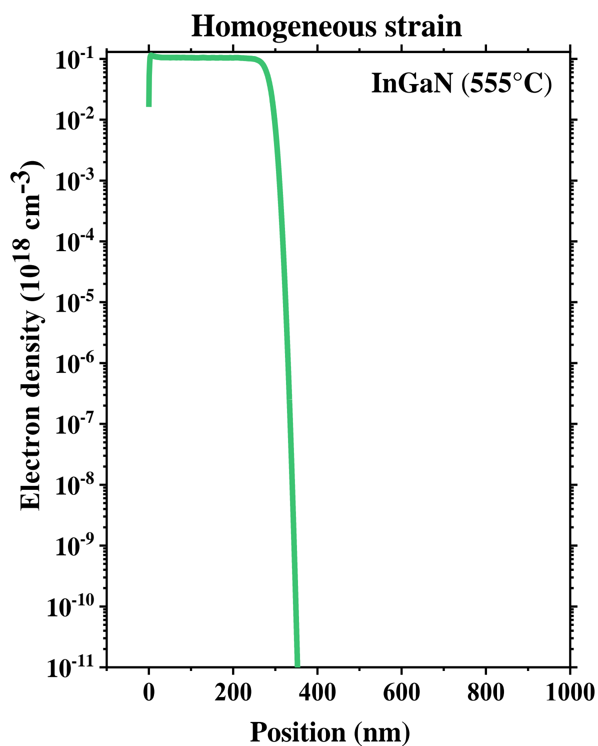

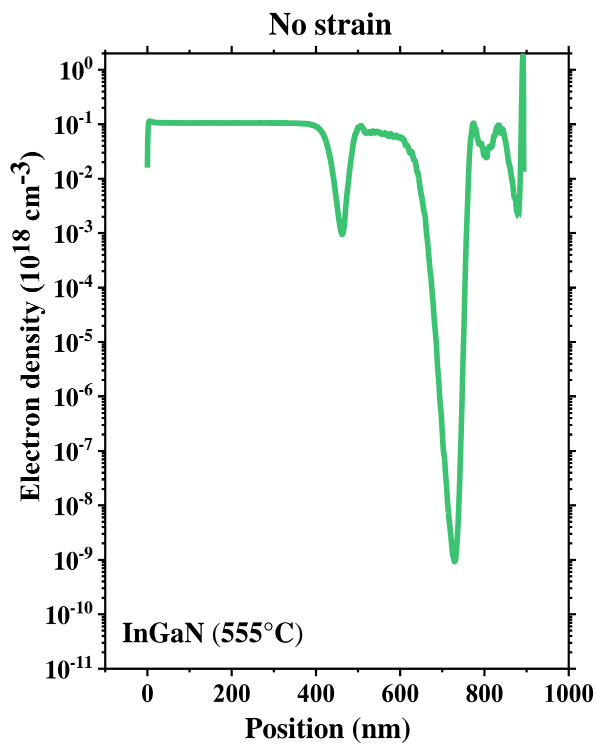

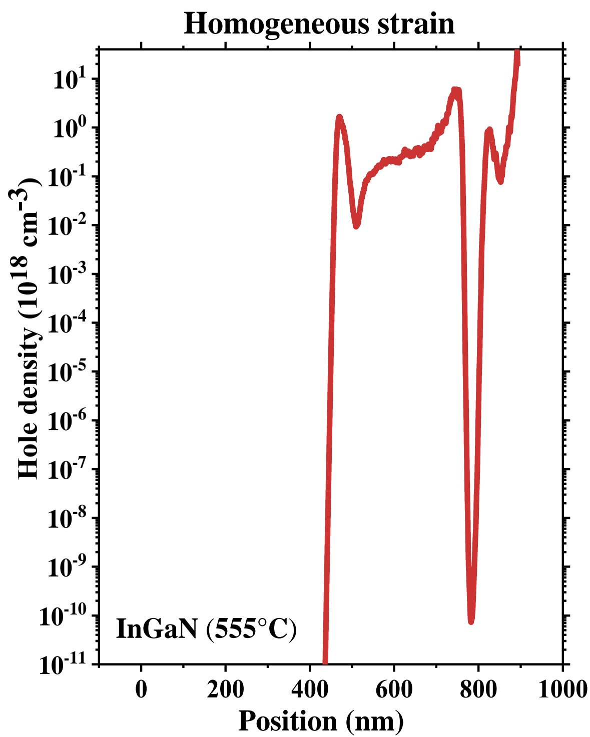

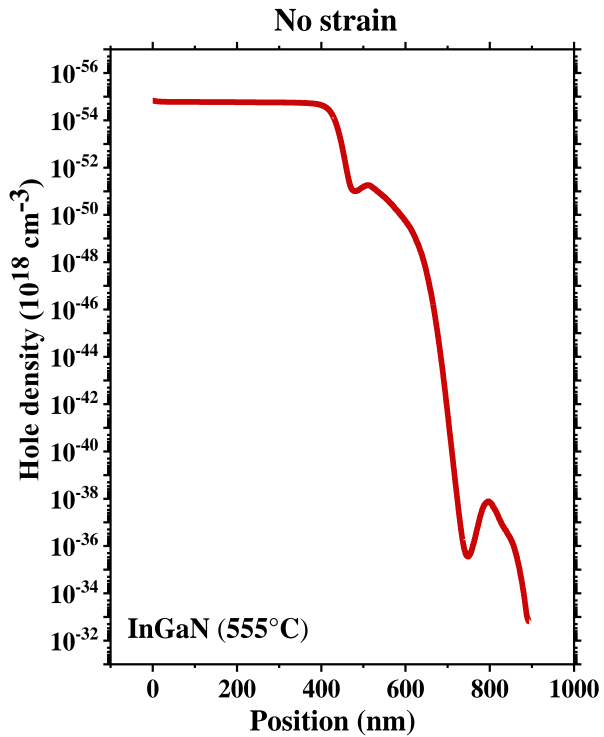

Figure 61. Electron and hole density in InGaN (555 °C).

Figure 62 shows the SIMS In profile after importing into in $nextnano^3$ for graded InGaN that was grown at 515 °C.

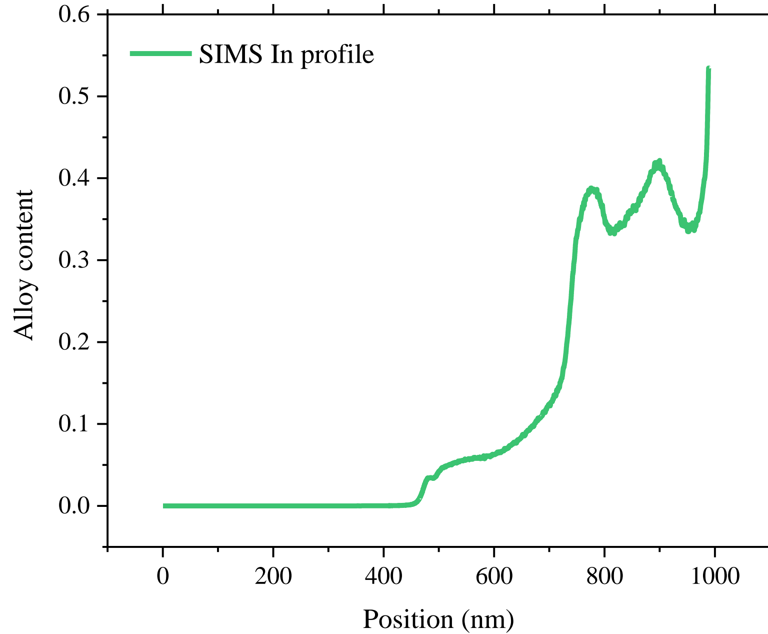

Figure 62. In profile for graded InGaN (515 °C).

The band diagram is shown in Figure 63 and Figure 64 for the strained and relaxed cases, respectively. In the homogenous strain, there was a similarity to the band diagram of the 555 °C sample, as it started with p-type GaN and the interface with the substrate formed a depletion region. Again, the active layer was p-type doped material just by polarization doping without the introduction of any dopants. At the region where there was a change in In profile, there were p-type and n-type InGaN materials. However, for the relaxed case, again, the loss of the piezoelectric component of the polarization doping was significant enough to remove the possibility of a p-type doping.

Table 9 displays the band gap energies that were simulated in $nextnano^3$. It shows a constant band gap energy for both strain states. The band gap decreased with decreased growth

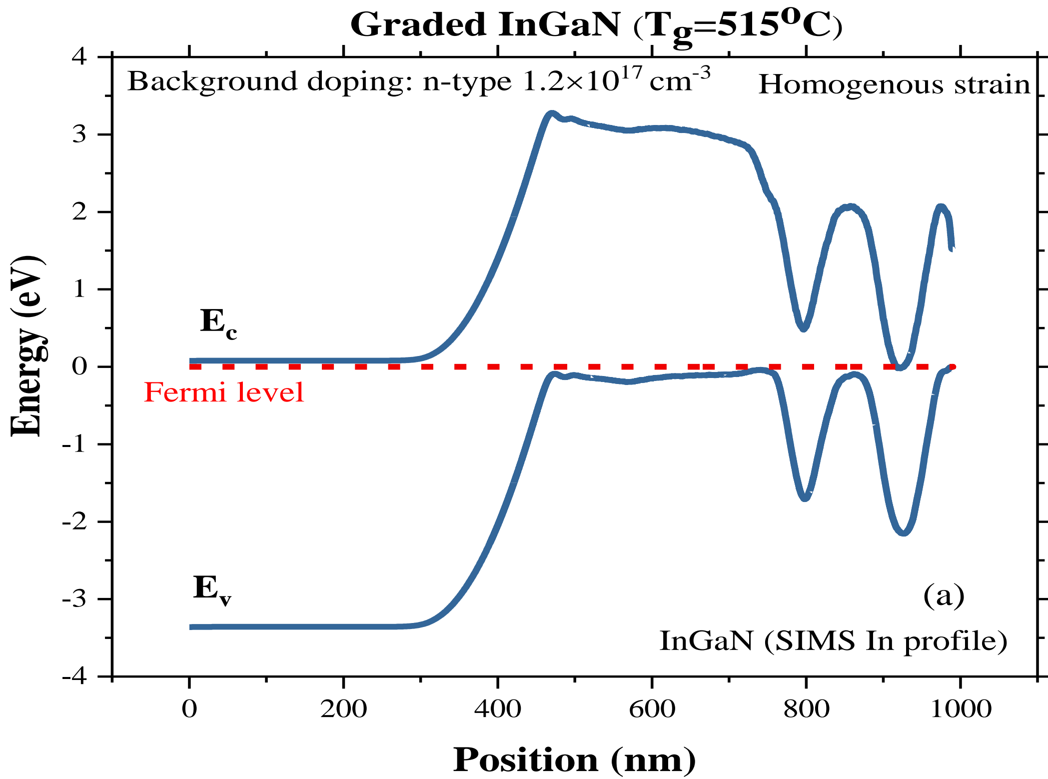

Figure 63. The band diagram for strained InGaN (515 °C).

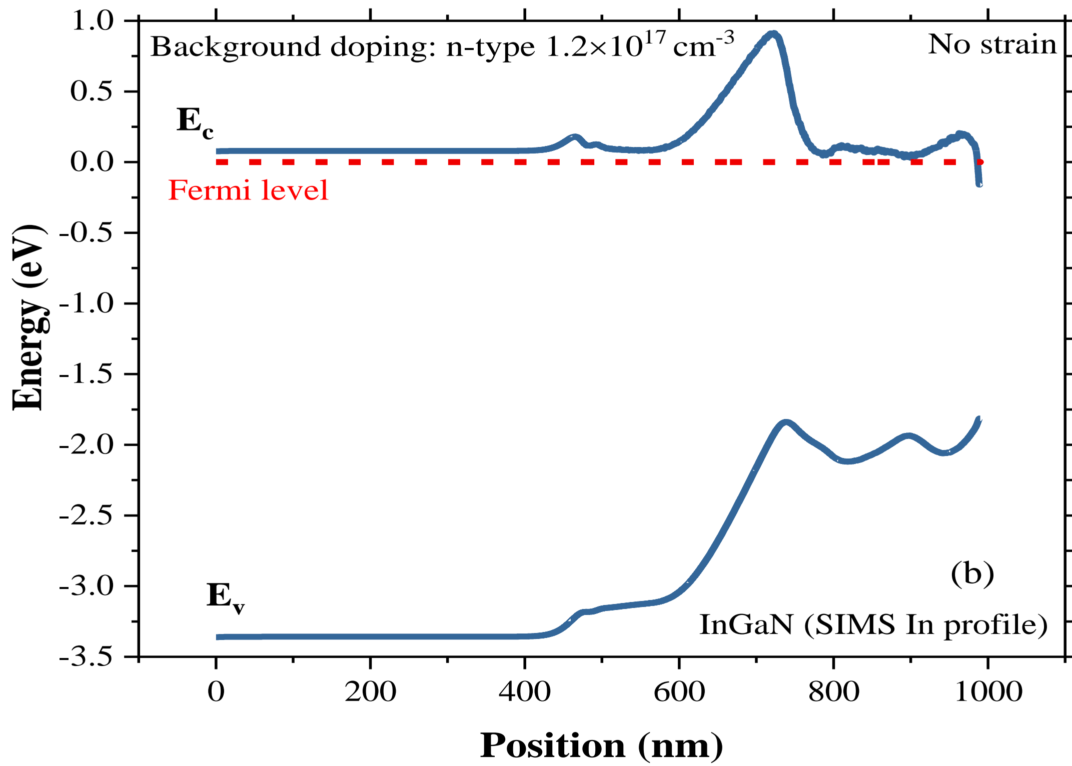

Figure 64. The band diagram for fully relaxed InGaN (515 °C).

temperature, which indicated higher In content matching the experiments. Again, the XRD-RSM surface average band gap energy, 1.9 eV, was closer, which corresponds to 40% In content.

Table 9. The energy band gap and the corrsponding In composition for InGaN (515 °C).

Quantum region	Energy (eV) (Homogenous strain)	Energy (eV) (No strain)
All structure	1.76	1.84
Surface (30 nm)	1.76	1.84
Surface (200 nm)	1.76	1.84

The wave functions of the electron and hole were again mostly localized at the surface as shown in Figure 65 and Figure 66. The transition energy between the e484 electron state and the hh1 heavy hole state for the homogenous strain condition was 1.76 eV at ~987 nm (49% In) while the fully relaxed condition e1-hh1 was 1.84 eV at ~989 nm (51% In).

The probability of the transition increased from 83.95% to 92.36%. Figure 67 demonstrates the electron and hole densities for graded InGaN (515 °C). Similar to the higher temperature growth, the polarization doping resulted in a complicated charge density as a result of the unexpectedly complicated In profiles.

Figure 68 demonstrates the In SIMS profile as it was imported into nextnano^3 for graded InGaN that was grown at 475°C. This again was used to determine the band gap diagram and doping densities as well as the optical transition and wavefunctions. In the homogeneous strain condition in Figure 69, the band diagram showed p-type GaN and a similar depletion region at the substrate interface as the other two samples. However, the active layer included p-type and n-

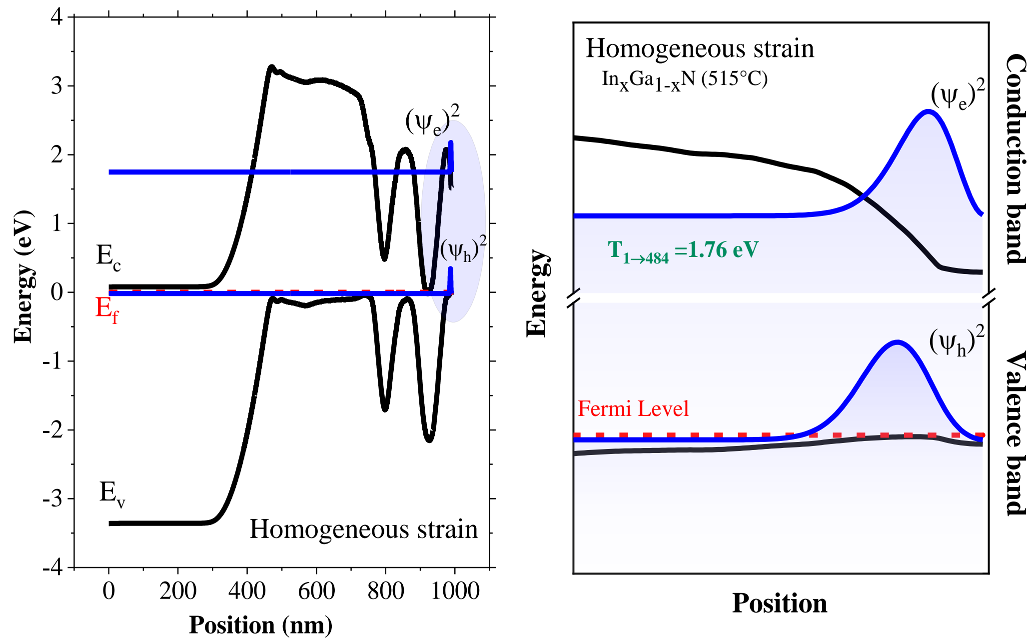

Figure 65. InGaN (515°C) band diagram and electron and hole wavefunction for homogenous strain state

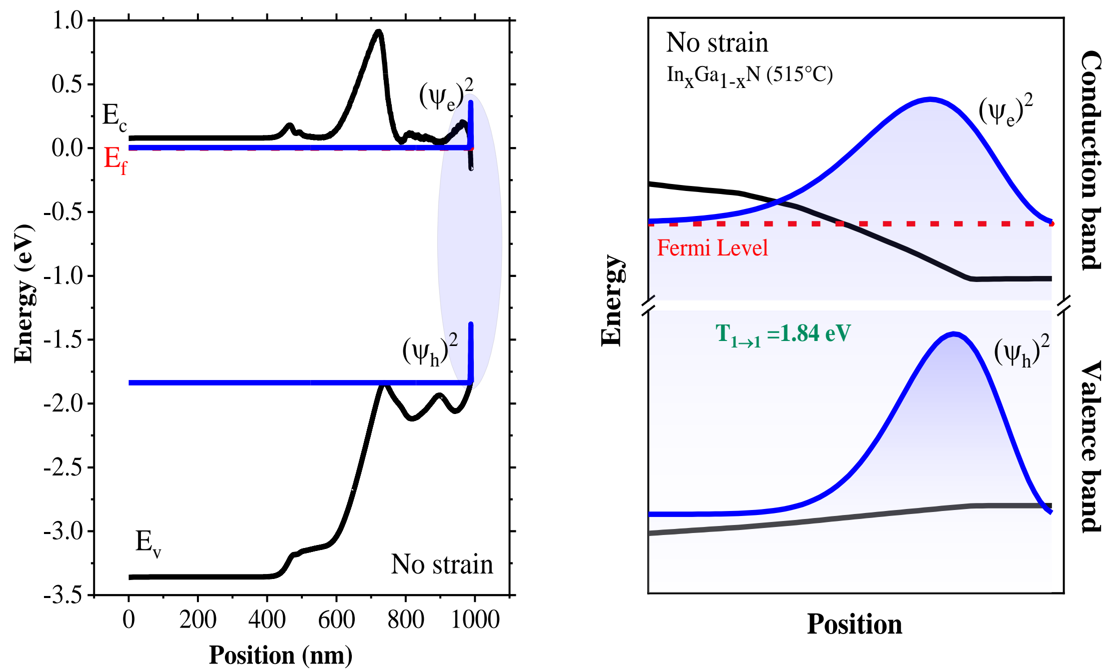

Figure 66. InGaN (515°C) band diagram and electron and hole wavefunction for no strain state

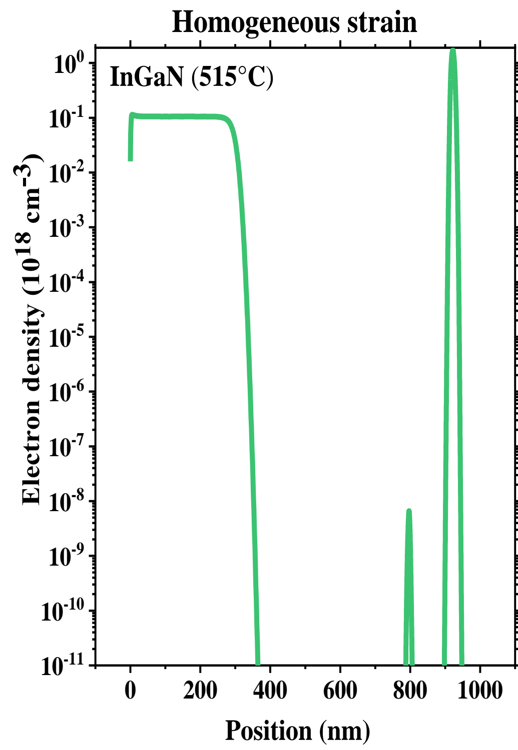

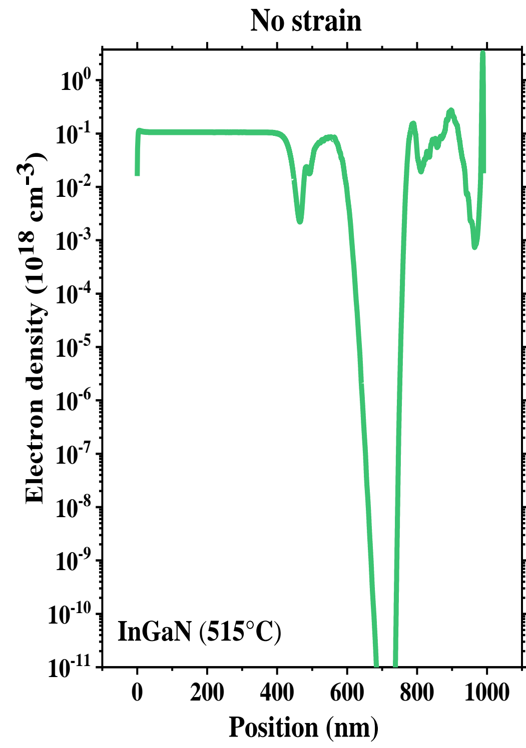

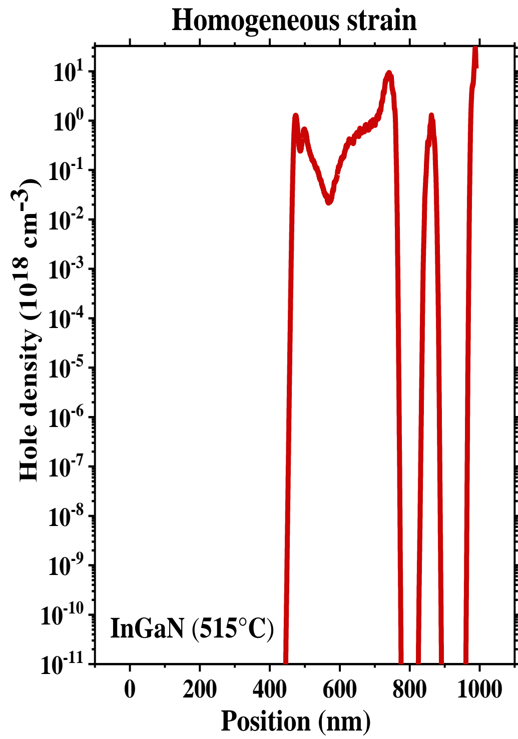

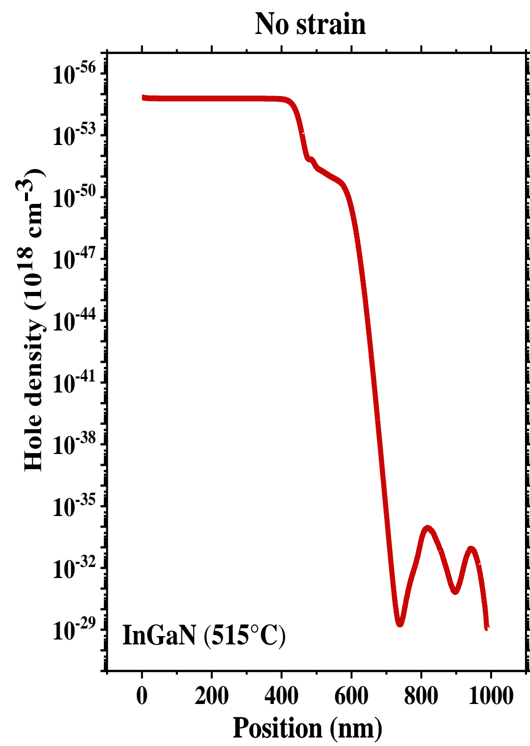

Figure 67. Electron and hole density in InGaN (515 °C).

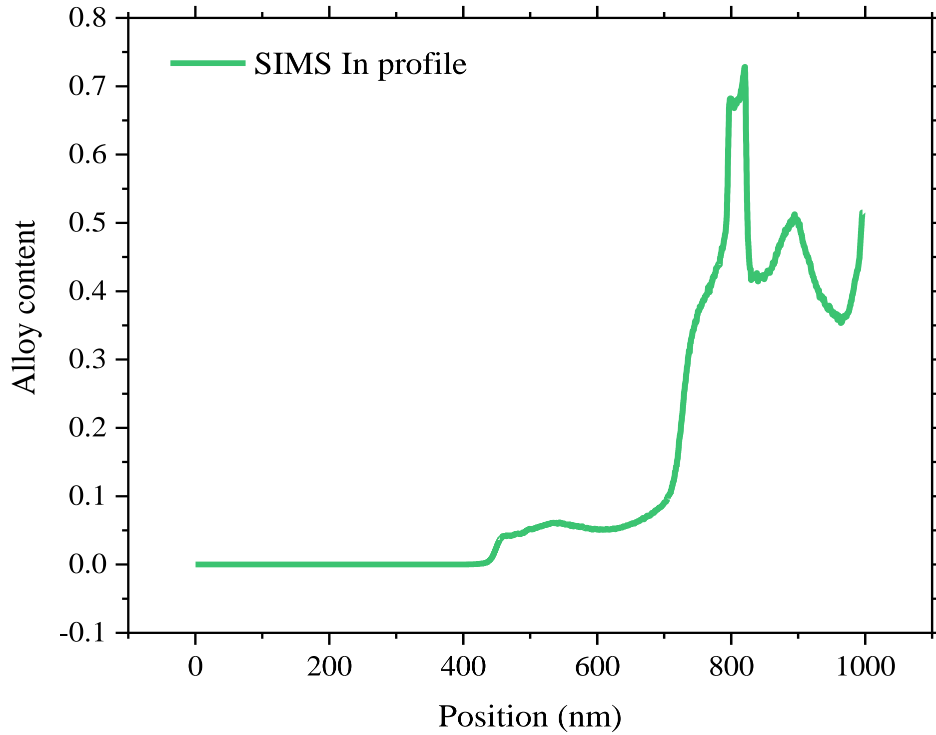

Figure 68. In profile for graded InGaN (475 °C).

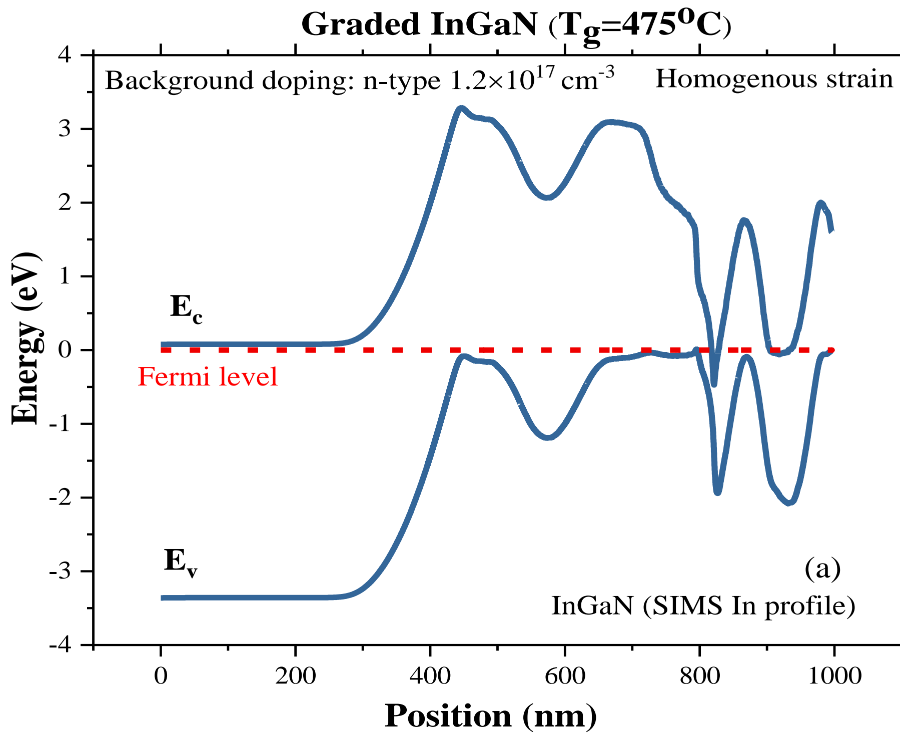

Figure 69. The band diagram for strained InGaN (475 °C).

type near the surface as a result of the complicated In profiles determined by SIMS. However, even there, the fully relaxed material demonstrated primarily n-type material throughout. This is shown in Figure 70.

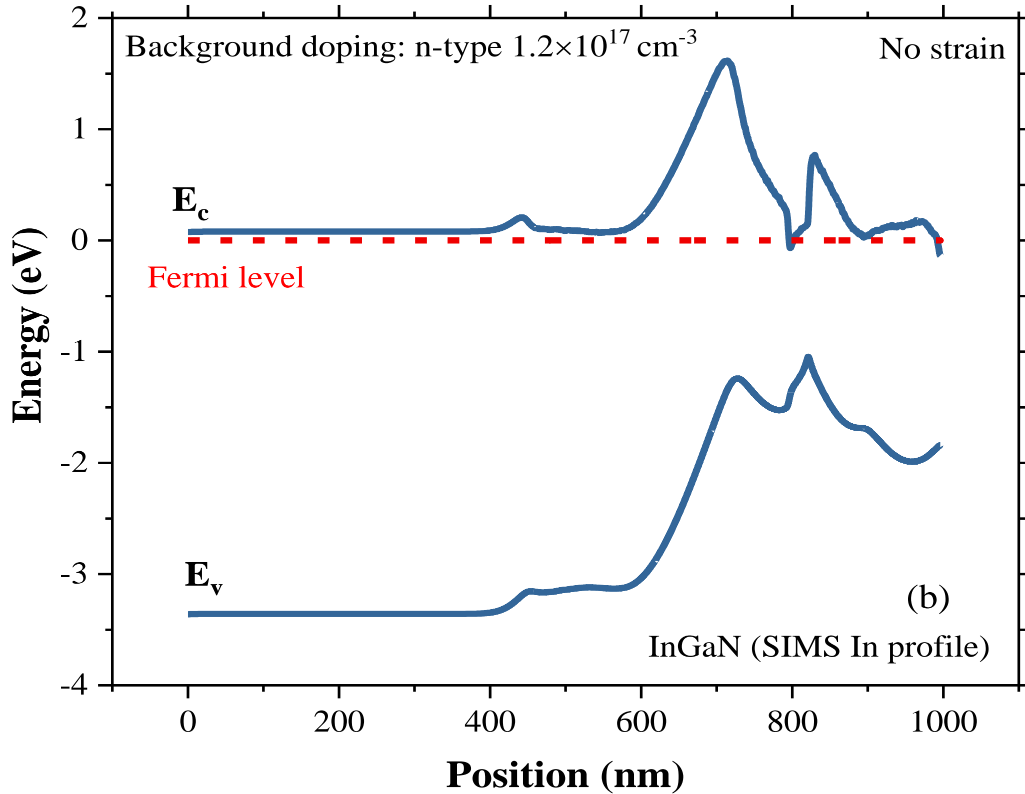

Figure 70. The band diagram for fully relaxed InGaN (475 °C).

As the band diagram was changing especially near the surface, it affected the band gap energies, so they varied at the surface compared to the rest of the structure, as shown in Table 10. The PL band gap energy was close to the band gap for the whole structure, even though it was expected from the laser penetration depth that the laser only reached the interface between grade, up and grade down. However, the accumulation of In on the surface for all the samples affected the results.

Table 10. The energy band gap and the corrsponding In composition for InGaN (475 °C).

Quantum region	Energy (eV) (Homogenous strain)	Energy (eV) (No strain)
All structure	1.43	1.31
Surface (30 nm)	1.83	1.88
Surface (200 nm)	1.83	1.31

The wavefunctions of the electron and hole in Figure 72 and Figure 71 show that the position is close to the interface between the grade up and grade down region where, naively, the largest In content and the smallest bandgap would be expected.

In the homogenous strain, the transition energy of e447-hh1 was 1.43 eV at ~795 nm which corresponded to 66% In content, and the transition energy for no strain state e216-hh1 is 1.31 eV at 820 nm which corresponded to 46% In content.

Again, the electron and hole densities in Figure 73 were complex and interchanged between p-type and n-type material. This was due to the In profile that was not linearly graded as intended.

Looking at the nextnano^3 simulation results using the SIMS In profile, the polarization doping in the material requires more investigation. Some things that need to be taken into account: the layer thicknesses, the doping profiles, or even adding Mg to assist the p-type polarization doping in the material.

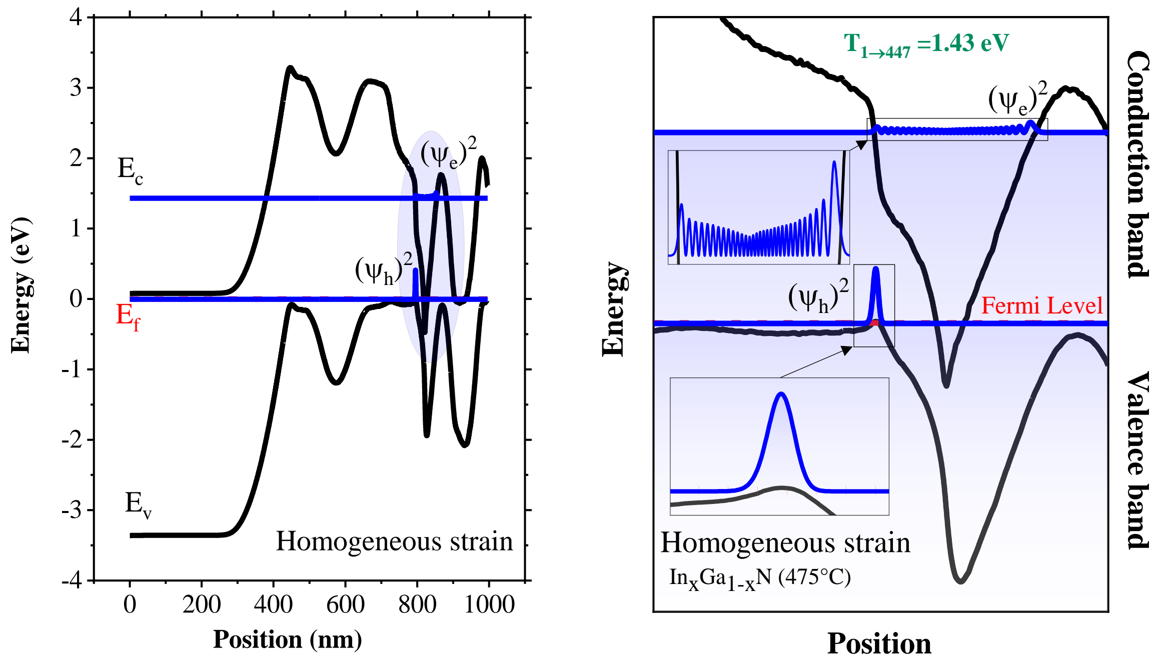

Figure 71. InGaN (475 °C) band diagram and electron and hole wavefunction for homogenous strain state

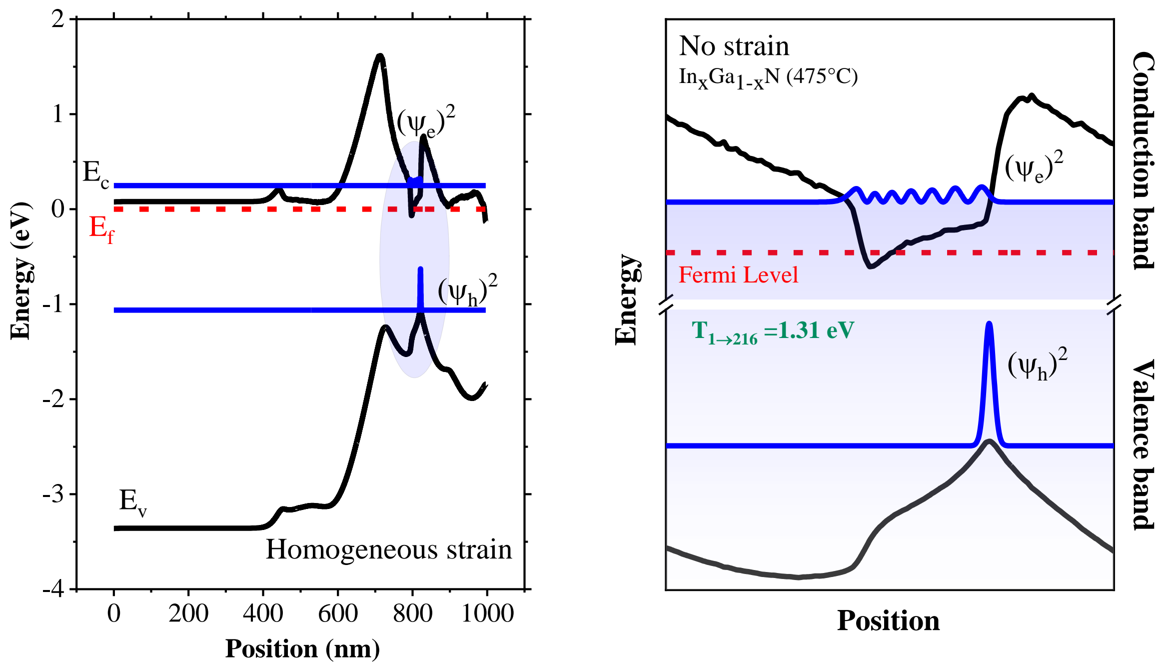

Figure 72. InGaN (475 °C) band diagram and electron and hole wavefunction for the no strain state.

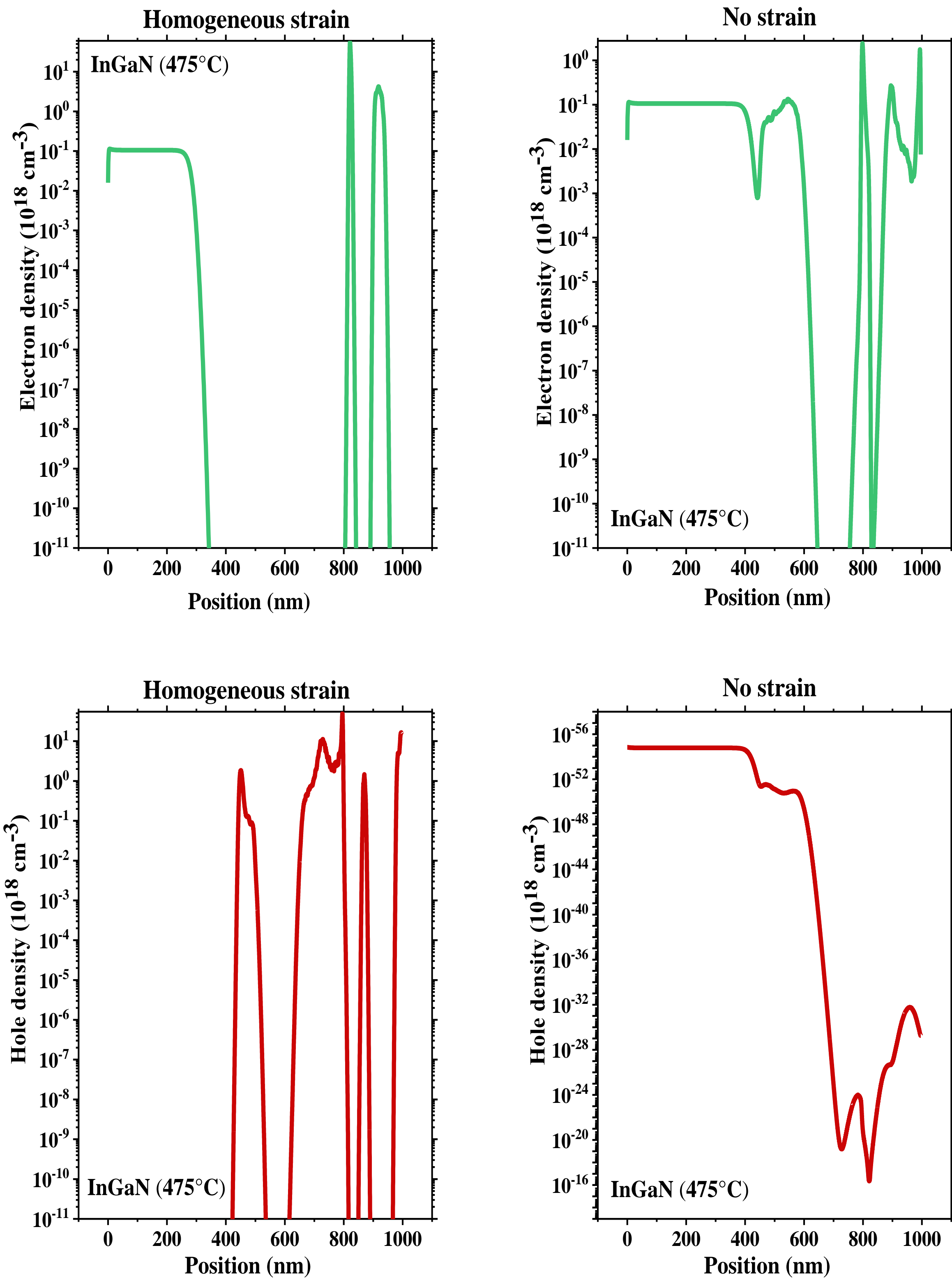

Figure 73. Electron and hole density in InGaN (475 °C).

Chapter 5: Full Composition $In_xGa_{1-x}N$ Thick Film Grown by Molecular Beam Epitaxy

5.1 Structure and band diagram simulation

A full composition graded InGaN structure was also grown and studied in which the In composition was graded linearly from 3% to 100% over 1000 nm and reverse graded from 100% to 70% over 100 nm. To begin the study, this structure was simulated in nextnano[3].

Figure 74 shows the In profile that was simulated for the ideal case.

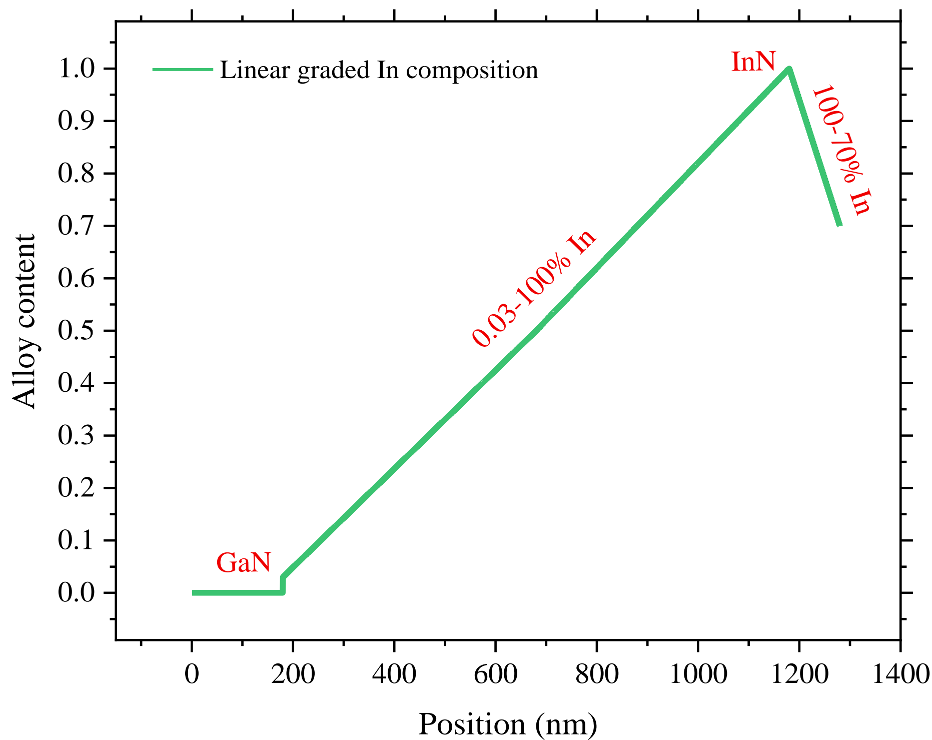

Figure 74. The In profile for the ideal case.

Figure 75 and Figure 76 show the band diagram of this structure for both the homogenous strain case and the no strain case. Again, similar to the ideal band diagrams seen for the 50% graded samples, the homogeneous strained system demonstrated strong p-type

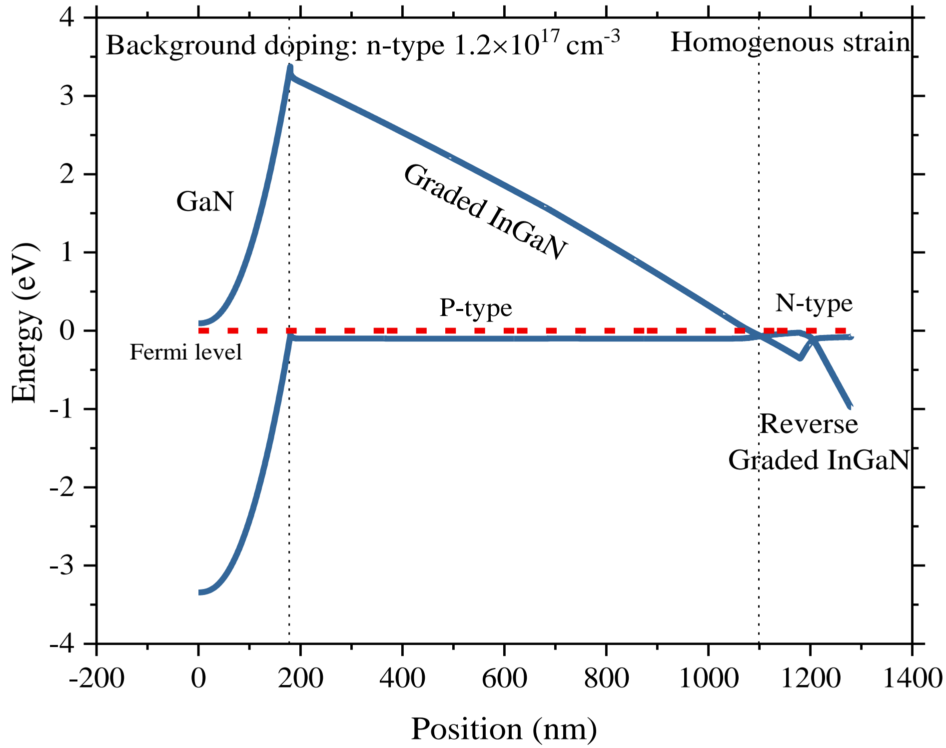

Figure 75. The band diagram for strained InGaN (475 + 400 °C).

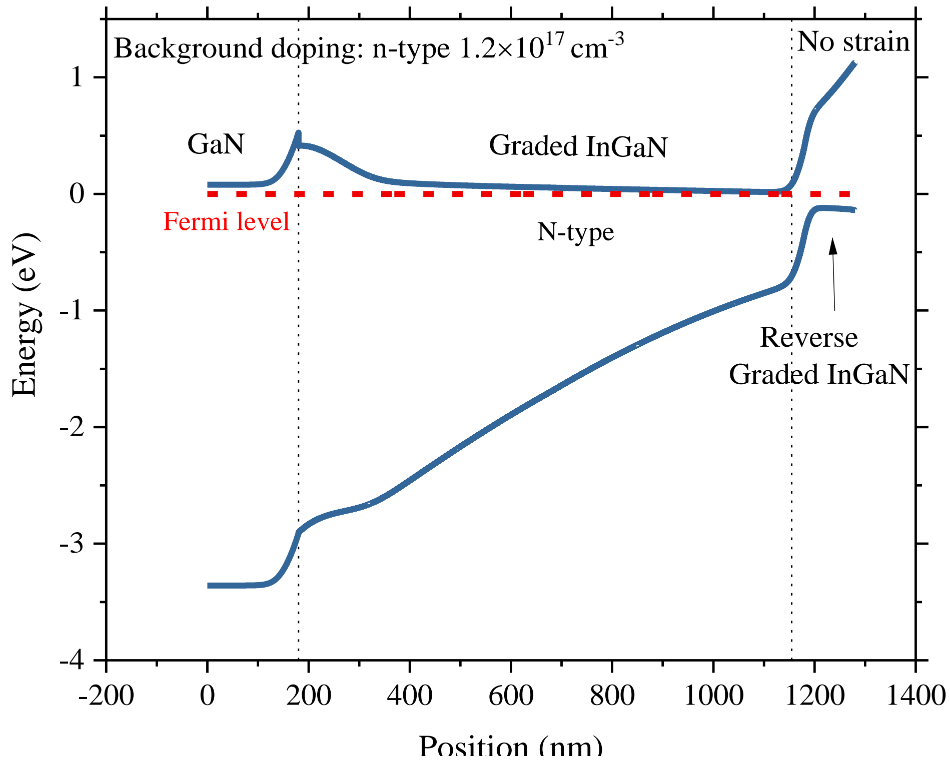

Figure 76. The band diagram for fully relaxed InGaN (475 + 400 °C).

polarization doping throughout the grade-up region, and n-type in the reverse grade region, while the no strain simulation showed the exact opposite. An interesting difference though is that for the strained system, when the concentration reached greater than ~90% In, the bandgap inverted, i.e., the valence band edge became higher in energy than the conduction band edge. This can be seen more closely in Figure 77, where the bandgap was plotted for both the strained and unstrained cases as functions of the In composition.

There, the relaxed (no strain) InGaN was calculated using Vegard's law in Equation 1, while the strained material band gap was extracted using nexnano[3] simulation for InGaN material at different compositions using the appropriate bowing parameters and deformation potentials.

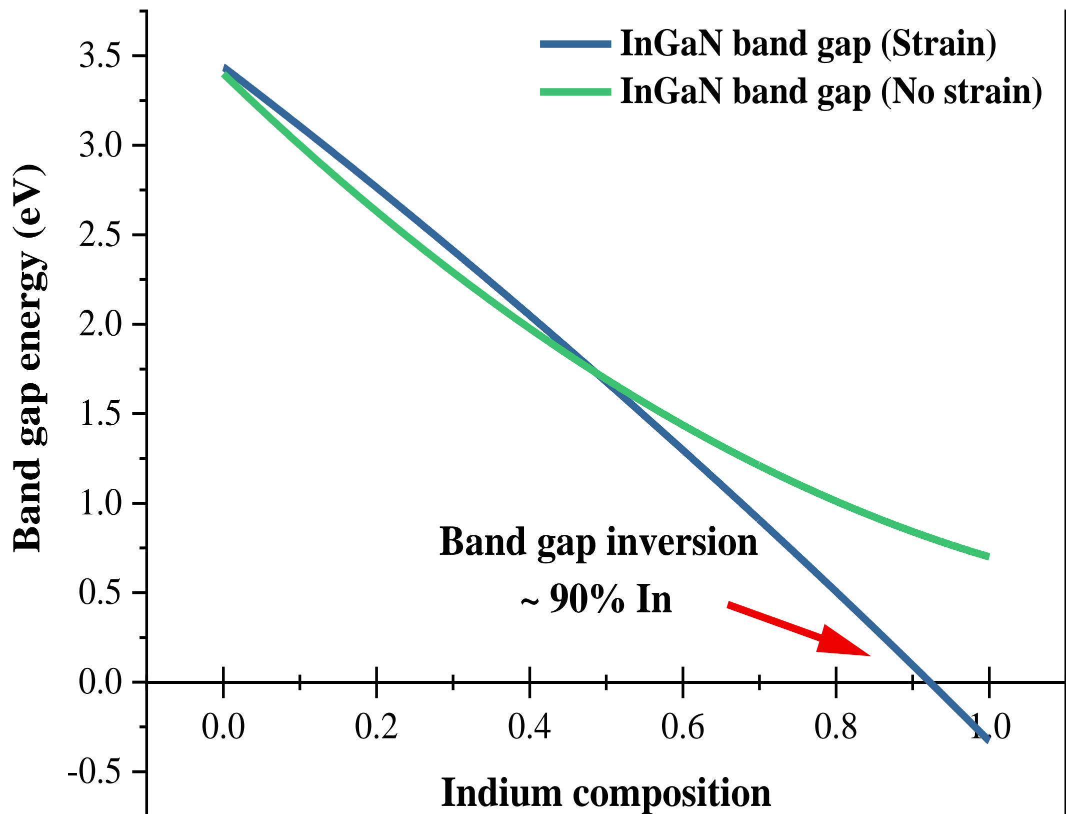

Figure 77. InGaN band gap against In composition for strained and relaxed material.

This point of inversion was a theoretical point, and definitely of interest, but in that case, there was little chance that the material would be strained to the GaN substrate lattice spacing. In fact, as will be shown below, the material showed no evidence of this.

Table 11 shows the band gap energies for the ideal case at both strain conditions. In the homogenous strain, the band gap was inverted so the band gap was negative. However, -0.30 eV at ~1160 nm corresponded to 98% In content. This was close to where the inversion occurred as shown in Figure 75. For the fully relaxed sample, the band gap energy was 0.93 eV at ~1200 nm which corresponded to 94%. At different depths, the band gap energies varied.

Table 11. The energy band gap for graded full composition InGaN.

Quantum region	Energy (eV) (Homogenous strain)	Energy (eV) (No strain)
All structure (0-1280 nm)	-0.30	0.93
Surface (30 nm)	0.66	1.14
Surface (70 nm)	0.12	0.93
Surface (120 nm)	-0.30	0.93
Surface (200 nm)	-0.30	0.94

The electron and hole wavefunctions are presented in Figure 78 and Figure 79. In the homogenous strain, the transition happened at the inversion region. For the fully relaxed layer, the transition happened at the interface between the graded InGaN and reverse graded InGaN. The hole and electron density are shown in Figure 80. Again, the homogenously strained simulation showed a high density of holes in the active layer and electrons in the top layer. On the other hand, the relaxed state (no strain) was almost exactly reversed.

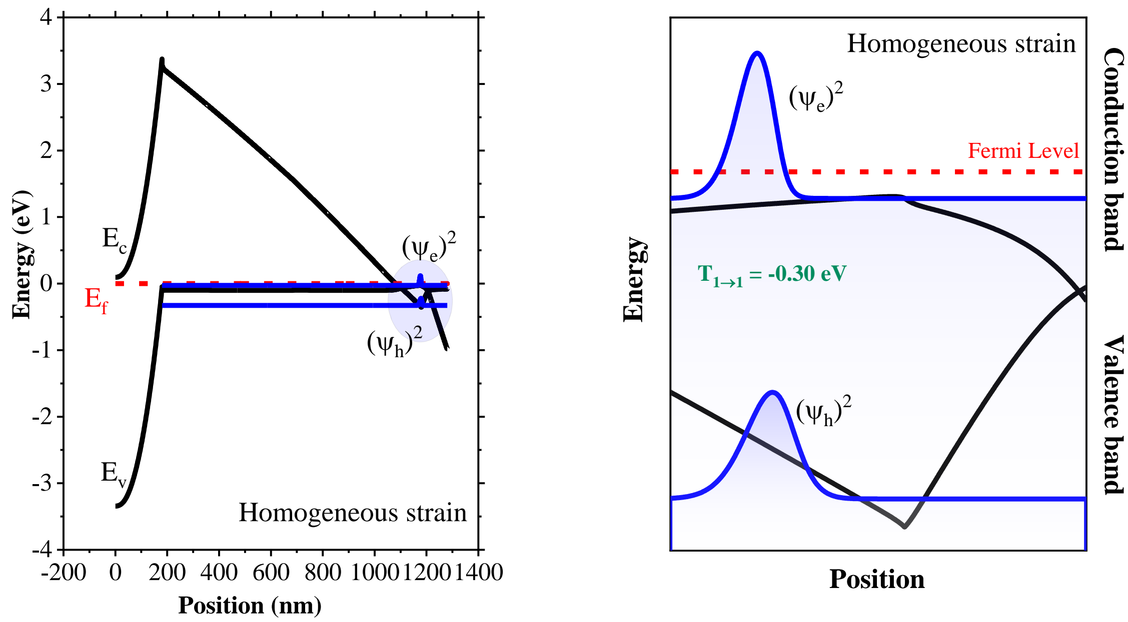

Figure 78. Graded InGaN band diagram and electron and hole wavefunction for homogenous strain state.

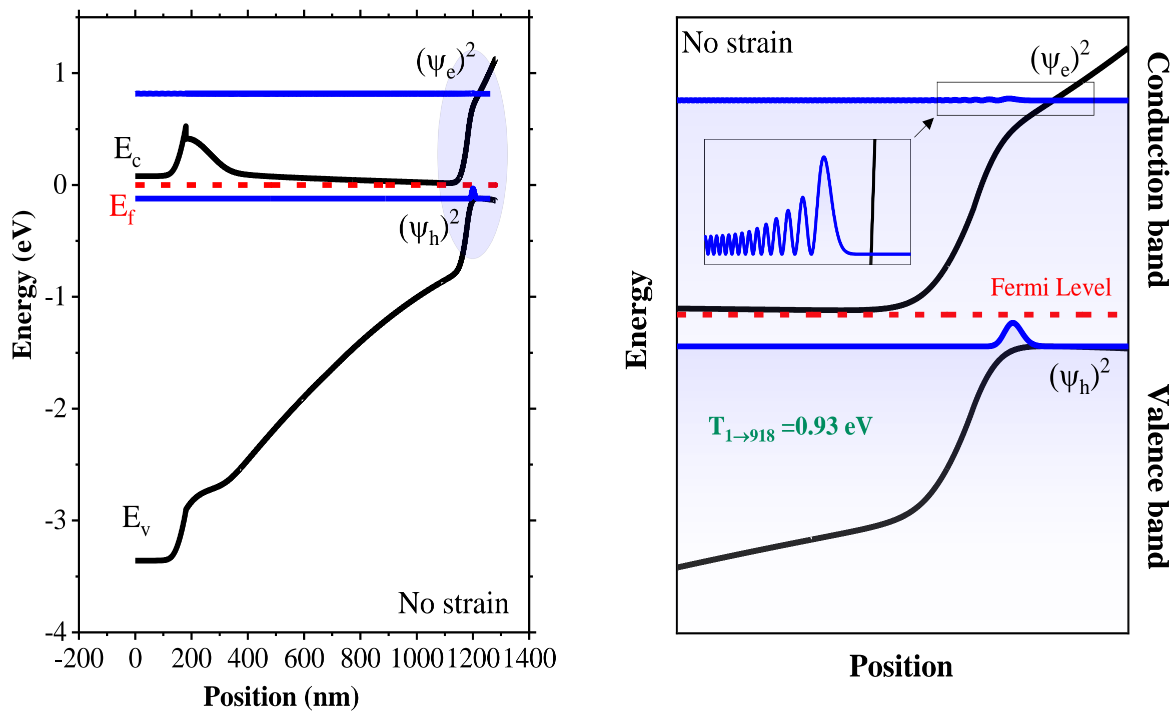

Figure 79. Graded InGaN band diagram and electron and hole wavefunction for no strain state.

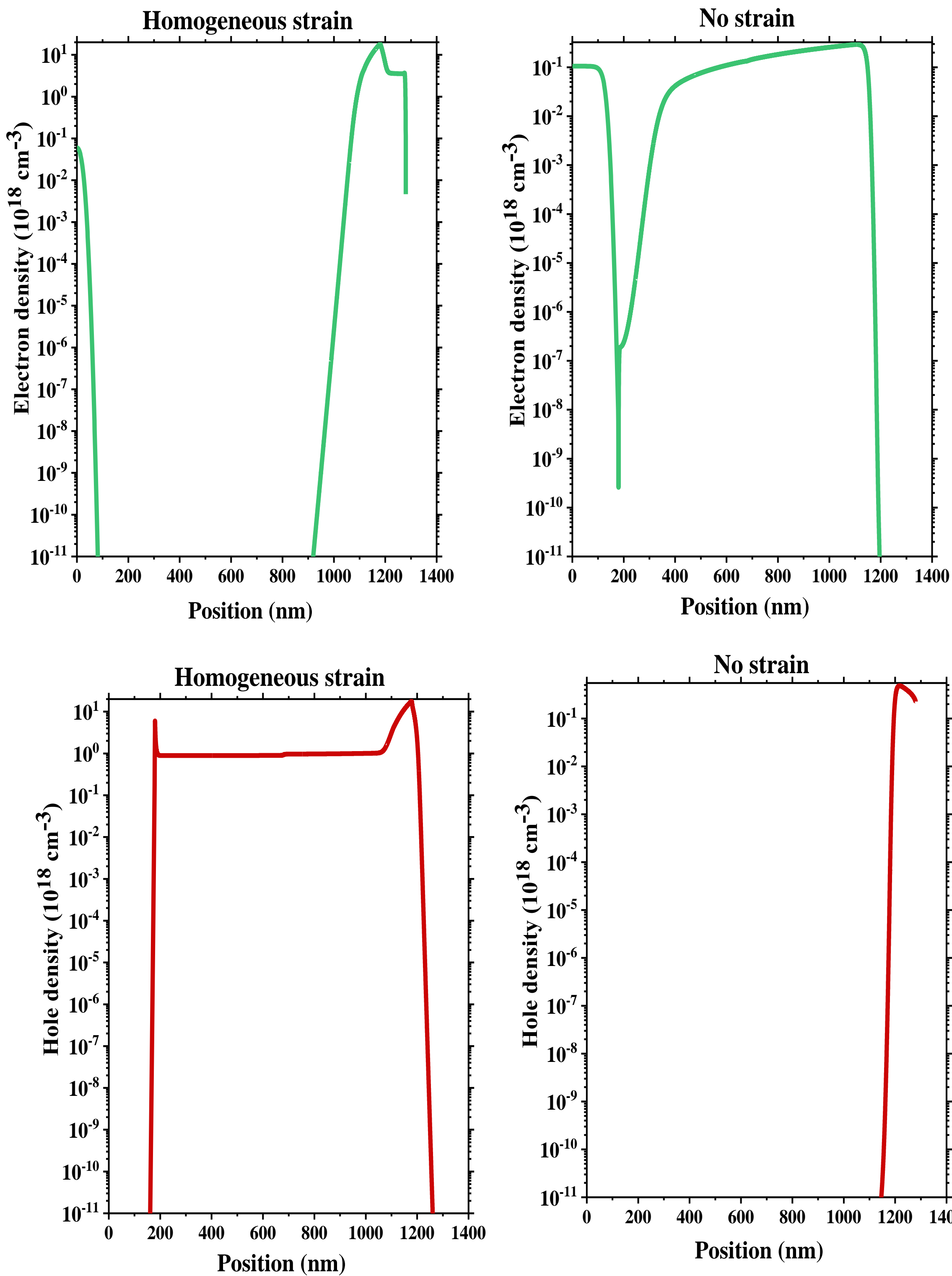

Figure 80. The electron and hole density for full graded InGaN.

Figure 81 shows a schematic diagram of the sample structure as designed for growth. Similar growth conditions previously mentioned in Chapter 4 were applied to this structure. First, the back surface of the sapphire was coated with a titanium (Ti) film around 1 µm thick to uniformly absorb the heat in the substrate. This coat was then removed using a buffered oxide etch (BOE) to be able to study the material by transmission measurements.

The growth was done on c-plane unintentionally-doped GaN templates on sapphire substrates via plasma assisted molecular beam epitaxy (PAMBE).

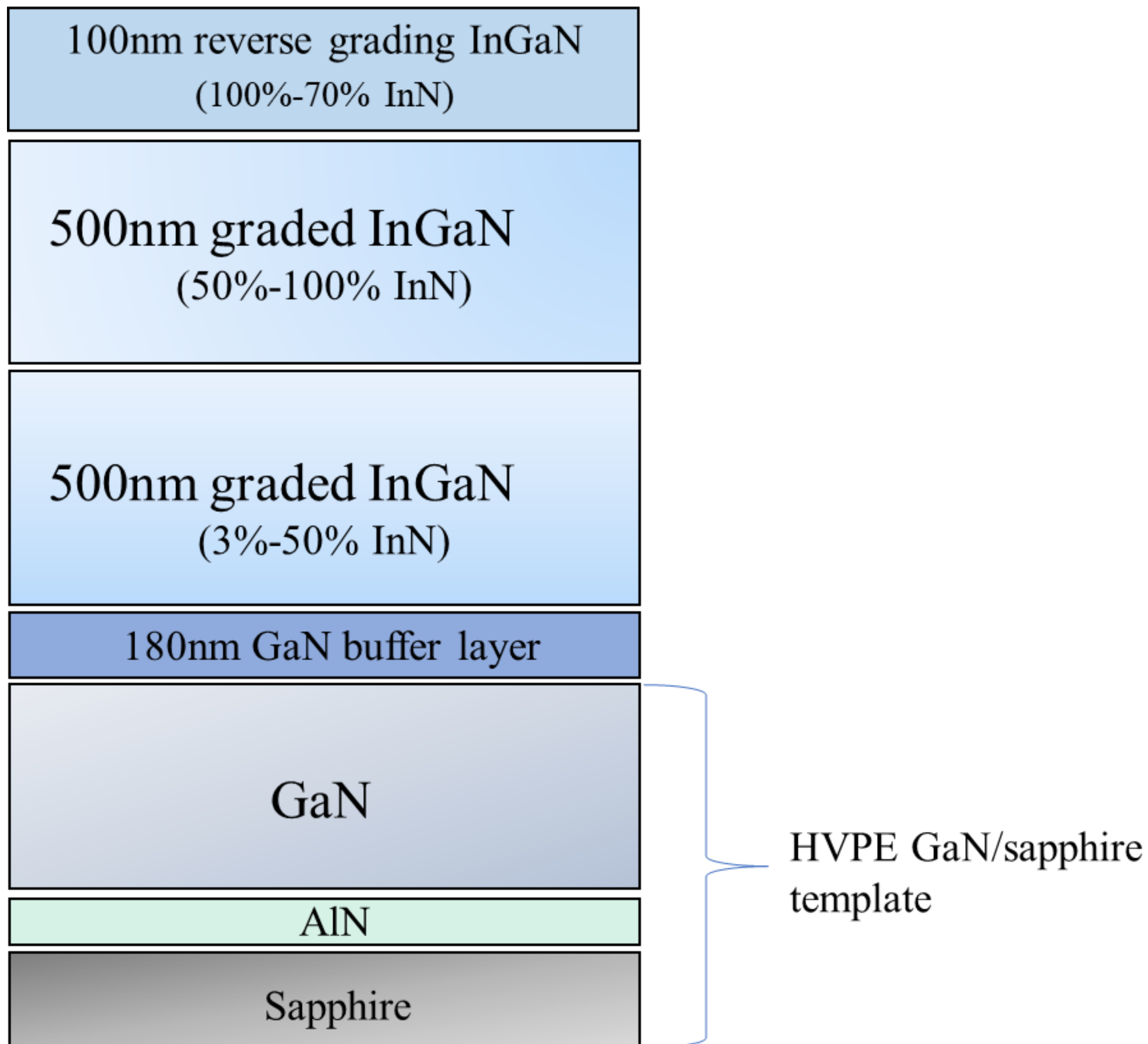

Figure 81. A schematic diagram for graded InGaN sample (475 + 400 °C).

The growth started with a GaN buffer layer (180 nm) at a 775 °C to serve as a clean surface for the following growth.

The previous set of samples in Chapter 4 showed higher In content at a low growth temperature (475 °C) and, in-fact, was able to demonstrate the designed 50% In content maximum. This growth temperature was therefore chosen to grow the first half of this full graded sample to ensure high enough In incorporation. Thus, a full graded composition-thick InGaN layer was grown first at a 475 °C with an In content gradient from 3% to 50% over 500 nm.Then, another 500 nm InGaN layer with graded In composition from (50% to 100%) was grown at lower growth temperature (400 °C) to incorporate higher In content. Another thin layer, 100 nm, was then grown at 400 °C with In content reverse gradient (100% to 70%) to create a p-n junction through polarization doping. Based on previous work that was done studying the initial growth of InN on GaN substrate, 400 °C was chosen to incorporate higher In content. This growth temperature showed InN that was grown successfully on a GaN substrate[105].

The growth of this structure is investigated in the following sections. Both the structural and the optical properties were examined experimentally. Similarly, as was done with the previous set of samples, nextnano3 was used to simulate the full composition graded InGaN using SIMS profile.

5.2 Experimental Results and Discussions

5.2.1 Atomic Force Microscopy (AFM)

AFM images (5 × 5 μm) and (1× 1 μm) are represented in Figure 82. The surface morphology showed a 3D-like structure and was attributed to the In accumulation on the surface.

At the low growth temperature that the sample was grown at (475 °C), and then even lower (400 °C) for the top 600 nm layer, the surface was covered with In.

The roughness was found to be 6.15 nm for a 1× 1 μm scan that is shown in (b), and 8.57 nm for 5 × 5 μm scan. These numbers were similar to the values that were found for the other sample sets (515 °C) at 6.31 nm to about 8.26 nm for graded InGaN that was grown at 475 °C. This indicated that the surface was almost flat with these step-like structures which could be as result of a bunching effect.

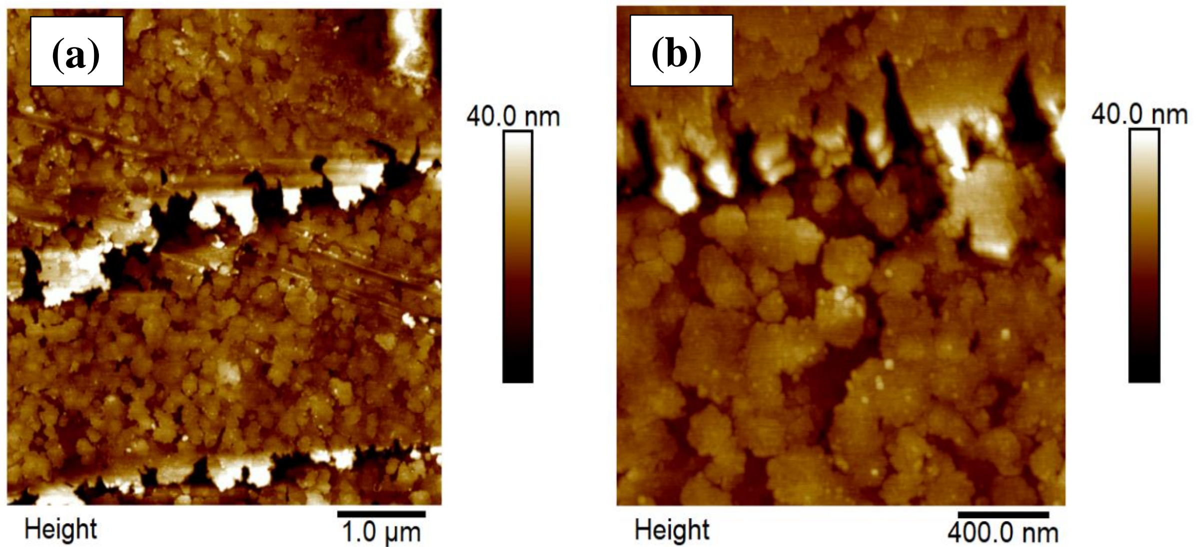

Figure 82. AFM images of 5 × 5 μm in (a) and 1× 1 μm in (b).

5.2.2 Optical microscope images

The optical microscope images in Figure 83 for the full composition graded InGaN showed large and dense droplet accumulation on the surface, with some of them reaching around 45 nm in diameter. The sample was completely covered with In after the growth was done. Then the optical microscope was used to investigate the surface after about 30 minutes of HCl etching. As was explained previously for the other set of samples, the small droplets tended to merge into

one large droplet. In other words, the larger In droplets absorbed the surrounding In adatoms, as proposed by Wu et al.[94]. Then a breakdown happened when the droplet surface tension increased, so the volume of the metal droplet increased after HCl etching as shown in Figure 83(b).

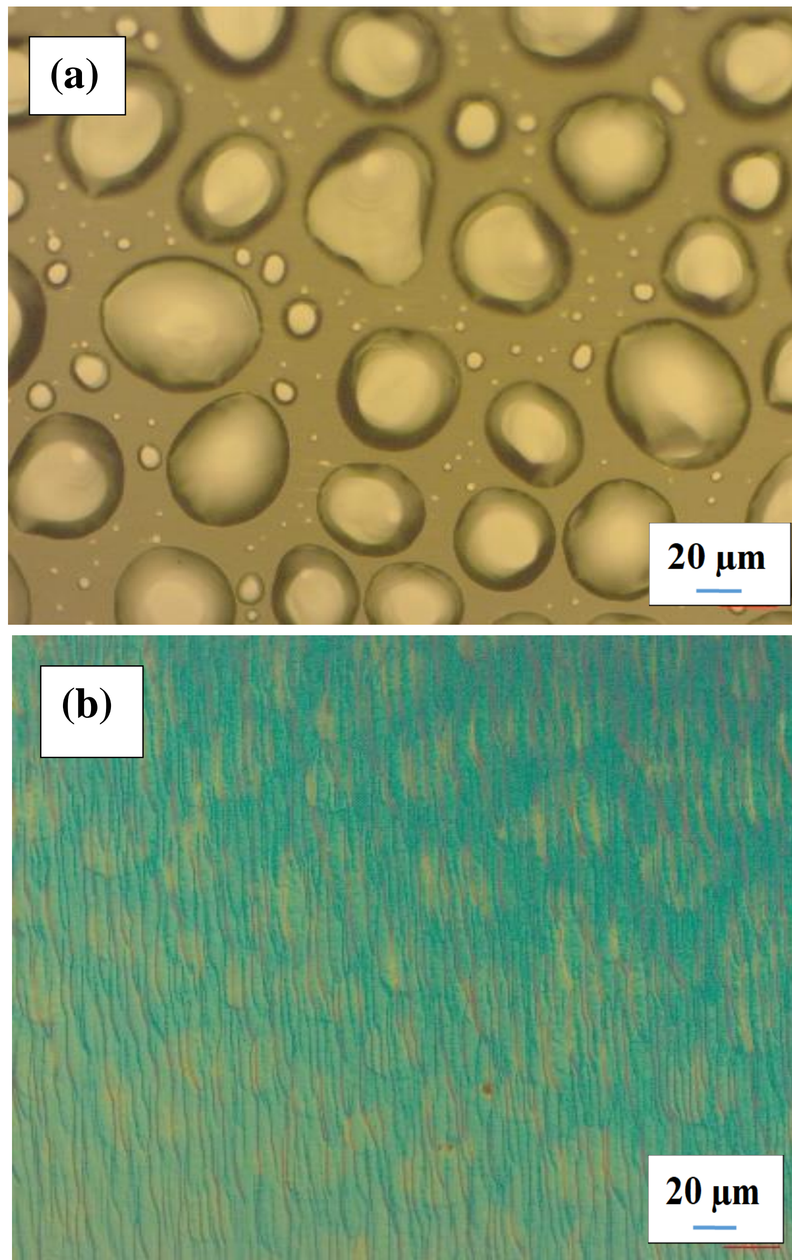

Figure 83. Optical microscope images for graded InGaN (475 °C + 400 °C): (a) before HCl etching and (b) after HCl etching.

5.2.3 Transmission

Figure 84 shows the transmission spectra of the full graded composition InGaN/GaN structure at room temperature. Looking at the curve, the absorption started gradually from 1900 nm to 1200 nm without a sharp absorption edge which represents a graded material. The sharp cutoff absorption edge at 3.4 eV for GaN was not present in graded InGaN; instead, there was a graded absorption edge that confirmed the graded material. The band gap was 0.86 eV which corresponded to approximately 92% In content, as shown in Figure 85 and was found by the Tauc plot method.

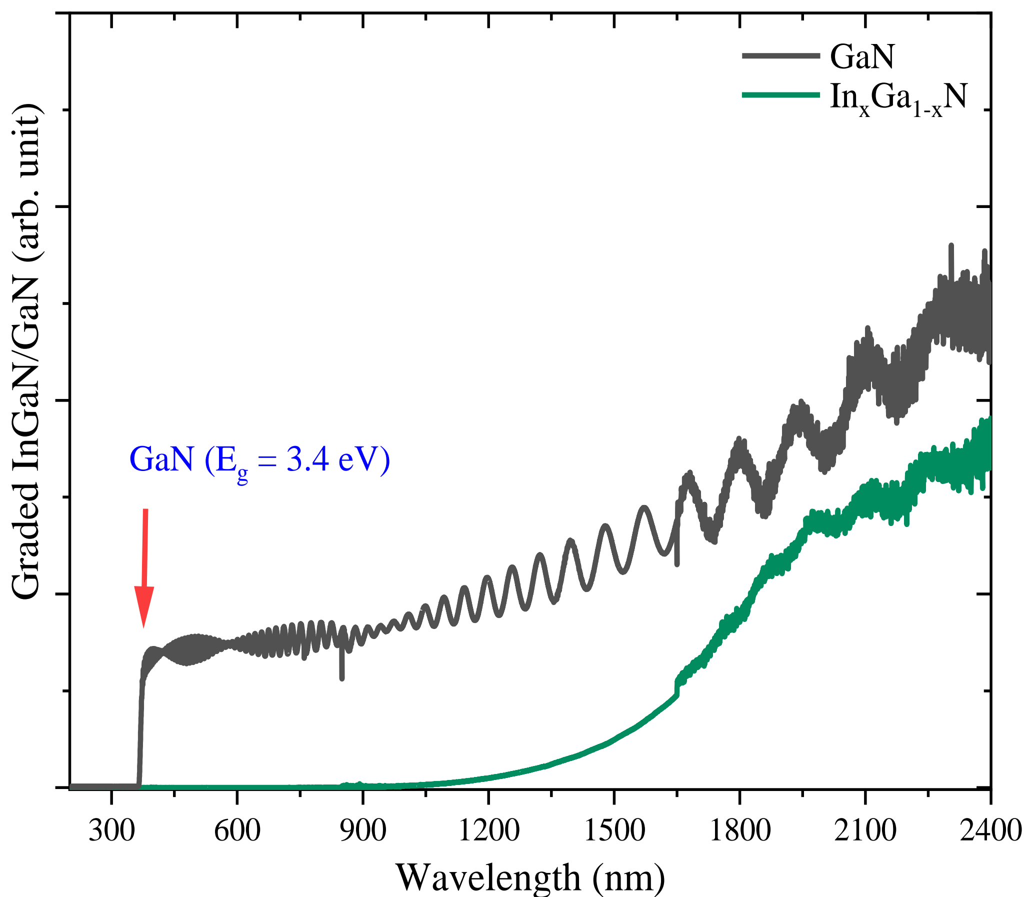

Figure 84. Transmission spectra for graded InGaN (475 °C + 400 °C).

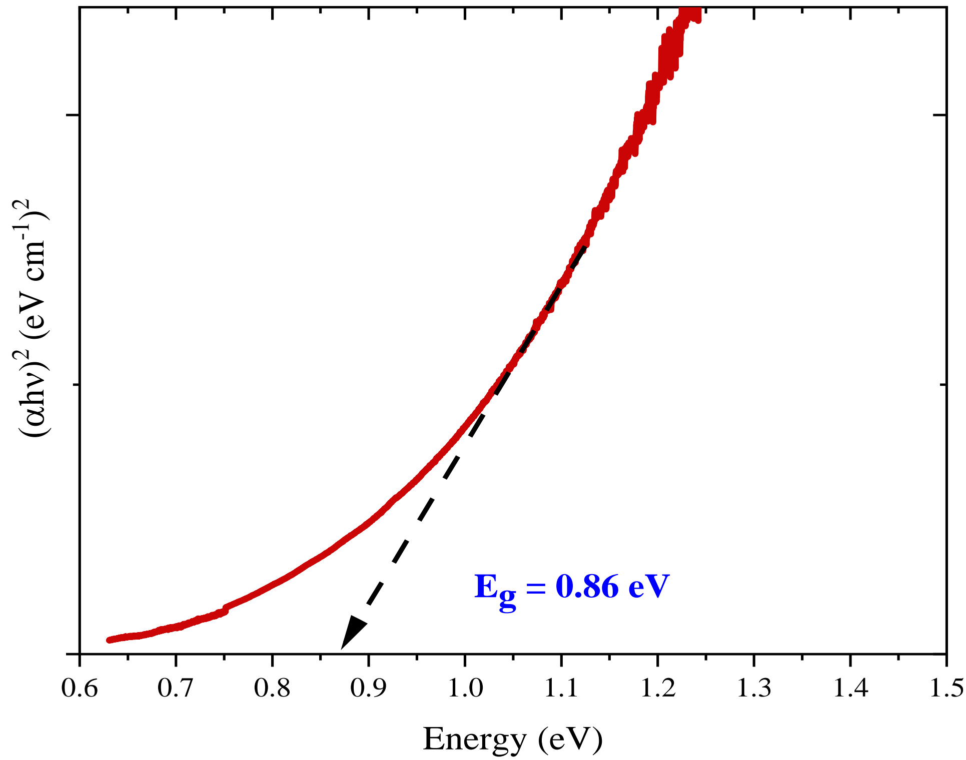

Figure 85. Tauc plot for graded InGaN (475°C+400°C).

5.2.4 Room temperature photoluminescence

Figure 86 shows room-temperature micro photoluminescence (μ-PL) spectra of the full composition graded sample. The μ-PL study demonstrated the optical properties of the material's peak position and spectral bandwidth.

The system was equipped with a single channel detector cooled with liquid nitrogen (N_2) that could detect in the spectral sensitivity range from 300 nm up to 2000 nm. The measurement was taken at room temperature with a He–Ne laser (632 nm) as an excitation source in a backscattering configuration.

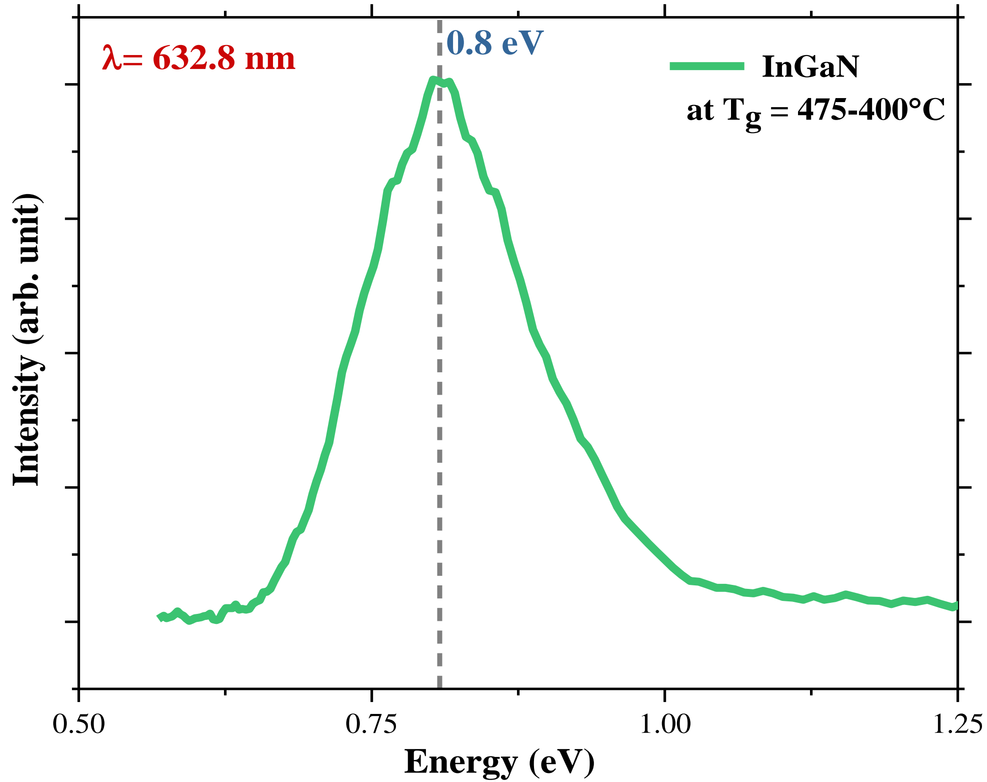

Figure 86. Room temperature PL measurement for graded InGaN.

The peak maximum that represented the band gap energy was at 0.8 eV (1760 nm) which corresponds to about 100% In mole fraction. A Gaussian fit was used to find the peak which was at 1760 nm and the full width at half maximum (FWHM) that was extremely broad at about 368 nm. This wide spectrum is a typical characteristic for graded materials with different band gaps, and it is important when it comes to photovoltaic applications since it will cover most of the solar spectrum.

There was a small redshift in the band gap when comparing the band gap of the PL spectra to the band gap that was calculated using the Tauc plot and transmission data. These variations in the band gap depend on the methods of measurement, but they were all in a good agreement.

The laser penetration depth in InGaN for laser 632.8 nm was calculated using the single composition formula from 50% to 100% In content, since the energy of the incident laser is less than the band gap of the material when InGaN has an In mole fraction of 40% or less so light does not get absorbed.

The penetration depth using the absorption coefficient ranged from 231 nm for $In_{0.50}Ga_{0.50}N$ to 78.7 nm for InN, and the average depth was 121.66 nm. However, transmission measurement averages the band gap of the entire structure.

The peak emission that was at about 0.8 eV was close to 0.7 eV for InN peak emission. A band gap energy of InN between 0.8 to 0.7 eV was observed at room temperature[106]. This was expected as the last layer of the growth was graded from 100% to 70% In. It meant that InN was close to the surface and PL measurement was only probing the surface.

5.2.5 X-Ray Diffraction (XRD)

X-ray diffraction measurements of the full composition graded sample are shown in Figure 87. Figure 87a shows the symmetric omega-2theta measurements around the (0002) peak of GaN. The observed range of the XRD (0002) diffraction peaks from 17.29° (GaN) to 15.67° (InN) indicates full In composition. The shoulder in between these two peaks confirmed the composition gradient.

The red curve showed XRD of the sample before In droplet etching. Then, the droplets were etched using hydrochloric acid (HCl) and the measurement was performed again as presented in the blue curve. It is clear that there were In peaks at 16.46° and 18.14° in the red curve before In droplet etching. That was confirmed in the blue curve after etching where they were not present anymore.

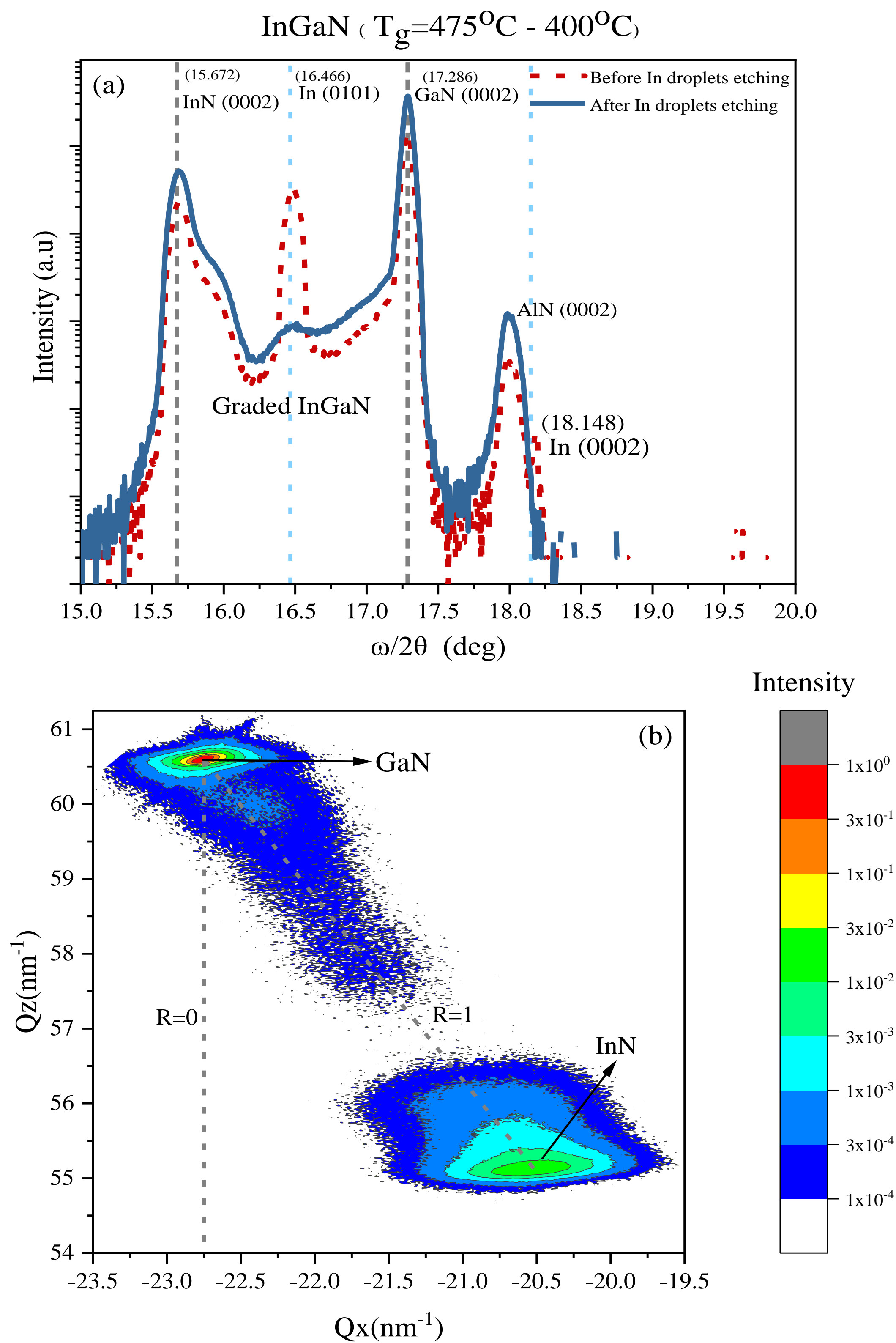

Figure 87. XRD ω/2θ of the plane (0002) and RSM for full graded InGaN.

The RSM in Figure 87b showed a fully relaxed graded InGaN material since the graded InGaN was aligned on the inclined relaxation dashed line (R=1). The composition was determined using the measured lattice constants and the relaxed lattice constants as well as the Poisson ratio. Therefore, the InGaN peak that was down the relaxation line was corresponded to InN material.

5.2.6 Secondary Ion Mass Spectrometry (SIMS)

The SIMS depth profile for the full composition graded InGaN as demonstrated in Figure 88 showed that In was incorporated almost linearly in the first 500 nm layer. Then, it quickly reached 100% In in the second layer and remained almost constant.

In the reverse layer, In content dropped from 100% to about 70% for the reverse layer grading and then jumped back to about ~89%.

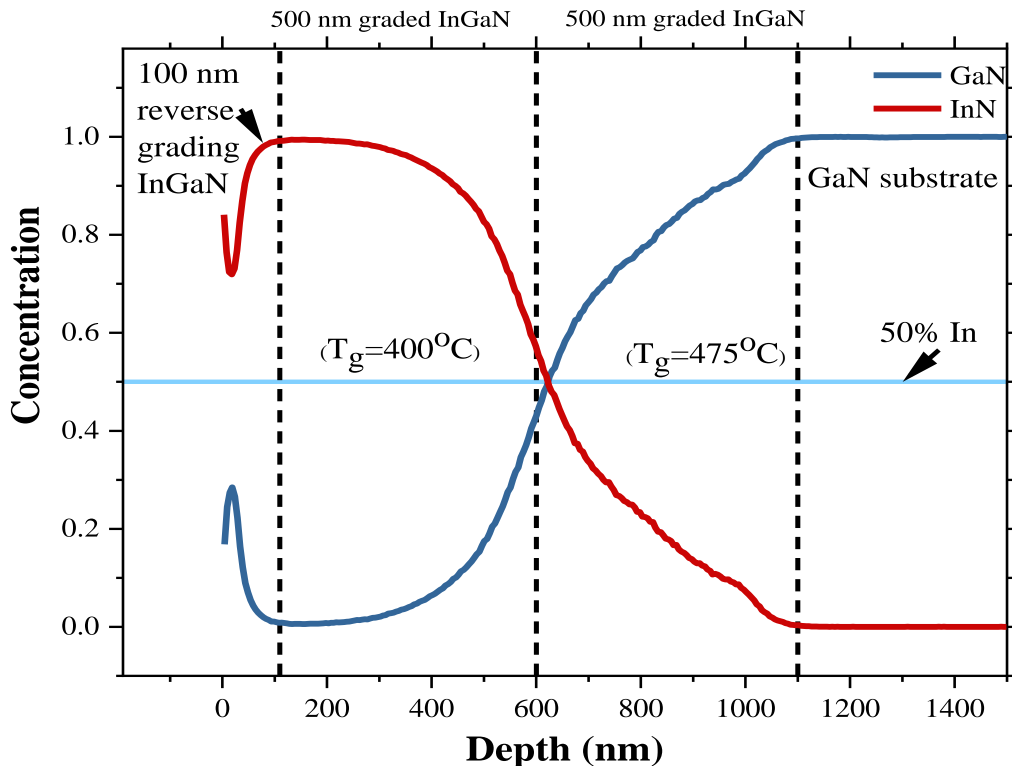

Figure 88. Graded full composition InGaN SIMS profile.

All the samples in SIMS measurements showed high In composition on the surface, which could explain the PL measurements. PL measurements did not show the same maximum In content in the XRD or SIMS results. That was due to the limited absorption coefficient of the laser in the graded InGaN layer. Table 12 shows the compositions that were found using these different methods.

Table 12. Experimental band gap energy for graded full composition InGaN.

Measurement method	InGaN(475+400°C) E_g
Transmission (Average band gap)	0.86 eV (88%)
XRD-Reciprocal Space Map (Surface average band gap)	~1 eV (100 %)
Photoluminescence (Observable band gap)	0.8 eV (92%)

Nextnano[3] was then used to simulate the In SIMS profile and compare it with the ideal case and the experimental results. Figure 89 shows the In profile imported into nextnano[3] for the

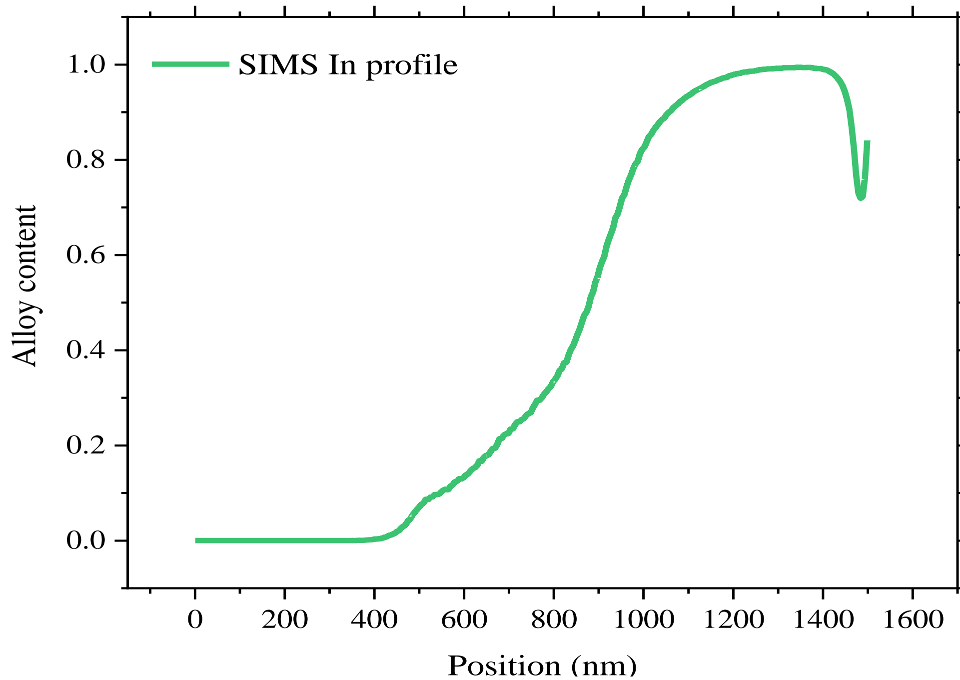

Figure 89. In SIMS profile for graded full composition InGaN.

full composition graded InGaN that was graded over 1μm (0-100% In) and then was reverse graded (100% to 70% In) over 100 nm.

The band diagram in Figure 90 in the homogenous strain case shows that the polarization doping resulted in n-type GaN and the interface of the heterostructure is the depletion region. The active layer is a p-type material to the point where the inversion occurs in the band diagram.

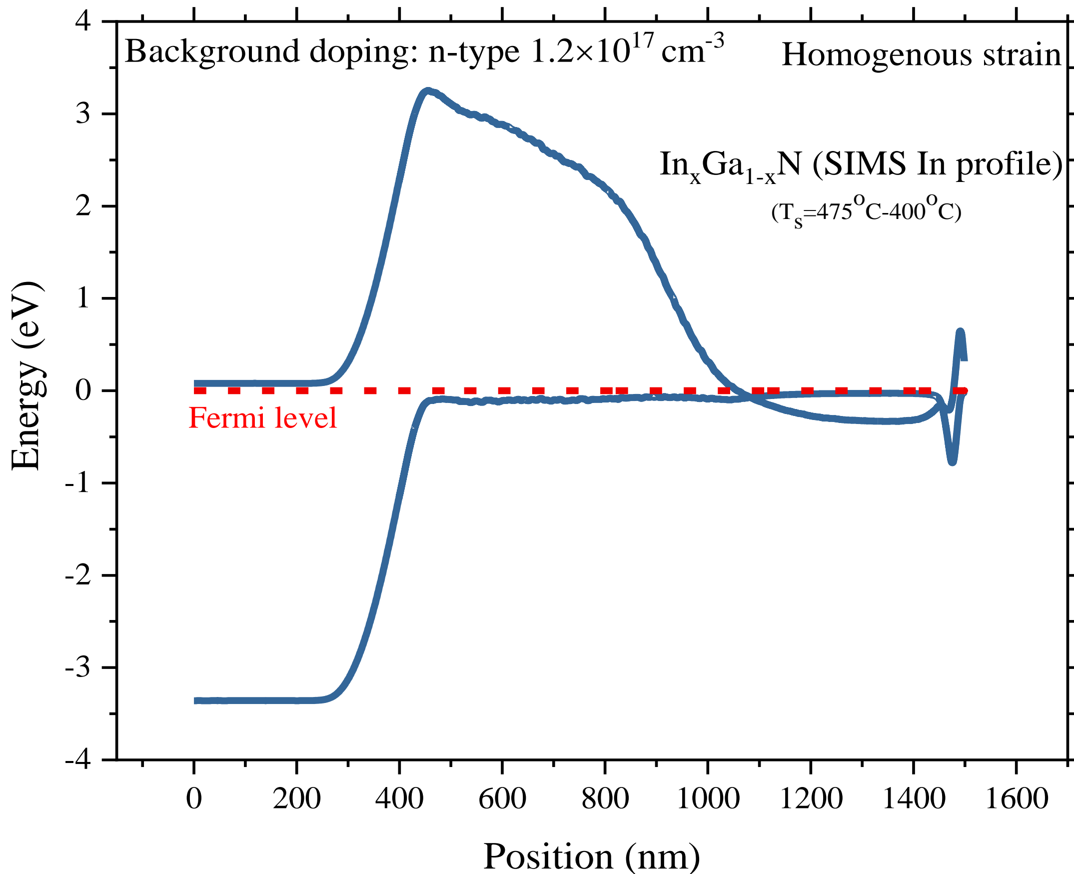

Figure 90. InGaN (475°C + 400 °C) band diagram for homogeneous strain.

In the no strain material band structure in Figure 91, the Fermi level is closer to the conduction band, meaning that it forms an n-type material. However, the surface forms a p-type layer where the reverse grading happens.

The relaxed case represents more the experiment since XRD-RSM showed almost full relaxation for full graded InGaN where the peaks of InGaN are exactly on the relaxation line.

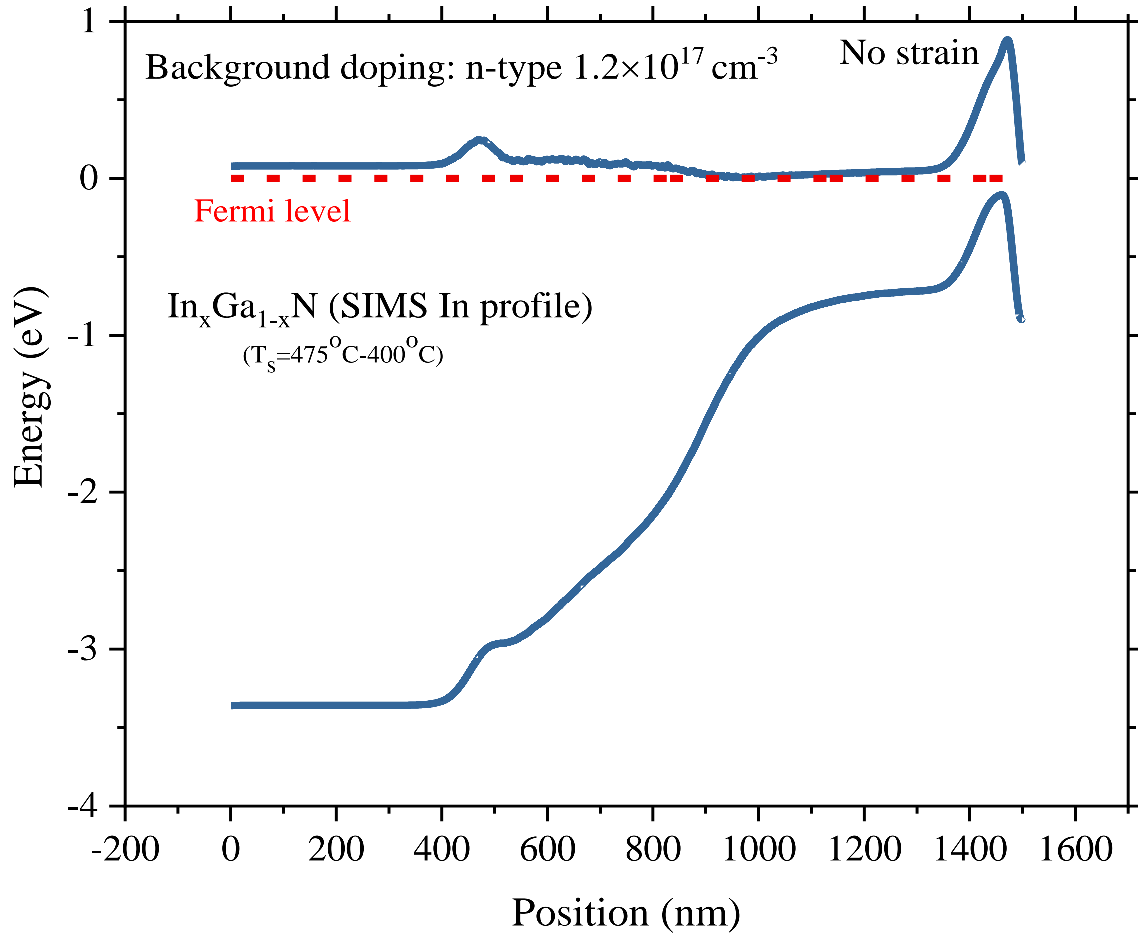

Figure 91. InGaN (475°C + 400 °C) band diagram for no strain.

Table 13 shows the simulated band gap energies for the whole structure of graded InGaN using the In SIMS profile as well as the band gap energy at different depths. Comparing the experimental results of the band gap energy for graded full composition InGaN in Table 12, the fully relaxed band gap at the surface was closer to the transmission average band gap but less

than the PL (92%), which could have been affected by the In accumulation on the surface that gives a signal from the surface.

Table 13 The energy band gap for full graded composition InGaN (475°+400C).

Quantum region	Energy (eV) (Homogenous strain)	Energy (eV) (No strain)
All structure (0-1280 nm)	-0.30	0.94
Surface (30 nm)	0.59	1.22
Surface (70 nm)	0.59	0.91
Surface (120 nm)	-0.29	0.93
Surface (200 nm)	-0.30	0.93

The wavefunctions of the electron and hole where the highest transition probability happens was at the surface for both strain states in Figure 92 and Figure 93 .

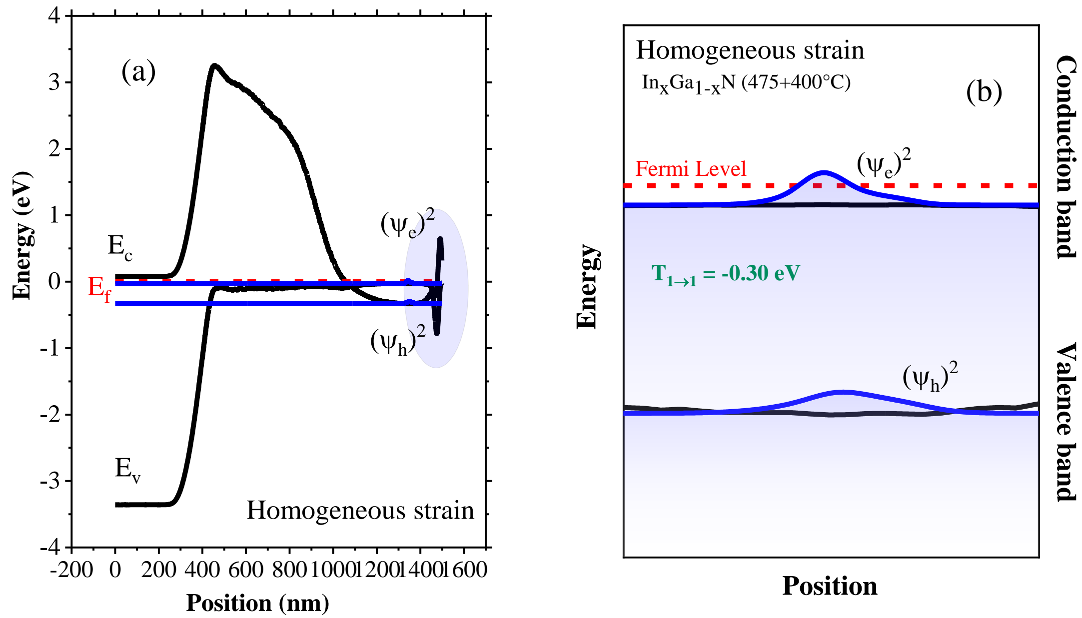

Figure 92. InGaN (475 °C + 400 °C) band diagram and electron and hole wavefunction for homogenous strain state.

The transition energy was -0.30 eV for e1-hh1 in the homogenous strain state at ~1350 nm (99.5%), Figure 92. However, in the fully relaxed case the transition energy was 0.93 eV for e918-hh1 at ~1460 nm (90.8%), Figure 93. The probability of transition decreased from 92.4% for homogenous strain to 3.11% for no strain.

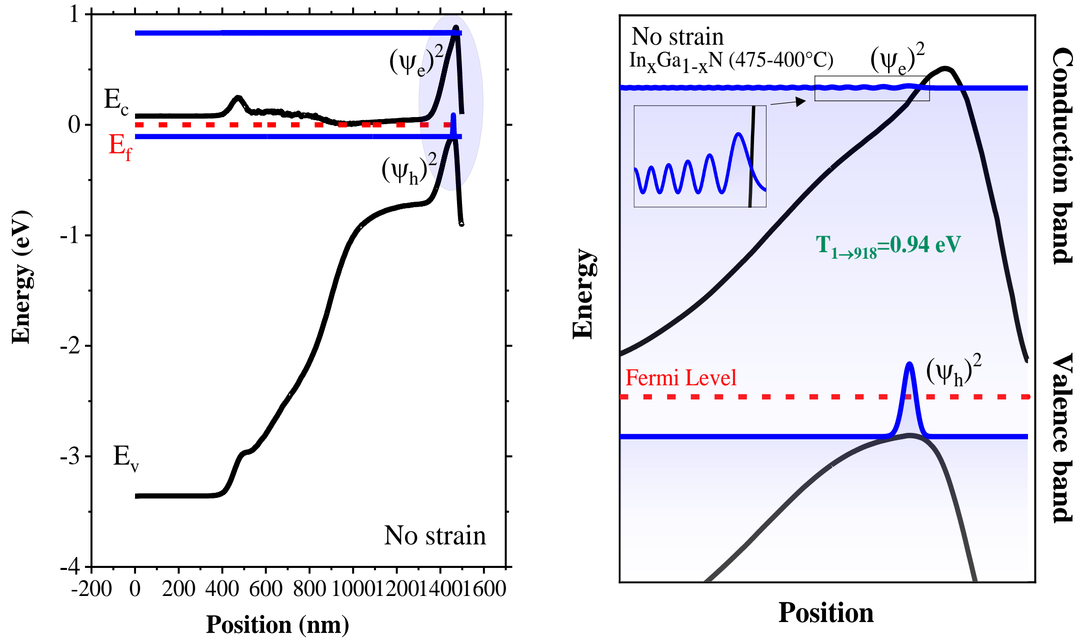

Figure 93. InGaN (475 °C + 400 °C) band diagram and electron and hole wavefunction for no strain state.

Figure 94 shows the electron and hole density which demonstrated n-type active layer and p type top layer in the relaxed state. This was the opposite of what was expected from the literature.

5.2.7 Transmission Electron Microscope (TEM)

The graded layers can be seen in Figure 95 using transmission electron microscopy (TEM). The first graded layer (3%-50% In) was grown at 475 °C over 500 nm, while the other graded

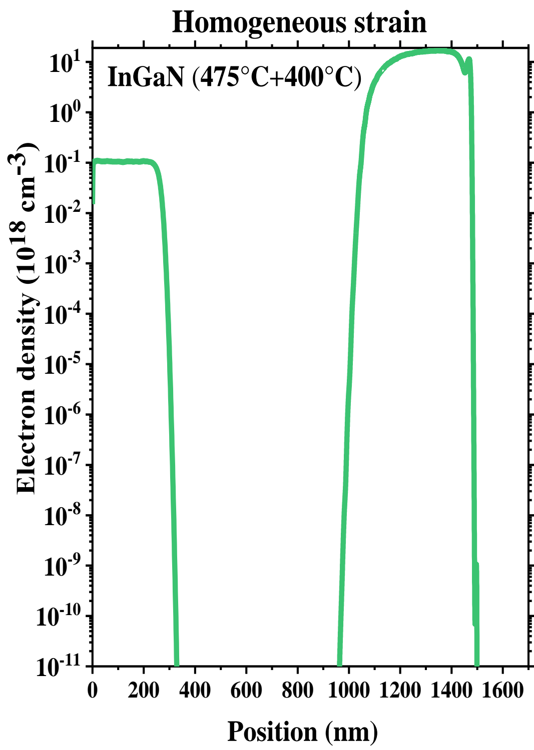

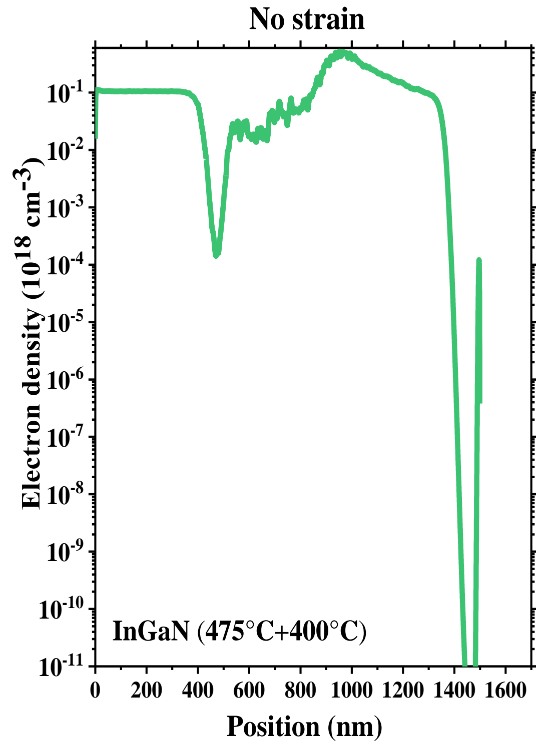

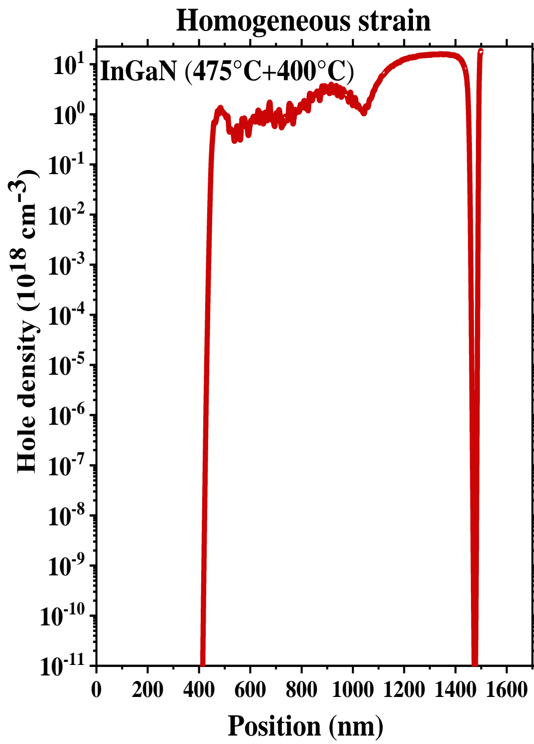

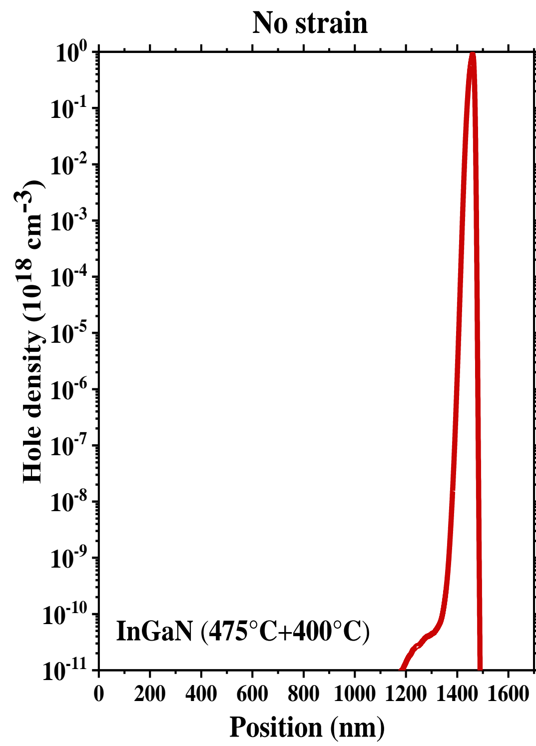

Figure 94. Electron and hole density for full graded InGaN.

layer (50%-100% In) was grown at the lower temperature of 400 °C. Then, a reverse graded layer (100%-70% In) was grown over 100 nm.

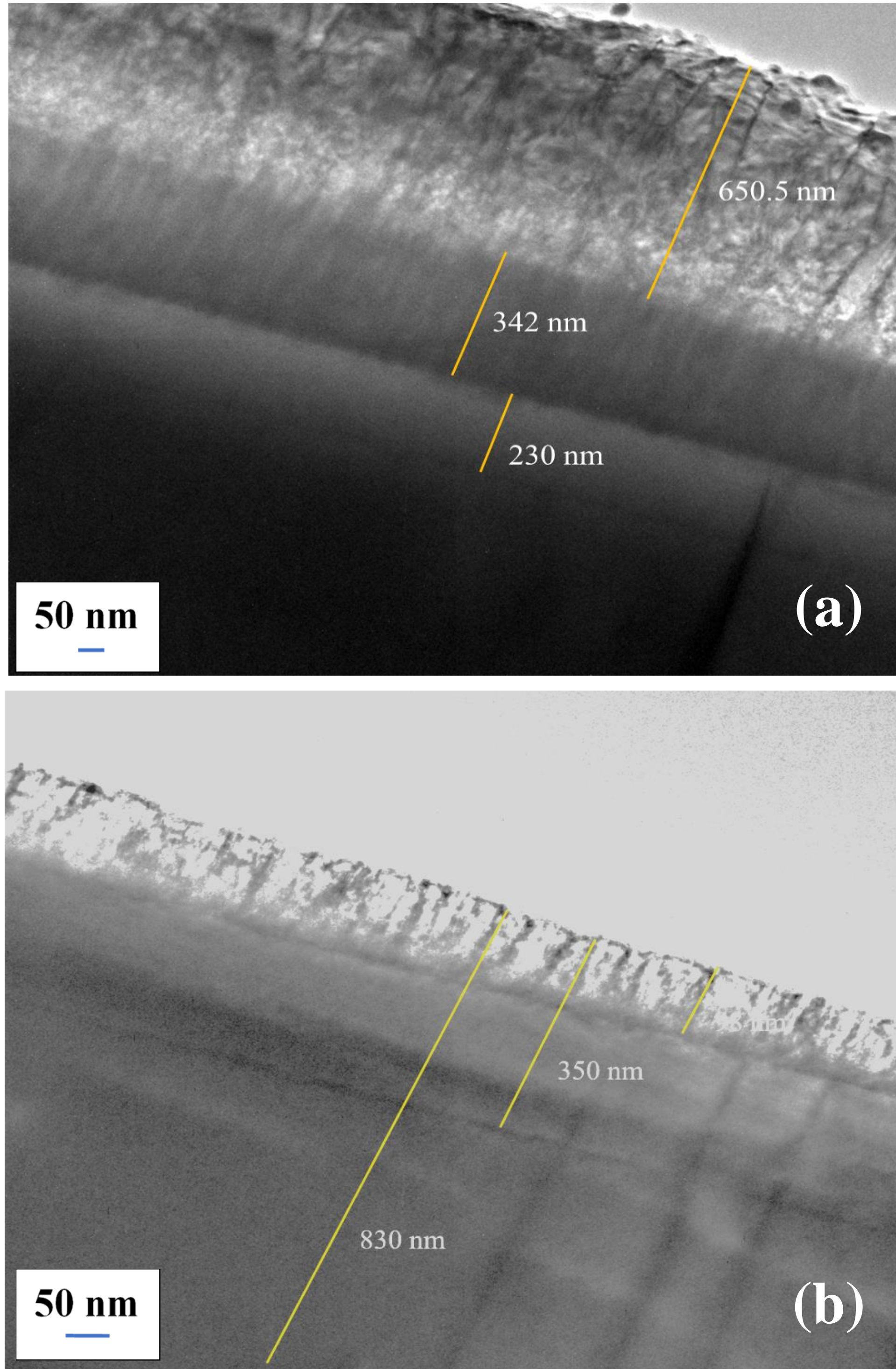

Figure 95. TEM images for graded full composition InGaN.

Figure 96(a) high-resolution TEM images exhibit that graded composition InGaN was grown epitaxially on the GaN substrate. Figure 96(b) shows the Fast Fourier Transform (FFT) image lattice image that proves it was crystalline film.

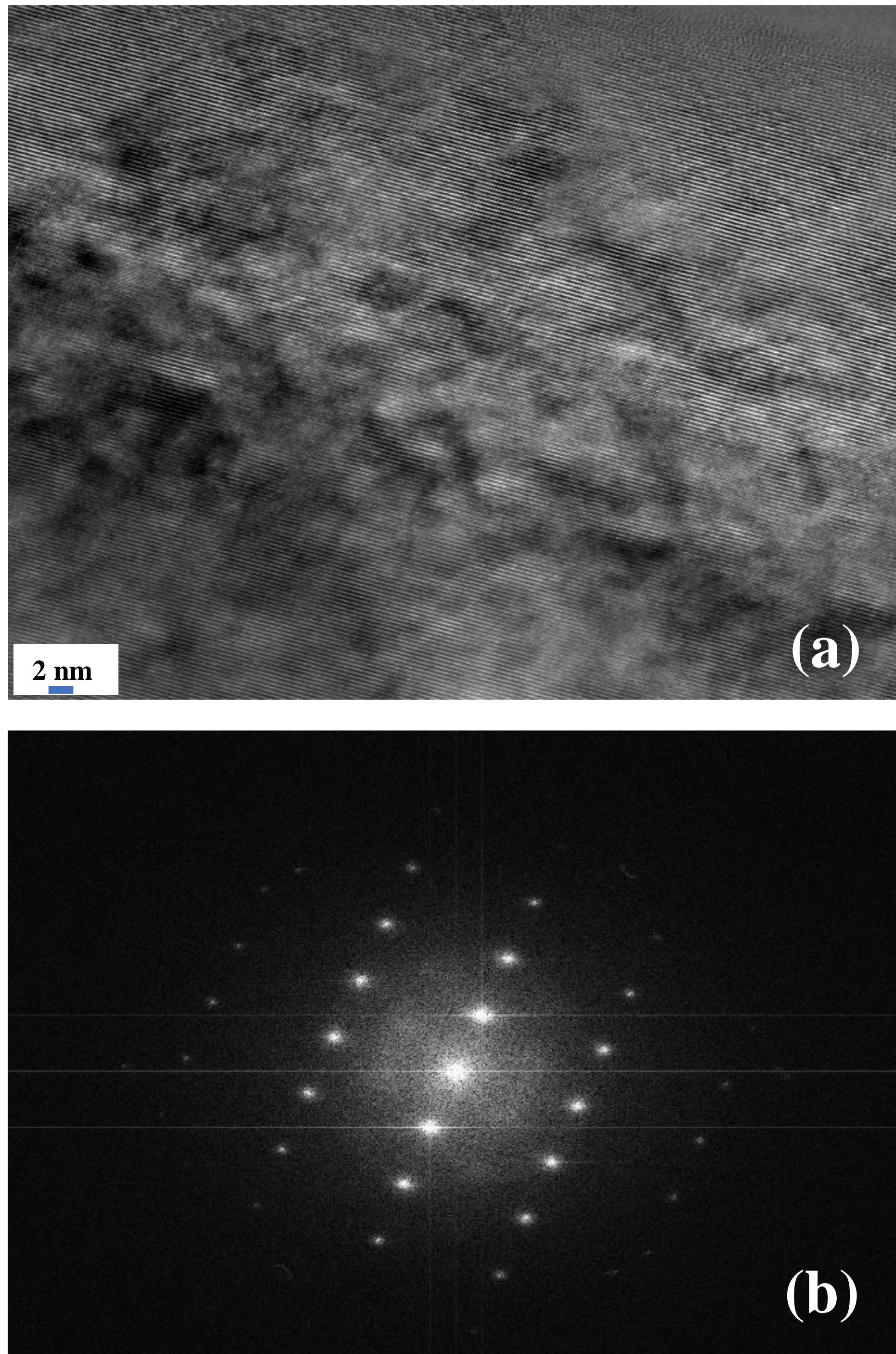

Figure 96. TEM and FFT images for full graded composition InGaN.

These layers are shown in Figure 95(a). However, the different contrast variations confirmed the graded In composition which usually is an indication of the indium fluctuation content in a constant composition InGaN material. Additionally, the lighter contrast was after the 342 nm layer where the growth temperature was lowered to 400 °C.

Figure 97 shows energy dispersive x-ray spectroscopy (EDS) measurements that evaluate the In composition profile in the graded layer.

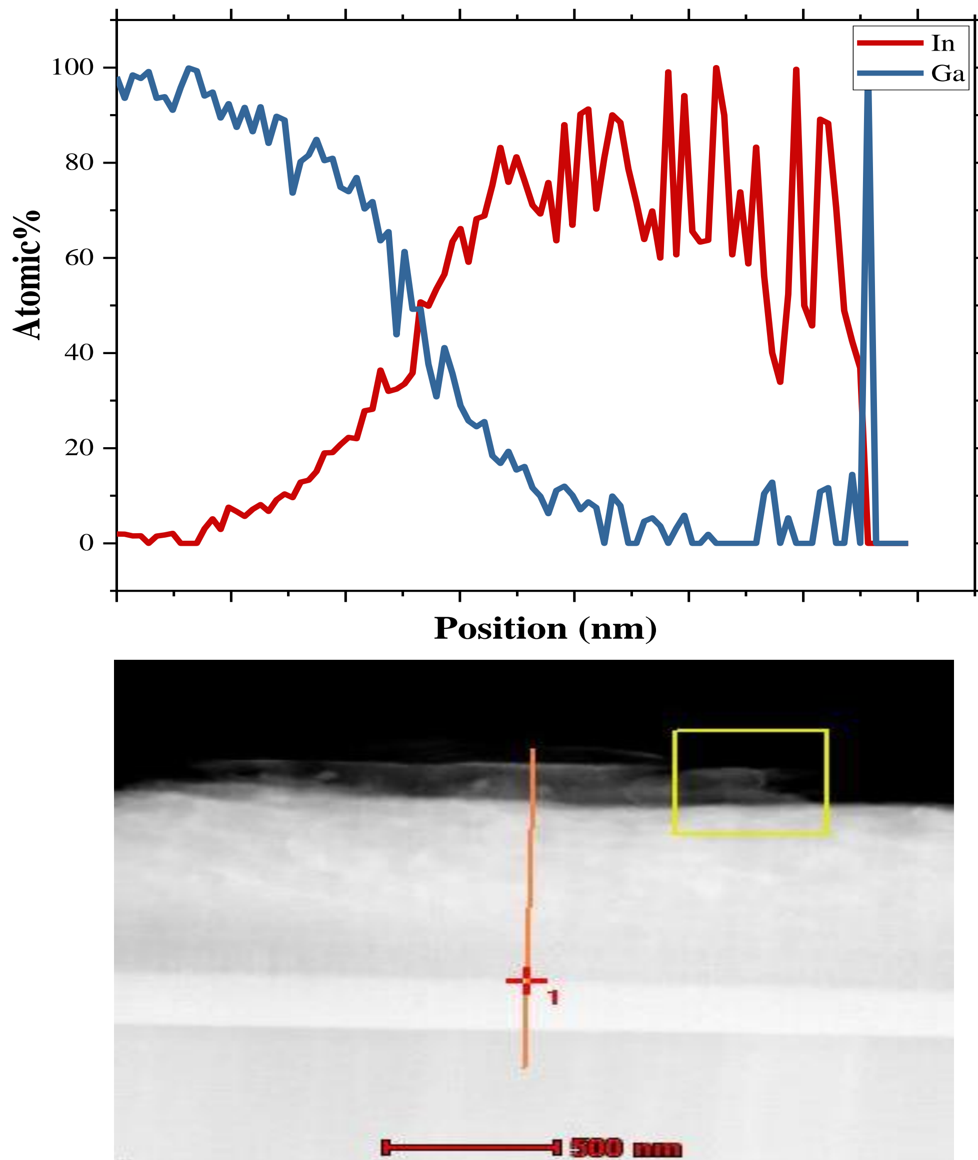

Figure 97. EDS image that shows the composition profile in the graded InGaN layer.

The line was taken along the graded layer's direction of growth. The composition profile was in a good agreement with SIMS results. However, SIMS measurement is considered more precise and reliable compared to EDS.

Note that the small yellow box was a reference as the sample moved during the line scan measurements. This reference helped to correct for the drift.

Chapter 6: A Growth Model for Graded InGaN

The growth of InGaN is controlled and affected by many different parameters: the polarity of the substrate, the impinging flux of Ga, In, and N, the ratio of metal/N, as well as the substrate temperature during growth.

Additionally, the strain that is introduced in each layer during the growth strongly influences the composition of subsequent layers[107].

It was reported that In incorporation in $In_xGa_{1-x}N$ films increased when decreasing the growth temperature[108]. Moreover, it was observed that there is a linear dependency of the amount of In incorporated in the film on the In-flux and an inverse relationship with the growth temperature.

The difference in sticking coefficients of Ga and In, In segregation, as well as thermal desorption could explain these properties. Other factors that affect In incorporation are the growth conditions such as the high indium segregation at the metal-rich condition and the high desorption of In at the near stoichiometric condition[109],[110].

Additionally, under metal-rich conditions, the In content generally depends on the Ga flux even at a constant Ga/In ratio because Ga is preferentially incorporated into InGaN over In. On the other hand, only the Ga/In ratio affects the In composition under N-rich conditions[111].

A simple growth model was proposed to interpret the results from SIMS. The growth was modeled by assuming metal fluxes from the effusion cells which change exponentially with temperature. Additionally, a starting flux was taken to be slightly Ga rich, which is a normal condition for GaN growth with an additional In flux equal to that required to grow $In_{0.03}Ga_{0.97}N$, assuming strictly stoichiometric flux conditions.

Subsequently, the compositionally graded growth was modeled by simultaneously

decreasing the Ga cell temperature and increasing the In cell temperature linearly such that at the end of the ramp the fluxes would be equal to those required to grow $In_{0.5}Ga_{0.5}N$ or InN, assuming strictly stoichiometric flux conditions.

Figure 98, Figure 99, Figure 100, and Figure 101 show the results of these simulation. The main features presented here are:

1) a large excess of Ga initially saturates the growth to be entirely GaN;

2) while Ga is in excess, In accumulates on the surface without incorporation;

3) when the Ga excess is finally consumed by growth and/or evaporation, the In excess begins to incorporate at a maximum metal to N ratio, i.e., the growth proceeds under a metal rich condition where the In is in excess;

4) when the excess In is finally consumed, the composition drops suddenly and the growth proceeds under a N rich condition until the final layers; and,

5) during the last layers, the flux of the In finally catches up to the N and the growth proceeds in a metal rich condition, again with In in excess.

In this growth model, only the first graded layer of the structure was simulated. The SIMS data that were simply modeled are in Figure 53, Figure 54, Figure 55, and Figure 88.

These plots show similar behavior to some of the features in the In profiles that were found using SIMS measurements. One is that In incorporated faster with a lower growth temperature. Second, the maximum In expected was higher as the temperature decreased.These simulations show that Ga excess plays a major role in growth. Once the Ga excess becomes low enough or is consumed, the accumulated In starts to incorporate in the material. Thus, at higher temperature such as in Figure 98, excess Ga is higher compared to the other growth temperatures which prohibits the In incorporation in the material until it is all consumed.

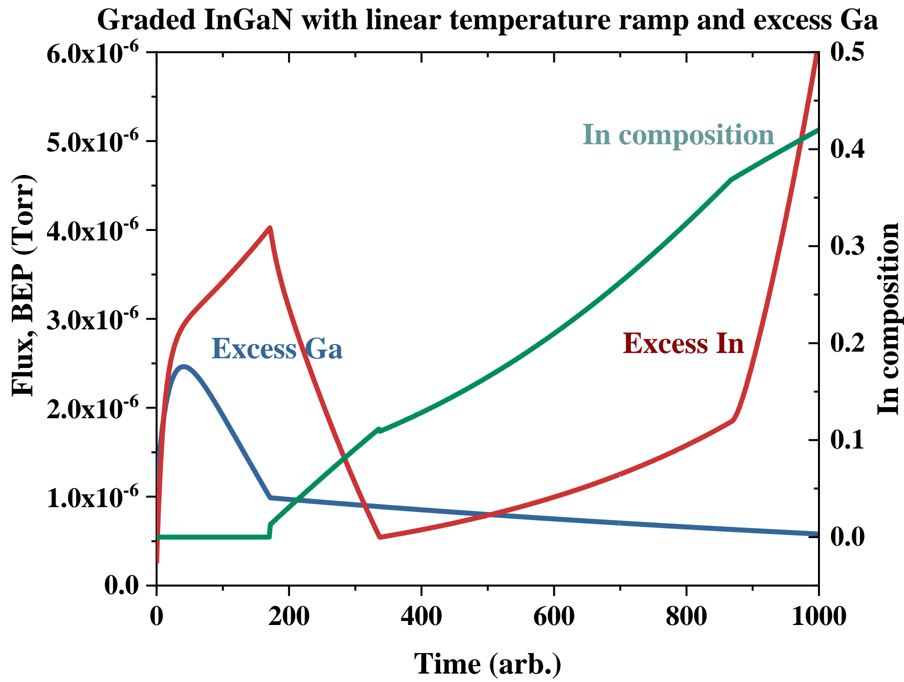

Figure 98. Simulation of In SIMS profile for graded InGaN (555°C).

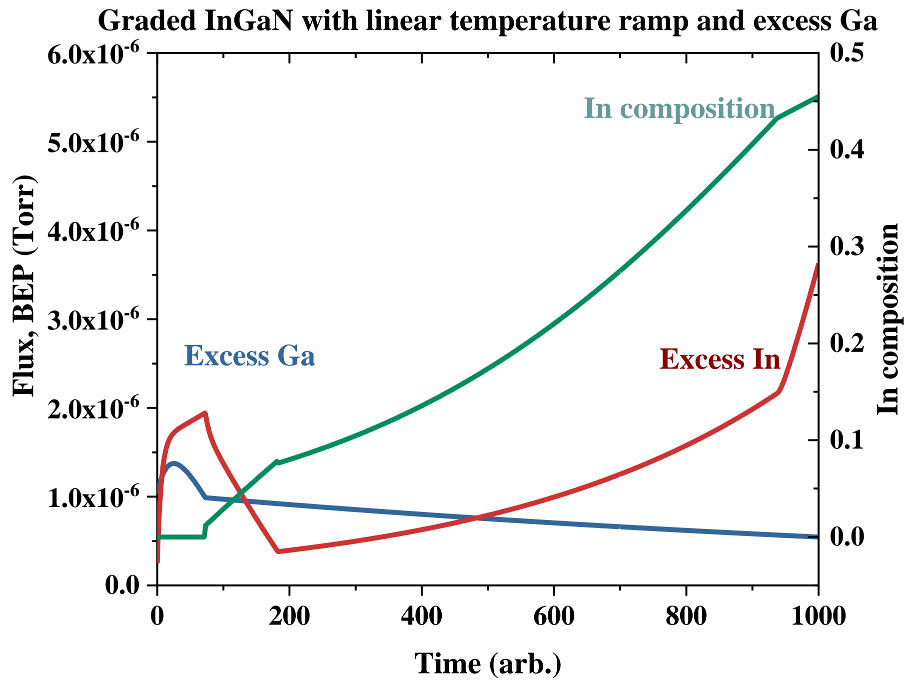

Figure 99. Simulation of In SIMS profile for graded InGaN (515°C).

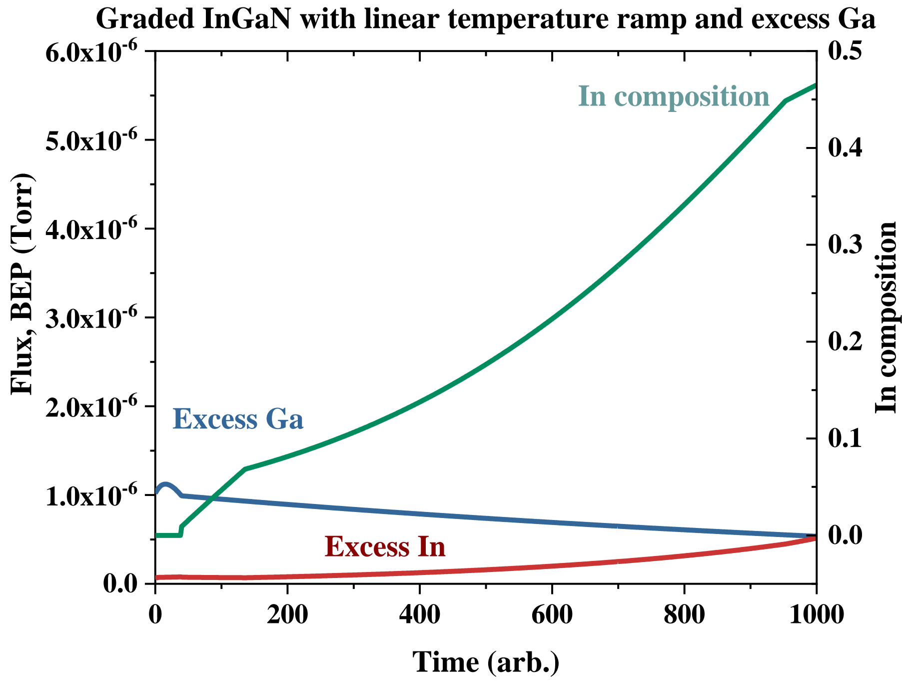

Figure 100. Simulation of In SIMS profile for graded InGaN (475°C).

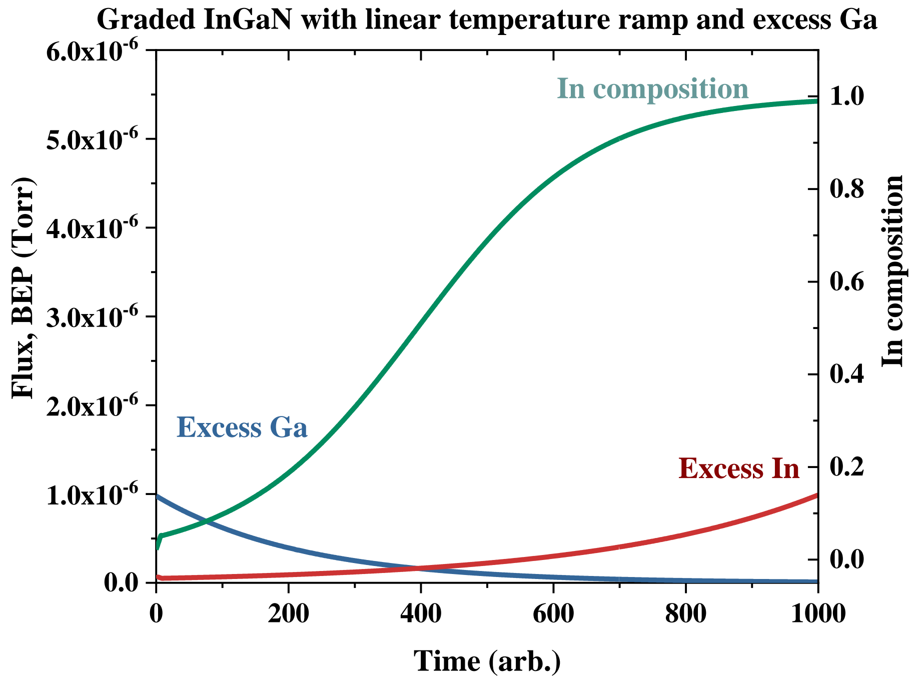

Figure 101. Simulation of In SIMS profile for graded InGaN (475+400°C).

This results in less maximum In than expected, showing 41% rather than 50% In. Also, for graded InGaN that was grown at 515 °C, Figure 99 shows higher In content at 45% as In started to incorporate faster. A further increase in maximum In was shown in Figure 100 at 47%.

Additionally, the first stage of growth is GaN with no In incorporation, matching the SIMS profile to be 170 nm, 70 nm, and 38 nm for InGaN grown at 555 °C,515 °C and 475 °C respectively. That was done by decreasing the excess Ga as the temperature decreased.

For the full graded composition in Figure 101 InGaN, the curve is very similar to the experimental results. In this case, Ga excess is so low that In started to incorporate at the first stage of growth, which led to the expected maximum In content (100%).

Other factors could contribute to the profile that was shown in SIMS results and were not included in this simple model, such as strain buildup and relaxation. Different theories have calculated the critical thickness that could help explain the relaxation incidents at which there is a jump in In composition.

These theories or strain relaxation models are basically the same but different in how they calculate the strain energy and the misfit dislocation energy. The strain energy that could occur as a result of mismatch between the lattice constant of the film and the substrate is proportional to the thickness of "pseudomorphic" epitaxial layer. This leads to a high-quality material and thermodynamically stable critical thickness. This was first explained by Frank and Van der Merwe[112].

The Matthews and Blakeslee relaxation model (Equation 22) and People and Bean relaxation model (Equation 23) are similar in considering the misfit dislocation explicitly. However, People and Bean added "an areal energy density" indicating that the misfit dislocation

will replace the film strain when the areal energy density of the film exceeds the areal strain energy.

$$h_c = \frac{b}{8\pi f}\frac{1-\nu\cos^2\theta}{(1+\nu)\cos\lambda}\left(\ln\frac{h_c}{b}+1\right) \qquad \text{(Equation 22)}$$

$$h_c \approx \frac{1}{16\sqrt{2\pi}}\left(\frac{1-\nu}{1+\nu}\right)\frac{b}{af^2}\ln\frac{h_c}{b} \qquad \text{(Equation 23)}$$

where h_c is the critical thickness, b is the Burger vector, f is the misfit, θ is the angle between the Burger vector and dislocation line, and λ is the angle between the slip direction and the film plane direction[113],[112],[114].

Figure 102 shows the results of their calculations of the critical thickness[114]. To compare the In profile in Figure 53 for InGaN (555 °C), if it is assumed that 717 nm was a relaxation point where the In increased suddenly, the thickness was about 250 nm before that jump. The average In content was about 9.5%.

Using the curve of People and Bean in Figure 102 (red curve) which is usually closer to the experimental results, the critical thickness almost matches the In profile. On the other hand, at about 870 nm just before the second jump in composition, the critical thickness is about 66 nm with an average In composition of about 29%. Then, compared to the red curve, it is found to be higher than the critical thickness value from the curve (8 nm). This is attributed to the fact that these calculations are considering that InGaN is strained to the substrate (GaN) while in the graded layer that is not the case when it comes to the top layer away from the substrate. Therefore, only the first few layers would follow the relaxation models.

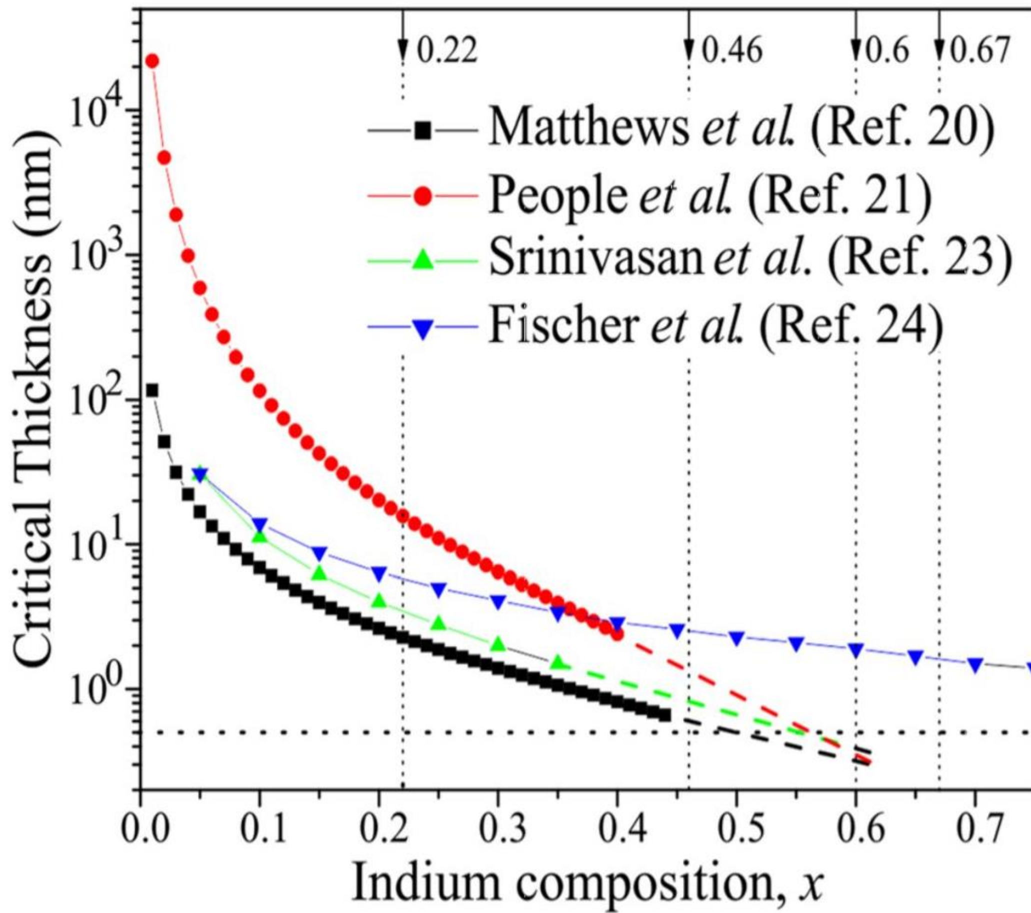

Figure 102. The critical thickness for graded InGaN vs. In composition from different theories.

The In profile for InGaN (475 °C) has a thickness of about 247 nm at an average In content of 7%. Comparing that In content to the People and Bean curve, the critical thickness is about 300 nm. These assumptions confirm that these points are relaxation events that occur as a result of the accumulated strain in the film that reached the dislocation energy.

Using nextnano^3 strain values for InGaN (555 °C) as a function of position that were extracted from Figure 103 and Equation 23, the critical thickness could be determined. Note that the Burgers vector that was used in the calculations was the lattice constant as an approximation.

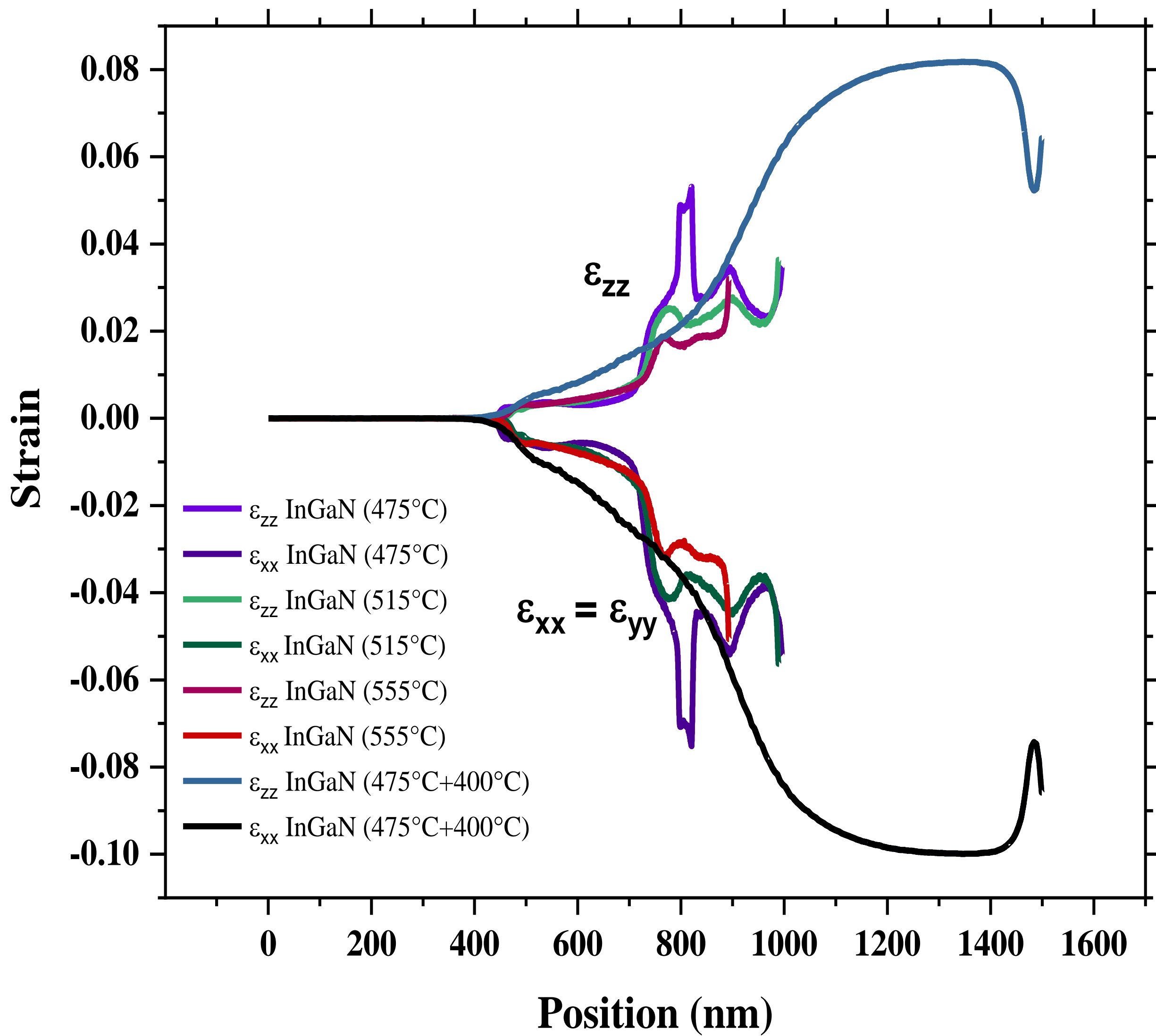

Figure 103. Simulation of strain component for graded InGaN.

The average critical thickness of the position 518 nm to 710 nm was 177 nm, and for positions 803 and 873 nm was 2 nm. The critical thickness that was calculated using nextnano[3] and the critical thickness from the People and Bean in Figure 102 were found to be comparable.

Table 14 shows the critical thickness calculated values. The blue shaded rows represent the points that are closer to GaN substrate before the jump in In composition. The grey shaded

rows represent the points with high In composition closer to the surface. The average was calculated for each two points.

Table 14. The critical thickness calculated values.

Position (nm)	In (%)	a (nm)	ν	ε_{xx}	hc (nm)
518	5	0.320	0.524	-0.0055	316
710	12	0.322	0.524	-0.0134	38
803	26	0.327	0.590	-0.0286	4
873	30	0.329	0.602	-0.0326	2

Chapter 7: Strain -RSM-Raman-Scattering Study of Graded $In_xGa_{1-x}N$ Thick Film

Raman scattering as well as x-ray reciprocal space mapping (RSM) were used to determine the InN mole fraction and strain relaxation.

7.1 Lattice Parameters and Composition (RSM)

The lattice parameters and In compositions could be determined through analysis of the x-ray reciprocal space maps (RSM). The measured coordinates Qx and Qz for each peak in the RSM were converted to the corresponding lattice constants of the wurtzite structure a and c using the following equations [102], [115], [116]:

$$a = -\left(\frac{8\pi}{3}\right) \times \frac{(h^2 + k^2)}{Qx} \quad \text{(Equation 24)}$$

$$c = 2\pi \times \frac{l}{Qz} \quad \text{(Equation 25)}$$

The XRD calculations of the measured in-plane "a" and out-of-plane "c" lattice parameters as well as the relaxed parameters $a_0(x)$ and $c_0(x)$ that were calculated using Vegard's law are presented in Table 14. These equations were used to calculate the in-plane ε_{xx} and out-of-plane strain ε_{zz} components:

$$\varepsilon_{zz} = \frac{[c - c_0(x)]}{c_0(x)} \quad \text{(Equation 26)}$$

$$\varepsilon_{xx} = \frac{[a - a_0(x)]}{a_0(x)} \quad \text{(Equation 27)}$$

Also, the relaxation degree was calculated using:

$$R = \frac{[a(L) - a_0(S)]}{[a_0(L) - a_0(S)]} \quad \text{(Equation 28)}$$

where (L) stands for the layer, a(L) is the measured and a_0 (L) is the relaxed lattice constant; and (S) stands for the substrate and a_0 (S) is the relaxed, in-plane lattice constant [117]. Table 15 shows the calculated in-plane and out-of-plane strain components and the relaxation degree in each sample for both top (TL) (the peak that was not strained to GaN) and bottom (BL) InGaN layers near the GaN peak.

Table 15. The converted lattice constants.

Sample	a measured (10^{-10} m)	c measured (10^{-10} m)	a relaxed (10^{-10} m)	c relaxed (10^{-10} m)	x%
InGaN (555 °C) BL	3.18	5.21	3.19	5.20	4
InGaN (555 °C) TL	3.26	5.42	3.30	5.35	33
InGaN (515 °C) BL	3.19	5.24	3.20	5.21	6.7
InGaN (515 °C) TL	3.31	5.44	3.32	5.39	41
InGaN (475 °C) BL	3.21	5.22	3.21	5.23	9
InGaN (475 °C) TL	3.37	5.44	3.36	5.44	50
InGaN (400 °C) BL	3.23	5.23	3.23	5.25	14
InGaN (400 °C) TL	3.53	5.69	3.53	5.69	100

Table 16. Strain and relaxation degree calculations.

Sample	x (%)	C_{13} (Pa)	C_{33} (Pa)	ε_z	ε_x	R (%)
InGaN (555 °C) BL	4	10.3×10^{10}	39.8×10^{10}	12.8×10^{-3}	-12.4×10^{-3}	9.92
InGaN (555 °C) TL	33	9.94×10^{10}	34.5×10^{10}	1.34×10^{-3}	-3.99×10^{-3}	65.26
InGaN (515 °C) BL	6.7	10.2×10^{10}	39.4×10^{10}	4.37×10^{-3}	-4.87×10^{-3}	26.50
InGaN (515 °C) TL	41	9.85×10^{10}	33.1×10^{10}	9.63×10^{-3}	-7.78×10^{-3}	82.35
InGaN (475 °C) BL	9	10.2×10^{10}	38.8×10^{10}	-0.923×10^{-3}	-2.00×10^{-3}	80.02
InGaN (475 °C) TL	50	9.75×10^{10}	31.5×10^{10}	0.864×10^{-3}	1.10×10^{-3}	100
InGaN (400 °C) BL	14	10.1×10^{10}	38×10^{10}	-3.81×10^{-3}	-0.811×10^{-3}	94.93
InGaN (400 °C) TL	100	9.20×10^{10}	22.4×10^{10}	-0.359×10^{-3}	-2.10×10^{-3}	98.13

As can be seen from Tables 15 and 16, the BL films all had low In concentrations and high strain (low relaxation value), while the TL films had high In concentrations and relatively low strain (high relaxation value), but overall, the In concentrations increased and the residual strain decreased as the growth temperature decreased.

In all cases, the in-plane strain component (ε_x) was negative, demonstrating compressive strain, except for the 475 °C sample. There the resulting sign was opposite, demonstrating tensile strain for the average material. This can be understood if there was a relaxed layer underneath a strained layer, which had lower In content.

Looking at SIMS result for the sample in Figure 55, there was a spike in In concentration (from 35% to 70%). Thus, the layer with high In content was relaxed and then the other layers grown on top with lower In content were under tensile strain due to the smaller lattice constants. The growth on smaller lattice constant led to compressive strain while the growth on larger lattice constant led to tensile strain[118]. The negative signs for out-of-plane strain component for the low temperature samples was a resulted of the big InGaN peak that results in an error.

Additionally, there were other contributions to the strained material from different layers in the growth. Thus, different points were taken for the peak position and then the average and standard deviations were calculated. For the graded InGaN (475 °C) BL (9% In), the average of out of plane strain was -1.19×10^{-3} and the standard deviation is 5.06×10^{-4}.

For full graded composition InGaN, the average for the out of plane strain in TL (100% In) was 4.62×10^{-4} and the standard deviation was 3.40×10^{-4}. On the other hand, the BL (14%) out-of-plane strain was -3.12×10^{-3} and the standard deviation was 7.30×10^{-4}.

Table 15 also shows the relaxation degree (R%) which increased with increased In content, which was expected as was observed in the RSM. The graded InGaN material was aligned on the relaxation line.

7.2 Raman Scattering for Graded InGaN:

The strain was evaluated again using room temperature Raman scattering which was used to analyze the surface of the graded layer. As previously stated in Chapter Three, in the back scattering configuration that was used in these experiments, only A1(LO) and E2 phonon modes were allowed[78], [119].

PL background was present as displayed in Figure 96 and has been subtracted in the following figures. Figure 105 shows Raman signal before PL background subtraction.

Figure 106 exhibits the phonon modes A1(LO) for the graded InGaN layers as well as a GaN template and InN that was grown on GaN for comparison. These data were all excited using a 632.8 nm HeNe laser. The spectra of GaN shows E_2 and A_1(LO) as demonstrated in Figure 104.

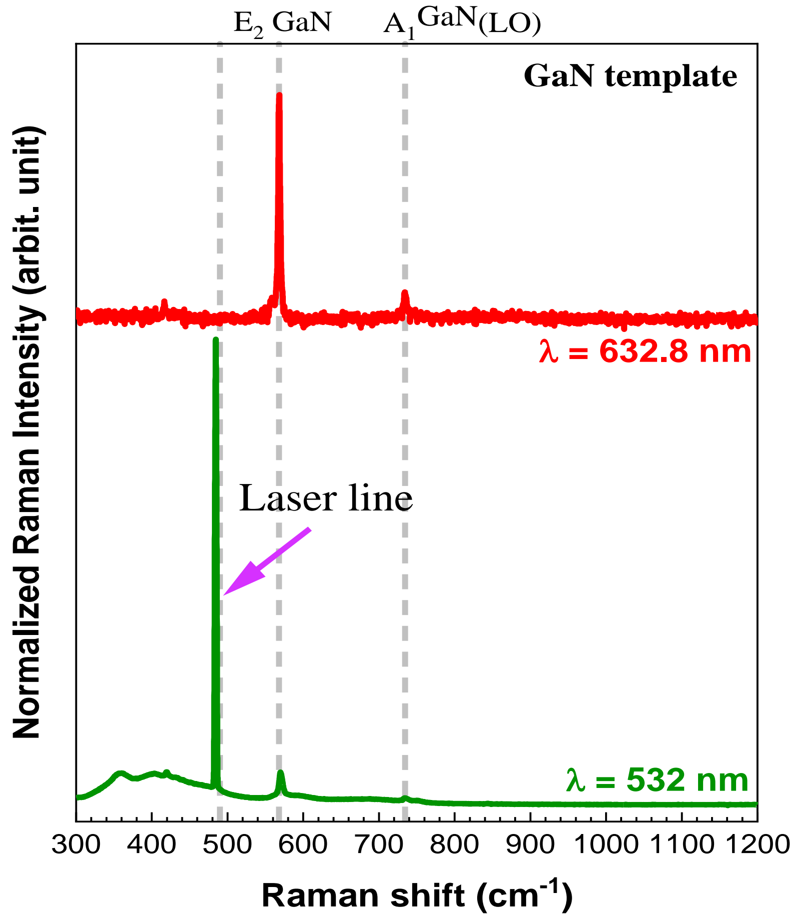

Figure 104. GaN template Raman spectra.

The frequency of A1(LO) phonon mode was blue shifted which indicated higher In content as the growth temperature decreased. This was in good agreement with all previous measurements. The broadening of the peak increased for higher In content as well which indicated there was In fluctuation that again confirmed the graded composition.

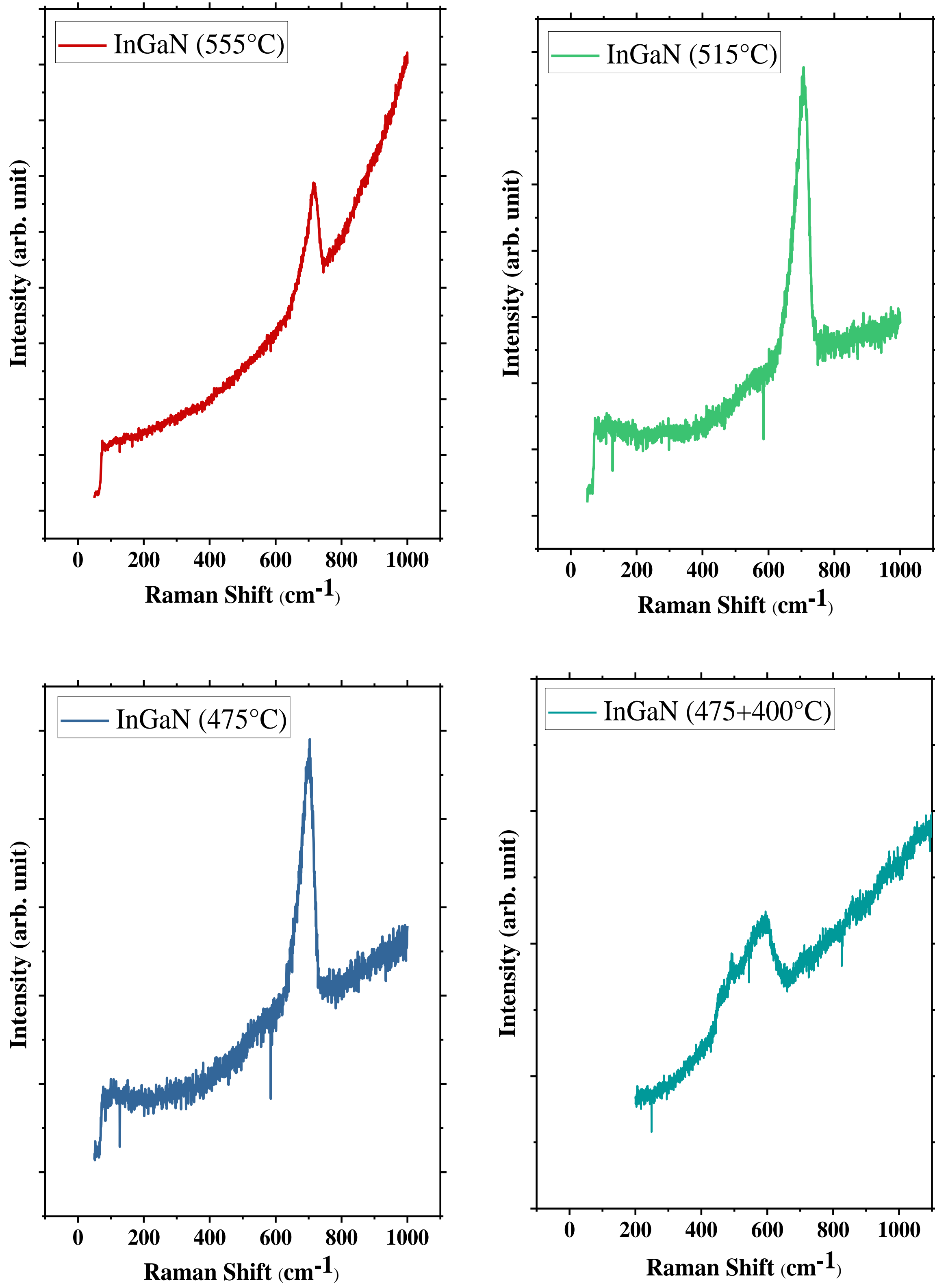

Figure 105. Raman scattering for graded InGaN excited with a 532 nm laser line.

.

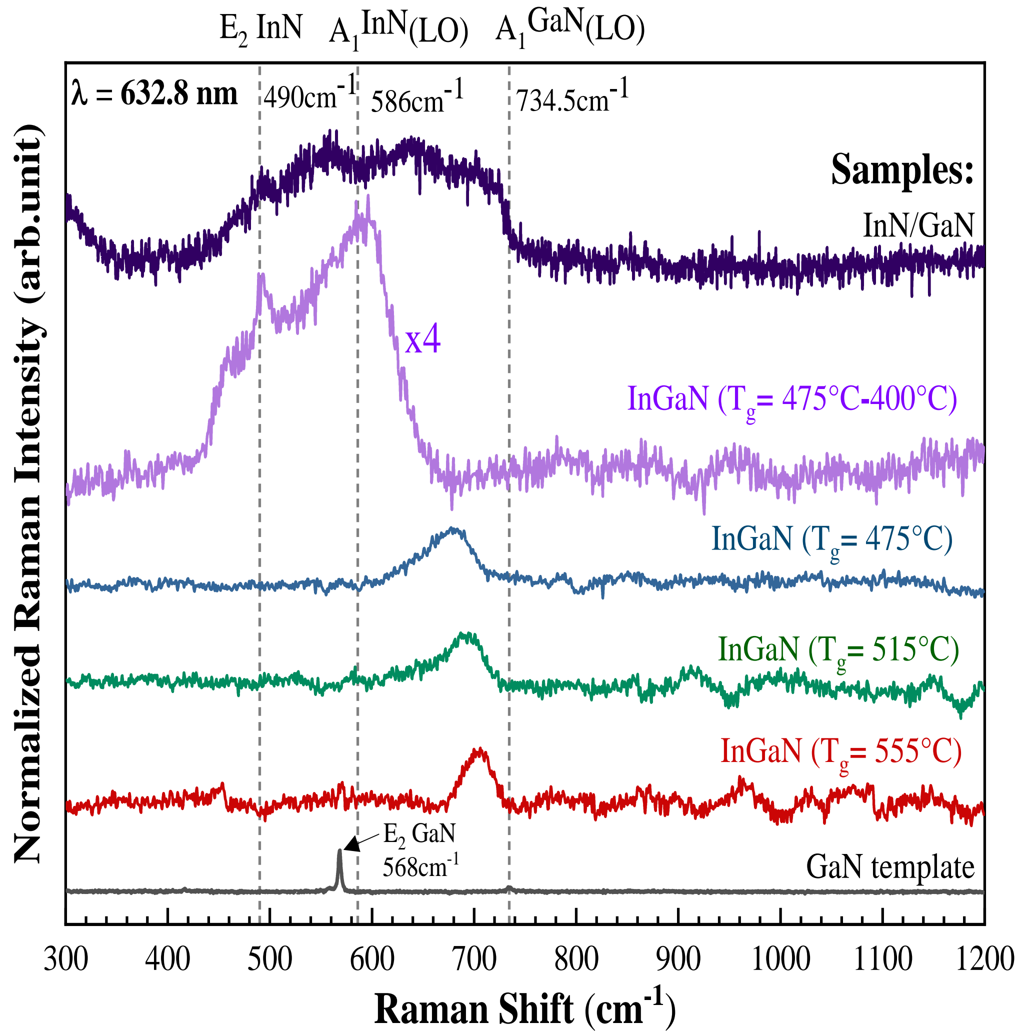

Figure 106. Room temperature Raman spectra of graded InGaN excited with a 632.8 nm laser.

Raman scattering was also performed using an excitation wavelength of 532 nm. Figure 107 shows the Raman spectra for the graded InGaN material with a similar behavior as the other wavelength. This was due to the penetration depth of the laser since the accumulation of In on the surface would absorb the laser before it penetrated further in the material. However, there were small variations in the A1(LO) frequencies as shown in Figure 110.

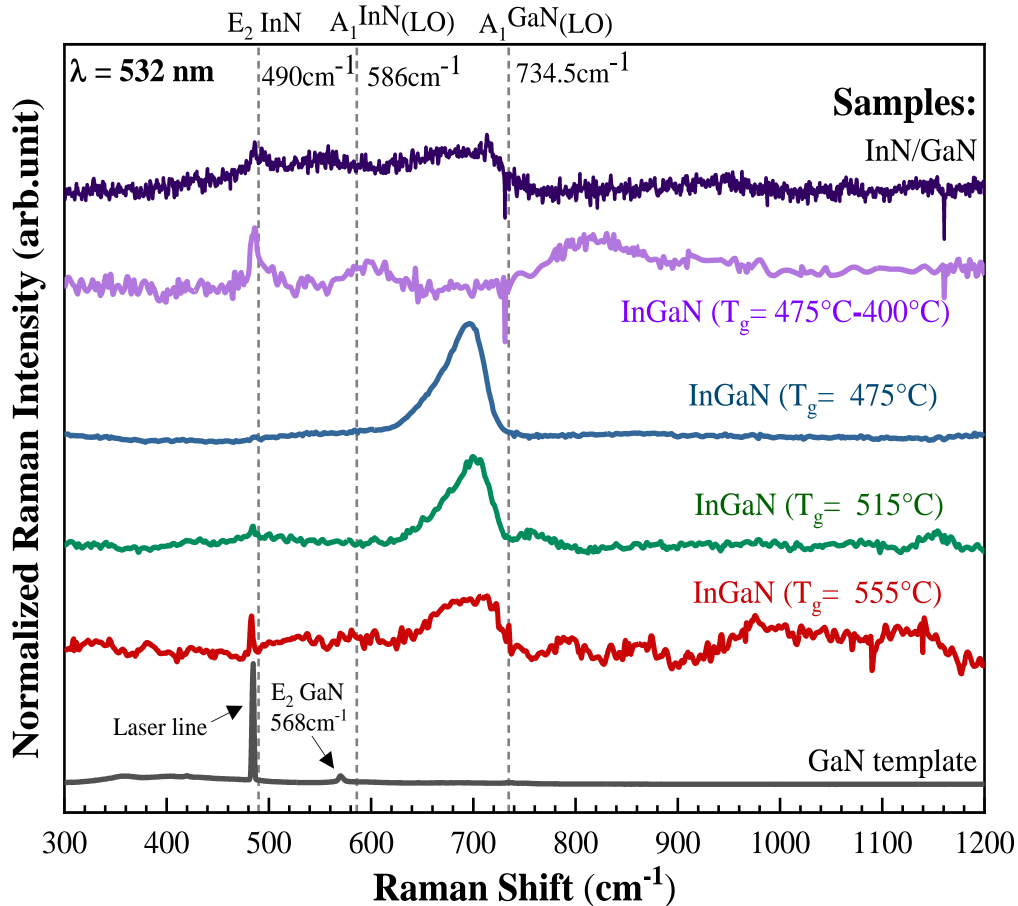

Figure 107. Raman spectra of graded InGaN excited with 532 nm laser.

To make it clear, Figure 109, and Figure 108show the full graded InGaN A1(LO) phonon peak and InN/GaN A1(LO) phonon peaks under the two excitation laser sources

Grille et al. studied the phonon modes of the ternary alloy and predicted one mode behavior for InGaN in wurtzite structure and modeled the mode behavior with composition with the Modified random-element isodisplacement (MREI) model[120]. This predicts a continuous and linear frequency relationship with composition, a "one mode behavior" for the A_1(LO) phonon mode. Figure 110 shows this relationship (dashed line) using the following equation along with the peak positions measured from Figure 106 and Figure 107[121]:

$$\omega_0(x) = (736\pm1) - (149\pm2)\,x \qquad \text{(Equation 29)}$$

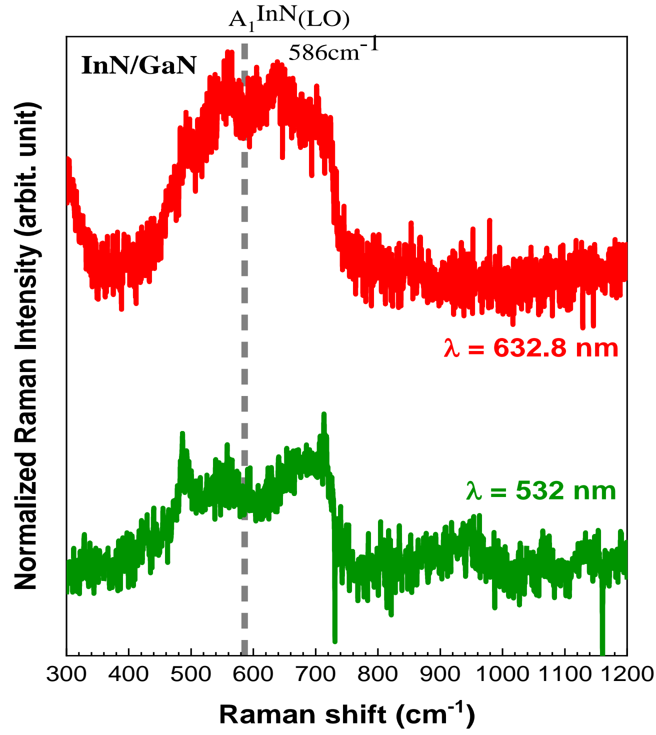

Figure 108. InN/GaN Raman spectra.

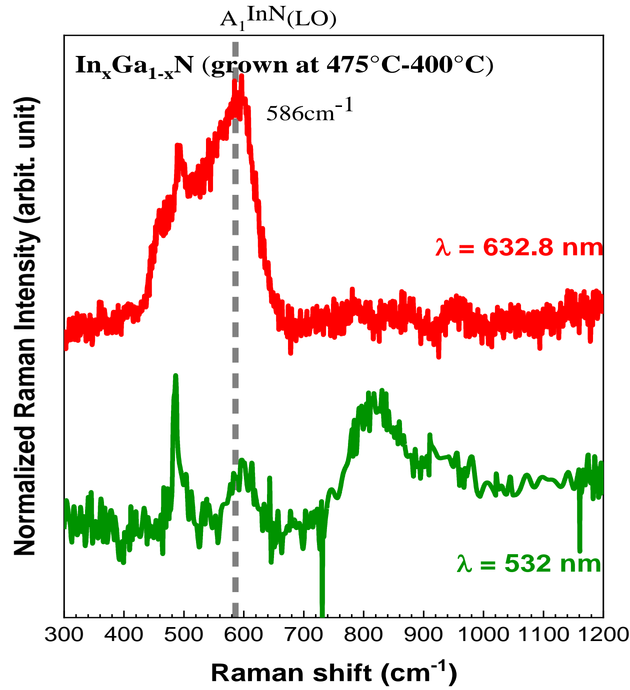

Figure 109. Full graded InGaN Raman spectra.

The frequencies of the A1(LO) modes detected using the green laser (532 nm) as excitation were slightly higher than those excited with the red laser (632.8 nm) as demonstrated in Figure 110. The difference in penetration depth of the two excitation sources could explain the result. The composition was different at different depths as well as the strain which resulted in a frequency shift.

Thus, it was important to consider the light attenuation to determine where the observed signal was coming from which depended on the band gap of the material. The penetration depth (h) of the green and red laser in InGaN was calculated in Table 17 and Table 18 using the absorption coefficient as a function of the wavelength ($\alpha(\lambda)$) as previously mentioned in Chapter Four for a UV laser.

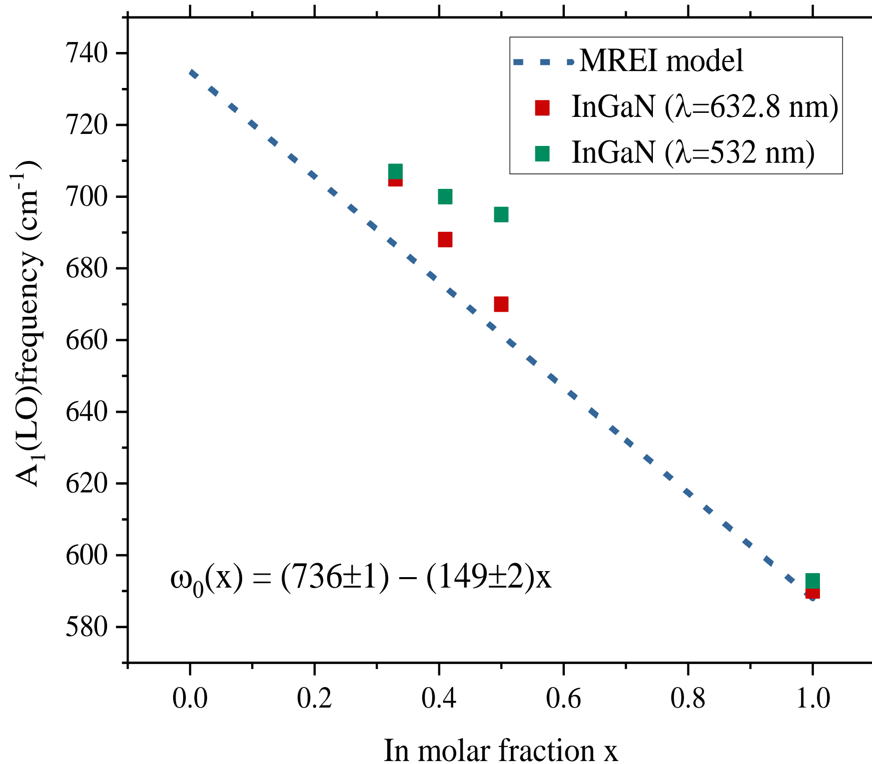

Figure 110. Measured frequency of the A_1(LO) phonon and the MREI model (dashed line).

Table 17. The penetration depth for 532 nm laser.

x	a_{fit}	b_{fit}	E_g (eV)	$E-E_g$ (eV)	α (cm^{-1})	Depth (cm)	Depth (nm)
0.30	0.74	0.29	2.29	0.04	17558.55	5.7×10^{-5}	569.52
0.32	0.68	0.34	2.22	0.11	27633.11	3.62×10^{-5}	361.88
0.34	0.64	0.38	2.16	0.17	34610.26	2.89×10^{-5}	288.93
0.36	0.60	0.42	2.09	0.23	40446.49	2.47×10^{-5}	247.24
0.38	0.58	0.46	2.04	0.29	45801.6	2.18×10^{-5}	218.33
0.40	0.56	0.49	1.97	0.35	50982.19	1.96×10^{-5}	196.15
0.42	0.55	0.53	1.92	0.41	56141.3	1.78×10^{-5}	178.12
0.44	0.54	0.56	1.86	0.47	61350.57	1.63×10^{-5}	162.99
0.46	0.53	0.59	1.80	0.53	66634.62	1.5×10^{-5}	150.07
0.48	0.53	0.61	1.75	0.58	71990.25	1.39×10^{-5}	138.91
0.50	0.53	0.64	1.69	0.64	77398.07	1.29×10^{-5}	129.20
0.60	0.57	0.72	1.44	0.89	104125.94	9.6×10^{-6}	96.04
0.70	0.61	0.74	1.21	1.12	127419.43	7.85×10^{-6}	78.48
0.80	0.64	0.71	1.01	1.32	144248.94	6.93×10^{-6}	69.32
0.90	0.65	0.62	0.84	1.49	153001.62	6.54×10^{-6}	65.35
1.00	0.68	0.47	0.70	1.63	153589.48	6.51×10^{-6}	65.11

Using Poisson's ratio, the strain could be determined using the following relationship:

$$\Delta\omega(x) = [2a - b\nu]\varepsilon_{xx}(x) \quad \text{(Equation 30)}$$

$$\nu = \frac{\varepsilon_{zz}(x)}{\varepsilon_{xx}(x)} \quad \text{(Equation 31)}$$

where $\Delta\omega(x) = \omega_{exp} - \omega_0$, (experimental Raman frequency - relaxed material frequency), a and b are deformation potential constants[122], [123], ν is Poisson's ratio, and $\varepsilon_{xx}(x)$ and $\varepsilon_{zz}(x)$ are in plane and out of plane strain components, respectively[121]. Table 19 shows the results of strain calculations for graded InGaN.

Table 18. The penetration depth for a 632.8 nm laser.

x	a_{fit}	b_{fit}	E_g (eV)	$E-E_g$ (eV)	α (cm^{-1})	Depth (cm)	Depth (nm)
0.42	0.55	0.53	1.92	0.04	15419.89	6.49×10^{-5}	648.51
0.44	0.54	0.56	1.86	0.10	24321.29	4.11×10^{-5}	411.16
0.46	0.53	0.59	1.80	0.16	31266.37	3.2×10^{-5}	319.83
0.48	0.53	0.61	1.75	0.21	37472.07	2.67×10^{-5}	266.87
0.50	0.53	0.64	1.69	0.27	43318.82	2.31×10^{-5}	230.85
0.60	0.57	0.72	1.44	0.52	70316.712	1.42×10^{-5}	142.21
0.70	0.61	0.74	1.21	0.75	93739.367	1.07×10^{-5}	106.67
0.80	0.64	0.71	1.01	0.95	111576.23	8.96×10^{-6}	89.62
0.90	0.65	0.62	0.84	1.12	122478.93	8.16×10^{-6}	81.65
1.00	0.68	0.47	0.70	1.26	126575.02	7.9×10^{-6}	79.00

Table 19. The measured Raman frequencies and the calculated strain components.

Sample	x (RSM) %	ω (cm^{-1})	ω_0 (cm^{-1})	ε_z	ε_x
InGaN(555 °C)	33	705	686.49	5.78×10^{-3}	-9.43×10^{-3}
InGaN(515 °C)	41	688	674.73	4.22×10^{-3}	-6.62×10^{-3}
InGaN(475 °C)	50	670	661.5	2.76×10^{-3}	-4.14×10^{-3}
InGaN(400 °C)	100	590	588	0.719×10^{-3}	-0.876×10^{-3}

The values of in-plane strain decreased as In content increased in the graded InGaN material. This matched the results in RSM strain calculations that had close values on the order of 10^{-3}.

7.2.1 Strain Corrected Frequency

Based on the in-plane and out-of-plane strain values from the XRD reciprocal space maps in Table 15, for high temperature growth the samples exhibited a higher degree of strain compared to the lower temperature sample (In-rich) material.

Also, it was observed in Figure 86 that only the fully relaxed sample that was grown at 400 °C followed the dashed line of the MREI model. Thus, the strain-free frequency had to be corrected for the measured A1(LO) frequencies and the out-of-plane strain values from XRD-RSM. Assuming biaxial strain as well as using the deformation potential that corresponds to the surface composition in each sample, the corrections were made using the following equation.

$$\omega_0(x) = \omega_{exp.} - \left(b_\lambda(x) - \frac{a_\lambda(x) C_{33}(x)}{C_{13}(x)}\right)\varepsilon_z \qquad \text{(Equation 32)}$$

where $a_\lambda(x)$ and $b_\lambda(x)$ are the composition dependent deformation potentials, C_{33} and C_{13} are elastic constants for the wurtzite structure that were found for each composition using Vegard's law, and ε_z is the out-of-plane strain[124]. The corrected frequencies are tabulated in Table 20.

Figure 111 shows the strain corrected values along with the uncorrected values for the 632.8 nm excitation. These correspond to the model very well indicating that the XRD and Raman measurements are self-consistent and that the graded InGaN layers are well behaved according to strain theory.

Table 20. The strain corrected frequency.

Sample	x%	A_1(LO) ω (cm^{-1})	A_1(LO) Corrected ω (cm^{-1})
InGaN(555 °C)	33	705	685.67
InGaN(515 °C)	41	688	674.08
InGaN(475 °C)	50	670	668.91
InGaN(400 °C)	100	590	589.92

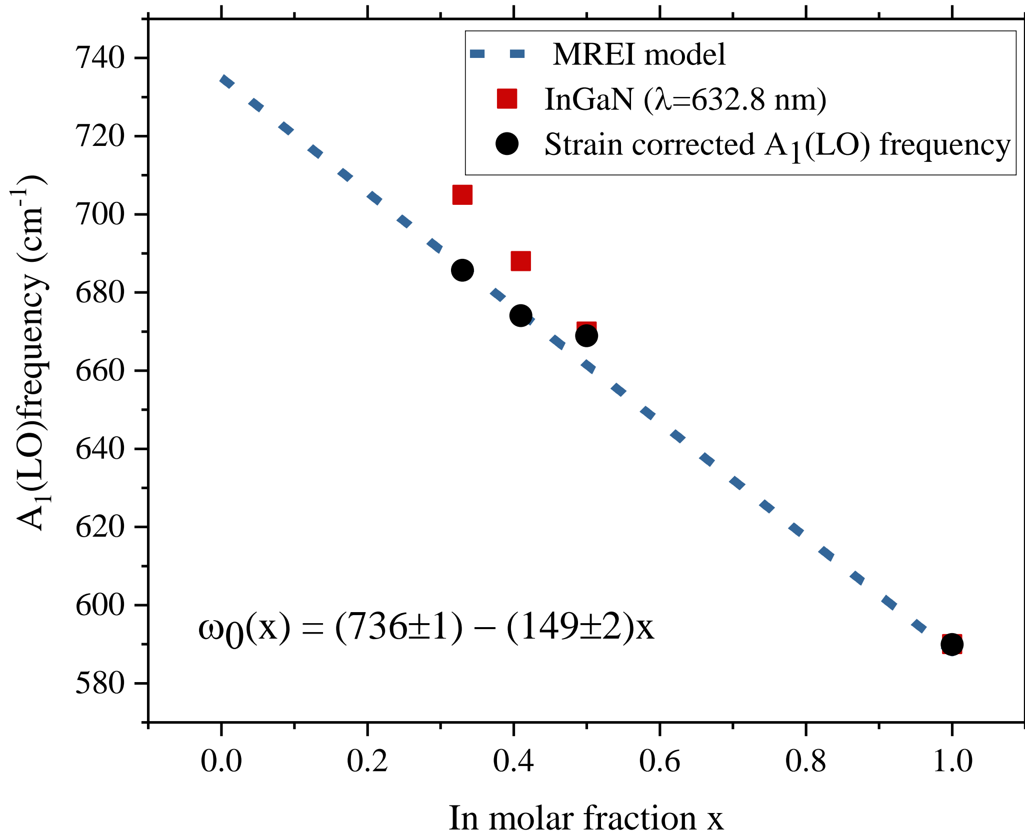

Figure 111. The strain corrected A1(LO) frequency.

Chapter 8: Preliminary Results for Future Work

This chapter demonstrates the results of a full graded composition solar cell device. It is important to note that the simulation showed insufficient polarization doping to get both p-type and n-type. nextnano[3] band diagram simulation showed n-type in the active layer with very small p- type material in the top layer. However, it was just a first attempt to examine how this material behaves as a solar cell. That attempt will help future work on this material.

MATLAB was used to calculate the optical generation rate for the full composition graded InGaN as well as the efficiency of the device. The parameters that were used are listed in Table 21 [62], [125]. The calculations were performed assuming a relaxed material.

Table 21. The parameters of GaN and InN that were used in the simulation.

Parameter	GaN	InN
Band gap E_g (eV)	3.4	0.7
Dielectric constant	8.9	10.5
Electron mass m_e/m_0	0.2	0.05
Hole mass m_h/m_0	1.25	0.6
Electron lifetime τ_e (ns)	1	1
Hole lifetime τ_h (ns)	1	1

The intrinsic carrier concentrations were calculated using the following equations[126], [127]:

$$n_i = (N_c N_v)^{\frac{1}{2}} \exp\left(\frac{-E_g}{2k_B T}\right) \qquad \text{(Equation 33)}$$

where N_c *and* N_v are the effective densities of states in the conduction band and valence band and can be found as follows:

For GaN: $$N_c = 4.3 \times 10^{14} \times T^{\frac{3}{2}}\ (cm^{-3})$$ (Equation 34)

$$N_v = 8.9 \times 10^{15} \times T^{\frac{3}{2}}\ (cm^{-3})$$ (Equation 35)

For InN: $$N_c = 1.76 \times 10^{14} \times T^{\frac{3}{2}}\ (cm^{-3})$$ (Equation 36)

$$N_v = 10^{16} \times T^{\frac{3}{2}}\ (cm^{-3})$$ (Equation 37)

The solar spectrum AM1.5 was used, and the absorption coefficient was calculated using Equation 17 in Chapter Four. The generation rate is defined as the intensity times the absorption coefficient.

$$G = \alpha \times I$$ (Equation 38)

Due to the multiple layers in the graded material with different absorption coefficients, the incident light intensity (I_0) will change as it passes each layer as demonstrated in Figure 112. Thus, for layer one, the generation rate is $G_1 = \alpha_1 \times I_1$, for layer two the generation rate is $G_2 = \alpha_2 \times I_2$, and so on.

The absorbed light must also be treated layer by layer. Therefore, the light intensity after layer one is $I_1 = I_0 e^{-\alpha_1 t}$ and the light intensity after layer two is $I_2 = I_1 e^{-\alpha_2 t} = I_0 e^{-\alpha_1 t} e^{-\alpha_2 t}$. This means that light intensity in layer N is:

$$I_N = I_0 e^{-\sum_0^n \alpha_i t}$$ (Equation 39)

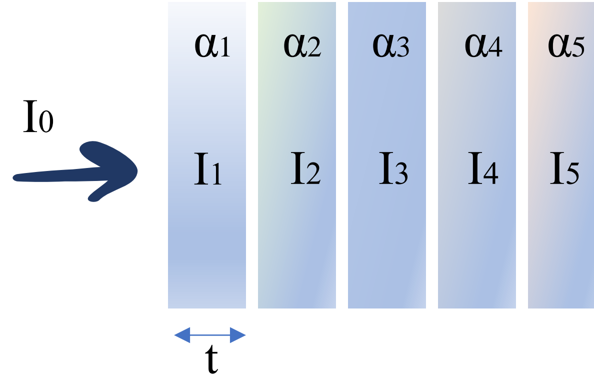

Figure 112. A schematic diagram for the light intensity passing through a graded material.

If each layer is then taken to go to zero thickness, the intensity at depth x can be given as a continuum:

$$I_0(x) = I_0 \exp\left[-\int_0^x \alpha(\grave{x})d\grave{x}\right] \qquad \text{(Equation 40)}$$

Thus, the generation rate at depth x:

$$G(x) = \alpha(x) I_0 \exp\left[-\int_0^x \alpha(\grave{x})d\grave{x}\right] \qquad \text{(Equation 41)}$$

The total generation rate, including wavelength dependence is:

$$G(x,\lambda) = \alpha(x,\lambda) I_0(\lambda) \exp\left[-\int_0^x \alpha(\grave{x},\lambda)d\grave{x}\right] \qquad \text{(Equation 42)}$$

Then integrating over wavelength and depth gives:

$$G_{Total} = \int_0^t \int_0^\infty G(x,\lambda)\ d\lambda\, dx \qquad \text{(Equation 43)}$$

where t is the total thickness of the film.

Figure 113 shows the composition profile of In that was simulated to get the optical generation

rate. The optical generation rate is displayed in Figure 114.

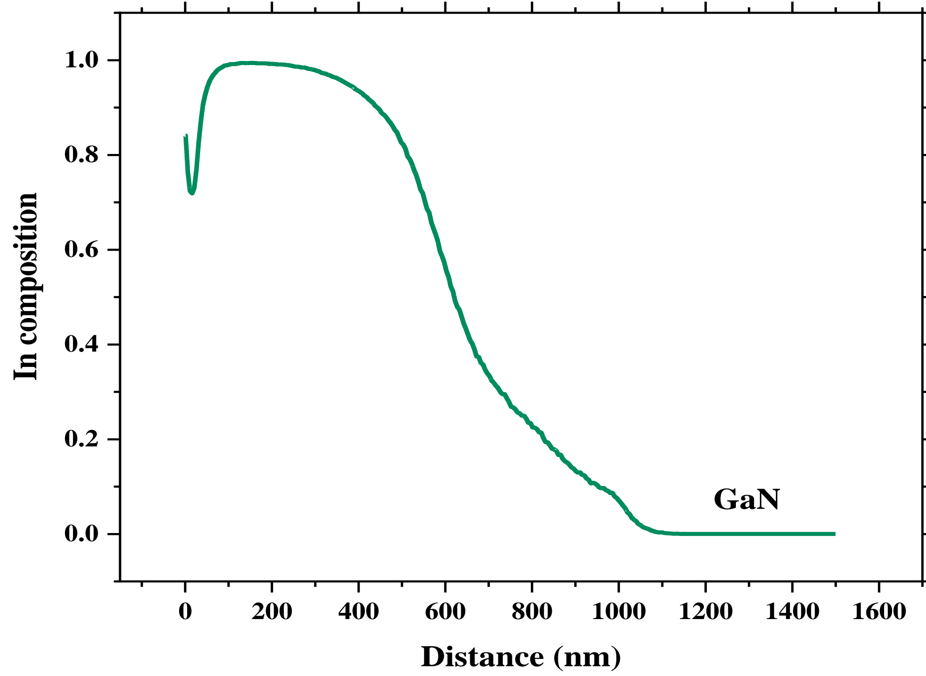

Figure 113. In profile from SIMS measurements.

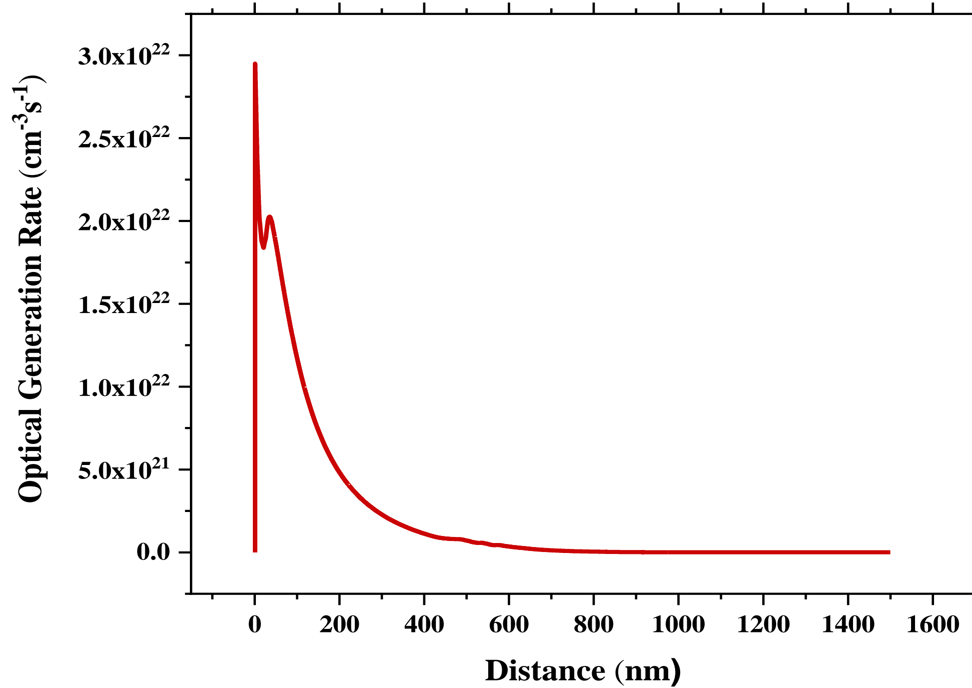

Figure 114. The optical generation rate in graded InGaN.

It is clear how the GaN layer generated few carriers while the optical generation rate increased with increasing In composition. This was a result of the AM1.5 spectrum which has only a small amount of light above the GaN band gap[62].

This simulation was done assuming the light was incident on the InN material first using the In profile in Figure 115. However, Figure 116 shows the calculated optical generation rate if the light is incident on the GaN substrate first.

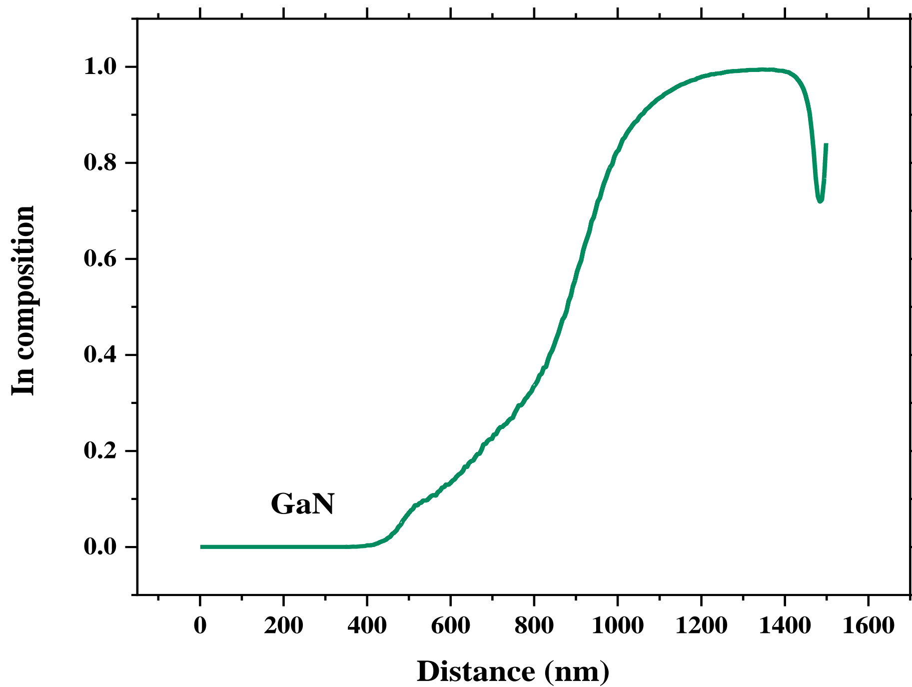

Figure 115. In profile from SIMS measurements.

8.1. Experimental details

The detailed steps for the fabrication of the solar cell device are as follows:

The sample was cleaned with acetone and methanol. Then, a positive photoresist was applied that is 7.71 μm thick.

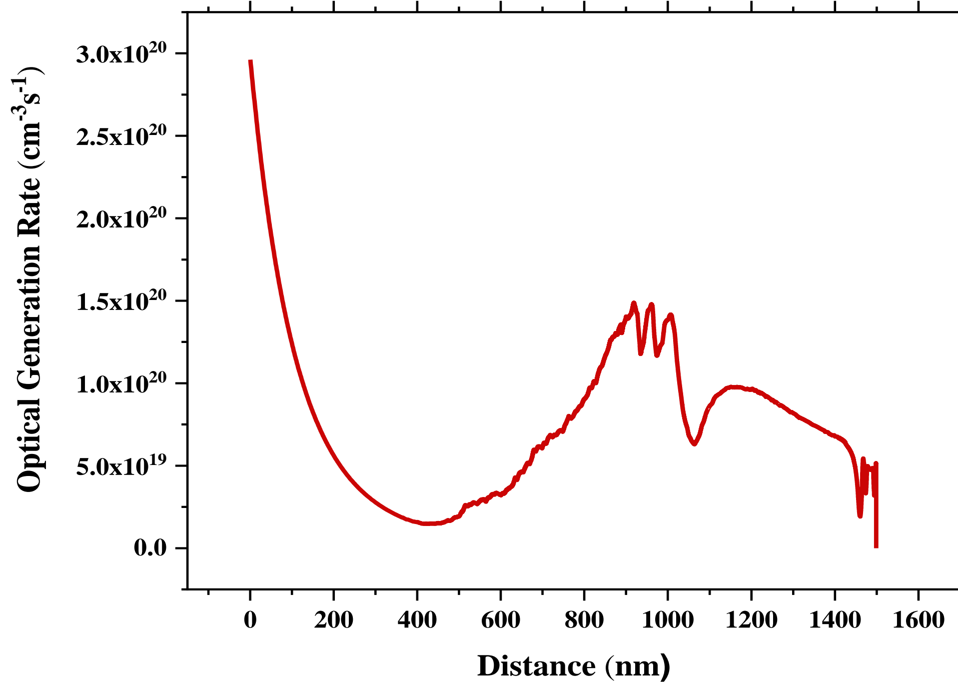

Figure 116. The optical generation rate in graded InGaN.

The sample after that was soft-backed, and the thickness of photoresist was confirmed using Dektak-3.

The mesa mask shown in Figure 117 was then mounted in the Karl Suss MJB-3 mask aligner followed by the sample mounted and aligned to the mask window. The exposure time (51 sec) was calculated using this equation:

$$\text{Exposure time} = \frac{\text{Exposure dose } \times \text{photoresist thickness}}{\text{lamp intensity}} \qquad \text{(Equation 44)}$$

After that, the sample was exposed to UV light and transferred to a developer (developed in AZ300MIF). Then, the sample was blow-dried using a dry N_2 gun. The optical microscope was used to see the developed pattern under bright field, white light illumination.

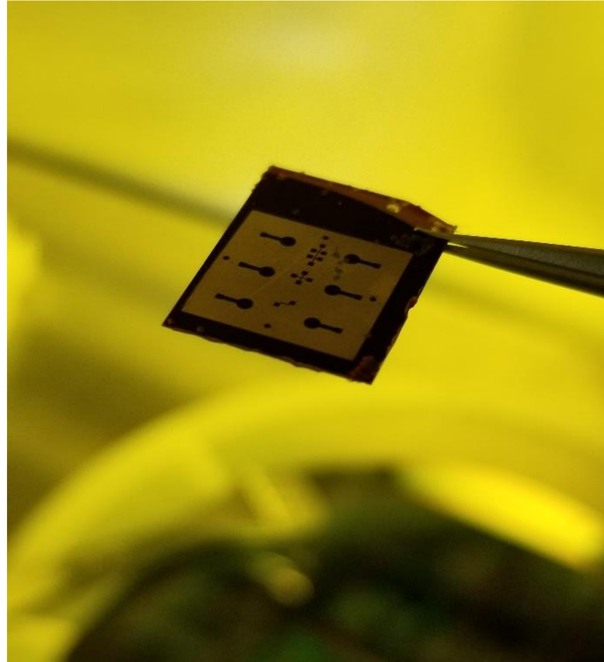

Figure 117. The mesa mask.

Again, Dektak-3 was employed to measure the photoresist thickness. The developed areas should not have any remaining resist.

The required time for InGaN etching (130 sec) was then calculated using the following equation:

$$\text{The required time to etch} = \frac{\text{The required thickness to etch}}{\text{etch rate}} \quad \text{(Equation 45)}$$

A dry etch was then performed (an etch rate of III-N is 6.36 nm/sec and the etch rate of photoresist is 8.79 nm/sec). The development of the structure was inspected in the optical microscope.

The positive photoresist was removed with acetone and methanol using a spin coater, and Dektak-3 was used to measure the etched depth. The samples were then ready for the top side and back side contacts. Positive photoresist (PR thickness 5.65 μm) was applied, and under a

contact mask in the Karl Suss mask aligner the sample was exposed to the UV light (37.5 sec).

After that, the sample was developed in a (AZ300MIF) developer to remove the exposed photoresist for about 2 minutes. The metal stack used for top contact (p- type) was: Ni/Au/Ni/Au (20/20/20/100) nm.

Then, the photoresist was lifted off of in an acetone bath (1 minute at 40°C). Similarly, the steps for the n-type contact were repeated. The metal stack used for back contact (n type) was: Ti/Al/Ti/Au (20/100/45/60) nm. [A schematic diagram illustrating these standard photolithography steps are presented below].

Figure 118 shows the contact mask that was designed to study the effect of different grid designs. The grid geometry has a great impact on the absorption of the light since it determines the loss due to shadowing in addition to the carrier lifetime.

The idea in this work was to have both top and back metal contacts on the top side (growth direction). Then, the light would be absorbed from the back side (the sapphire substrate).

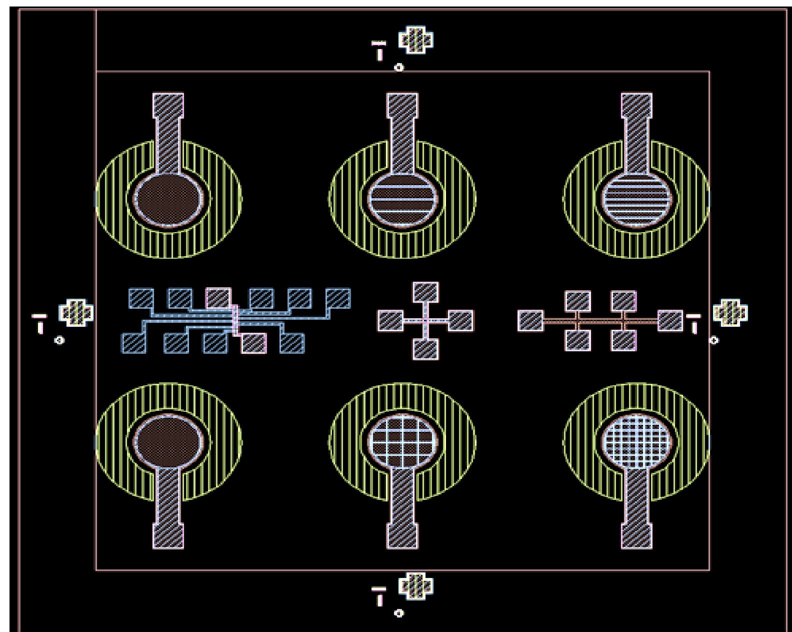

Figure 118. The contact mask.

However, this device was an initial attempt to study the device which will help make an optimized solar cell for future work.

Figure 119 shows the final device that was ready for electrical measurements after it was loaded in the chip carrier and wire bonded.

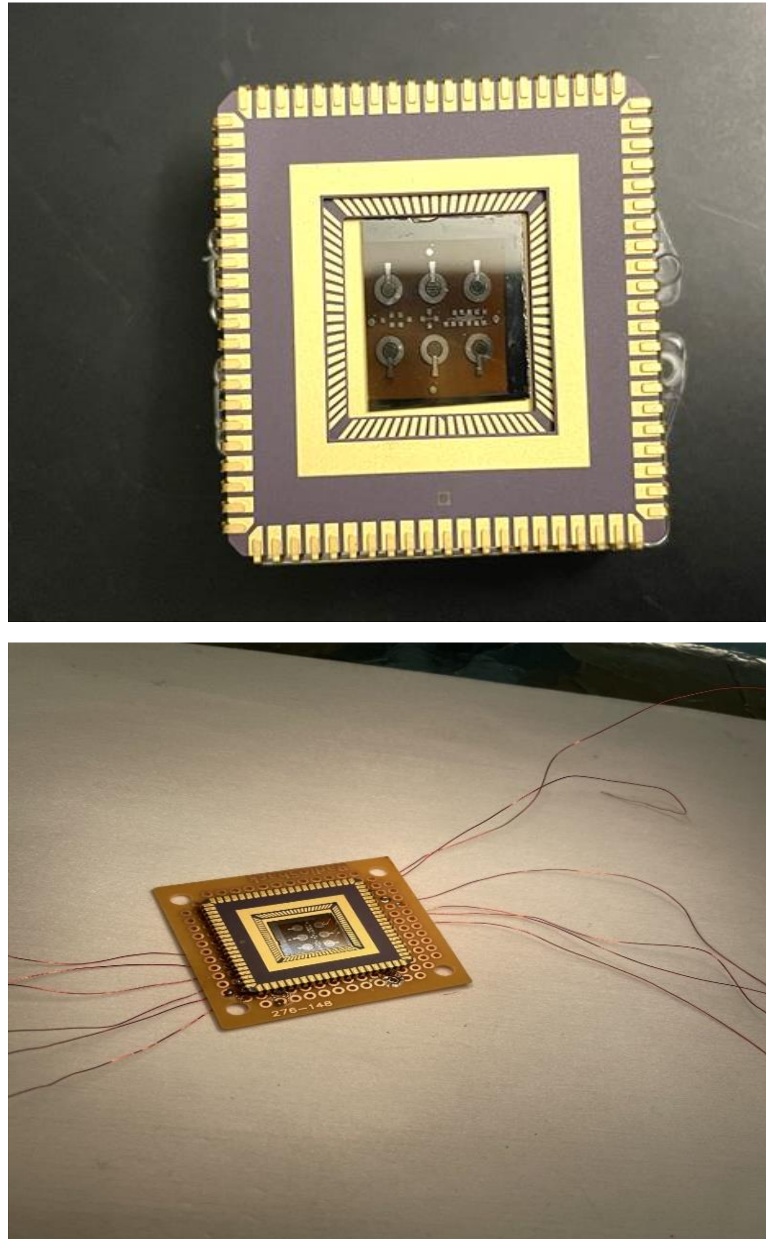

Figure 119. The graded InGaN device in a chip carrier.

8.2. Results and Discussions

The IV measurements were done using a solar simulator system that included a tungsten lamp light source. The light generated from the lamp and the intensity (1000 W/m^2) approximated the Air Mass 1.5 (AM1.5) spectra. The bias voltage was swept from -1 to 1 V using a Keithley system. The I-V curve as shown in Figure 120 under illumination and dark behaved like a photoresistor[128].

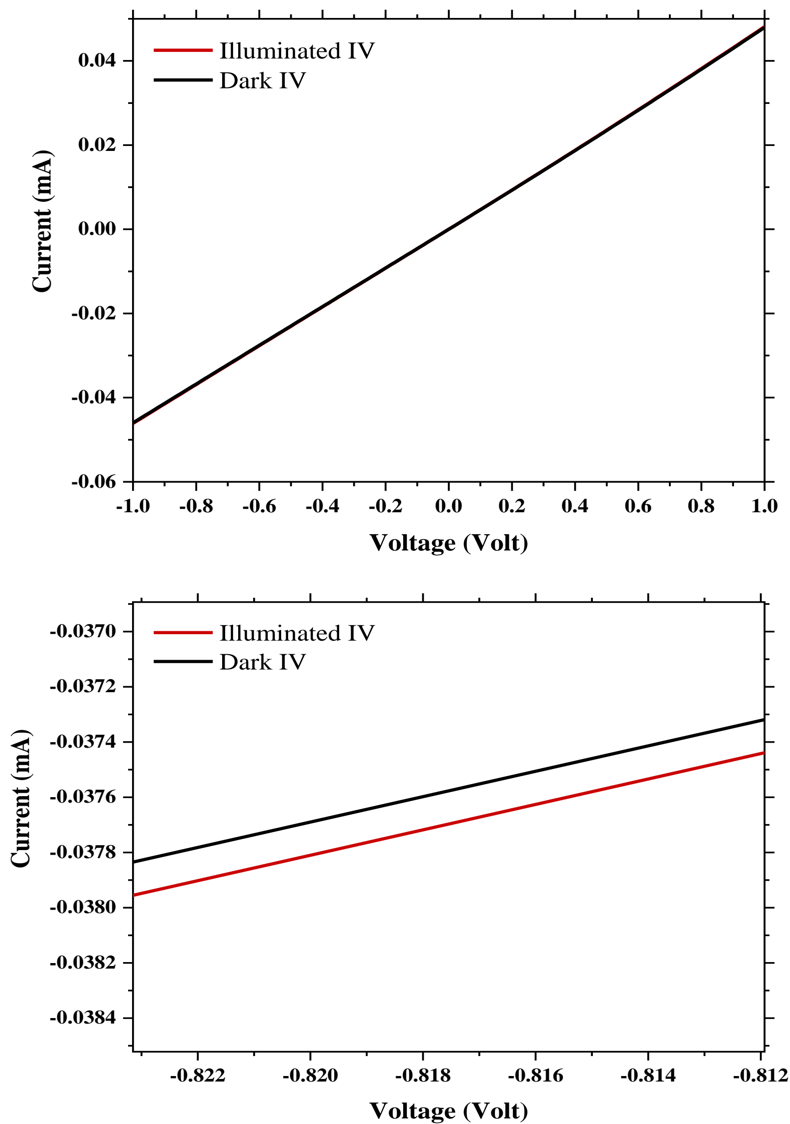

Figure 120. Current-voltage measurements of graded InGaN device under dark and illumination.

The photoresistor is a device that is used to detect the existence or lack of light as it is sensitive to the light[129].

The photocurrent is demonstrated in Figure 121, which is basically the current under illumination minus the current under dark. It shows that the device was generating a photocurrent, but only very weakly. The lack of a diode like an IV curve was attributed to multiple reasons in both material growth and fabrication process.

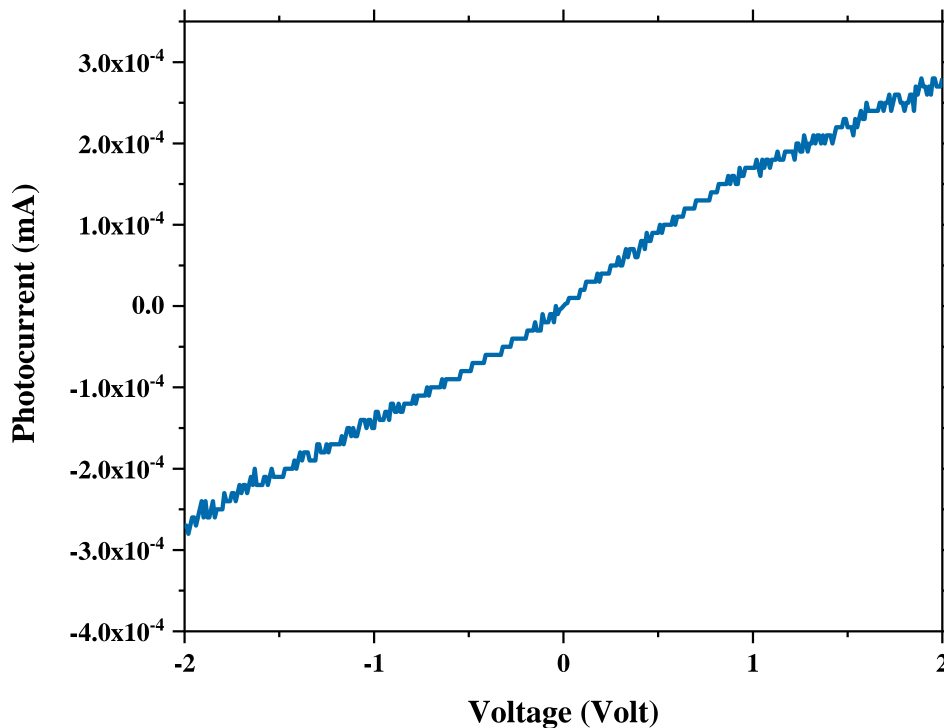

Figure 121. The photocurrent of graded InGaN.

Figure 122 shows the I-V curve first derivative. It can help to get some quantities when comparing the fitting equation to the non-ideal diode equation[130].

The non-ideal diode equation:

$$I = I_0 \left(e^{\frac{qv}{nKT}} - 1 \right) \quad \text{(Equation 46)}$$

$$\grave{I} = \frac{dI}{dV} = I_0 \frac{q}{nKT} e^{\frac{qV}{nKT}} = \frac{1}{R} e^{\frac{qV}{nKT}} \qquad \text{(Equation 47)}$$

The exponential fitting equation:

$$y = A\left(e^{bx}\right) \qquad \text{(Equation 48)}$$

Comparing the fitting equation to Equation 47:

$$A = I_0 \frac{q}{nKT} \qquad \text{(Equation 49)}$$

$$b = \frac{q}{nKT} \qquad \text{(Equation 50)}$$

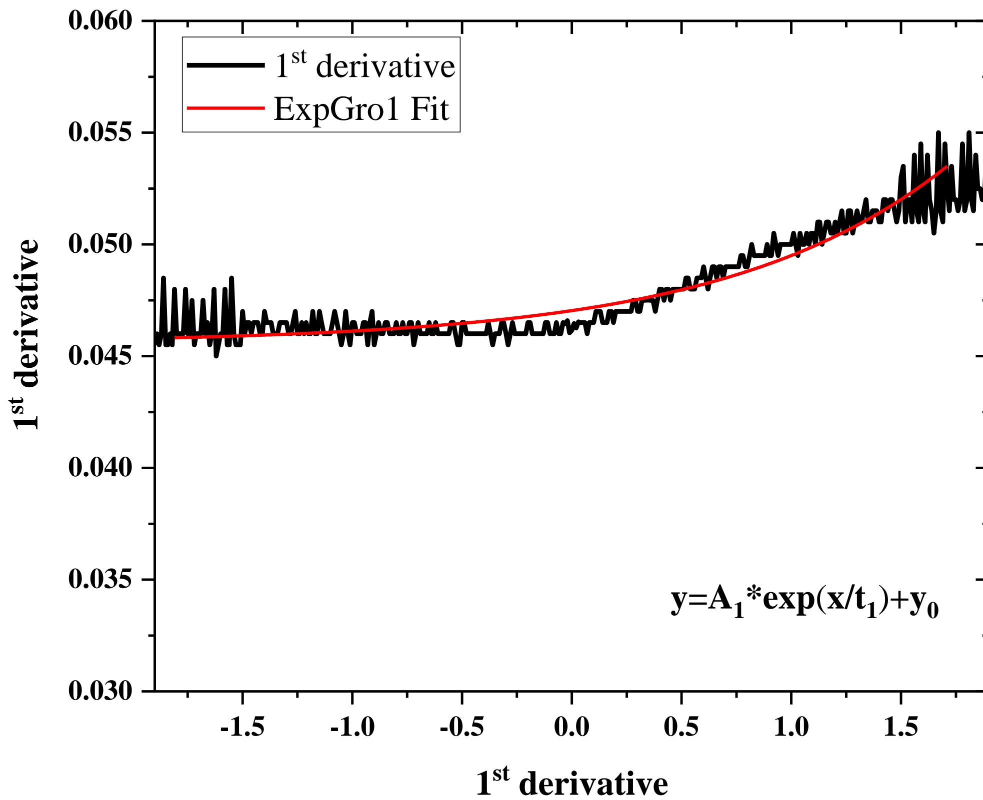

Figure 122. The IV curve first derivative.

Then, the ideality factor, n, was calculated and shown in Table 22. Ideality factors typically are between one and two. This is due to the carrier drift-diffusion process as well as the Sah–Noyce–Shockley generation-recombination process.

Table 22. The calculated ideality factor using IV curve measurements.

IV measurements	A1 (1/Ω)	t1 (V)	b=1/t1 (1/V)	n (unitless)	I_0 (A)	R (Ω)
IV -Illuminated	0.00146	1.01062	9.89E-01	39	9.21E+15	6.85E+02
IV-dark	0.00164	1.10804	0.902494	42.80	1.13E+16	609.7561

The competition between these two processes results in high ideality factor range. However, if the ideality factor is higher than two, it was is attributed to the current leakage and the trap assisted tunneling[131].

The calculated ideality factor was large for the illuminated and dark current measurements 39 and 42.80, respectively. The large ideality factor was connected in previous reports to the existence of a shunt resistance[131].

The external quantum efficiency measurement (EQE) was used to determine the device behavior at different wavelengths. It calculates the ratio of generated electrons to the number of incident photons. The measurements were taken at different bias voltages. The response or the EQE percentage was very weak and noisy.

Therefore, the EQE measurement was run without a sample to check these features in the spectra whether it was a result of the sample or the Xenon lamp spectra. As expected, the EQE response was similar for both cases with and without a sample as shown in Figure 123. However, the sample did demonstrate a significantly higher EQE signal than the background. Therefore,

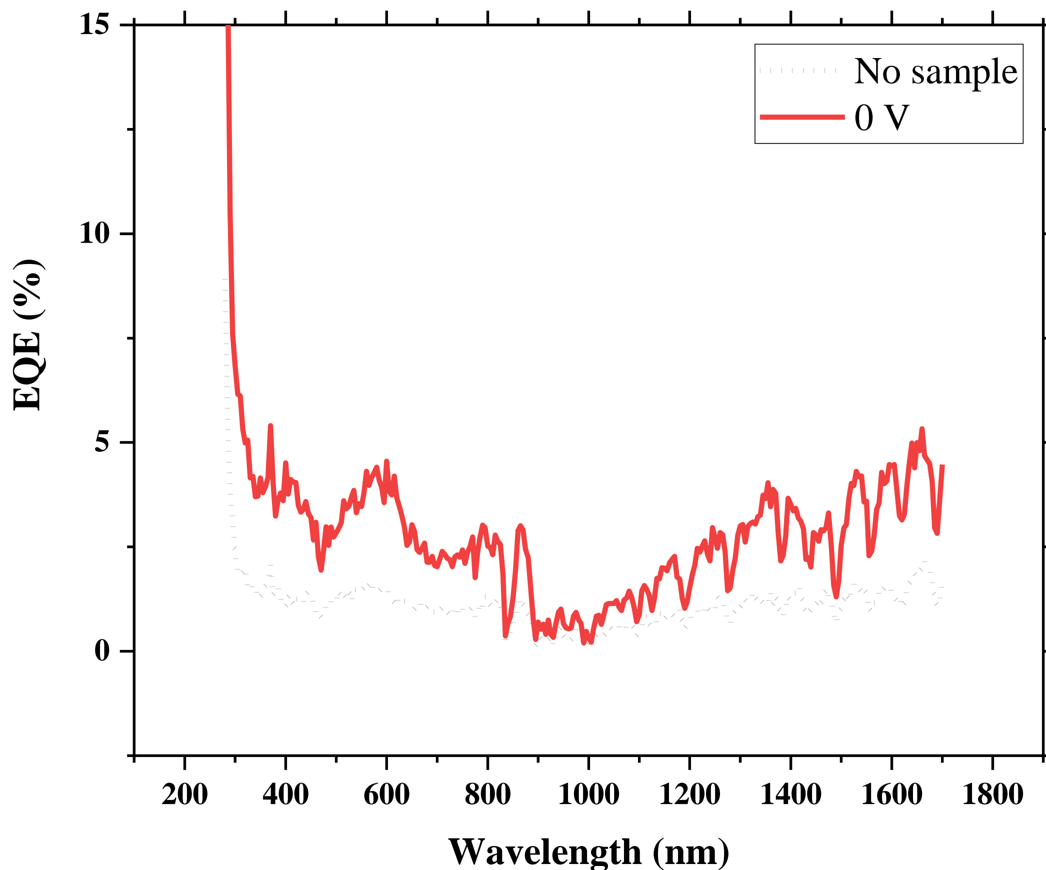

Figure 123. EQE spectrum for graded InGaN device.

the two scans were subtracted. Figure 124 shows the EQE for different wavelengths as an example at different bias voltages.

Based on these preliminary results, the device was not generating a photocurrent which could be as a result of a short in the device. Another important possible reason was that the polarization doping was not enough to create p-type and n- type as expected. Looking at the band diagram simulation and the carrier density in Chapter Five, it showed for the no strain case, the active layer was n- type instead of p- type while the surface is only very weakly p- type.

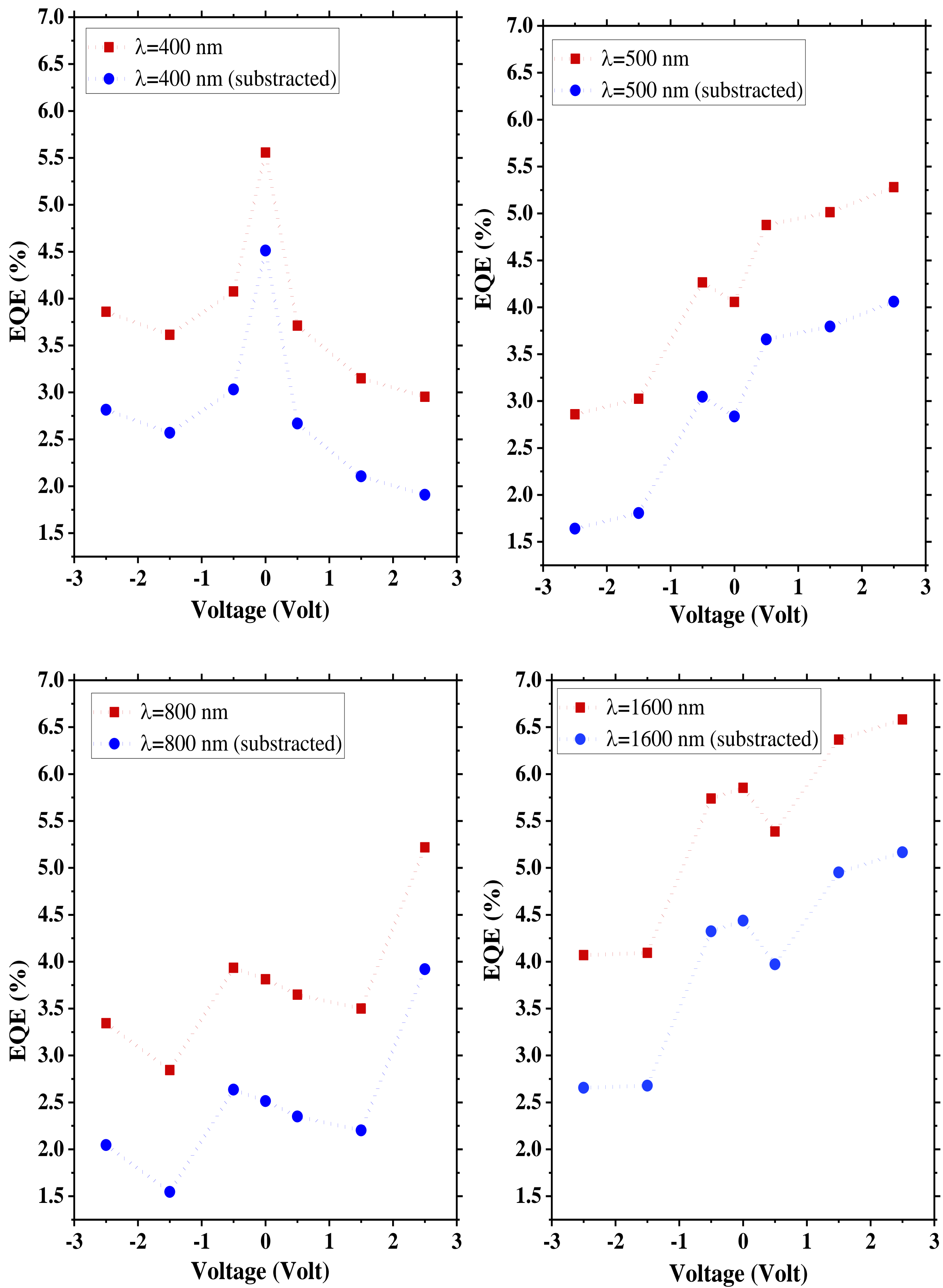

Figure 124. EQE for certain wavelength at different bias voltages.

8.3. Summary

Thick, compositionally graded InGaN films have been successfully grown on GaN templates by molecular beam epitaxy. By lowering the growth temperature from 555 °C to 475 °C, it was demonstrated that maximum indium compositions on the order of 50% through optical absorption and XRD RSMs were achieved. Photoluminescence artificially indicated much higher In content due to internal fields arising from the uncontrolled polarization doping. Additionally, PL showed no evidence for phase separation, in that it indicates single phase recombination in the power dependence, i.e., no state filling or quantum confined Stark effect. Generally, transmission or absorption measurements are deemed more useful to determine the composition of thin films, however, the ambiguity seen here as to where to define the bandgap made this technique difficult to interpret. The accumulation of In increased as the growth temperature decreased, as shown in optical microscope images and SEM. Additionally, SIMS measurements exhibited the concentration profile along the grown layer and revealed some interesting features that need more investigation and optimization of the growth parameters. None of the samples met the expected In profile except the full graded InGaN layer was almost linearly graded and reached 100% maximum In. However, all samples showed an increase in In content on the surface. TEM confirmed the graded composition through EDS as well as the contrast difference in the layers. Also, it showed almost 1100 nm graded InGaN thickness, which confirmed the planned growth thickness. A growth model was proposed to explain aspects of the SIMS In profile and the growth conditions. Furthermore, the band structure was simulated using ideal graded In composition and the real data that was extracted from SIMS measurements.

8.4. Conclusion

This dissertation was mainly focused on examining the graded InGaN material. The growth in MBE was performed at different growth temperatures and it was found that higher In concentration was incorporated as the growth temperature decreased. This was found and confirmed via optical and structural characterization. The optimal growth temperature to incorporate 50% In was 475 °C and the optimal growth temperature to incorporate 100% In was 400 °C. Additionally, the growth of full graded InGaN was achieved and confirmed using SIMS measurements. The optical properties of full graded InGaN showed InN band gap around 0.8 eV (92%) and 0.86 eV (88%). Moreover, the graded InGaN solar cell showed very small current in IV measurements, but the EQE measurements showed absorption in whole solar spectrum. Optimizations are required for future work.

8.5. Future work

Optimization of the growth conditions should be done as well as and growing full graded composition InGaN on a polished sapphire substrate in order to illuminate the graded structure from the back side of the grading, i.e., the GaN or high energy side. Polarization doping and doping enhancement needs to be investigated to get the p-type and n-type materials that are required to form a good p-n junction. Thus, introduction of Mg dopants is suggested for future work as well as optimizing the device fabrication process. Additionally, studies of the contact quality for higher efficiency is significant.

References

1. E. Gibney, “Nobel for blue LED that revolutionized lighting,” *Nature*, vol. 514, no. 7521. Nature Publishing Group, pp. 152–153, Oct. 07, 2014. doi: 10.1038/514152a.

2. J. Wu, W. Walukiewicz, W. Shan, K. M. Yu, J. W. Ager, S. X. Li, E. E. Haller, H. Lu, and W. J. Schaff, “Temperature dependence of the fundamental band gap of InN,” *J. Appl. Phys.*, vol. 94, no. 7, pp. 4457–4460, Oct. 2003, doi: 10.1063/1.1605815.

3. I. Vurgaftman and J. R. Meyer, “Band parameters for nitrogen-containing semiconductors,” *Journal of Applied Physics*, vol. 94, no. 6, *J. Appl. Phys.*, pp. 3675–3696, Sep. 15, 2003. doi: 10.1063/1.1600519.

4. Q. Wei, “Polarization Effects in Group III-Nitride Materials and Devices - NASA/ADS,” Arizona State University, 2012.,pp.3-4, Accessed: Jan. 07, 2021. [Online]. Available: https://ui.adsabs.harvard.edu/abs/2012PhD

5. R. A. Ferreyra, C. Zhu, A. Teke, and H. Morkoç, “Group III-nitrides,” in *Springer Handbooks*, Springer, 2017, p. 1. doi: 10.1007/978-3-319-48933-9_31.

6. D. Gregušová, M. Blaho, Š. Haščík, P. Šichman, A. Laurenčíková, A. Seifertová, J. Dérer, F. Brunner, J. Würfl, and J. Kuzmík,“Polarization-Engineered n^+GaN/InGaN/AlGaN/GaN Normally-Off MOS HEMTs,” *Phys. status solidi*, vol. 214, no. 11, p. 1700407, Nov. 2017, doi: 10.1002/pssa.201700407.

7. R. Collazo and N. Dietz, “CHAPTER 8. The Group III-Nitride Material Class: from Preparation to Perspectives in Photoelectrocatalysis,” in Photoelectrochemical Water Splitting: Materials, Processes and Architectures book, 2013, H. Lewerenz, L. Peter pp. 193–222. doi: 10.1039/9781849737739-00193, RSC publication.

8. W. Paszkowicz, S. Podsiadło, and R. Minikayev, “Rietveld-refinement study of aluminium and gallium nitrides,” in *Journal of Alloys and Compounds*, Nov. 2004, vol. 382, no. 1–2, pp. 100–106. doi: 10.1016/j.jallcom.2004.05.036.

9. A. Belabbes, J. Furthmüller, and F. Bechstedt, “Electronic properties of polar and nonpolar InN surfaces: A quasiparticle picture,” *Phys. Rev. B - Condens. Matter Mater. Phys.*, vol. 84, no. 20, p. 205304, Nov. 2011, doi: 10.1103/PhysRevB.84.205304.

10. F. Bernardini, V. Fiorentini, and D. Vanderbilt, “Spontaneous polarization and piezoelectric constants of III-V nitrides,” *Phys. Rev. B - Condens. Matter Mater. Phys.*, vol. 56, no. 16, pp. R10024–R10027, Oct. 1997, doi: 10.1103/PhysRevB.56.R10024.

11. S. Krishnamoorthy, D. N. Nath, F. Akyol, P. S. Park, M. Esposto, and S. Rajan, “Polarization-engineered GaN/InGaN/GaN tunnel diodes,” *Appl. Phys. Lett.*, vol. 97, no. 20, p. 203502, Nov. 2010, doi: 10.1063/1.3517481.

12. S. A. Kazazis, E. Papadomanolaki, and E. Iliopoulos, “Polarization-engineered InGaN/GaN solar cells: Realistic expectations for single heterojunctions,” *IEEE J.*

Photovoltaics, vol. 8, no. 1, pp. 118–124, Jan. 2018, doi: 10.1109/JPHOTOV.2017.2775164.

13. Y. J. Lee, Y. C. Yao, and Z. P. Yang, "Numerical Analysis on Polarization-Induced Doping III-Nitride n-i-p Solar Cells," *IEEE Photonics J.*, vol. 7, no. 1, Feb. 2015, doi: 10.1109/JPHOT.2015.2392374.

14. J. Simon, V. Protasenko, C. Lian, H. Xing, and D. Jena, "Polarization-induced hole doping in wide-band-gap uniaxial semiconductor heterostructures," *Science (80-.).*, vol. 327, no. 5961, pp. 60–64, Jan. 2010, doi: 10.1126/science.1183226.

15. Z. H. Zhang, S. Tiam Tan, Z. Kyaw, W. Liu, Y. Ji, Z. Ju, X. Zhang, X. Wei Sun, and H. Volkan Demir, "P-doping-free InGaN/GaN light-emitting diode driven by three-dimensional hole gas," *Appl. Phys. Lett.*, vol. 103, no. 26, p. 263501, Dec. 2013, doi: 10.1063/1.4858386.

16. Y. Enatsu, C. Gupta, S. Keller, S. Nakamura, and U. K. Mishra, "P-n junction diodes with polarization induced p-type graded in x Ga1-xN layer," *Semicond. Sci. Technol.*, vol. 32, no. 10, p. 105013, Sep. 2017, doi: 10.1088/1361-6641/aa89d7.

17. Y. Zhao, H. Fu, G. T. Wang, and S. Nakamura, "Toward ultimate efficiency: progress and prospects on planar and 3D nanostructured nonpolar and semipolar InGaN light-emitting diodes," *Adv. Opt. Photonics*, vol. 10, no. 1, p. 246, Mar. 2018, doi: 10.1364/aop.10.000246.

18. K. Hestroffer, F. Wu, H. Li, C. Lund, S. Keller, J. S. Speck, and U. K. Mishra, "Relaxed c-plane InGaN layers for the growth of strain-reduced InGaN quantum wells," *Semicond. Sci. Technol.*, vol. 30, no. 10, p. 105015, Sep. 2015, doi: 10.1088/0268-1242/30/10/105015.

19. D. Seidlitz, "Growth and characterization of InN and In-rich InGaN alloys by migration-enhanced plasma-assisted MOCVD", Technische Universitaet Berlin (Germany), August 2019, pp. 12.

20. R. Kour, S. Arya, S. Verma, A. Singh, P. Mahajan, and A. Khosla, " Review—Recent Advances and Challenges in Indium Gallium Nitride ($In_xGa_{1-x}N$) Materials for Solid State Lighting ," *ECS J. Solid State Sci. Technol.*, vol. 9, no. 1, p. 015011, Nov. 2020, doi: 10.1149/2.0292001jss.

21. V. Woods and N. Dietz, "InN growth by high-pressures chemical vapor deposition: Real-time optical growth characterization," *Mater. Sci. Eng. B Solid-State Mater. Adv. Technol.*, vol. 127, no. 2–3, pp. 239–250, Feb. 2006, doi: 10.1016/j.mseb.2005.10.032.

22. F. K. Yam and Z. Hassan, "InGaN: An overview of the growth kinetics, physical properties and emission mechanisms," *Superlattices and Microstructures*, vol. 43, no. 1. Academic Press, pp. 1–23, Jan. 01, 2008. doi: 10.1016/j.spmi.2007.05.001.

23. P. Waltereit, O. Brandt, K. H. Ploog, M. A. Tagliente, and L. Tapfer, “Indium Surface Segregation during Growth of (In,Ga)N/GaN Multiple Quantum Wells by Plasma-Assisted Molecular Beam Epitaxy,” *Phys. status solidi*, vol. 228, no. 1, pp. 49–53, Nov. 2001, doi: 10.1002/1521-3951(200111)228:1<49::AID-PSSB49>3.0.CO;2-C.

24. I. Ho and G. B. Stringfellow, “Solid phase immiscibility in GaInN,” *Appl. Phys. Lett.*, vol. 69, no. 18, pp. 2701–2703, Oct. 1996, doi: 10.1063/1.117683.

25. S. Y. Karpov, “Suppression of phase separation in InGaN due to elastic strain,” *MRS Internet J. Nitride Semicond. Res.*, vol. 3, no. 1, p. 16, Dec. 1998, doi: 10.1557/s1092578300000880.

26. A. Blakers, N. Zin, K. R. McIntosh, and K. Fong, “High efficiency silicon solar cells,” in *Energy Procedia*, Jan. 2013, vol. 33, pp. 1–10. doi: 10.1016/j.egypro.2013.05.033.

27. “9.10: Semiconductor p-n Junctions - Chemistry LibreTexts.” [Online]. Available: https://chem.libretexts.org/Courses/UWWhitewater/Chem_260%3A_Inorganic_Chemistry_(Girard)/09%3A_Electronic_Properties_of_Materials__Superconductors_and_Semiconductors/9.10%3A_Semiconductor_p-n_Junctions [Accessed May 17, 2021].

28. M. Aldawsari, “Epitaxial Growth of Silicon on Poly-Crystalline Si Seed layer at Low Temperature by Using Hot Wire Chemical Vapor Deposition,” *University of Arkansas, pp.*3, May 2015,

29. “IV Curve | PVEducation.” [Online]. Available: https://www.pveducation.org /pvcdrom/solar-cell-operation/iv-curve [Accessed May 17, 2021].

30. L. Solymar, D. Walsh, and R. R. A. Syms, *Principles of semiconductor devices*, vol. 1. Oxford University Press, 2018. doi: 10.1093/oso/9780198829942.003.0009.

31. “Radiative (Band-to-Band) Recombination - Engineering LibreTexts.” [Online]. Available: https://eng.libretexts.org/Bookshelves/Materials_Science /Supplemental_Modules_(Materials_Science)/Solar_Basics/C._Semiconductors_and_Solar_Interactions/IV._Recombination_of_Charge_Carriers/2._Radiative_(Band-to-Band)_Recombination [Accessed May 28, 2021].

32. A. McAllister, D. Bayerl, and E. Kioupakis, “Radiative and Auger recombination processes in indium nitride,” *Appl. Phys. Lett.*, vol. 112, no. 25, p. 251108, Jun. 2018, doi: 10.1063/1.5038106.

33. “Types of Recombination | PVEducation.” [Online]. Available: https://www.pveducation.org/pvcdrom/pn-junctions/types-of-recombination [Accessed May 28, 2021].

34. J. L. Gray, “The Physics of the Solar Cell,” in *Handbook of Photovoltaic Science and Engineering*, John Wiley & Sons, Ltd, 2005, pp. 61–112. doi: 10.1002/0470014008.ch3.

35. “Standard Solar Spectra | PVEducation.” [Online]. Available:https://www.pveducation.org /pvcdrom/appendices/standard-solar-spectra [Accessed May 28, 2021].

36. “Solar Cell Parameters | PVEducation.” [Online]. Available: https://www.pveducation.org /pvcdrom/solar-cell-operation/solar-cell-parameters [Accessed May 28, 2021].

37. “Parameters of a Solar Cell and Characteristics of a PV Panel.” [Online]. Available: https://www.electricaltechnology.org/2020/09/parameters-characteristics-solar-panel.html [Accessed May 28, 2021].

38. D. Holec, Y. Zhang, D. V. S. Rao, M. J. Kappers, C. McAleese, and C. J. Humphreys, “Equilibrium critical thickness for misfit dislocations in III-nitrides,” *J. Appl. Phys.*, vol. 104, no. 12, p. 123514, Dec. 2008, doi: 10.1063/1.3033553.

39. D. Holec, P. M. F. J. Costa, M. J. Kappers, and C. J. Humphreys, “Critical thickness calculations for InGaN/GaN,” *J. Cryst. Growth*, vol. 303, no. 1 SPEC. ISS., pp. 314–317, May 2007, doi: 10.1016/j.jcrysgro.2006.12.054.

40. S. Pereira, M. R. Correia, E. Pereira, K. P. O’Donnell, C. Trager-Cowan, F. Sweeney, and E. Alves, “Compositional pulling effects in $In_xGa_{1-x}N/GaN$ layers: A combined depth-resolved cathodoluminescence and Rutherford backscattering/channeling study,” *Phys. Rev. B*, vol. 64, no. 20, p. 205311, Nov. 2001, doi: 10.1103/PhysRevB.64.205311.

41. T. Paskova, V. Darakchieva, E. Valcheva, P. P. Paskov, B. Monemar, and M. Heuken, “Growth of GaN ona-plane sapphire: in-plane epitaxial relationships and lattice parameters,” *Phys. status solidi*, vol. 240, no. 2, pp. 318–321, Nov. 2003, doi: 10.1002/pssb.200303368.

42. T. B. Eldred, M. Abdelhamid, J. G. Reynolds, N. A. El-Masry, J. M. Lebeau, and S. M. Bedair, “Observing relaxation in device quality InGaN templates by TEM techniques,” *Appl. Phys. Lett.*, vol. 116, no. 10, p. 102104, Mar. 2020, doi: 10.1063/1.5139269.

43. A. G. Bhuiyan, K. Sugita, A. Hashimoto, and A. Yamamoto, “InGaN solar cells: Present state of the art and important challenges,” *IEEE J. Photovoltaics*, vol. 2, no. 3, pp. 276–293, 2012, doi: 10.1109/JPHOTOV.2012.2193384.

44. J. Yang, D. G. Zhao, D. S. Jiang, Z. S. Liu, P. Chen, L. Li, L. L. Wu, L. C. Le, X. J. Li, X. G. He, H. Wang, J. J. Zhu, S. M. Zhang, B. S. Zhang, and H. Yang, “Effects of polarization and p-type GaN resistivity on the spectral response of InGaN/GaN multiple quantum well solar cells,” *Chinese Phys. B*, vol. 23, no. 6, p. 068801, Apr. 2014, doi: 10.1088/1674-1056/23/6/068801.

45. K. Hiramatsu, N. A. Kawaguchi, Y.Shimizu, M.Sawaki, N.Zheleva, T.Davis, Robert F.Tsuda, H.Taki, W.Kuwano, and K. Oki, “The Composition Pulling Effect in MOVPE Grown InGaN on GaN and AlGaN and its TEM Characterization,” *MRS Internet Journal of Nitride Semiconductor Research (MIJ-NSR)*, 2014. 2, E6. doi:10.1557/S1092578300001320

46. A. Even, G. Laval, O. Ledoux, P. Ferret, D. Sotta, E. Guiot, F. Levy, I. C. Robin, and A. Dussaigne, “Enhanced In incorporation in full InGaN heterostructure grown on relaxed InGaN pseudo-substrate,” *Appl. Phys. Lett.*, vol. 110, no. 26, p. 262103, Jun. 2017, doi: 10.1063/1.4989998.

47. S. Kusanagi, Y. Kanitani, Y. Kudo, K. Tasai, A. A. Yamaguchi, and S. Tomiya, “InGaN quantum wells with improved photoluminescence properties through strain-controlled modification of the InGaN underlayer,” *Jpn. J. Appl. Phys.*, vol. 58, no. SC, p. SCCB28, May 2019, doi: 10.7567/1347-4065/ab0f11.

48. H. Saitoh, W. Utsumi, H. Kaneko, and K. Aoki, “The phase and crystal-growth study of group-III nitrides in a 2000°C at 20GPa region,” *J. Cryst. Growth*, vol. 300, no. 1, pp. 26–31, Mar. 2007, doi: 10.1016/j.jcrysgro.2006.10.201.

49. D. N. Nath, E. Gür, S. A. Ringel, and S. Rajan, “Growth model for plasma-assisted molecular beam epitaxy of N-polar and Ga-polar InxGa1−xN,” *J. Vac. Sci. Technol. B, Nanotechnol. Microelectron. Mater. Process. Meas. Phenom.*, vol. 29, no. 2, p. 021206, Mar. 2011, doi: 10.1116/1.3562277.

50. A. V. Lobanova, A. L. Kolesnikova, A. E. Romanov, S. Y. Karpov, M. E. Rudinsky, and E. V. Yakovlev, “Mechanism of stress relaxation in (0001) InGaN/GaN via formation of V-shaped dislocation half-loops,” *Appl. Phys. Lett.*, vol. 103, no. 15, p. 152106, Oct. 2013, doi: 10.1063/1.4824835.

51. T. B. Eldred, M. Abdelhamid, J. G. Reynolds, N. A. El-Masry, J. M. Lebeau, and S. M. Bedair, “Observing relaxation in device quality InGaN templates by TEM techniques,” *Appl. Phys. Lett.*, vol. 116, no. 10, p. 102104, Mar. 2020, doi: 10.1063/1.5139269.

52. C. Boney, I. Hernandez, R. Pillai, D. Starikov, A. Bensaoula, M. Henini, M. Syperek, J. Misiewicz, and R. Kudrawiec, “Growth and characterization of ingan for photovoltaic devices,” in *2010 35th IEEE Photovoltaic Specialists Conference*, Jun. 2010, pp. 003316–003321. doi: 10.1109/PVSC.2010.5617082.

53. B. R. Jampana, A. G. Melton, M. Jamil, N. N. Faleev, R. L. Opila, I. T. Ferguson, and C. B. Honsberg, “Design and Realization of Wide-Band-Gap (2.67 eV) InGaN p-n Junction Solar Cell,” *IEEE Electron Device Lett.*, vol. 31, no. 1, pp. 32–34, Jan. 2010, doi: 10.1109/LED.2009.2034280.

54. N. G. Young, R. M. Farrell, Y. L. Hu, Y. Terao, M. Iza, S. Keller, S. P. DenBaars, S. Nakamura, and J. S. Speck, “High performance thin quantum barrier InGaN/GaN solar cells on sapphire and bulk (0001) GaN substrates,” *Appl. Phys. Lett.*, vol. 103, no. 17, p. 173903, Oct. 2013, doi: 10.1063/1.4826483.

55. Y. Zhang, M. J. Kappers, D. Zhu, F. Oehler, F. Gao, and C. J. Humphreys, “The effect of dislocations on the efficiency of InGaN/GaN solar cells,” *Sol. Energy Mater. Sol. Cells*, vol. 117, pp. 279–284, Oct. 2013, doi: 10.1016/j.solmat.2013.06.022.

56. X. Zheng, L. Tang, D. Zhang, J. Dong, and H. Yang, “Effect of contact spreading layer on photovoltaic response of InGaN-based solar cells,” *Phys. status solidi*, vol. 208, no. 1, pp. 199–201, Jan. 2011, doi: 10.1002/pssa.201026289.

57. A. Mukhtarova, S. Valdueza-Felip, L. Redaelli, C. Durand, C. Bougerol, E. Monroy, and J. Eymery, “Dependence of the photovoltaic performance of pseudomorphic InGaN/GaN multiple-quantum-well solar cells on the active region thickness,” *Appl. Phys. Lett.*, vol. 108, no. 16, p. 161907, Apr. 2016, doi: 10.1063/1.4947445.

58. Y.-L. Tsai, S.-W. Wang, J.-K. Huang, L.-H. Hsu, C.-H. Chiu, P.-T. Lee, P. Yu, C.-C. Lin, and H.-C. Kuo, “Enhanced power conversion efficiency in InGaN-based solar cells via graded composition multiple quantum wells,” *Opt. Express*, vol. 23, no. 24, p. A1434, Nov. 2015, doi: 10.1364/OE.23.0A1434.

59. H. C. Lee, Y. K. Su, W. H. Lan, J. C. Lin, K. C. Huang, W. J. Lin, Y. C. Cheng, and Y. H. Yeh, “Study of Electrical Characteristics of GaN-Based Photovoltaics With Graded $In_xGa_{1-x}N$ Absorption Layer,” *IEEE Photonics Technol. Lett.*, vol. 23, no. 6, pp. 347–349, Mar. 2011, doi: 10.1109/LPT.2010.2103304.

60. C. A. M. Fabien, A. Maros, C. B. Honsberg, and W. A. Doolittle, “III-Nitride Double-Heterojunction Solar Cells With High In-Content InGaN Absorbing Layers: Comparison of Large-Area and Small-Area Devices,” *IEEE J. Photovoltaics*, vol. 6, no. 2, pp. 460–464, Mar. 2016, doi: 10.1109/JPHOTOV.2015.2504790.

61. X. T. Zheng, T. Wang, P. Wang, X. X. Sun, D. Wang, Z. Y. Chen, P. Quach, Y. X. Wang, X. L. Yang, F. J. Xu, Z. X. Qin, T. J. Yu, W. K. Ge, B. Shen, and X. Q. Wang, “Full-composition-graded InxGa1-xN films grown by molecular beam epitaxy,” *Appl. Phys. Lett.*, vol. 117, no. 18, p. 182101, Nov. 2020, doi: 10.1063/5.0021811.

62. G. F. Brown, J. W. Ager, W. Walukiewicz, and J. Wu, “Finite element simulations of compositionally graded InGaN solar cells,” *Sol. Energy Mater. Sol. Cells*, vol. 94, no. 3, pp. 478–483, Mar. 2010, doi: 10.1016/j.solmat.2009.11.010.

63. T. Xu, “LEDs based on III-nitride quantum dots and quantum wells grown by molecular beam epitaxy,” Boston University, 2007.p. 1879.

64. A. J. Ptak, “Principles of Molecular Beam Epitaxy,” in *Handbook of Crystal Growth: Thin Films and Epitaxy: Second Edition*, vol. 3, Elsevier Inc., 2015, pp. 161–192. doi: 10.1016/B978-0-444-63304-0.00004-4.

65. A. K. Bilgili, Ö. Akpınar, M. K. Öztürk, C. Başköse, S. Özçelik, and E. Özbay, “Investigation of structural, optical and morphological properties of InGaN/GaN structure,” *Appl. Phys. A Mater. Sci. Process.*, vol. 125, no. 1, p. 36, Jan. 2019, doi: 10.1007/s00339-018-2338-2.

66. “SolidSpec-3700i/3700iDUV - Features : SHIMADZU (Shimadzu Corporation).” [Online]. Available: https://www.shimadzu.com/an/products/molecular-spectroscopy/uv-vis/uv-vis-nir-spectroscopy/solidspec-3700i3700iduv/features.html [Accessed May 25, 2021].

67. “Selecting a CCD Camera for Spectroscopic Applications - HORIBA.” [Online]. Available: https://www.horiba.com/en_en/ccd-camera-spectroscopic-applications/ [Accessed May 25, 2021].

68. Rajiv Kohli and K.L. Mittal, “Chapter 3. Methods for Assessing Surface Cleanliness,” in *Developments in Surface Contamination and Cleaning, Volume 12*, Elsevier, 2019, pp. 23–105. doi: 10.1016/b978-0-12-816081-7.00003-6.

69. M. Kaliva and M. Vamvakaki, “Nanomaterials characterization,” in *Polymer Science and Nanotechnology*, Elsevier, 2020, pp. 401–433. doi: 10.1016/B978-0-12-816806-6.00017-0.

70. Chiu Soon Wong, “X-Ray Diffraction Techniques for Future Advanced CMOS Metrology Challenges,” Dublin City University, July 2013.p.20.

71. “Scanning Electron Microscopy (SEM).” [Online]. Available: https://serc.carleton.edu /research_education/geochemsheets/techniques/SEM.html (accessed May 28, 2021).

72. B. J. Inkson, “Scanning Electron Microscopy (SEM) and Transmission Electron Microscopy (TEM) for Materials Characterization,” in *Materials Characterization Using Nondestructive Evaluation (NDE) Methods*, Elsevier Inc., 2016, pp. 17–43. doi: 10.1016/B978-0-08-100040-3.00002-X.

73. K. Akhtar, S. A. Khan, S. B. Khan, and A. M. Asiri, “Scanning electron microscopy: Principle and applications in nanomaterials characterization,” in *Handbook of Materials Characterization*, Springer International Publishing, 2018, pp. 113–145. doi: 10.1007/978-3-319-92955-2_4.

74. “The Transmission Electron Microscope | CCBER.” [Online]. Available: https://www.ccber.ucsb.edu/ucsb-natural-history-collections-botanical-plant-anatomy/transmission-electron-microscope [Accessed May 28, 2021].

75. G. Binnig, C. F. Quate, and C. Gerber, “Atomic force microscope,” *Phys. Rev. Lett.*, vol. 56, no. 9, pp. 930–933, Mar. 1986, doi: 10.1103/PhysRevLett.56.930.

76. R. Kohli and K. L. Mittal, *Developments in Surface Contamination and Cleaning: Detection, Characterization, and Analysis of Contaminants*. Elsevier Inc., 2012. pp. 307-331, doi: 10.1016/C2009-0-64375-0.

77. “Atomic Force Microscopy - Nanoscience Instruments.” [Online]. Available: https://www.nanoscience.com/techniques/atomic-force-microscopy/ [Accessed Jun. 18, 2021].

78. S. Hernández, R. Cuscó, D. Pastor, L. Artús, K. P. O'Donnell, R. W. Martin, I. M. Watson, Y. Nanishi, and E. Calleja, "Raman-scattering study of the InGaN alloy over the whole composition range," *J. Appl. Phys.*, vol. 98, no. 1, p. 013511, Jul. 2005, doi: 10.1063/1.1940139.

79. Z. Zhang, Z. Xu, Y. Song, T. Liu, B. Dong, J. Liu, and H. Wang, "Interfacial stress characterization of GaN epitaxial layer with sapphire substrate by confocal Raman spectroscopy," *Nami Jishu yu Jingmi Gongcheng/Nanotechnology Precis. Eng.*, vol. 4, no. 2, p. 23002, Jun. 2021, doi: 10.1063/10.0003818.

80. "Growth and Characterization of InN and In-Rich InGaN Alloys by Migration-Enhanced Plasma-Assisted MOCVD- Daniel Seidlitz - Google Books." [Online]. Available: https://books.google.com/books/about/Growth_and_Characterization_of_InN_and_I.html?id=C7dRzQEACAAJ [Accessed May 10, 2021].

81. V. Y. Davydov, V. V. Emtsev, I. N. Goncharuk, A. N. Smirnov, V. D. Petrikov, V. V. Mamutin, V. A. Vekshin, S. V. Ivanov, M. B. Smirnov, and T. Inushima, "Experimental and theoretical studies of phonons in hexagonal InN," *Appl. Phys. Lett.*, vol. 75, no. 21, pp. 3297–3299, Nov. 1999, doi: 10.1063/1.125330.

82. V. Y. Davydov, Y. E. Kitaev, I. Goncharuk, A. Smirnov, J. Graul, O. Semchinova, and D. Uffmann, "Phonon dispersion and Raman scattering in hexagonal GaN and AlN," *Phys. Rev. B - Condens. Matter Mater. Phys.*, vol. 58, no. 19, pp. 12899–12907, Nov. 1998, doi: 10.1103/PhysRevB.58.12899.

83. "Secondary Ion Mass Spectrometer (SIMS)." [Online]. Available: https://serc.carleton.edu/msu_nanotech/methods/SIMS.html [Accessed May 28, 2021].

84. S. Birner, S. Hackenbuchner, M. Sabathil, G. Zandler, J. A. Majewski, T. Andlauer, T. Zibold, R. Morschl, A. Trellakis, and P. Vogl, "Modeling of semiconductor nanostructures with nextnano3," *Acta Phys. Pol. A*, vol. 110, no. 2, pp. 111–124, 2006, doi: 10.12693/APhysPolA.110.111.

85. "simulation-flow-control." [Online]. Available: https://www.nextnano.de/nextnano3/input_parser/keywords/simulation-flow-control.htm [Accessed May 16, 2021].

86. C. E. Dreyer, A. Janotti, C. G. Van de Walle, and D. Vanderbilt, "Correct implementation of polarization constants in wurtzite materials and impact on III-nitrides," *Phys. Rev. X*, vol. 6, no. 2, p. 021038, Jun. 2016, doi: 10.1103/PhysRevX.6.021038.

87. F. Bernardini, V. Fiorentini, and D. Vanderbilt, "Accurate calculation of polarization-related quantities in semiconductors," *Phys. Rev. B - Condens. Matter Mater. Phys.*, vol. 63, no. 19, Nov. 2000, doi: 10.1103/PhysRevB.63.193201.

88. X. Wang, S. Liu, N. Ma, L. Feng, G. Chen, F. Xu, N. Tang, S. Huang, K. J. Chen, S. Zhou, and B. Shen, “High-electron-mobility InN layers grown by boundary-temperature-controlled epitaxy,” *Appl. Phys. Express*, vol. 5, no. 1, p. 015502, Jan. 2012, doi: 10.1143/APEX.5.015502.

89. P. Lefebvre, T. Taliercio, A. Morel, J. Allègre, M. Gallart, B. Gil, H. Mathieu, B. Damilano, N. Grandjean, and J. Massies, “Effects of GaAIN barriers and of dimensionality on optical recombination processes in InGaN quantum wells and quantum boxes,” *Appl. Phys. Lett.*, vol. 78, no. 11, pp. 1538–1540, Mar. 2001, doi: 10.1063/1.1352664.

90. M. Azadmand, L. Barabani, S. Bietti, D. Chrastina, E. Bonera, M. Acciarri, A. Fedorov, S. Tsukamoto, R. Nötzel, and S. Sanguinetti, “Droplet Controlled Growth Dynamics in Molecular Beam Epitaxy of Nitride Semiconductors,” *Sci. Rep.*, vol. 8, no. 1, pp. 1–8, Dec. 2018, doi: 10.1038/s41598-018-28984-9.

91. “ZEISS Microscopy Online Campus | Microscopy Basics | Enhancing Contrast in Transmitted Light.” [Online]. Available: http://zeiss-campus.magnet.fsu.edu/ articles/basics/contrast.html [Accessed Jun. 26, 2021].

92. “ZEISS Microscopy Online Campus | Microscopy Basics | Reflected Light Microscopy.” [Online]. Available: http://zeiss-campus.magnet.fsu.edu/articles/basics/reflected.html [Accessed Jun. 26, 2021].

93. X. Zheng, H. Liang, P. Wang, X. Sun, Z. Chen, T. Wang, B. Sheng, Y. Wang, L. Chen, D. Wang, and others, “Effect of indium droplets on growth of InGaN film by molecular beam epitaxy,” *Superlattices Microstruct.*, vol. 113,pp. 650-656, 2018.

94. J. Wu, Z. M. Wang, A. Z. Li, M. Benamara, S. Li, and G. J. Salamo, “Nanoscale footprints of self-running gallium droplets on GaAs surface,” *PLoS One*, vol. 6, no. 6, p. 20765, 2011, doi: 10.1371/journal.pone.0020765.

95. A. Senichev, B. Dzuba, T. Nguyen, Y. Cao, M. A. Capano, M. J. Manfra, and O. Malis, “Impact of growth conditions and strain on indium incorporation in non-polar m-plane (10 1¯0) InGaN grown by plasma-assisted molecular beam epitaxy,” *APL Mater.*, vol. 7, no. 12, p. 121109, Dec. 2019, doi: 10.1063/1.5121445.

96. A. Khan, A. M. Toufiq, F. Tariq, Y. Khan, R. Hussain, N. Akhtar, and S. ur Rahman, “Influence of Fe doping on the structural, optical and thermal properties of α -MnO_2 nanowires,” *Mater. Res. Express*, vol. 6, no. 6, p. 065043, Mar. 2019, doi: 10.1088/2053-1591/ab0aaf.

97. T. Wang, B. Daiber, J. M. Frost, S. A. Mann, E. C. Garnett, A. Walsh, and B. Ehrler, “Indirect to direct bandgap transition in methylammonium lead halide perovskite,” Energy Environ. Sci., no.10, pp.509-515, 2016, doi: 10.1039/c6ee03474h.

98. A. F. Wright, K. Leung, and M. van Schilfgaarde, “Effects of biaxial strain and chemical ordering on the band gap of InGaN,” *Appl. Phys. Lett.*, vol. 78, no. 2, pp. 189–191, Jan. 2001, doi: 10.1063/1.1338490.

99. M. Hocker, P. Maier, L. Jerg, I. Tischer, G. Neusser, C. Kranz, M. Pristovsek, C. J. Humphreys, R. A. R. Leute, D. Heinz, O. Rettig, F. Scholz, and K. Thonke, “Determination of axial and lateral exciton diffusion length in GaN by electron energy dependent cathodoluminescence,” *J. Appl. Phys.*, vol. 120, no. 8, Aug. 2016, doi: 10.1063/1.4961417.

100. R. Belghouthi, S. Taamalli, F. Echouchene, H. Mejri, and H. Belmabrouk, “Modeling of polarization charge in N-face InGaN/GaN MQW solar cells,” *Mater. Sci. Semicond. Process.*, vol. 40, pp. 424–428, Jul. 2015, doi: 10.1016/j.mssp.2015.07.009.

101. H. Sun, Z. Ji, H. Wang, H. Xiao, S. Qu, X. Xu, A. Jin, and H. Yang, “Transfer and recombination mechanism of carriers in phase-separated InGaN quantum wells,” *J. Appl. Phys.*, vol. 114, no. 9, p. 093508, Sep. 2013, doi: 10.1063/1.4820395.

102. A. V. Kuchuk, H. V. Stanchu, C. Li, M. E. Ware, Y. I. Mazur, V. P. Kladko, A. E. Belyaev, and G. J. Salamo, “Measuring the depth profiles of strain/composition in AlGaN-graded layer by high-resolution x-ray diffraction,” *J. Appl. Phys.*, vol. 116, no. 22, p. 224302, Dec. 2014, doi: 10.1063/1.4904083.

103. A. V. Kuchuk, P. M. Lytvyn, C. Li, H. V. Stanchu, Y. I. Mazur, M. E. Ware, M. Benamara, R. Ratajczak, V. Dorogan, V. P. Kladko, A. E. Belyaev, and G. G. Salamo, “Nanoscale Electrostructural Characterization of Compositionally Graded $Al_xGa_{1-x}N$ Heterostructures on GaN/Sapphire (0001) Substrate,” *ACS Appl. Mater. Interfaces*, vol. 7, no. 41, pp. 23320–23327, Oct. 2015, doi: 10.1021/acsami.5b07924.

104. Y. Zhang, X. Zhou, S. Xu, Z. Wang, Z. Chen, J. Zhang, J. Zhang, and Y. Hao, “Effects of growth temperature on the properties of InGaN channel heterostructures grown by pulsed metal organic chemical vapor deposition,” *AIP Adv.*, vol. 5, no. 12, p. 127102, Dec. 2015, doi: 10.1063/1.4937127.

105. A. Alnami, “Studies of Initial Growth of GaN on InN,” *University of Arkansas.*, Dec. 2019, [Online]. Available:https://scholarworks.uark.edu/etd/3484 [Accessed: Jul. 09, 2021].

106. J. Wu, W. Walukiewicz, K. M. Yu, J. W. Ager III, E. E. Haller, H. Lu, and W. J. Schaff, “Indium nitride: a narrow gap semiconductor.” Aug. 14, 2002. [Online]. Available: https://escholarship.org/uc/item/8b75c2h3 [Accessed: Jul. 09, 2021].

107. S. Valdueza-Felip, E. Bellet-Amalric, A. Núñez-Cascajero, Y. Wang, M.-P. Chauvat, P. Ruterana, S. Pouget, K. Lorenz, E. Alves, and E. Monroy, “High In-content InGaN layers synthesized by plasma-assisted molecular-beam epitaxy: Growth conditions, strain relaxation, and In incorporation kinetics,” *J. Appl. Phys.*, vol. 116, no. 23, p. 233504, Dec. 2014, doi: 10.1063/1.4903944.

108. H. Chen, R. M. Feenstra, J. E. Northrup, J. Neugebauer, and D. W. Greve, “Indium incorporation and surface segregation during InGaN growth by molecular beam epitaxy,” MRS Internet Journal of Nitride Semiconductor Research, vol. 6, p. e11, 2001.

109. H. Naoi, M. Kurouchi, D. Muto, T. Araki, T. Miyajima, and Y. Nanishi, “Growth of high-quality In-rich InGaN alloys by RF-MBE for the fabrication of InN-based quantum well structures,” *J. Cryst. Growth*, vol. 288, no. 2, pp. 283–288, Mar. 2006, doi: 10.1016/j.jcrysgro.2005.12.008.

110. Q. Zhuang, “Molecular beam epitaxy (MBE) growth of nitride semiconductors,” in *Nitride Semiconductor Light-Emitting Diodes (LEDs): Materials, Technologies, and Applications: Second Edition*, Elsevier, 2018, pp. 3–23. doi: 10.1016/B978-0-08-101942-9.00001-0.

111. C. Adelmann, R. Langer, G. Feuillet, and B. Daudin, “Indium incorporation during the growth of InGaN by molecular-beam epitaxy studied by reflection high-energy electron diffraction intensity oscillations,” *Appl. Phys. Lett.*, vol. 75, no. 22, pp. 3518–3520, Nov. 1999, doi: 10.1063/1.125374.

112. R. People and J. C. Bean, “Calculation of critical layer thickness versus lattice mismatch for Ge xSi1-x/Si strained-layer heterostructures,” *Appl. Phys. Lett.*, vol. 47, no. 3, pp. 322–324, Jun. 1985, doi: 10.1063/1.96206.

113. S. M. Hu, “Misfit dislocations and critical thickness of heteroepitaxy,” *J. Appl. Phys.*, vol. 69, no. 11, pp. 7901–7903, Jun. 1991, doi: 10.1063/1.347476.

114. A. M. Fischer, Y. O. Wei, F. A. Ponce, M. Moseley, B. Gunning, and W. A. Doolittle, “Highly luminescent, high-indium-content InGaN film with uniform composition and full misfit-strain relaxation,” *Appl. Phys. Lett.*, vol. 103, no. 13, p. 131101, Sep. 2013, doi: 10.1063/1.4822122.

115. S. Pereira, M. R. Correia, E. Pereira, K. P. O’Donnell, E. Alves, A. D. Sequeira, N. Franco, I. M. Watson, and C. J. Deatcher, “Strain and composition distributions in wurtzite InGaN/GaN layers extracted from x-ray reciprocal space mapping,” *Appl. Phys. Lett.*, vol. 80, no. 21, pp. 3913–3915, May 2002, doi: 10.1063/1.1481786.

116. D. J. Wallis, D. Zhu, F. Oehler, S. P. Westwater, A. Pujol, and C. J. Humphreys, “Measuring the composition of AlGaN layers in GaN based structures grown on 150 mm Si substrates using (2 0 5) reciprocal space maps,” *Semicond. Sci. Technol.*, vol. 28, no. 9, p. 94006, Sep. 2013, doi: 10.1088/0268-1242/28/9/094006.

117. A. K. Bilgili, Ö. Akpinar, G. Kurtulus, M. K. Ozturk, S. Ozcelik, and E. Ozbay, “Structural properties of InGaN/GaN/Al2O3 structure from reciprocal space mapping,” *J. Mater. Sci. Mater. Electron.*, vol. 29, no. 14, pp. 12373–12380, Jul. 2018, doi: 10.1007/s10854-018-9351-2.

118. J. Han, M. H. Crawford, R. J. Shul, S. J. Hearne, E. Chason, J. J. Figiel, and M. Banas, “Monitoring and controlling of strain during MOCVD of AlGaN for UV optoelectronics,”

in *MRS Internet Journal of Nitride Semiconductor Research*, Dec. 1999, vol. 4, no. SUPPL. 1, pp. 811–816. doi: 10.1557/s109257830000346x.

119. Y. Zeng, J. Ning, J. Zhang, Y. Jia, C. Yan, B. Wang, and D. Wang, “Raman analysis of e2 (High) and a1 (lo) phonon to the stress-free gan grown on sputtered aln/graphene buffer layer,” *Appl. Sci.*, vol. 10, no. 24, pp. 1–12, Dec. 2020, doi: 10.3390/app10248814.

120. H. Grille, C. Schnittler, and F. Bechstedt, “Phonons in ternary group-III nitride alloys,” *Phys. Rev. B - Condens. Matter Mater. Phys.*, vol. 61, no. 9, pp. 6091–6105, Mar. 2000, doi: 10.1103/PhysRevB.61.6091.

121. M. R. Correia, S. Pereira, E. Pereira, J. Frandon, and E. Alves, “Raman study of the A1(LO) phonon in relaxed and pseudomorphic InGaN epilayers,” *Appl. Phys. Lett.*, vol. 83, no. 23, pp. 4761–4763, Dec. 2003, doi: 10.1063/1.1627941.

122. J. M. Wagner and F. Bechstedt, “Phonon deformation potentials of α-GaN and -AlN: An ab initio calculation,” *Appl. Phys. Lett.*, vol. 77, no. 3, pp. 346–348, Jul. 2000, doi: 10.1063/1.127009.

123. X. Wang, S. B. Che, Y. Ishitani, and A. Yoshikawa, “Experimental determination of strain-free Raman frequencies and deformation potentials for the E2 high and A1(LO) modes in hexagonal InN,” *Appl. Phys. Lett.*, vol. 89, no. 17, p. 171907, Oct. 2006, doi: 10.1063/1.2364884.

124. R. Oliva, J. Ibáñez, R. Cuscó, R. Kudrawiec, J. Serafinczuk, O. Martnez, J. Jiménez, M. Henini, C. Boney, A. Bensaoula, and L. Artús, “Raman scattering by the E 2h and A 1(LO) phonons of In xGa 1-xN epilayers (0.25 < x < 0.75) grown by molecular beam epitaxy,” *J. Appl. Phys.*, vol. 111, no. 6, p. 063502, Mar. 2012, doi: 10.1063/1.3693579.

125. C. A. M. Fabien and W. A. Doolittle, “Guidelines and limitations for the design of high-efficiency InGaN single-junction solar cells,” *Sol. Energy Mater. Sol. Cells*, vol. 130, pp. 354–363, Nov. 2014, doi: 10.1016/j.solmat.2014.07.018.

126. “NSM Archive - Indium Nitride (InN).” [Online]. Available:http://www.ioffe.ru/SVA/NSM/Semicond/InN/index.html [Accessed Jun. 27, 2021].

127. “NSM Archive - Gallium Nitride (GaN).” [Online]. Available:http://www.ioffe.ru/SVA/NSM/Semicond/GaN/index.html [Accessed Jun. 27, 2021].

128. J. Cao, Z. Wang, X. Zhan, Q. Wang, M. Safdar, Y. Wang, and J. He, “Vertical SnSe nanorod arrays: From controlled synthesis and growth mechanism to thermistor and photoresistor,” *Nanotechnology*, vol. 25, no. 10, p. 105705, Mar. 2014, doi: 10.1088/0957-4484/25/10/105705.

129. “Photoresistor Sensor.” [Online]. Available: https://diy.waziup.io/sensors/light/photoresistor.html [Accessed Jun. 26, 2021].

130. “Diode Equation | PVEducation.” [Online]. Available: https://www.pveducation.org/pvcdrom/pn-junctions/diode-equation [Accessed Jul. 02, 2021].

131. D. Zhu, J. Xu, A. N. Noemaun, J. K. Kim, E. F. Schubert, M. H. Crawford, and D. D. Koleske, “The origin of the high diode-ideality factors in GaInN/GaN multiple quantum well light-emitting diodes,” *Appl. Phys. Lett.*, vol. 94, no. 8, p. 81113, Feb. 2009, doi: 10.1063/1.3089687.

Appendix I: The Fabrication Process of Graded InGaN Solar Cell

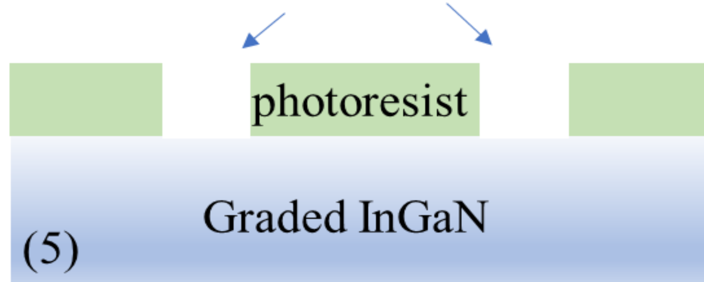

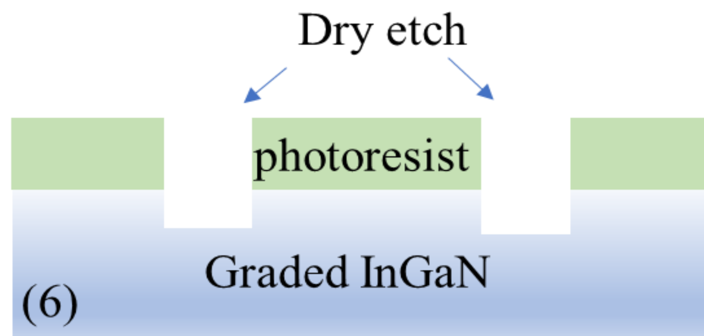

Remove photoresist

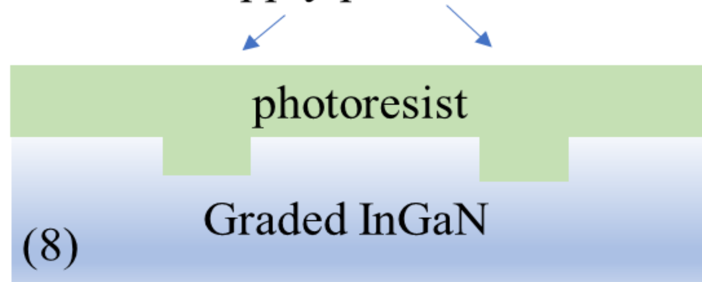

Contact mask

photoresist
Graded InGaN
(9)

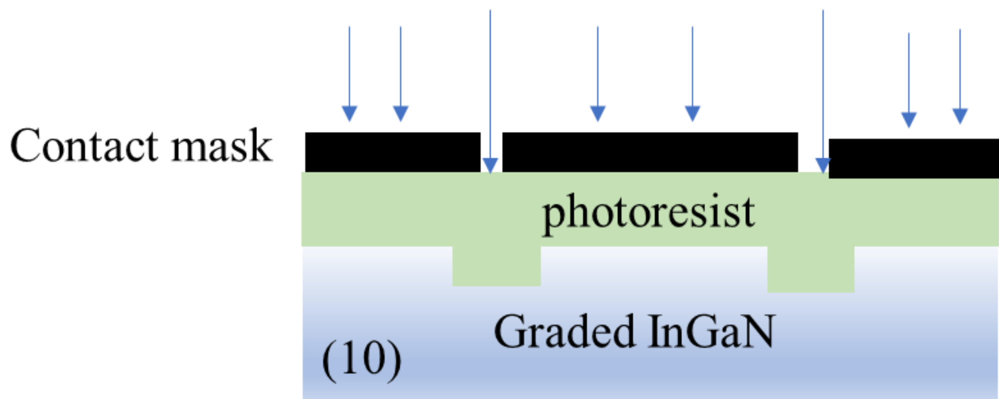
UV light
Contact mask
photoresist
Graded InGaN
(10)

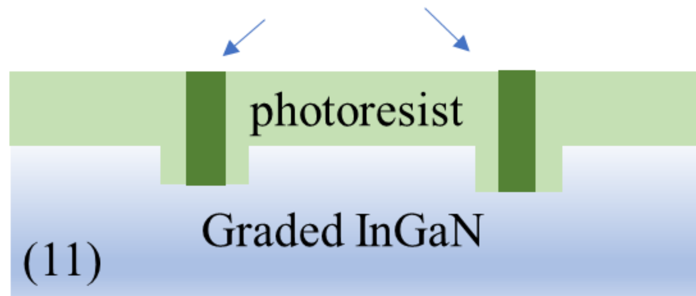
Exposed photoresist
photoresist
Graded InGaN
(11)

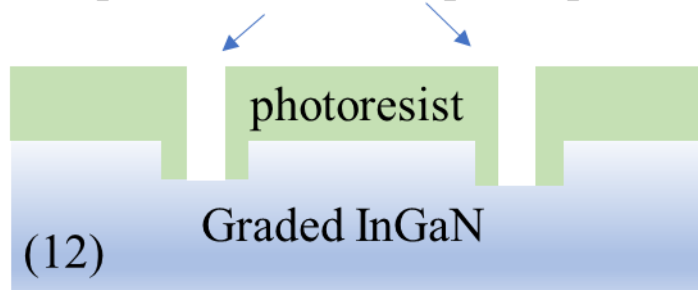
Developer remove the exposed photoresist
photoresist
Graded InGaN
(12)

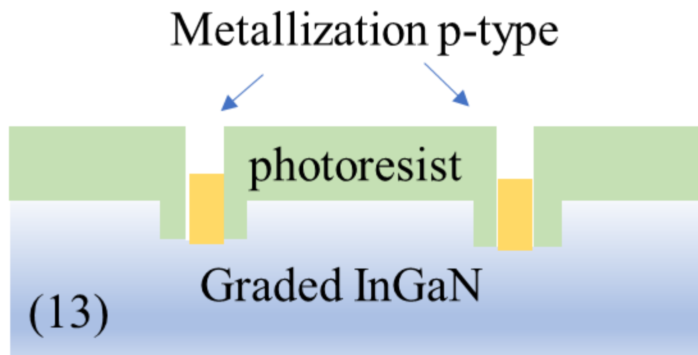

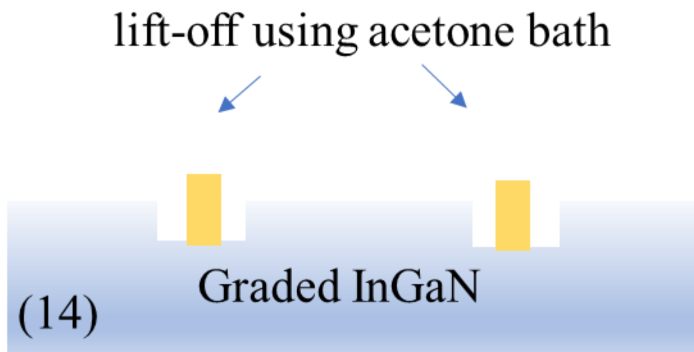

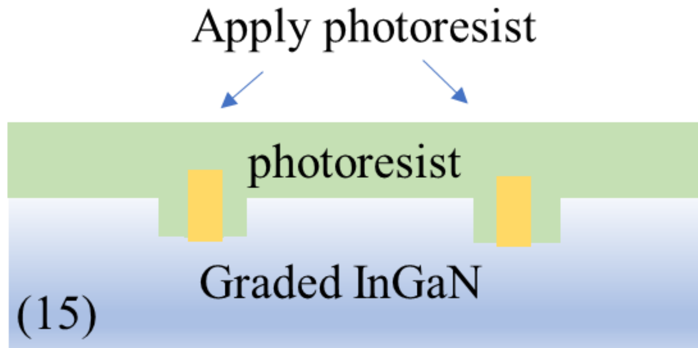

Contact mask

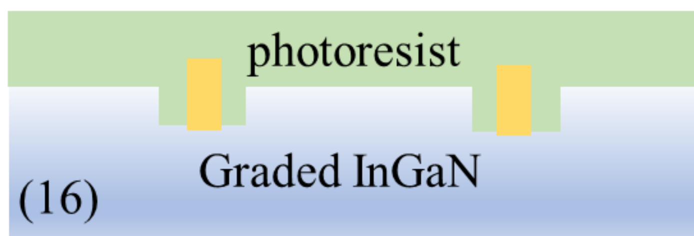

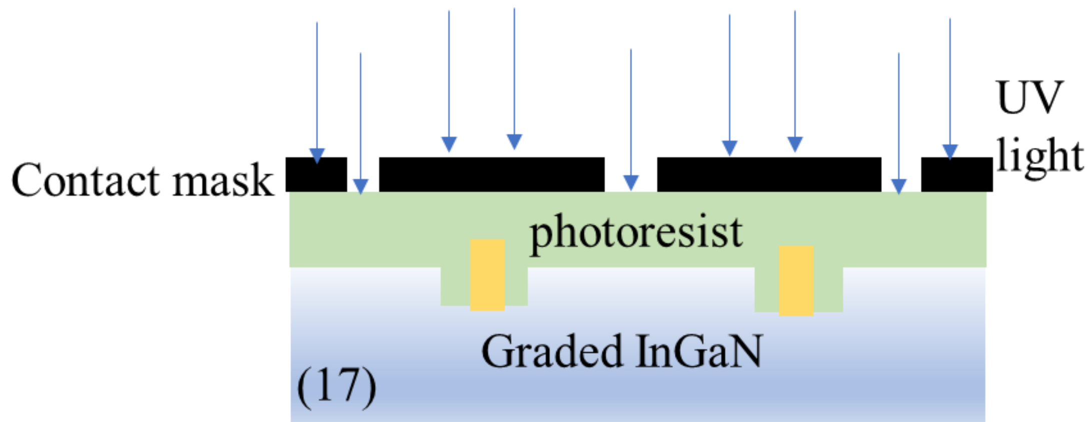
UV
light
Contact mask
photoresist
Graded InGaN
(17)

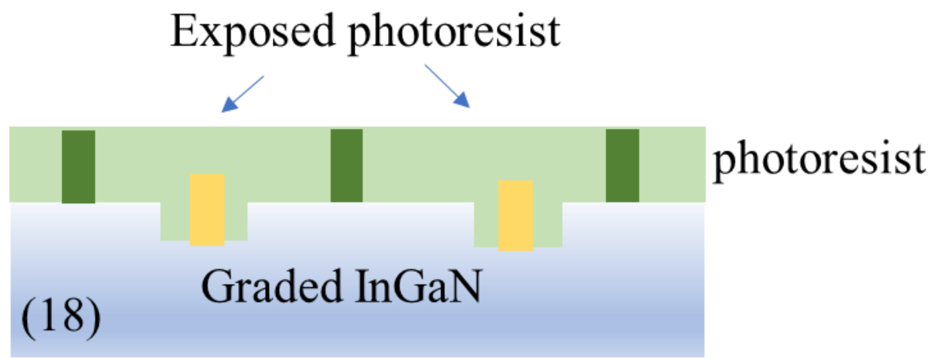
Exposed photoresist
photoresist
Graded InGaN
(18)

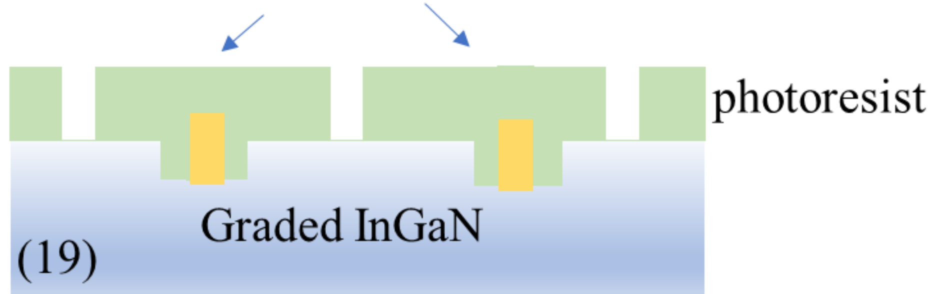
Developer remove the exposed photoresist
photoresist
Graded InGaN
(19)

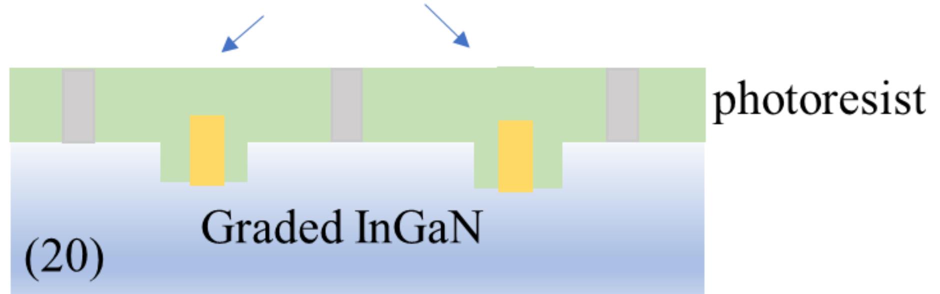
Metallization n-type
photoresist
Graded InGaN
(20)

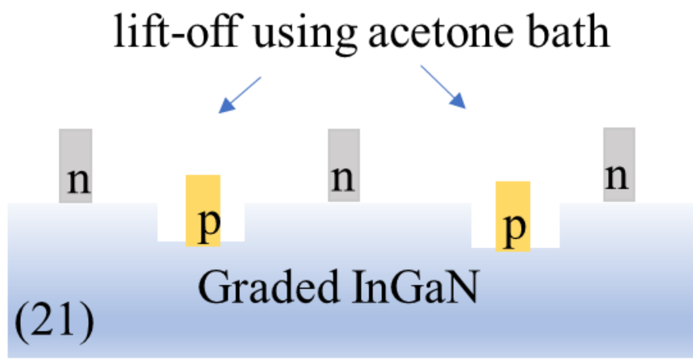
lift-off using acetone bath
n
p
n
p
n
Graded InGaN
(21)

Appendix A: Description of Research for Popular Publication

Three-Five Semiconductor Materials for Solar Cells Applications

By Manal Aldawsari

Sunlight is a source of life on this planet, not only for its heat and light, but also for mental and health benefits. It helps create strong bones of the human body through formation of vitamin D. Sunlight is also a great source for energy applications. Solar panels have been widely used to generate electricity as a renewable source of energy as well as to complement other sources of energy to reduce the dependence on fossil fuel.

Manal Aldawsari, a scientist and a graduate student at the University of Arkansas, has been passionate about the sun and its light and energy. Her research focus was on group III-nitride materials which have been proven to accomplish significant impact in the optoelectronics field.

Studying the material at nanoscale is a fascinating area of science. If you see, for example, a transmission electron microscope (TEM) sample, you would be surprised how tiny it is but how much information scientists can get out of it!

Working with Dr. Morgan Ware's team, we were able to make novel designs of InGaN materials (III-V) which can be used in optoelectronic devices. A solar cell is simply a device with a p-type material and an n-type material that are joined together to form a p-n junction. The working principle is converting the sunlight to electricity.

One thing that makes nitride materials attractive is the tunable band gap that changes with indium composition. This is what makes InGaN material have a wide band gap that spans the whole solar spectrum from ultraviolet region (UV) to near infrared (IR). However, there are

some challenges that are faced during the growth of the material. The growth of a thick material with full indium composition results in a defective material. Consequently, the optical and electrical performance of the device is jeopardized. Multiple approaches have been considered to produce high quality material, such as quantum wells, but there is still much room for improvement.

Full graded composition InGaN material is the solution. It is not only a solution for the growth of the material, but it also makes it possible for the sunlight to be completely absorbed at different depths in the material, hence, gaining the benefit of multijunction solar cells at lower cost.

Dr. Morgan Ware and his team have ongoing research developing this concept and investigating the graded InGaN material in different aspects. Optimization and studying the growth conditions and the material properties was the primary focus of Manal Aldawsari's PhD work. This material can then be utilized in different applications, particularly solar cells.

Appendix B: Executive Summary of Newly Created Intellectual Property

The following list of new intellectual property items were examined in this research:

1. Full graded composition InGaN with a reverse graded InGaN to create a p-n junction for solar cell application was investigated.
2. The optimal growth conditions were identified through a growth model.
3. The optical and structural characterization for graded InGaN.
4. Using SIMS In composition profile to simulate the band diagram as well as the optical transitions.

Appendix C: Potential Patent and Commercialization Aspects of Listed Intellectual Property Items

C.1 Patentability of Intellectual Property (Could Each Item be Patented)

There are no potential patent and commercialization aspects of listed intellectual property items. The list of new intellectual property items that were examined in this research cannot be patented because the results are based on existing knowledge and known methods.

C.2 Commercialization Prospects (Should Each Item Be Patented)

There is no commercialization prospects in this work.

C.3 Possible Prior Disclosure of IP

There is no possible prior disclosure of IP in this work.

Appendix D: Broader Impact of Research

D.1 Applicability of Research Methods to Other Problems

The use of graded InGaN material has great potential to improve different applications as a promising material for solar cells and sensitive photodetectors applications. The current solar cells have limitations in absorbing the solar spectrum. The low energy sunlight does not get absorbed while the high energy sunlight gets lost to heat which result in overall device performance degradation. Multijunction solar cells is one of the solutions to match the sunlight energy with different materials. This comes at the cost of the engineering simplicity and the expense.

The graded material makes it possible to absorb the whole sunlight spectrum at different depths with using only one material. This can be done by varying the In composition which results in changing the band gap of the material from near UV light to near IR covering the sunlight spectrum.

Other issues or challenges also can be tackled using graded InGaN such as doping the material as n or p type without adding dopants. Furthermore, applications for high temperatures or harsh environment also can be made using InGaN material such as concentrated solar cells. Another example is space solar power stations as GaN can tolerate the damage that can be caused by space radiation. Thus, this study helps to provide in depth understanding and characterization of the graded InGaN material that can contribute to advances in both research and applications. This information will open more opportunities for related InGaN structures to be grown and studied for future optoelectronic applications.

D.2 Impact of Research Results on U.S. and Global Society

Using InGaN material has a wide variety of applications such as lasers, light emitting diodes (LED) and solar cells. The impact of using graded InGaN material as an active layer for solar cell application is significant and was the focus of this research. The graded material helps to absorb the sunlight at different depths in the active layer utilizing the whole spectrum by using only one junction. Thus, it is similar to the multijunction solar cells but at a lower the cost.

Furthermore, exploring the graded InGaN material eases the path for further research in photovoltaic applications which is required to provide clean energy. This helps provide sustainable energy for not only the USA but also the world. Therefore, using III-V materials provides both economic advantages and environmental benefits for the US and global society.

D.3 Impact of Research Results on the Environment

The III-V materials are used in efficient-energy applications such as LED which is also cost effective. Furthermore, the temperature tolerance of InGaN material helps to save energy as high temperature devices do not require cooling systems.

Using InGaN based solar cells will save energy, decrease air pollution, and reduce the dependance on other sources of energy that are not renewable such as fossil fuel.

The impact of using InGaN material in applications such as LED and solar cells is well known as this material has been widely used previously. Therefore, it is well understood how to handle the chemical waste. All the safety standards were followed carefully in handling both the equipment and chemicals used in this research.

Appendix E: Microsoft Project for PhD. MicroEP Degree Plan

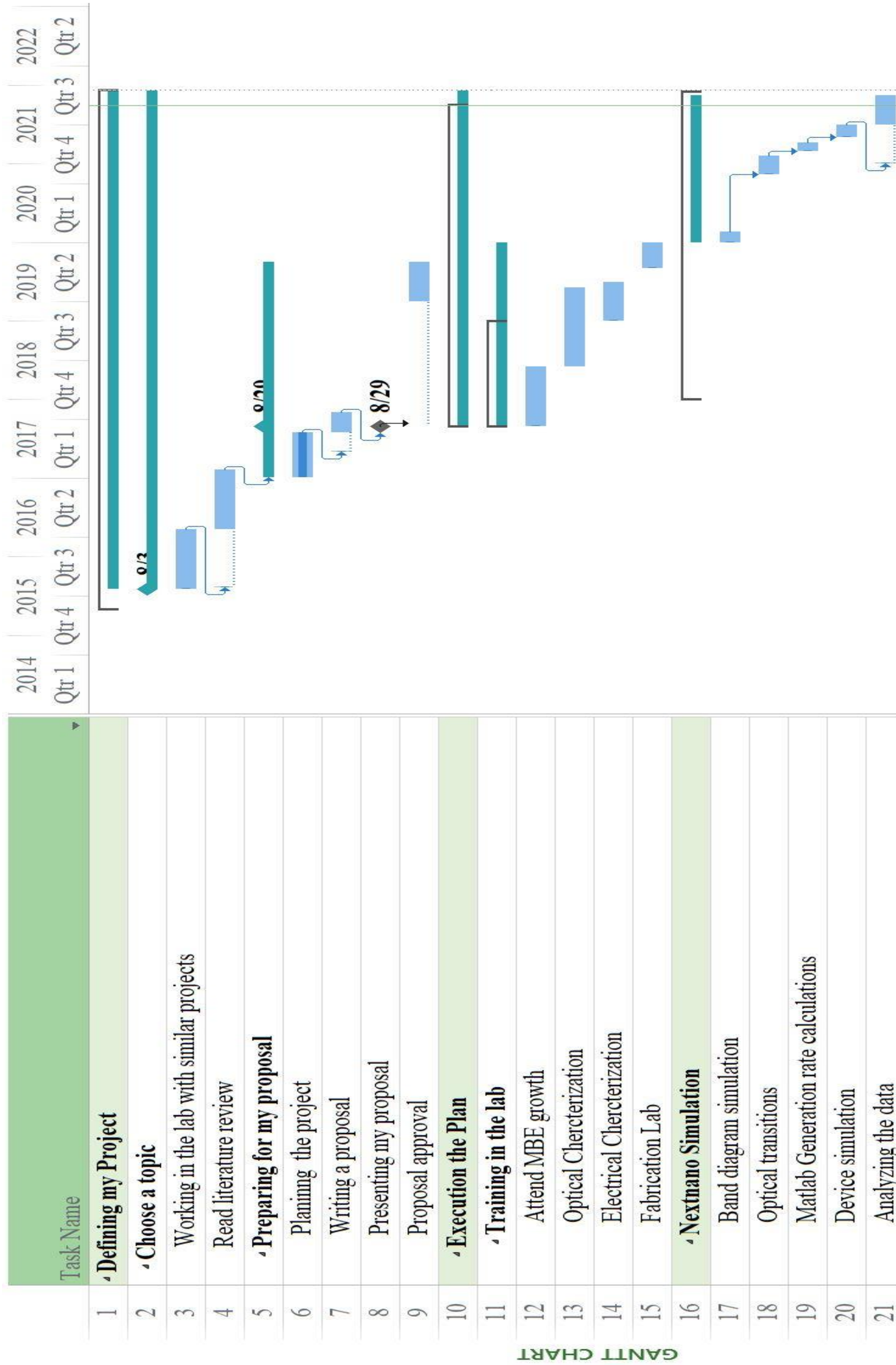

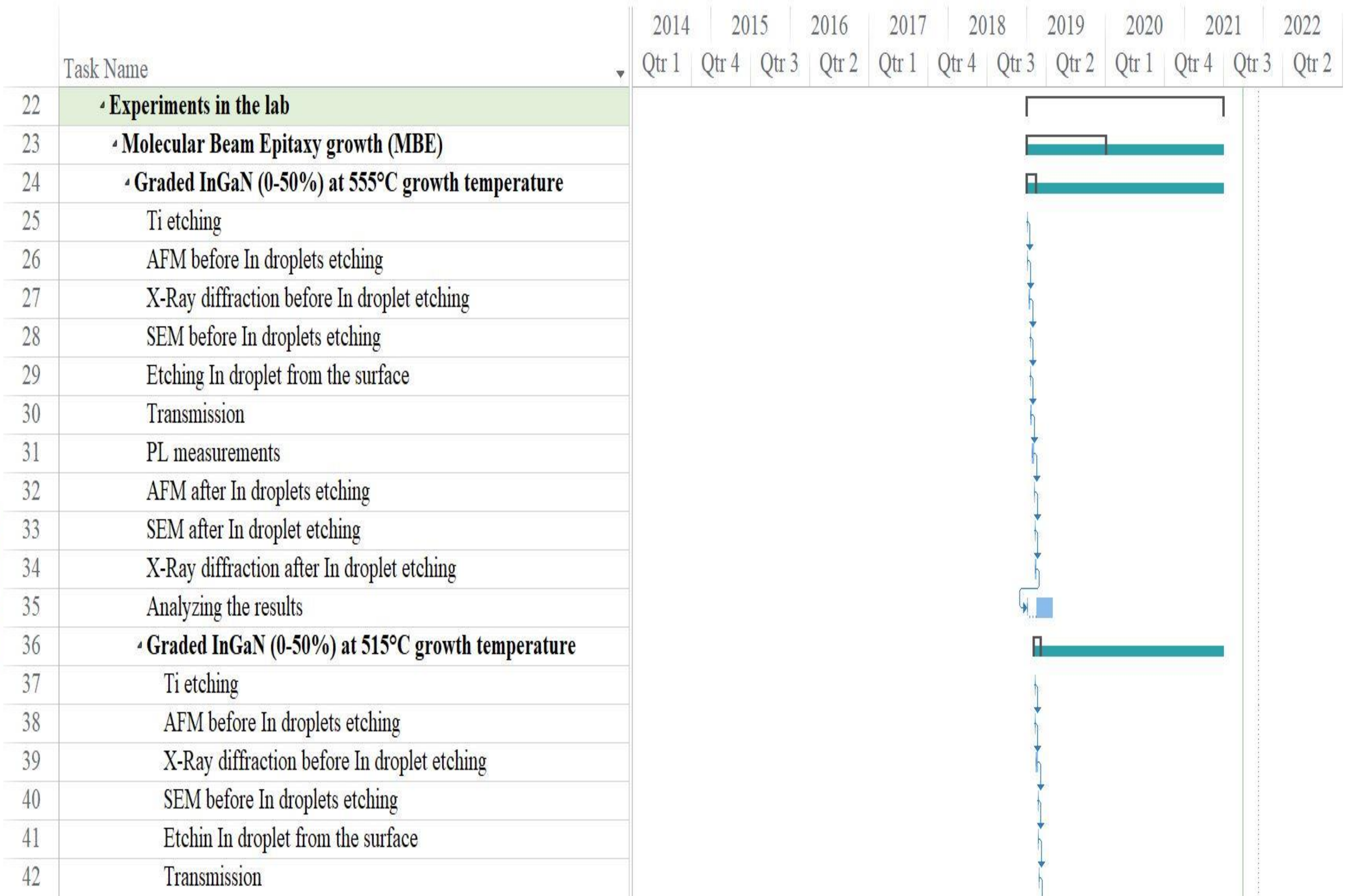
GANTT CHART
Task Name
2014
2015
2016
2017
2018
2019
2020
2021
2022
Qtr 1
Qtr 4
Qtr 3
Qtr 2
Qtr 1
Qtr 4
Qtr 3
Qtr 2
Qtr 1
Qtr 4
Qtr 3
Qtr 2
22 Experiments in the lab
23 Molecular Beam Epitaxy growth (MBE)
24 Graded InGaN (0-50%) at 555°C growth temperature
25 Ti etching
26 AFM before In droplets etching
27 X-Ray diffraction before In droplet etching
28 SEM before In droplets etching
29 Etching In droplet from the surface
30 Transmission
31 PL measurements
32 AFM after In droplets etching
33 SEM after In droplet etching
34 X-Ray diffraction after In droplet etching
35 Analyzing the results
36 Graded InGaN (0-50%) at 515°C growth temperature
37 Ti etching
38 AFM before In droplets etching
39 X-Ray diffraction before In droplet etching
40 SEM before In droplets etching
41 Etchin In droplet from the surface
42 Transmission

	Task Name
43	PL measurements
44	AFM after In droplets etching
45	SEM after In droplet etching
46	X-Ray diffraction after In droplet etching
47	Analyzing the results
48	**Graded InGaN (0-50%) at 475°C growth temperature**
49	Ti etching
50	AFM before In droplets etching
51	X-Ray diffraction before In droplet etching
52	SEM before In droplets etching
53	Etchin In droplet from the surface
54	Transmission
55	PL measurements
56	AFM after In droplets etching
57	SEM after In droplet etching
58	X-Ray diffraction after In droplet etching
59	Analyzing the results
60	**Full graded composition grown at 475°C and 400°C**
61	Ti etching
62	AFM before In droplets etching
63	X-Ray diffraction before In droplet etching

GANTT CHART

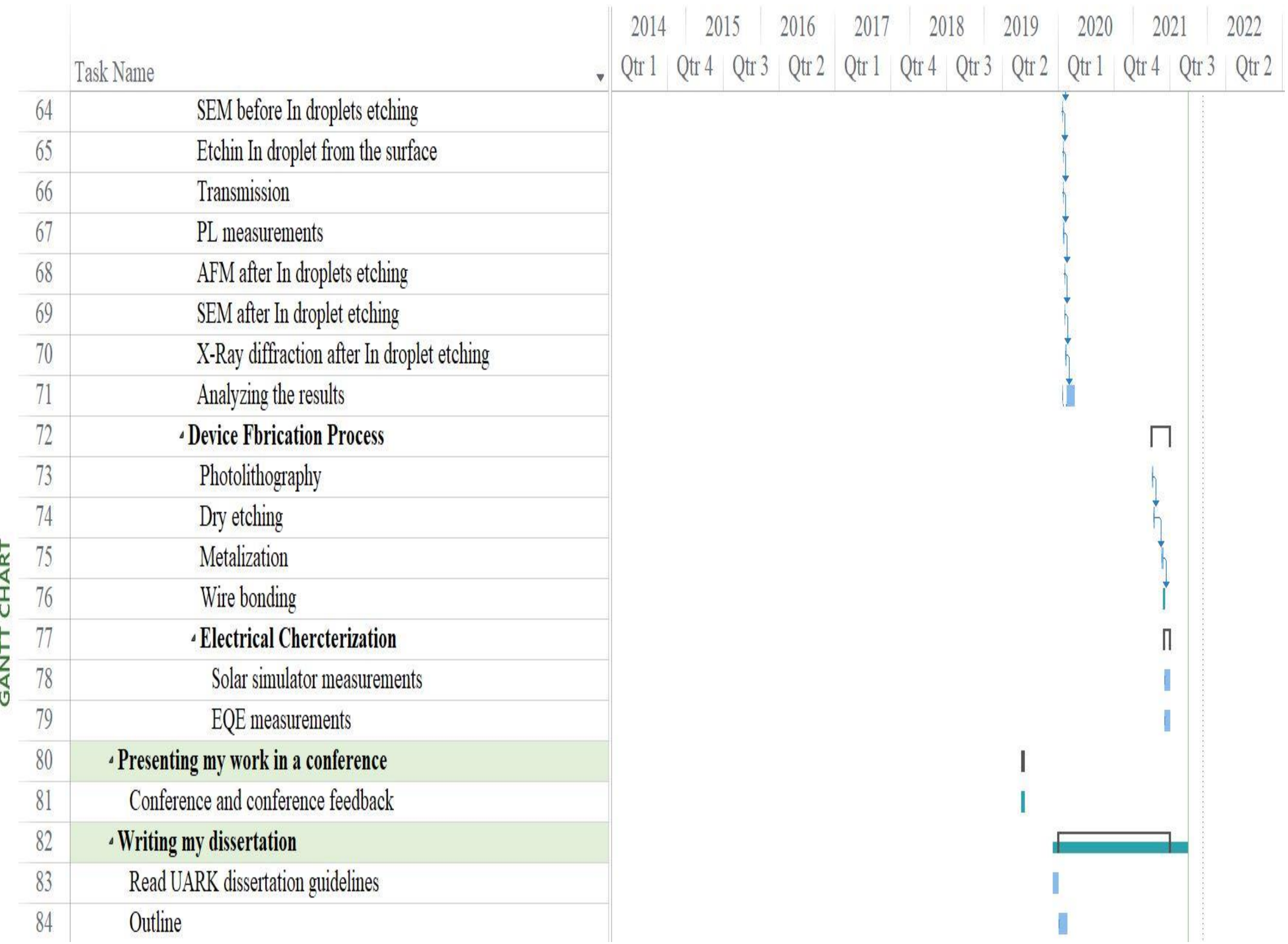

GANTT CHART
Task Name
2014 Qtr 1
2015 Qtr 4
2015 Qtr 3
2016 Qtr 2
2017 Qtr 1
2018 Qtr 4
2018 Qtr 3
2019 Qtr 2
2020 Qtr 1
2021 Qtr 4
2021 Qtr 3
2022 Qtr 2
64 SEM before In droplets etching
65 Etchin In droplet from the surface
66 Transmission
67 PL measurements
68 AFM after In droplets etching
69 SEM after In droplet etching
70 X-Ray diffraction after In droplet etching
71 Analyzing the results
72 Device Fbrication Process
73 Photolithography
74 Dry etching
75 Metalization
76 Wire bonding
77 Electrical Chercterization
78 Solar simulator measurements
79 EQE measurements
80 Presenting my work in a conference
81 Conference and conference feedback
82 Writing my dissertation
83 Read UARK dissertation guidelines
84 Outline

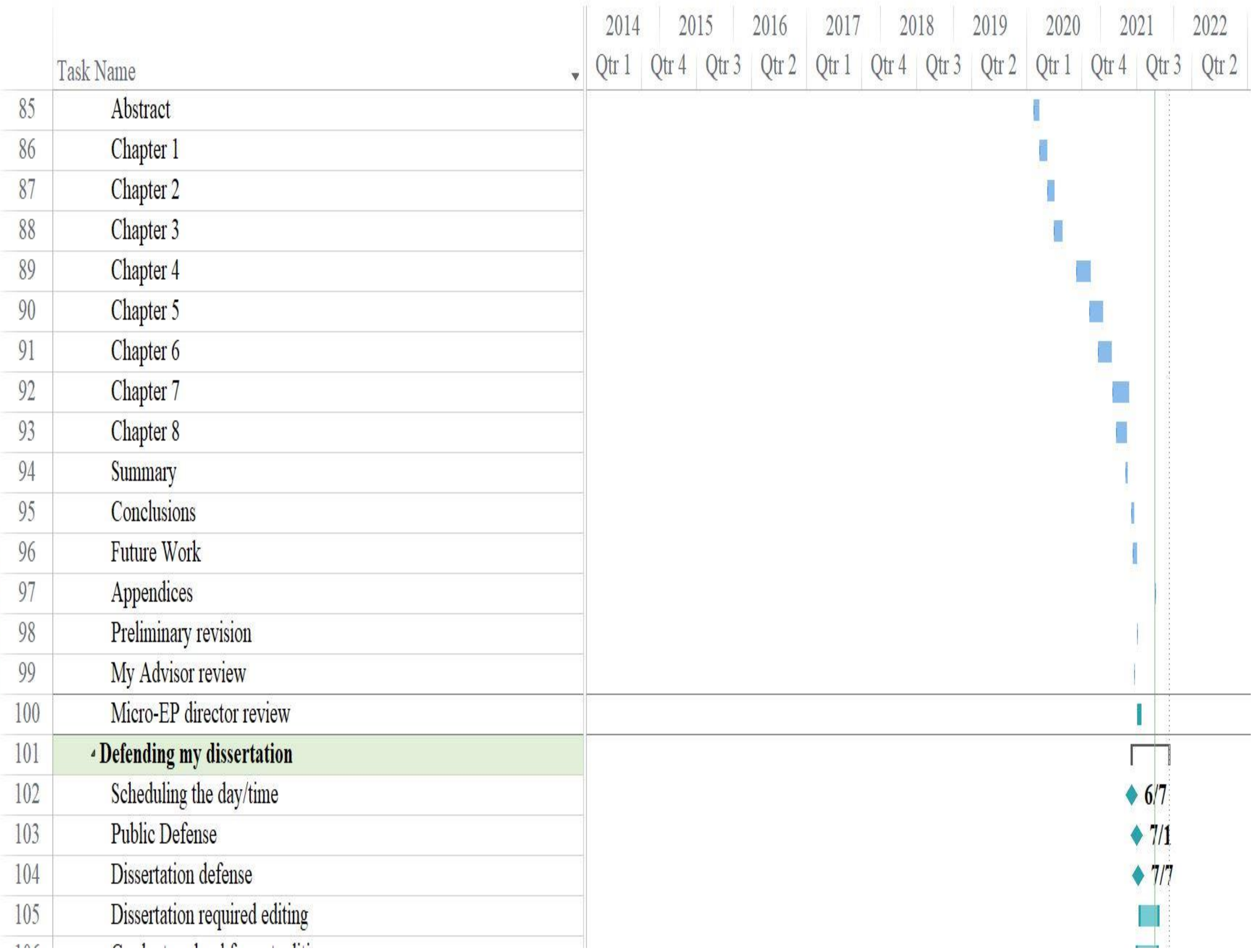

GANTT CHART
Task Name
2014 2015 2016 2017 2018 2019 2020 2021 2022
Qtr 1 Qtr 4 Qtr 3 Qtr 2 Qtr 1 Qtr 4 Qtr 3 Qtr 2 Qtr 1 Qtr 4 Qtr 3 Qtr 2
85 Abstract
86 Chapter 1
87 Chapter 2
88 Chapter 3
89 Chapter 4
90 Chapter 5
91 Chapter 6
92 Chapter 7
93 Chapter 8
94 Summary
95 Conclusions
96 Future Work
97 Appendices
98 Preliminary revision
99 My Advisor review
100 Micro-EP director review
101 Defending my dissertation
102 Scheduling the day/time
103 Public Defense
104 Dissertation defense
105 Dissertation required editing
6/7
7/1
7/7

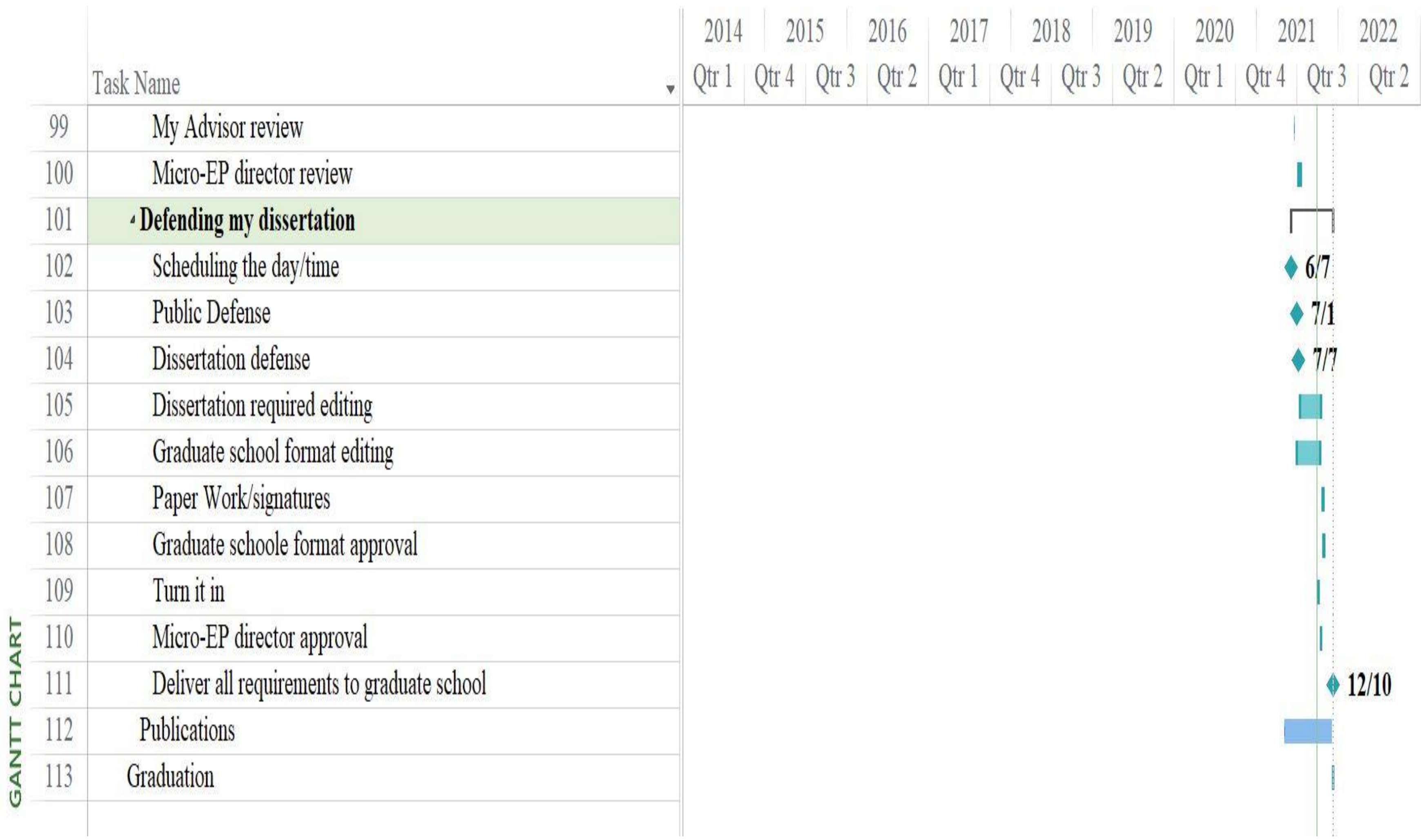

GANTT CHART
Task Name
2014 2015 2016 2017 2018 2019 2020 2021 2022
Qtr 1 Qtr 4 Qtr 3 Qtr 2 Qtr 1 Qtr 4 Qtr 3 Qtr 2 Qtr 1 Qtr 4 Qtr 3 Qtr 2
99 My Advisor review
100 Micro-EP director review
101 Defending my dissertation
102 Scheduling the day/time
103 Public Defense
104 Dissertation defense
105 Dissertation required editing
106 Graduate school format editing
107 Paper Work/signatures
108 Graduate schoole format approval
109 Turn it in
110 Micro-EP director approval
111 Deliver all requirements to graduate school
112 Publications
113 Graduation
6/7
7/1
7/7
12/10

Appendix F: Identification of All Software Used in Research and Dissertation Generation

Computer #1:
Model Number: HP ENVY 14t-u000 Windows 8 Business Laptop PC
Serial Number: 5CD4386MS1
Location: 4209 NE Meadow Creek Circle, Fayetteville Ar,72703
Owner: Manal Abdullah Aldawsari

Computer #2:
Model Number: Dell XPS 15 7590
Serial Number: 259Q3X2
Location: 4209 NE Meadow Creek Circle, Fayetteville Ar,72703
Owner: Manal Abdullah Aldawsari

Software #1:
Name: Microsoft Office 365-Student version
Purchased by: University of Arkansas Site License

Software #2:
Name: MATLAB R2018b
Purchased by: University of Arkansas Site License

Software #3:
Name: MATLAB R2019b
Purchased by: University of Arkansas Site License

Software #4:
Name: MATLAB R2020b
Purchased by: University of Arkansas Site License

Software #5:
Name: OriginPro 2015b (Research Lab) -Student Version
Purchased by: Manal Aldawsari

Software #6:
Name: OriginPro 2018b (Research Lab) -Student Version
Purchased by: Manal Aldawsari

Software #7:
Name: OriginPro 2019b (Research Lab)
Purchased by: Dr. Morgan Ware

Software #8:
Name: nextnano^3
Purchased by: Dr. Morgan Ware

Software #9:
Name: Nanoscope Analysis 1.5
Purchased by: Free

Software #10:
Name: ImageJ
Purchased by: Free

Software #11:
Name: Microsoft Project 2010
Purchased by: University of Arkansas Site License

Software #12:
Name: Dropbox
Purchased by: Free

Software #13:
Name: Mathematica
Purchased by: University of Arkansas Site License

Software #14:
Name: Mendeley
Purchased by: Free

Appendix G: All Publications Published, Submitted and Planned

Published:

P. K. Ghosh, H. V. Stanchu, Y. Maidaniuk, M. Sarollahi, **M. A. Aldawsari**, A. V. Kuchuk, Y. I. Mazur, G. J. Salamo, and M. E. Ware, "Investigation of the Structural and Optical Properties of Compositionally V-Graded Strained InxGa1–xN Layers," Phys. Status Solidi Basic Res., vol. 257, no. 4, Apr. 2020, doi: 10.1002/PSSB.201900591.

M. Sarollahi, P. K. Ghosh, **M. A. Aldawsari**, A. Kuchuk, and M. E. Ware, "Luminescence Properties of GaN/$In_xGa_{1-x}N$/$In_yGa_{1-y}N$ Double Graded Structures (Zigzag Quantum Wells)," J. Electron. Mater., vol. 49, no. 6, pp. 3512–3519, Jun. 2020, doi: 10.1007/S11664-020-08033-W.

M. Sarollahi, P. K. Ghosh, **M. A. Aldawsari**, S. Davari, M. I. Refaei, R. Alhelais, Y. I. Mazur, and M. E. Ware, "Experiment-simulation comparison of luminescence properties of GaN/InGaN/GaN double graded structures," J. Lumin., vol. 240, p. 118411, Dec. 2021, doi: 10.1016/J.JLUMIN.2021.118411.

M. Sarollahi, R. Allaparthi, R. Alhelais, **M. A. Aldawsari**, M. A. Refaei, M. H. U. Maruf, and M. E. Ware, "Effects of numbers of wells on optical properties of periodic InGaN graded structure," *https://doi.org/10.1117/12.2598268*, vol. 11800, pp. 54–60, Aug. 2021, doi: 10.1117/12.2598268.

Submitted:

Study of Simulation of GaN/InGaN Double Graded Structure and single quantum well solar cell under strain condition Mirsaeid Sarollahi, **Manal A. Aldawsari** et al, (submitted to journal of Vacuum Science & Technology B)

Planned:

Raman and x-ray reciprocal space mapping study of thick graded InGaN films grown by molecular beam epitaxy
Manal A. Aldawsari, Pijush K. Ghosh, Mirsaeid Sarollahi, Andrian Kuchuk, Morgan E Ware (In preparation)

Growth model for graded InGaN thick films
Manal A. Aldawsari, Pijush K. Ghosh, Mirsaeid Sarollahi, Morgan E Ware (In preparation)

Conferences:

Manal A. Aldawsari, Pijush K. Ghosh, Mirsaeid Sarollahi, Andrian Kuchuk, Morgan E Ware," *Optical Properties of Thick Compositionally Graded InGaN Films*" 13th International

Conference on Nitride Semiconductors ICNS-13 (2019), 7-12 July in Bellevue, Washington, USA.

Pijush K. Ghosh, Hryhorii V Stanchu, Yurii Maidaniuk, Mirsaeid Sarollahi, **Manal Aldawsari**, Andrian V Kuchuk, Yuriy I Mazur, Gregory J Salamo, Morgan E Ware,"*Investigation of the Growth, Structural, and Optical Properties of Compositionally V-Graded Strained* $In_xGa_{1-x}N$ *Layers*" 13th International Conference on Nitride Semiconductors ICNS-13 (2019), 7-12 July in Bellevue, Washington, USA.

Mirsaeid Sarollahi, Pijush K Ghosh, **Manal A Aldawsari**, Yurii Maidaniuk , Andrian Kuchuk, Yurii Maidaniuk, Gregory J Salamo, Morgan E Ware, "*Luminescent Properties of Zigzag-Graded InGaN Quantum Wells*" The 61st Electronic Materials Conference, June 26-28, 2019. University of Michigan Ann Arbor, Michigan, USA.

Mirsaeid Sarollahi, Rohith Allaparthi, Reem Alhelais, **Manal A. Aldawsari**, Malak A. Refaei, Md Helal Uddin Maruf, Morgan E. Ware "*Effects of numbers of wells on optical properties of periodic InGaN graded structure*" SPIE NanoScience + Engineering, 2021, August 1st-5^{th}2021, San Diego,CA.